EVALUATING FLUID-ROCK INTERACTIONS IN GEOTHERMAL AND CONTACT METAMORPHIC SYSTEMS

by

Kristie S. McLin

A dissertation submitted to the faculty of
The University of Utah
in partial fulfillment of the requirements for the degree of

Doctor of Philosophy

in

Geology

Department of Geology and Geophysics

The University of Utah

May 2012

The University of Utah Graduate School

STATEMENT OF DISSERTATION APPROVAL

The dissertation of **Kristie S. McLin**

has been approved by the following supervisory committee members:

John R. Bowman	, Chair	**3/5/2012** Date Approved
Joseph N. Moore	, Member	**3/5/2012** Date Approved
John P. Kaszuba	, Member	**2/6/2012** Date Approved
Erich U. Petersen	, Member	**3/5/2012** Date Approved
Ronald L. Bruhn	, Member	**3/5/2012** Date Approved

and by **D. Kip Solomon** , Chair of the Department of **Geology and Geophysics**

and by Charles A. Wight, Dean of The Graduate School.

ABSTRACT

The study of fluid-rock interactions provides insight into subsurface geologic processes, such as diagenesis, hydrothermal alteration and metamorphism. Understanding and predicting these interactions also helps us assess the geologic impact of hydrocarbon recovery and geothermal production and injection. Therefore, the study of fluid-rock interactions has both geologic and economic impact.

At the Dixie Valley geothermal field, NV, precipitated calcite and aragonite within a production well trapped boiling fluids in fluid inclusions. The trapped gases were analyzed and shown to be compositionally different than those sampled at the well head. The inclusions trapped a greater ratio of light gases CH_4 and H_2 to CO_2 than those sampled at the well head. This result indicates that the fluid inclusions trapped the initial steam fraction during boiling.

Declining performance of injection wells at the Coso and Salton Sea geothermal fields, CA, were found to result from mineral deposition in the near-wellbore environment during fluid injection. At Coso, opal-A and minor calcite scale mineral precipitates were found in cuttings from wells drilled near previously operating injection wells. At the Salton Sea, cuttings from a deepened injection well contained banded barite, fluorite, amorphous silica, and minor anhydrite scales. Mineral precipitation was modeled and predicted with the non-isothermal reactive transport modeling code TOUGHREACT. Geochemical simulations were also performed to predict the consequences of injecting

H_2SO_4 modified fluid for mitigating silica precipitation at Coso using TOUGHREACT. The models predict that silica precipitation will be reduced significantly by maintaining pH of 5 or less. This can be accommodated in the models by reducing the kinetic rate constant for silica precipitation. TOUGHREACT simulations also predict that corundum proppants will be chemically stable under geothermal conditions.

The formation of talc in the outer aureole of the Alta Stock does not define a regular isogradic surface, unlike isograds in the inner aureole. Examination of mineral and fluid stabilities in the H_2O-CO_2-NaCl system shows that several fluid evolution scenarios, including fluid immiscibility, may produce the observed talc heterogeneity.

For Ryan, Liam, Oona, and all of my very supportive family.

TABLE OF CONTENTS

ACKNOWLEDGEMENTS

I would like to thank my advisors, Dr. John R. Bowman and Dr. Joseph N. Moore, for making this dissertation possible. Their patience and attention to detail are much appreciated. I would also like to thank my committee members, Dr. John P. Kaszuba, Dr. Erich U. Petersen, and Dr. Ronald L. Bruhn, who put considerable effort into my degree program, as well.

My family has been so considerate, patient, and supportive. This is especially true of my husband Ryan, son Liam, and daughter Oona. Nana (Jody) and Dadu (Greg) Diehl, (Aunt) Elisa and (Aunt) Alaina Diehl, and Grandma (Debbie) and Grandpa (Steve) McLin all made considerable efforts to take care of us when we needed it the most. Without their help, this would not have been possible, so I thank them. My grandparents Joseph and Dolores Sobieski and Roland and Edith Diehl also provided much needed support along the way.

I would like to thank the US Department of Energy (DE-FG36-04GO14292 & -FG36-08GO18189) and the Petroleum Research Fund for the funding that made my dissertation projects possible.

Last, but certainly not least, I want to thank Dr. David I. Norman (1940-2008), who inspired me to pursue the path that led me here.

CHAPTER 1

MINERALOGY AND FLUID INCLUSION GAS CHEMISTRY OF PRODUCTION WELL MINERAL SCALE DEPOSITS AT THE DIXIE VALLEY GEOTHERMAL FIELD, USA

Abstract

At the Dixie Valley geothermal field, Nevada, USA, fluid boiling triggered the precipitation of carbonate scale minerals in concentric bands around tubing inserted into production well 28-33. When the tubing was removed, this mineral scale was sampled at 44 depth intervals between the well head and 1227 m depth. These samples provide a unique opportunity to evaluate the effects of fluid boiling on the scale mineralogy and geochemistry of the vapor and liquid phase. In this study, the mineralogy of the scale deposits and the composition of the fluid inclusion gases trapped in the mineral scales were analyzed.

The scale consists mainly of calcite from 670-1112 m depth and aragonite from 1125 to 1227 m depth, with traces of quartz and Mg smectite. Mineral textures, including hopper growth, twinning, and fibrous growth in the aragonite and banded deposits of fine grained calcite crystals, are the result of progressive boiling. The fluid inclusion noncondensable gas was dominated by CO_2. However, significant variations in He

relative to N_2 and Ar provide evidence that the geothermal reservoir consists of mixed source deeply circulating reservoir water and shallow, air saturated meteoric water. Gas analyses for many inclusions also showed higher CH_4 and H_2 relative to CO_2 than measured in gas sampled from this well, other production wells, and fumaroles. These inclusions are interpreted to have trapped CH_4 and H_2 enriched gas resulting from early stages of boiling.

Introduction

Geothermal systems provide natural laboratories for understanding the behavior and processes affecting fluids within the crust. The gas composition of geothermal fluids can provide important information on the fluid origin, temperature, and evolution (e.g. Giggenbach, 1980, 1986). Similarly, the gas composition of geothermal fluid inclusions can be used to trace fluid sources and histories. CO_2 is the dominant gas in geothermal waters, and where other data is absent, is also considered to be the dominant gaseous species in fluid inclusions from geothermal and epithermal systems (Hedenquist and Henley, 1985). However, investigations by Norman and Musgrave (1994), Graney and Kesler (1995), Norman et al. (1996, 1997, 1999), and Moore et al. (2000, 2001) suggest other gases (CH_4, H_2) may be present in significant concentrations. Moore et al. (2000, 2001) further suggest that higher concentrations of these light gases in fluid inclusions represent preferential partitioning of these gases into the vapor phase during early boiling. As with CO_2, these gases can significantly influence the ice melting temperature and therefore apparent salinities of the inclusion fluid, yielding estimates of salinities that are too high.

Boiling occurs in geothermal systems, either naturally or due to pressure changes during production. Phase separation within production wells can result in the deposition of carbonate and silicate minerals. Simmons and Christenson (1994) and Simmons and Browne (2000) described calcite deposition in boiling environments in geothermal wells. These scale minerals can significantly reduce flow in wells, and consequently scale inhibitor is used to mitigate their formation. However, failure of the inhibitor can lead to rapid mineral deposition, as was found in the Dixie Valley geothermal field production well 28-33. Carbonate and silicate minerals formed around tubing that was inserted into the well to deliver scale inhibitor. This scale was sampled at 44 depth intervals from inside the well head down to 1227 m depth when the tubing was removed. Because these mineral deposits spanned the boiling column as estimated by pressure distributions, the samples provide an opportunity to examine the effects of boiling on the scale mineralogy and textures. It also provides an unusual opportunity to compare the composition of gases measured at the well head with the compositions of gases trapped by fluid inclusions in the scale minerals during production of these fluids. There are no previous studies that have related the well gas chemistry to fluid inclusion gas chemistry in geothermal fields. In this study, we directly measure and relate gases trapped in fluid inclusions from these scale minerals to the chemistry of the gases sampled from well 28-33.

Geologic Setting

Dixie Valley is located 160 km northeast of Fallon, Nevada between the Stillwater and Clan Alpine Ranges (Fig. 1.1A). The valley trends NNE and is 120 km long by 20 km wide. Dixie Valley is located in the southern end of a region of elevated

heat flow known as the Battle Mountain High (Bergfeld et al., 2001). The geothermal reservoir is hosted in Triassic to Jurassic marine quartzite, siltstone, shale, and volcaniclastic rocks. The reservoir is overlain by a suite of oceanic crustal rocks that include gabbro, diorite, and basalt (Speed, 1976; Weibel, 1987; Lutz et al., 1997). The Triassic and Jurassic units are imbricated by three thrust faults and intruded by Cretaceous granodiorite (Goff et al., 2002). Oligocene ignimbrites and the Miocene Table Mountain Basalt overlie these older rocks in the valley (Goff et al., 2002). Most geologic units are extensively altered by hydrothermal activity (Goff et al., 2002).

Dixie Valley was formed by Basin and Range tectonic events. The geothermal field is classified as an "extensional" geothermal resource (Kennedy and van Soest, 2006). Fluid production is from the Stillwater fault zone (Fig. 1.1B). Thermal gradients indicate that heat is transported advectively through the fault system by upward flow of geothermal fluids (Blackwell et al., 2000, 2002).

The Dixie Valley power plant is located southeast of the Stillwater Range (Fig. 1.1B) and has operated continuously since 1988. The plant currently produces around 66 MWe. Production reservoir fluid temperatures are between 225 and 245^{o}C (Benoit, 1992; Bergfeld et al., 2001), though temperatures as high as 285^{o}C are found in wells drilled 5 km to the south (Blackwell, 2000). Production depths are between 2,400 and 2700 m (Kennedy and van Soest, 2006). The power plant and wells are located southeast of the surface expression of the Stillwater fault. Active and fossil hot springs and fumaroles lie along the fault zone from a few km north of the plant (Senator fumarole group) to an area 20 km to the southwest of the power plant (Dixie hot springs) (Bergfeld et al., 2001). In addition, hot fluids discharge into shallow aquifers in the region. Previous studies have

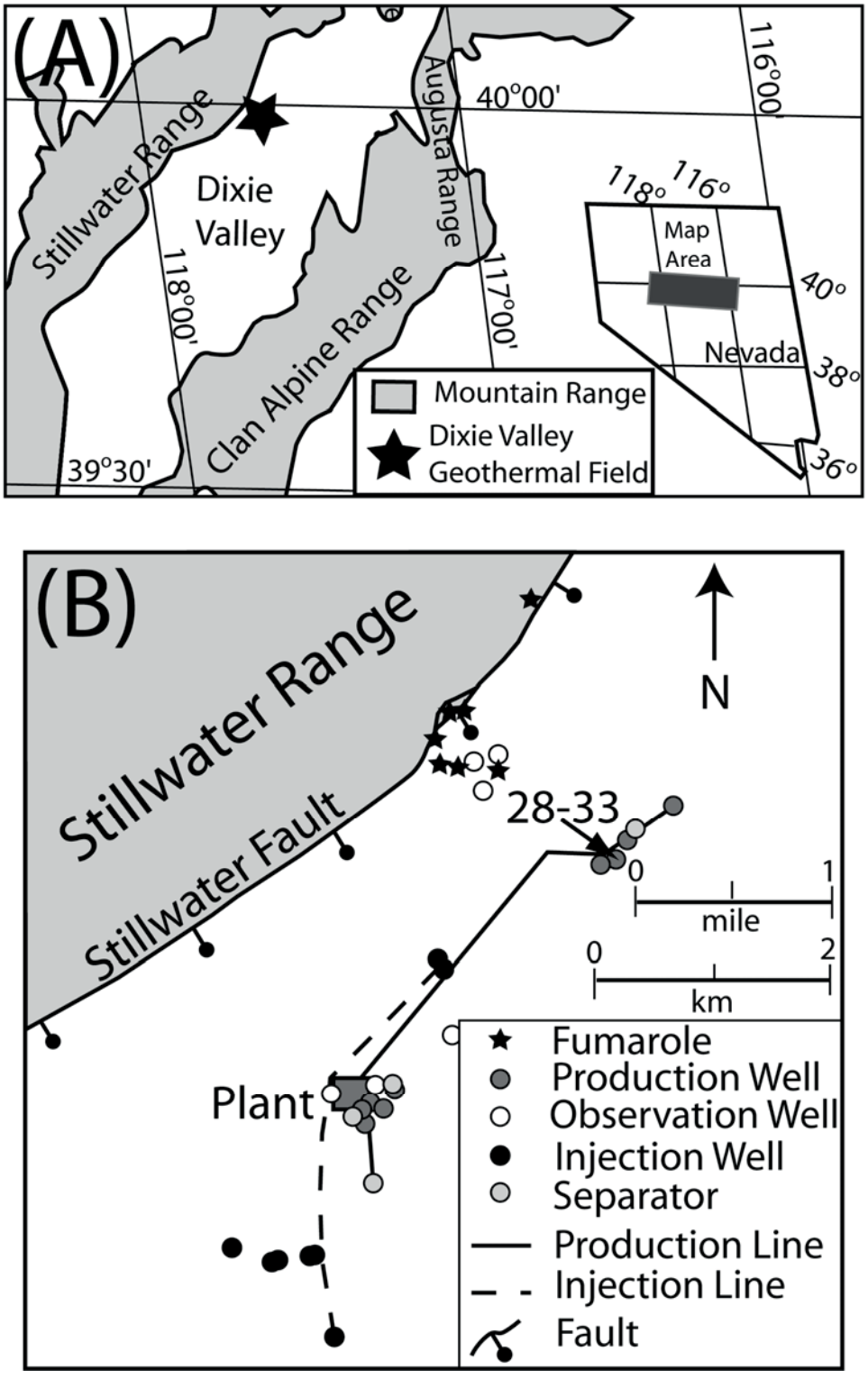

Fig. 1.1. Location maps of the Dixie Valley geothermal field. (A) Map showing location of Dixie Valley geothermal field, surrounding mountain ranges, and valleys (modified from Bergfeld et al. 2001). (B) Map showing location of the wells and fumaroles in the vicinity of the Dixie Valley geothermal power plant (modified from Goff et al. 2002).

measured the gas compositions discharged by wells, fumaroles, springs, and soils in the geothermal field and surrounding areas (e.g. Bergfeld et al., 2001; Goff et al., 2002; Kennedy and van Soest, 2006). The gas composition of the fumaroles indicates a mixture of air or gases from air saturated water and gases from a deeper geothermal source (Bergfeld et al., 2001). Their $\delta^{13}C$ values suggest that the reservoir CO_2 is produced by thermal decarbonation of hydrothermal calcite veins (Bergfeld et al., 2001). Helium isotope data imply mixing between a deeply sourced geothermal reservoir fluid and shallower meteoric waters. R_a values of 0.7-0.76 have been interpreted to indicate the presence of a mantle derived He component (Kennedy and van Soest, 2006).

History of Well 28-33

Drilling of well 28-33 was initiated in May, 1990 and completed in July, 1990. The well was drilled to a total measured depth (TD) of 2898 m. The main productive fractures were penetrated between 2784 and 2788 m depth. Temperature surveys for well 28-33 taken while the well was flowing are shown in Fig. 1.2. and indicate that initiation of boiling occurs between 1000 and 1200 m depth. During a 1993 clean out of the well, scale minerals on the well bore walls were found to be approximately 1 cm thick above 950 m depth. Below 950 m, no mineral scale was observed. Tubing was inserted into 28-33 after this clean out to deliver scale inhibitor into the well. Nalco 1340 HP was used as a scale inhibitor until 1998 when it was replaced by Nalco 9354. In 2001, after an acid cleanout of several production wells, Nalco 1340 HP was again used as the scale inhibitor in the Dixie Valley production wells. The tubing from 28-33 was removed during the

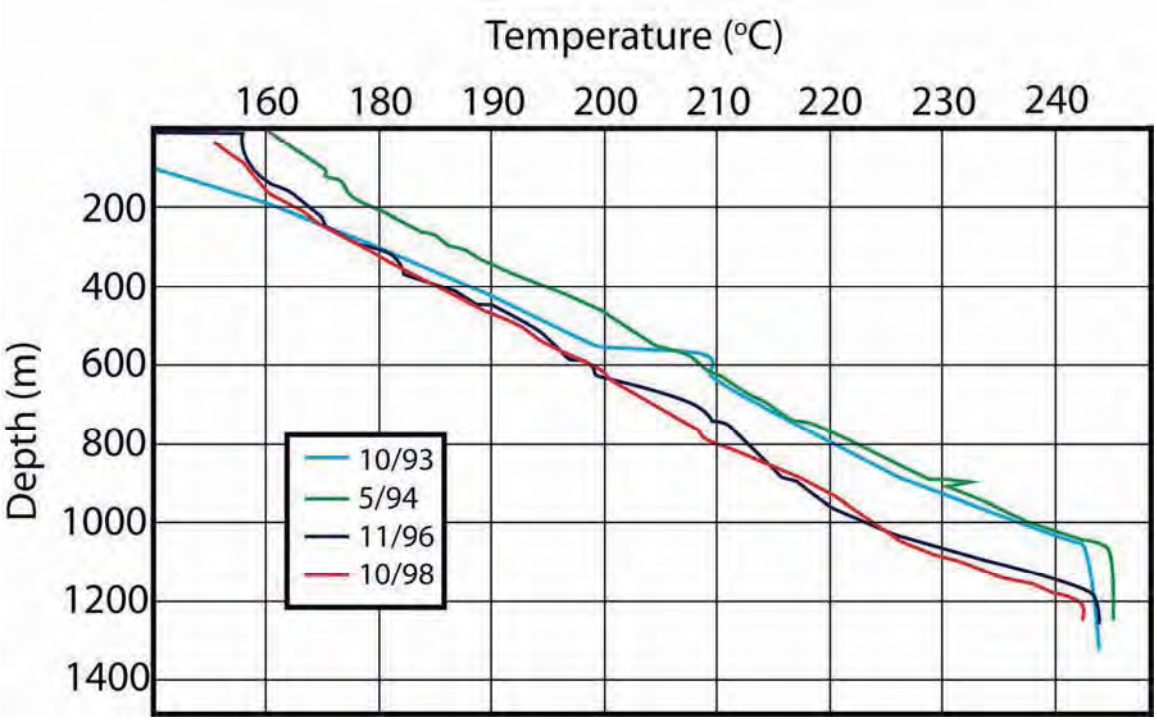

Fig. 1.2. Flowing temperature log for well 28-33 from 1993 to 1998. The break in slope between 1000 and 1200 m depth indicates the initiation of boiling. The temperature of the boiling point is depressed compared to that of pure water due to the presence of dissolved gases, such as CO_2.

Table 1.1

Well 28-33 Fluid Chemistry

Well 28-33 fluid chemistry, values in ppm.

Date	Lab pH	Na	K	Ca	Mg	Fe	Al	SiO_2	B	Li	HCO_3	CO_3	Cl	F	SO_4
09/23/93[a]	7.58	228	6.13	15.6	2.08			101	2.25	0.35	140	0	70.1	4.28	273
12/12/95[b]		433	70.9	9.19			1.55	629	10.5		132	35.0	463	16.4	214
10/07/96[b]		420	71.1	8.36			1.48	623	10.5		126	43.0	453	15.0	214
10/30/97[a]	9.13	429	70.1	7.40	0.02			642	9.47	2.24	115	52.8	470	15.4	199
11/05/97[b]		441	71.7	8.17		0.029		609	10.2		148	30.3	463	16.4	200
04/28/98[a]	9.01	447	67.8	7.50	<0.01			550	9.38	2.28	73.2	72.0	446	16.6	199
10/02/98[b]		417	63.9	8.54		0.020		534	10.7	1.75	140	31.0	454	15.0	211
10/21/98[a]	9.38	412	65.5	7.21	0.03			531	9.73	2.03	75.6	76.8	441	15.6	199
05/05/99[a]	9.10	432	66.2	6.68	0.02			561	9.60	2.24	85.0	74.0	483	16.3	213
01/24/00[b]		454	74.9	8.80		0.100		542	11.7	2.58	153	28.0	473	15.2	221
02/13/01[b]		448	58.7	6.47				587	9.86	2.11	199	23.9	463	15.8	238
07/27/01[b]		441	65.0	7.13				645	10.9	1.59	188	31.2	438	16.9	242
01/31/02[b]		459	62.4	7.21		0.055		548	10.0	1.98	167	21.5	443	16.0	234
04/27/04[b]		415	56.2	5.32				538	8.97	2.07	157	39.2	427	18.4	182

a. Reported by Goff et al. (2002)
b. Reported by Terra-Gen

Table 1.2

Well 28-33 Gas Chemistry

Well 28-33 gas chemistry as reported by Goff et al. (2002) reported as mol% dry gas (except for H_2O).

Date	Steam Fraction (y)	H_2O (mol% wet)	CO_2	H_2S	H_2	CH_4	C_2H_6	N_2	Ar	He	Comment
10/30/97	0.156	99.5	44.8	0.981	0.012	0.192		43.1	0.558	0.000	Air contamination
10/21/98		99.8	96.0	0.966	0.064	0.406	0.006	1.77	0.030	<0.0002	
05/05/99	0.159	99.6	97.8	0.596	0.027	0.253	0.004	0.909	0.023	0.001	

clean out process in 2001 (Fig. 1.3A). Fluid and gas chemistry analyses for well 28-33 are provided in Tables 1.1 and 1.2, respectively.

Methods

Scale Mineral Analysis

Concentric bands (Fig. 1.3B) and aggregates (Fig. 1.3C) of scale minerals deposited on the tubing pulled from well 28-33 were sampled at 44 depth intervals between 650 and 1200 m depth. The mineralogy and mineral abundances in the scale were estimated for 36 sample intervals using X-ray diffractometry (XRD).

X-ray Diffractometry

Whole rock and clay XRD were performed on each sample in the XRD laboratory at the Energy and Geoscience Institute at the University of Utah, using a Bruker D8 Advance X-ray diffactometer. Phase quantification using the Rietveld method (Rietveld, 1969) was performed using TOPAS software developed by Bruker Analytical X-ray Systems. The following operating parameters were used during the analyses: Cu-K-α radiation at 40 kV and 40 mA, 0.02^{o}2θ step size, 0.4 and 0.6 seconds per step for clay and bulk samples respectively. Clay samples (<5 μm) were examined from 2 to 45^{o}2θ before and after treatment with ethylene glycol and the bulk sample from 4 to 65^{o}2θ. The clay mineral abundances were determined from the Rietveld refinement of the bulk scans.

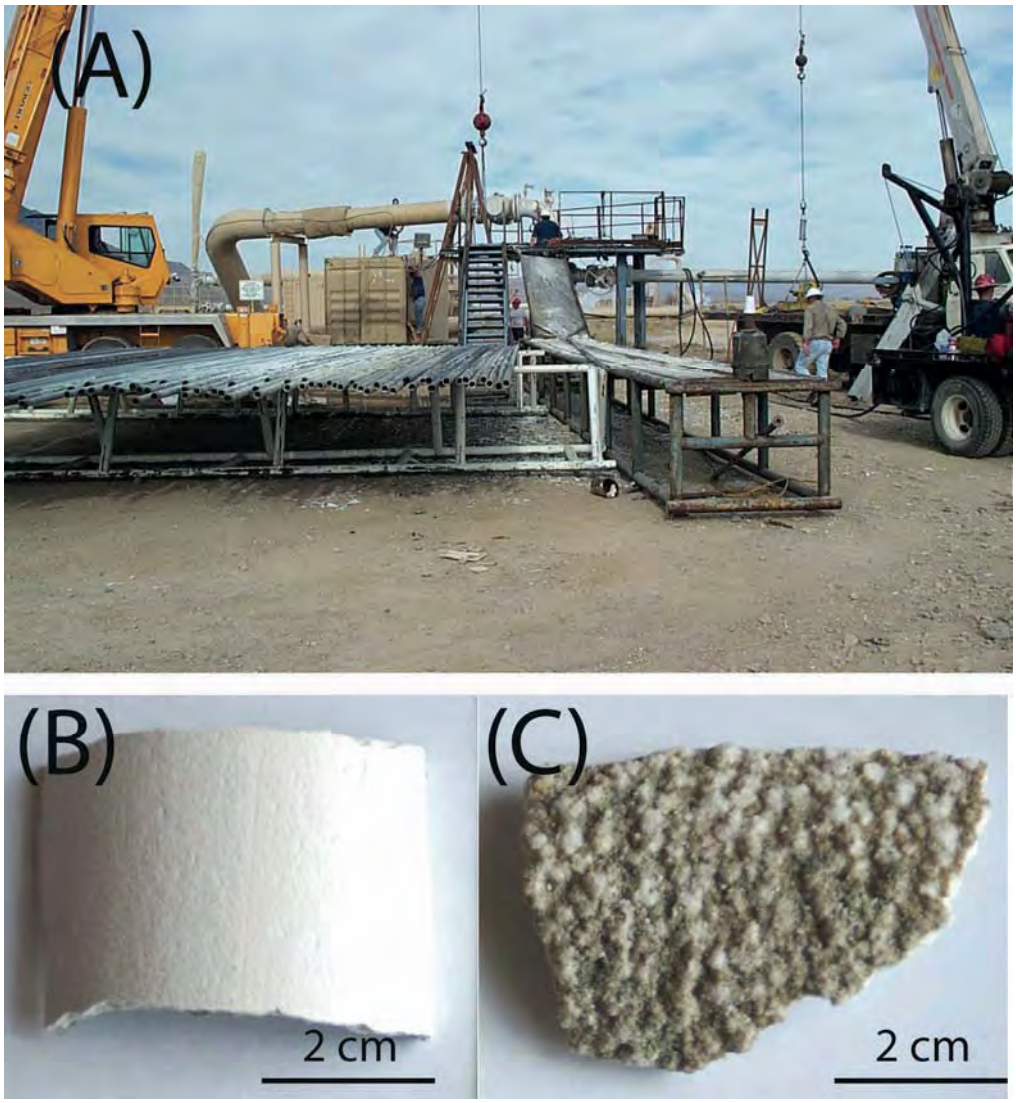

Fig. 1.3. Scale minerals deposited on tubing from well 28-33. (A) Tubing pulled from 28-33 with scale. (B) Fine grained scale from 844 m depth. (C) Coarsely crystalline scale from 1183 m depth.

Scanning Electron Microscopy

Scanning electron microscope (SEM) analyses were used to characterize the scale mineral textures. The samples were examined on a LEO tungsten filament electron source SEM at the Dixon Laser Institute at the University of Utah. An accelerating voltage of 20 kV was used.

Fluid Inclusion Gas Analysis

Liquid and vapor rich fluid inclusions are common in the carbonate scale samples (Figs. 1.4A and 1.4B). Although repeated efforts were made to prepare polished chips of the scale for microthermometric measurements, the small size of the fluid inclusions (generally 1-<3 μm) and the poor optical quality of the chips precluded measurement of their homogenization and ice melting temperatures.

Samples from 24 depth intervals between 700 to 1200 m depth in well 28-33 were selected for fluid inclusion gas analysis at the New Mexico Institute of Mining and Technology. The gases in the fluid inclusions represent a sample of the liquid and vapor phases in the boiling column trapped during a period of five years. Prior to the analysis, the samples are cleansed with NaOH or KOH to remove surface organics. Major and minor gases, including H_2O, CO_2, CH_4, H_2S, H_2, N_2, Ar, He, and C_{2-7} organic species contained in inclusions were analyzed with a Balzers QMS 420 quadrupole mass spectrometer after being released by crushing under vacuum. Norman and Sawkins (1987) and Norman et al. (1996) present details of this analytical technique. The crush-fast-scan (CFS) method used involves opening inclusions with a swift crush in a vacuum chamber housing the mass spectrometer. The volatiles are removed from the chamber by

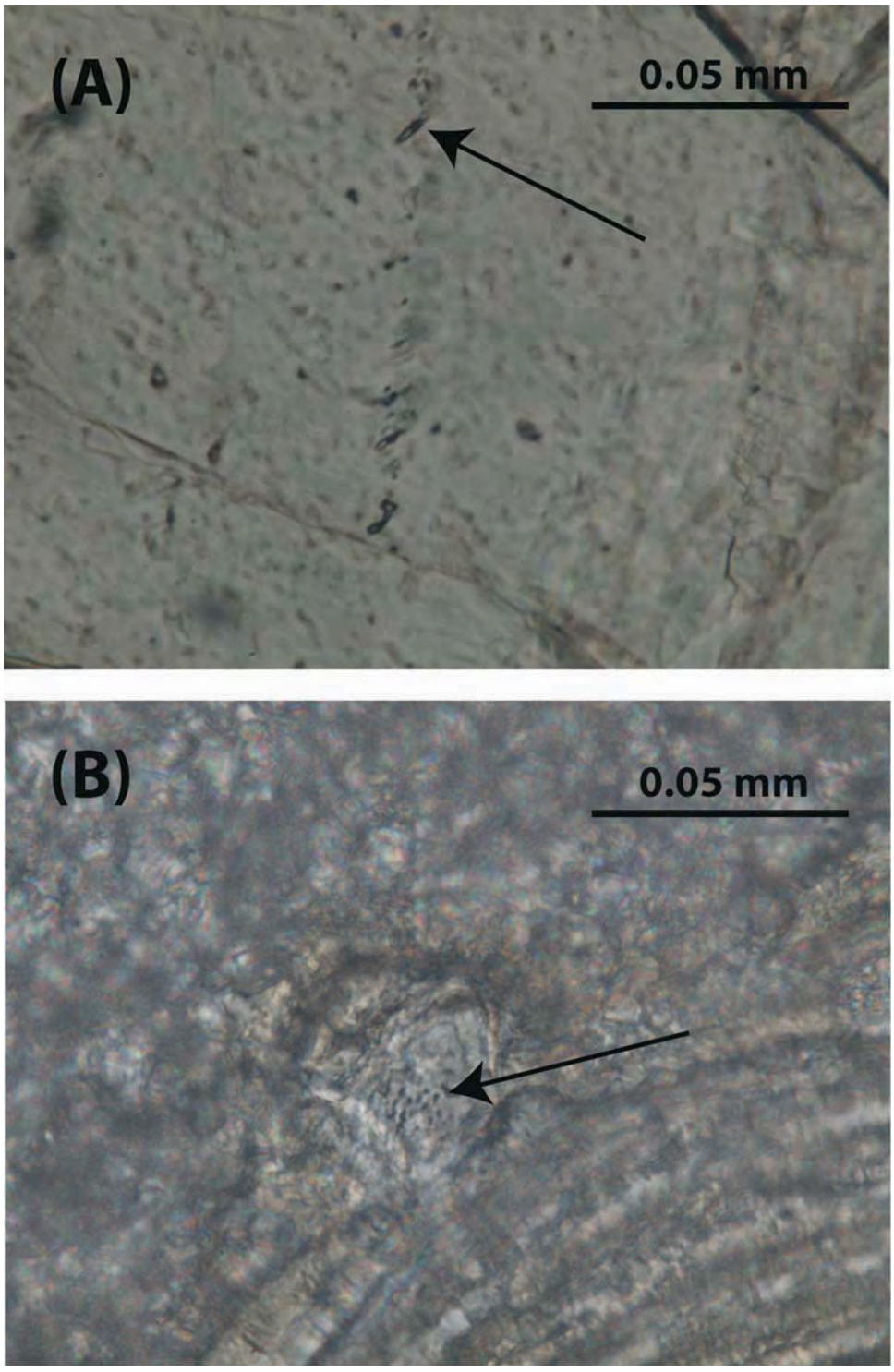

Fig. 1.4. Photomicrographs of fluid inclusions found in scale. (A) Unusually large (~5 mm) liquid rich fluid inclusions found in crystal from 1095 m depth. Arrow points to a liquid rich inclusion. (B) Fluid inclusions found in large crystal from 877 m depth. Arrow points to a group of small (<1 mm) fluid inclusions.

the vacuum pumping system in 1 to 2 s. Measurements are taken every 150 to 225 milliseconds by operating the quadrupole in a fast scan mode. Whole samples within each depth interval, not individual layers, were crushed in the CFS analysis. Each crush yields an analysis that could represent various proportions of liquid and vapor rich inclusions (Norman et al., 1997). Gas concentrations greater than 1 mol% suggest a fluid inclusion population dominated by vapor rich inclusions. Opening a 10 to 20 μm inclusion or group of smaller inclusions of equivalent volume provides the ideal amount of volatiles for the analysis. The volatile content of a 40 μm inclusion will overload the vacuum system, precluding analysis of the sample. Due to this limitation on the volume of gaseous species that can be collected and analyzed, inclusions that trapped gas rich steam will typically be underrepresented (Moore et al, 2000). Five to twenty crushes can be made on a 0.2 g sample with the expectation that some of the analyses will be failures. The precision of the CFS analyses was estimated from repeatability of gas ratio measurements. It is dependent on the size of the volatile burst, which ranges from 10 to 10^5 counts. Bursts with counts of less than 10^3 are rejected due to poor precision. Volatile bursts of about 10^5 counts yield a precision of 20 percent for gaseous specie/water ratios and 10 percent for gas/gas ratios. Because geothermal waters are low in O_2, it is routinely measured to determine if air contamination has occurred. No evidence of air contamination was detected in these analyses.

Ammonia is rarely detected due to interferences from secondary H_2O peaks at a mass to charge ratio (m/e) = 17 and 16. Helium concentrations below 30 ppm may be masked by the tail on the H_2 peak. Organic compounds, principally propane (C_3H_8) and propene (C_3H_6), may interfere with the detection of Ar. It is assumed that the peak

measured at m/e = 41 or 39 is solely from propene because it interferes more strongly with the Ar peak at m/e = 40 than propane. The amount of Ar is calculated by first subtracting the calculated contribution to the 40 m/e peak from propene. The maximum Ar value is taken as 20 percent of the propene (C_3H_6) peak height and is used to constrain the minimum N_2/Ar ratios in cases where there is such strong interference that data reduction indicates no detectable Ar.

Results

Mineral Scale

Mineral abundances for the 36 depth intervals, as determined by XRD, are plotted in Fig. 1.5. The mineral scales consist mainly of calcite and aragonite with minor Mg rich smectite and quartz. Aluminum bearing amorphous silica was found in the scale near the top of the well (Fig.1.6). Scale found deeper in the well consisted of individual bands of calcite, aragonite, or Mg smectite (Fig. 1.6B). Quartz is found in trace amounts between 844 and 888 m. Between 1112 and 1125 m depth (Fig. 1.5), there is a change from calcite as the dominant carbonate mineral in the scale at shallow depths to aragonite. While trace amounts of aragonite occur in the calcite dominated interval, there is very little calcite in the scale below 1125 m.

The aragonite crystals form layers of coarse grained crystals that are loosely bound and easily separated from each other. Aragonite crystals appear to have both irregular and curved surfaces. Hopper growth (Fig. 1.6C), twinning (Fig. 1.6D), and fibrous crystals (Fig. 1.6E) can be observed. In contrast, the calcite layers are denser and

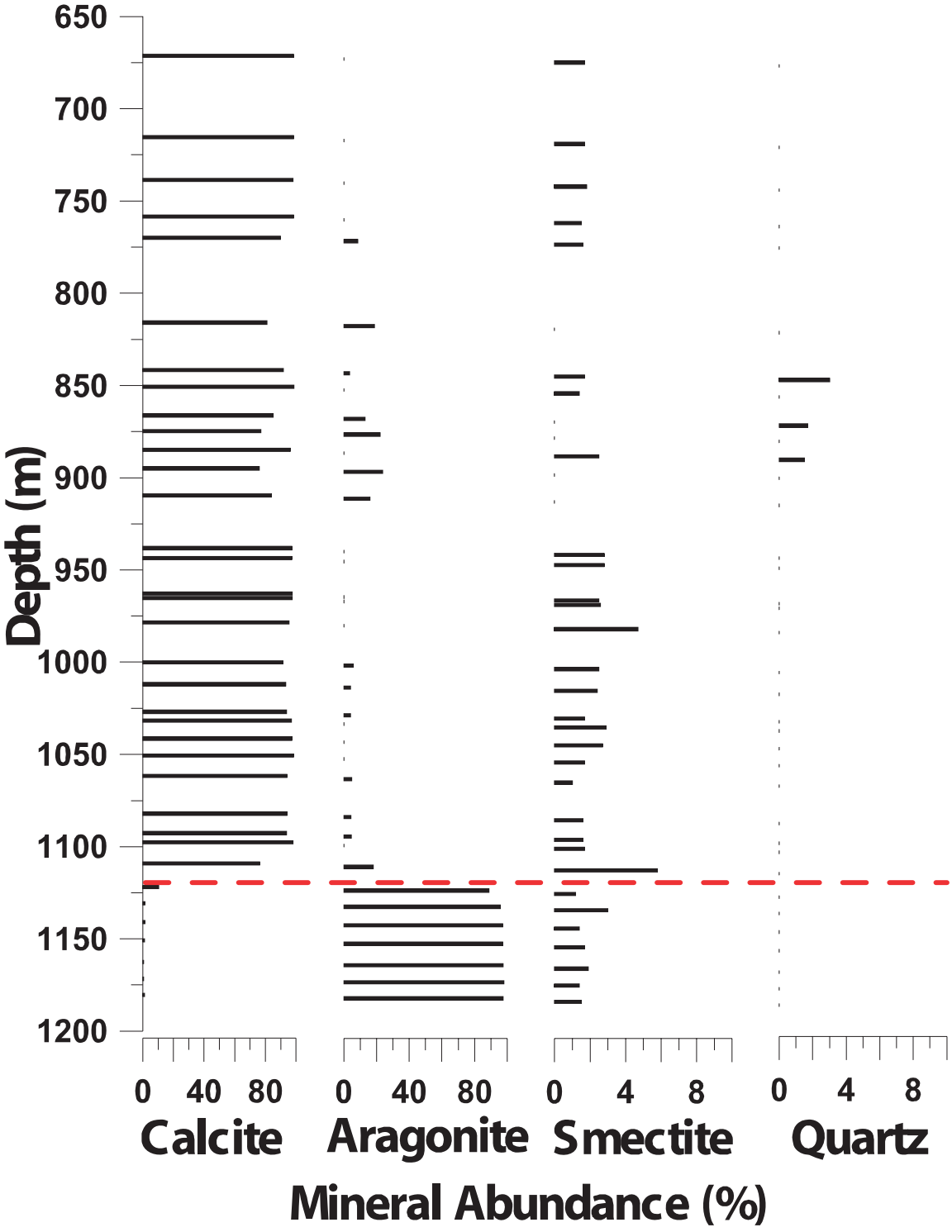

Fig. 1.5. Mineral abundance of scale deposits from XRD analysis. Red dashed line indicates the change from aragonite to calcite as the dominant form of $CaCO_3$.

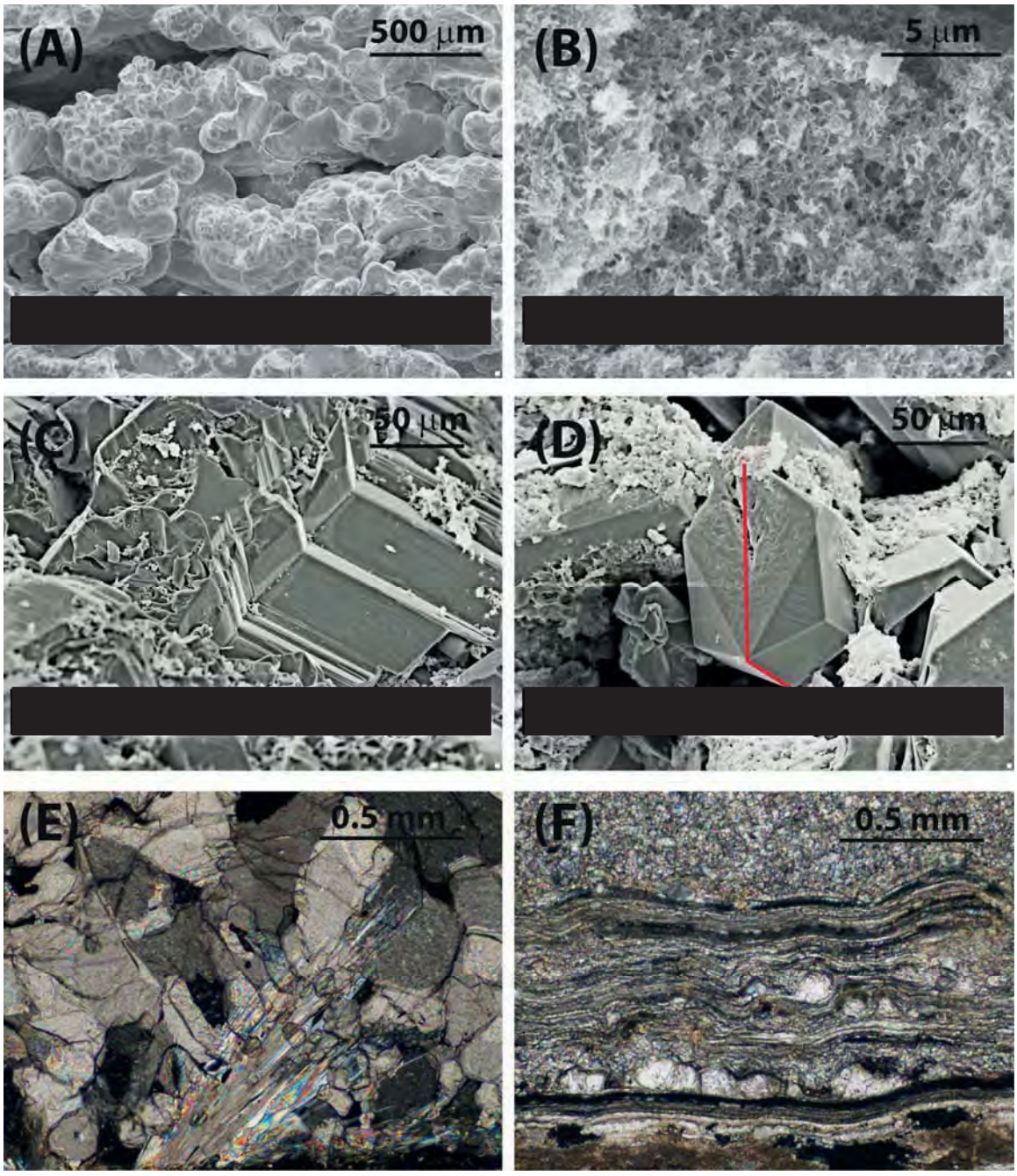

Fig. 1.6. SEM images and photomicrographs of scale minerals. (A) Aluminum rich amorphous silica scale found near the top of the well. (B) Mg smectite. (C) Aragonite crystals showing hopper growth. (D) Aragonite crystal showing twinning (twinning plane illustrated in red). (E) Both large, coarse and fibrous aragonite crystals. (F) Layers of fine, microcrystalline calcite.

more difficult to separate from each other. The calcite is finely crystalline to cryptocrystalline (Fig. 1.6F).

Fluid Inclusion Gases

Fluid inclusion gas composition data are reported in Table 1.3. The fluid inclusions are H_2O rich with less than 4% total gas (Fig. 1.7). Fluid inclusions in aragonite (depths of 1134 to 1183 m) have generally lower mol% gas than those analyzed in calcite (depths of 718 to 1100 m). Many of the analyses from calcite in this depth interval have gas concentrations greater than the solubility of CO_2 in water (<1 mol% wet gas) at the measured temperatures in this interval. Data for CO_2-CH_4-H_2 are shown in Fig. 1.8A, and for N_2-Ar-He in Fig. 1.9A; also plotted in both Figs. 1.8A and 1.9A are the wellhead compositions from 28-33. Inclusions display an appreciable range of CO_2/CH_4 and CO2/H_2 values that are generally lower than those measured at the well head (Fig. 1.8A). Gas analyses from shallow calcite samples are generally enriched in CO_2 relative to CH_4 and H_2 compared to analyses from the deeper aragonite samples. Most aragonite samples have higher He relative to N_2 and Ar compared to the calcite samples. Furthermore, aragonite samples define a linear trend of He enrichment at constant N_2/Ar away from the wellhead composition (Goff et al., 2002). Many analyses of the calcite samples are closer in composition to the wellhead gas composition (Fig. 1.9A). However, although many of the calcite samples appear to have lower Ar contents than the present-day well composition, the Ar in these samples may be anomalously low due to peak interference from propane and propene. Ar could not be detected in several samples due to this interference. For comparison, gas analyses of Dixie Valley wells and fumaroles

Table 1.3

Fluid inclusion gas chemistry

Fluid inclusion gas chemistry reported as mol % wet gas unless otherwise listed.

Depth (m)	Burst Size (counts)	H_2O	Total Gas	H_2	CH_4	CO_2	He	N_2	Ar	H_2S	C_2H_6	C_1/C_2 Geothermometer (^oC)
718	1223	96.9	3.12	0.046	0.155	1.20	4.00E-5	1.65	0.023	0.001	0.007	175
941	10390	99.3	0.72	0.003	0.008	0.526	7.60E-6	0.165	0.003	0.002	0.007	101
941	20760	99.4	0.55	0.003	0.009	0.351	6.87E-6	0.163	0.003	0.163	0.009	99
966	1780	99.2	0.82	0.010	0.012	0.582	0.000	0.191	0.002	0.002	0.004	124
966	1867	99.0	1.03	0.008	0.025	0.695	0.000	0.263	0.004	0.002	0.005	139
1003	3349	99.0	1.00	0.008	0.016	0.789	1.05E-5	0.165	0.002	0.002	0.004	132
1003	9813	98.4	1.57	0.015	0.025	1.21	1.51E-5	0.267	0.002	0.004	0.006	134
1024	7697	96.3	3.69	0.086	0.016	2.97	6.54E-5	0.524	0.007	0.008	0.012	104
1044	1489	99.3	0.74	0.010	0.005	0.628	1.55E-5	0.064	5.00E-4	0.004	0.009	81
1044	2123	99.0	0.98	0.010	0.010	0.856	1.10E-5	0.070	4.00E-4	0.004	0.008	102
1044	7299	98.6	1.41	0.049	0.012	1.17	4.11E-5	0.125	4.00E-4	0.006	0.007	111
1044	2232	99.0	0.95	0.011	0.016	0.779	2.55E-5	0.094	3.00E-4	0.004	0.007	115
1064	1072	98.0	2.01	0.009	0.012	1.76	3.14E-5	0.178	0.002	0.005	0.007	109
1064	2351	97.7	2.30	0.012	0.020	1.94	3.41E-5	0.268	0.004	0.005	0.011	112
1064	6748	98.0	2.02	0.051	0.015	1.65	7.63E-5	0.253	0.003	0.004	0.014	108
1064	2714	98.5	1.55	0.013	0.022	1.28	3.36E-5	0.198	0.003	0.003	0.011	115
1100	13160	97.4	2.63	0.076	0.010	2.11	7.30E-5	0.339	0.003	0.010	0.012	92
1100	23370	97.4	2.57	0.087	0.014	2.07	7.48E-5	0.299	0.002	0.009	0.008	110
1100	4854	98.5	1.52	0.014	0.015	1.24	1.58E-5	0.178	0.001	0.003	0.004	129
1134	5323	99.7	0.33	0.005	0.035	0.233	0.000	0.017	nd	0.003	0.006	142
1134	7498	99.7	0.33	0.012	0.061	0.181	3.90E-6	0.023	nd	0.004	0.008	147
1134	4691	99.7	0.28	0.014	0.038	0.168	6.37E-6	0.018	nd	0.003	0.006	143
1154	82650	99.6	0.35	0.047	0.003	0.196	1.27E-4	0.058	0.001	0.011	0.019	51

Table 1.3 continued

Fluid inclusion gas chemistry reported as mol % wet gas unless otherwise listed.

Depth (m)	Burst Size (counts)	H_2O	Total Gas	H_2	CH_4	CO_2	He	N_2	Ar	H_2S	C_2H_6	C_1/C_2 Geothermometer (^oC)
1154	91140	99.7	0.26	0.030	0.002	0.146	1.03E-4	0.043	6.00E-4	0.010	0.013	53
1154	107300	99.8	0.19	0.025	0.002	0.102	2.00E-4	0.024	4.00E-4	0.009	0.009	64
1165	3124	99.8	0.22	0.003	0.015	0.147	0.000	0.036	5.00E-4	0.001	0.008	111
1165	48230	99.8	0.19	0.003	0.002	0.136	2.82E-5	0.016	1.00E-4	0.005	0.012	53
1174	93510	99.8	0.15	0.023	0.004	0.092	7.19E-4	0.009	2.00E-4	0.007	0.008	78
1174	48950	99.8	0.22	0.012	0.007	0.162	4.62E-5	0.012	1.00E-4	0.005	0.012	84
1174	81840	99.8	0.18	0.023	0.005	0.111	4.12E-4	0.013	2.00E-4	0.006	0.009	81
1183	85960	99.8	0.19	0.028	0.004	0.111	7.41E-4	0.013	3.00E-4	0.007	0.011	74
1183	6923	99.9	0.13	0.001	0.001	0.095	6.88E-6	0.022	3.00E-4	0.001	0.003	71
1154	36150	99.3	0.73	0.094	0.005	0.421	9.21E-5	0.140	0.002	0.012	0.030	50
1154	22940	99.6	0.45	0.063	0.003	0.252	5.53E-5	0.094	0.001	0.006	0.014	55
1154	55800	99.5	0.47	0.066	0.003	0.272	5.73E-5	0.075	0.001	0.011	0.025	42

nd=not detected

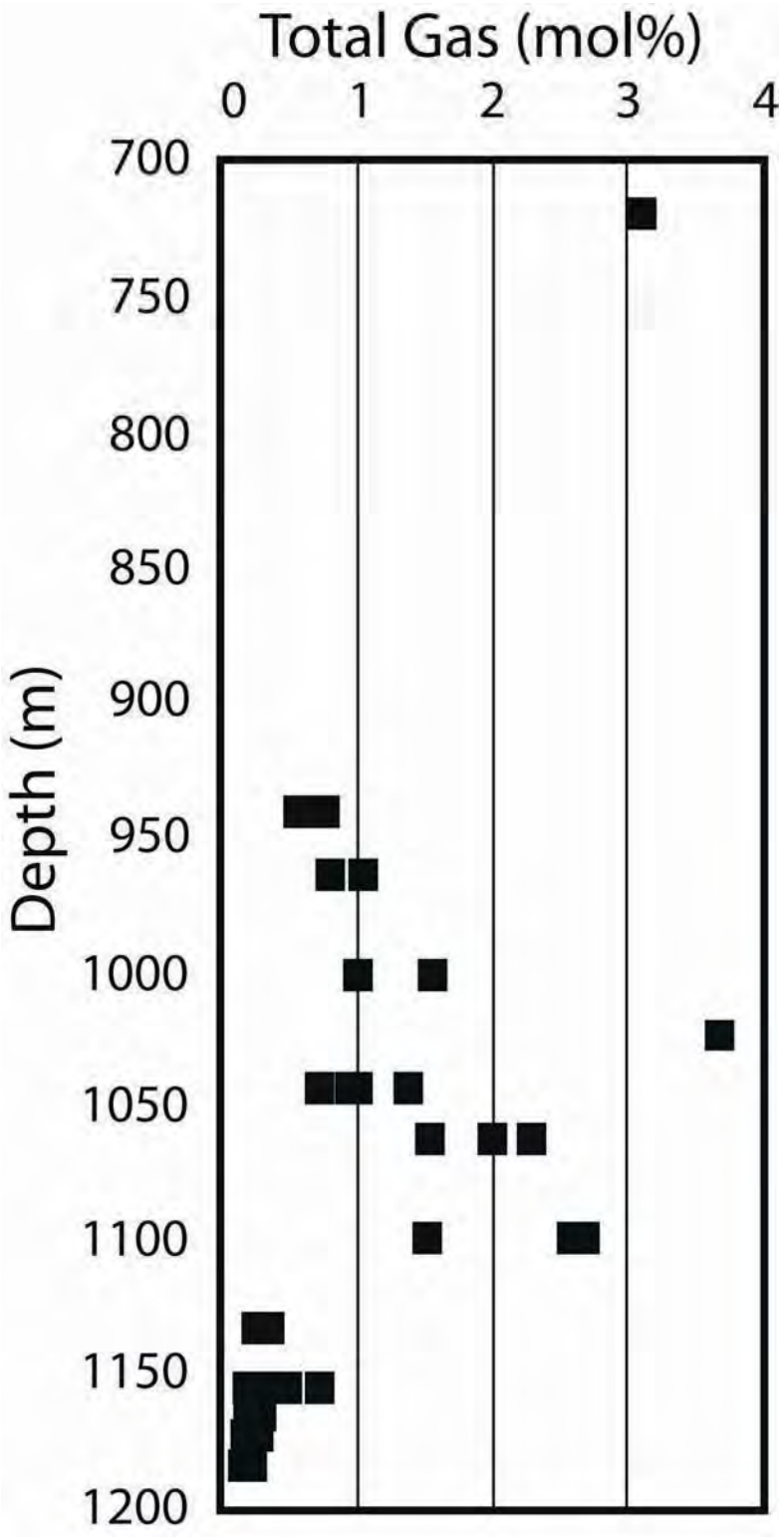

Fig. 1.7. Total dry gas from fluid inclusion analyses.

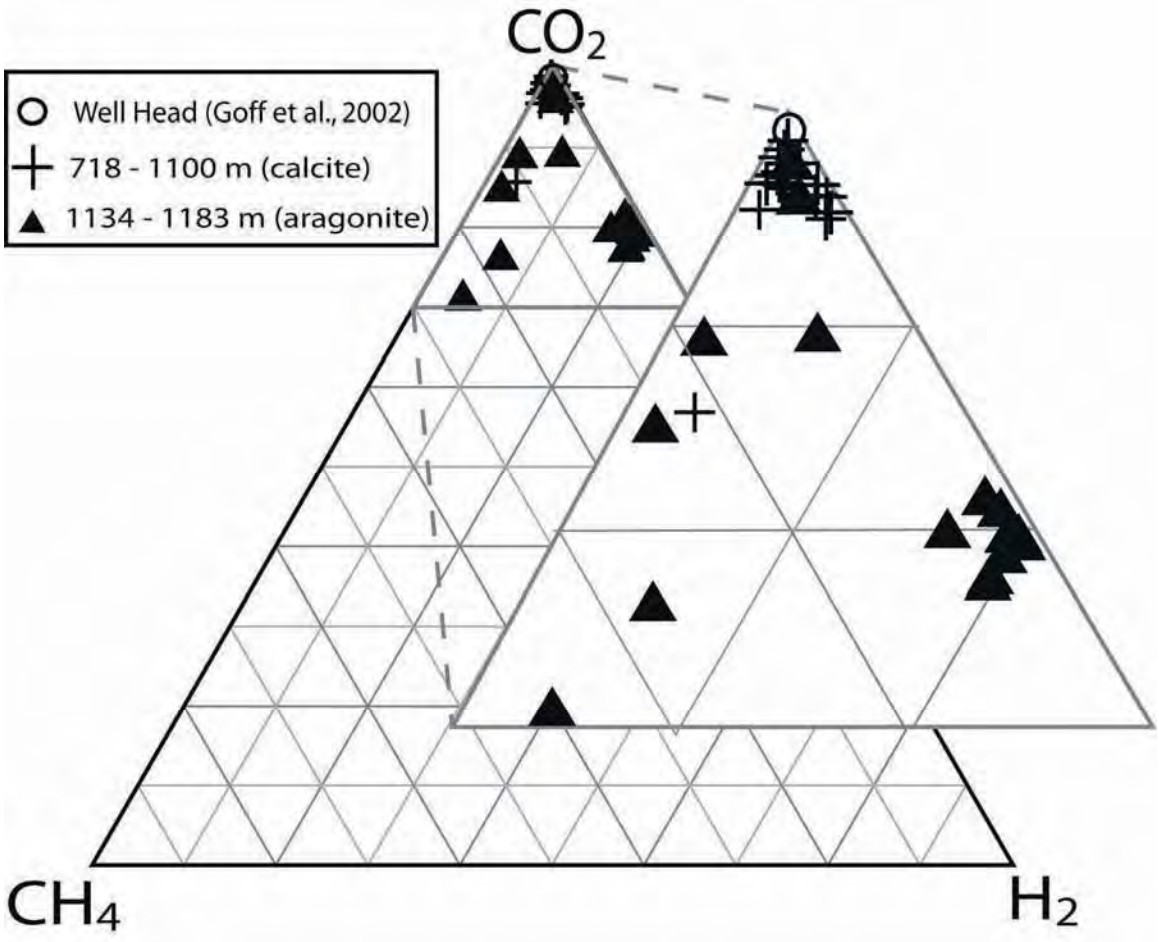

Fig. 1.8. CO_2-CH_4-H_2 plots. (A) Relative CO_2-CH_4-H_2 composition of well head gas (n=3) and fluid inclusion gas analyses from calcite (n=19) and aragonite (n=16) scale samples. Aragonite analyses show a broad range in CO_2/CH_4 and CO_2/H_2 values, while calcite analyses (with one exception) show a composition overwhelmingly dominated by CO_2. Well head gas analyses (Goff et al., 2002) also show high CO_2 relative to CH_4 and H_2.

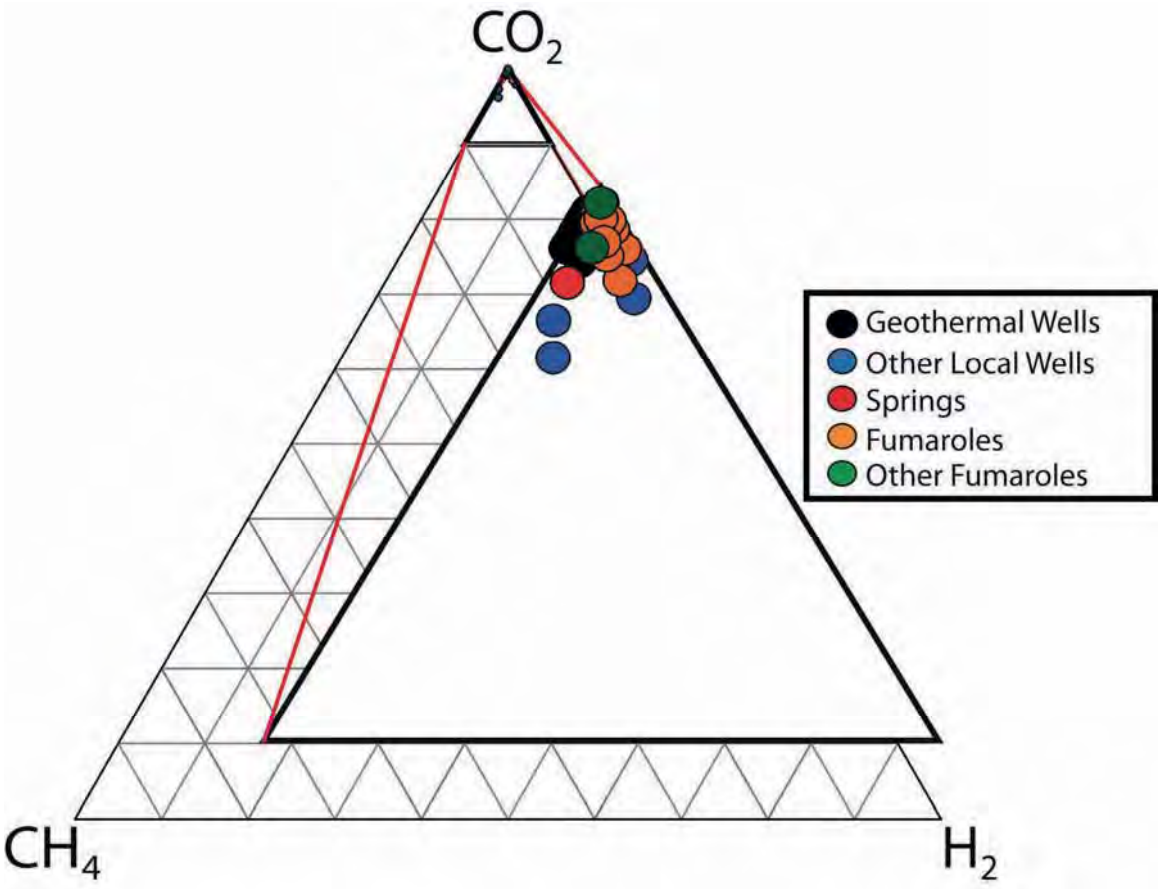

Fig. 1.8. continued. (B) Relative CO_2-CH_4-H_2 composition of Dixie Valley area wells and fumaroles. Gas analyses show dominance of CO_2 relative to CH_4 and H_2.

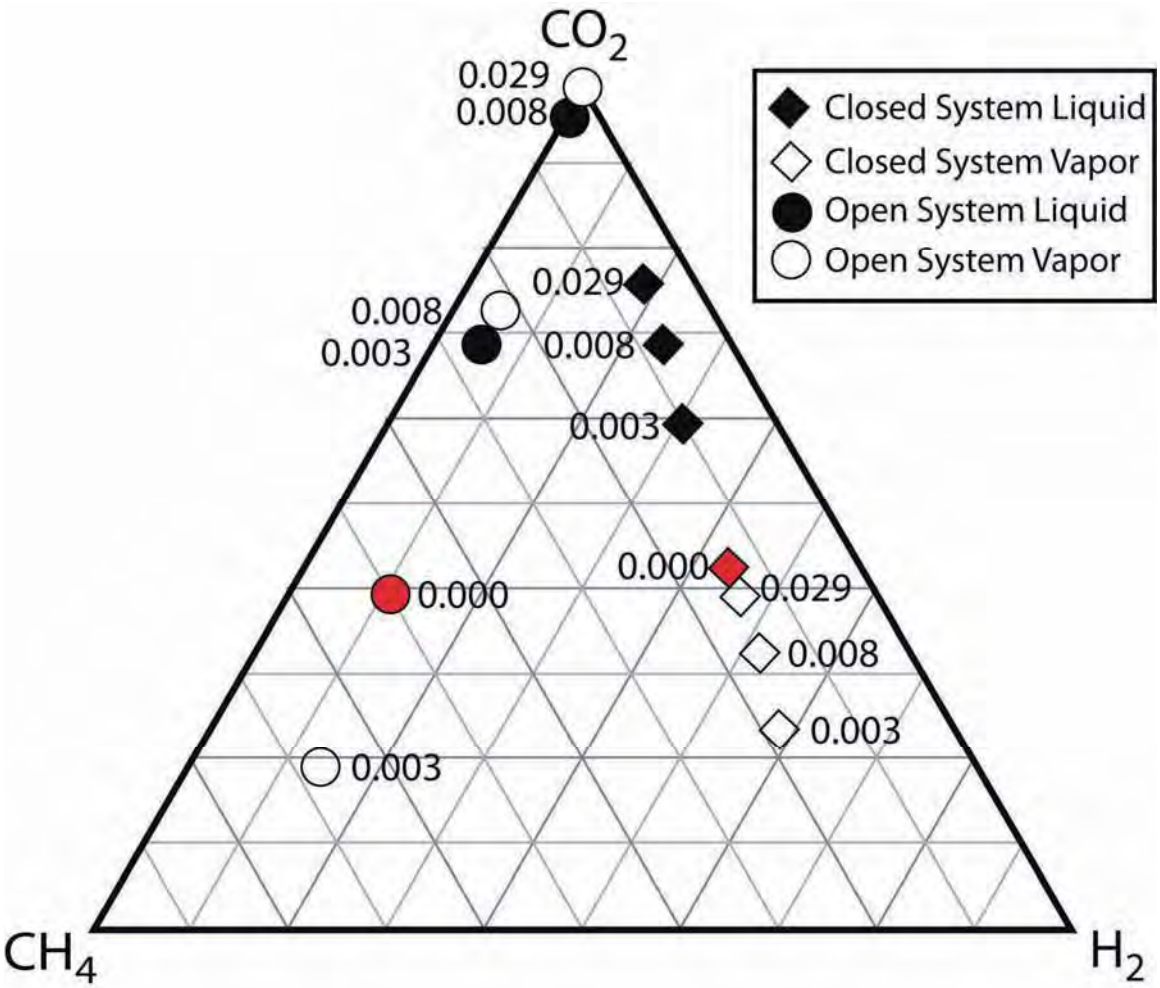

Fig. 1.8. continued. (C) Relative CO_2-CH_4-H_2 compositional changes associated with closed system and open system boiling. The red symbols represent the initial composition of the fluid (43% H_2, 15% CH_4, 42% CO_2 for a closed system and 10% H_2, 50% CH_4, and 40% CO_2 for an open system). The numbers on the plot are the steam fraction (y) associated with each composition plotted. Upon commencement of boiling (y=0.003) in an open or closed system, the vapor (open symbols) becomes enriched in CH_4 and H_2, while the liquid becomes depleted in these gases, moving the composition of the residual liquid to higher CO_2 relative to CH_4 and H_2 (for example, note compositions of residual liquid at 0.003 and 0.008 steam fractions). With progressive boiling in an open or closed system, both liquid and vapor compositions move to higher CO_2 relative to CH_4 and H_2 compared to their compositions at y=0.003. The measured y value, determined from steam and liquid at the well head of 28-33, was 0.156 in 1997 and 0.159 in 2009.

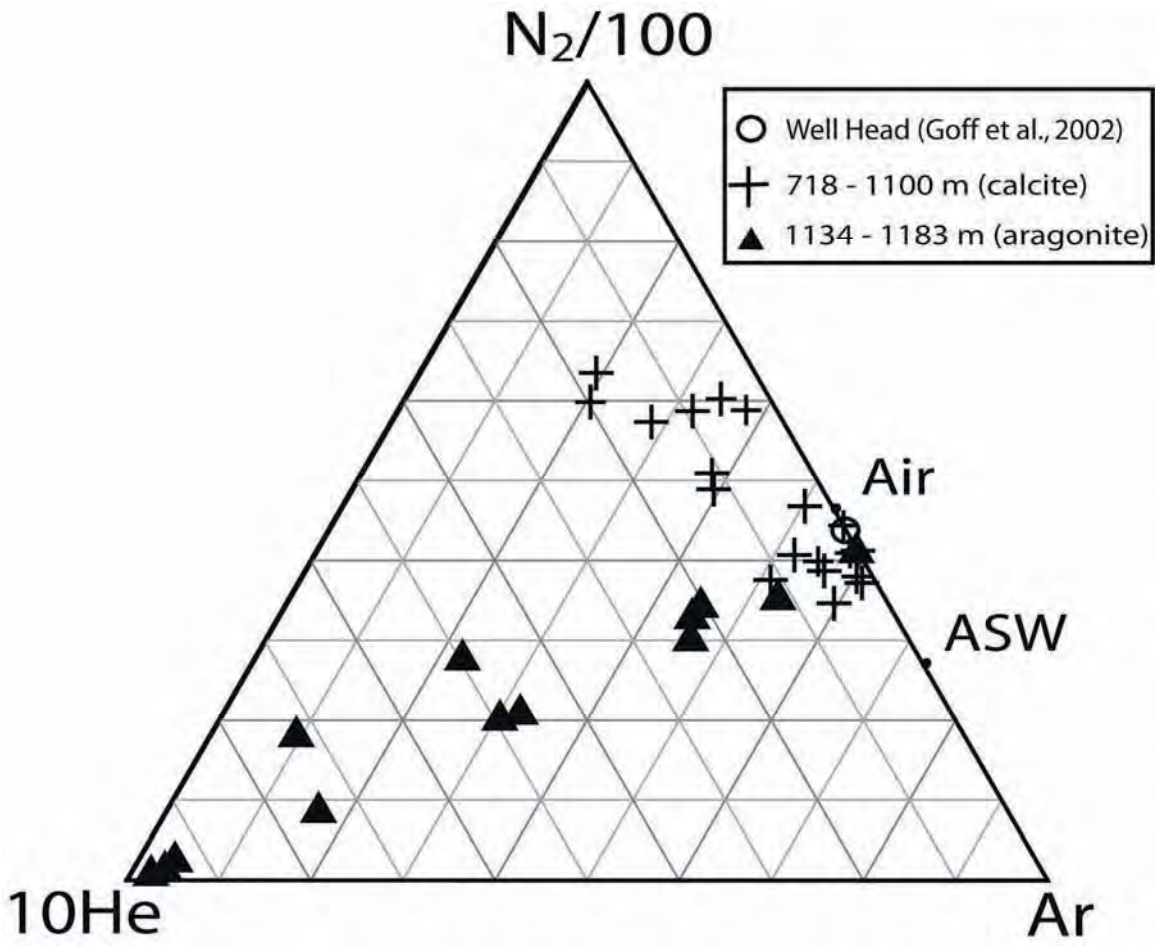

Fig. 1.9. N_2-Ar-He plots. (A) Relative N_2-Ar-He composition of well head gas (n=3) and fluid inclusion gas analyses from calcite (n=19) and aragonite (n=13) scale samples. Aragonite analyses show a broad range of He contents and relatively consistent N_2/Ar ratio. Calcite samples all have low He relative to N_2 and Ar. Well head gas analyses plot within this range of He relative to N_2 and Ar. Some calcite analyses have high N_2/Ar ratios. These anomalous ratios reflect low Ar values due to interference of propane and propene peaks in detecting Ar. The compositions of air and air saturated water (ASW) are plotted for reference.

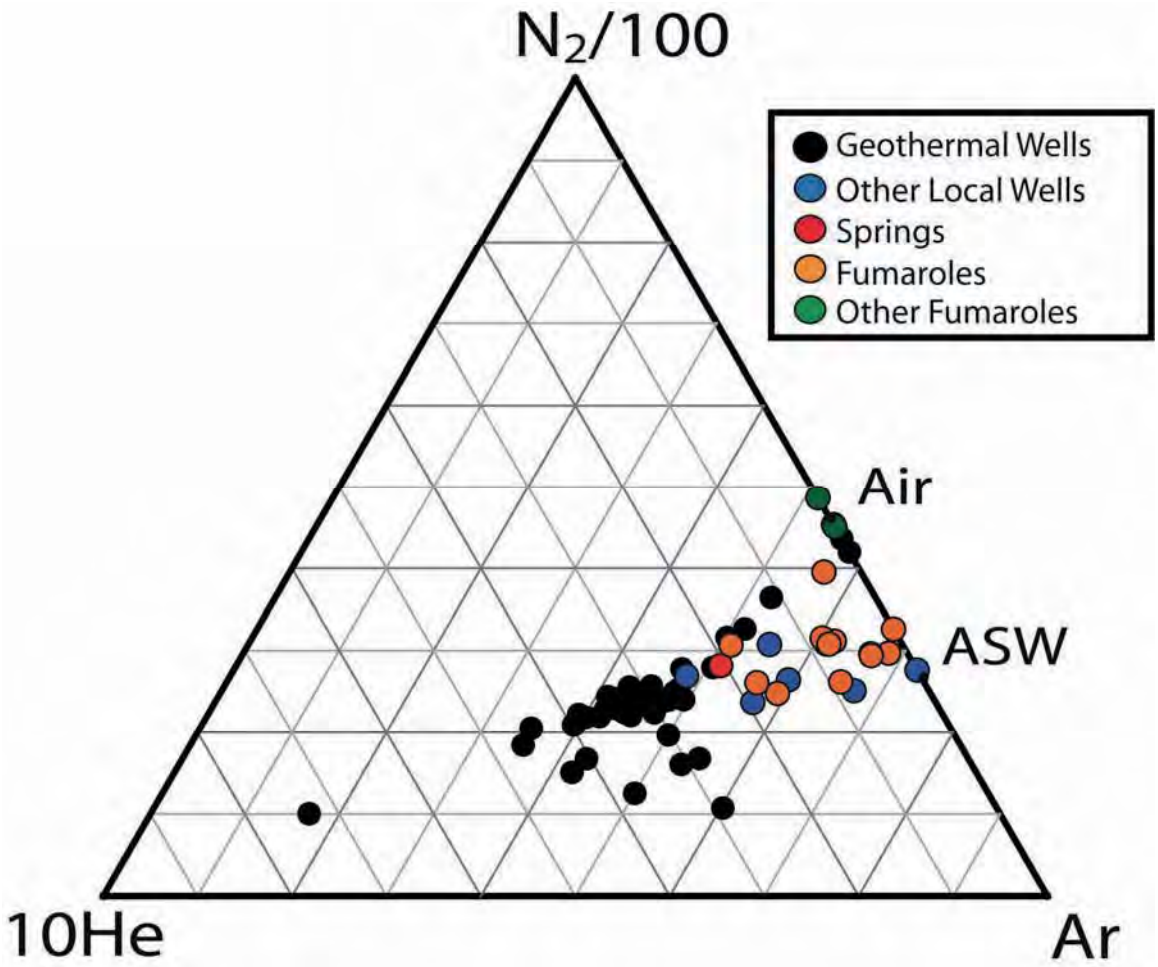

Fig. 1.9. continued. (B) Relative N_2-Ar-He composition of Dixie Valley area wells and fumaroles. The geothermal wells follow a trend of varying He content at relatively consistent N_2/Ar ratio. Samples from nongeothermal local wells, springs, and fumaroles have lower He relative to N_2 and Ar than most of the geothermal well samples in the area. The compositions of air and air saturated water (ASW) are plotted for reference.

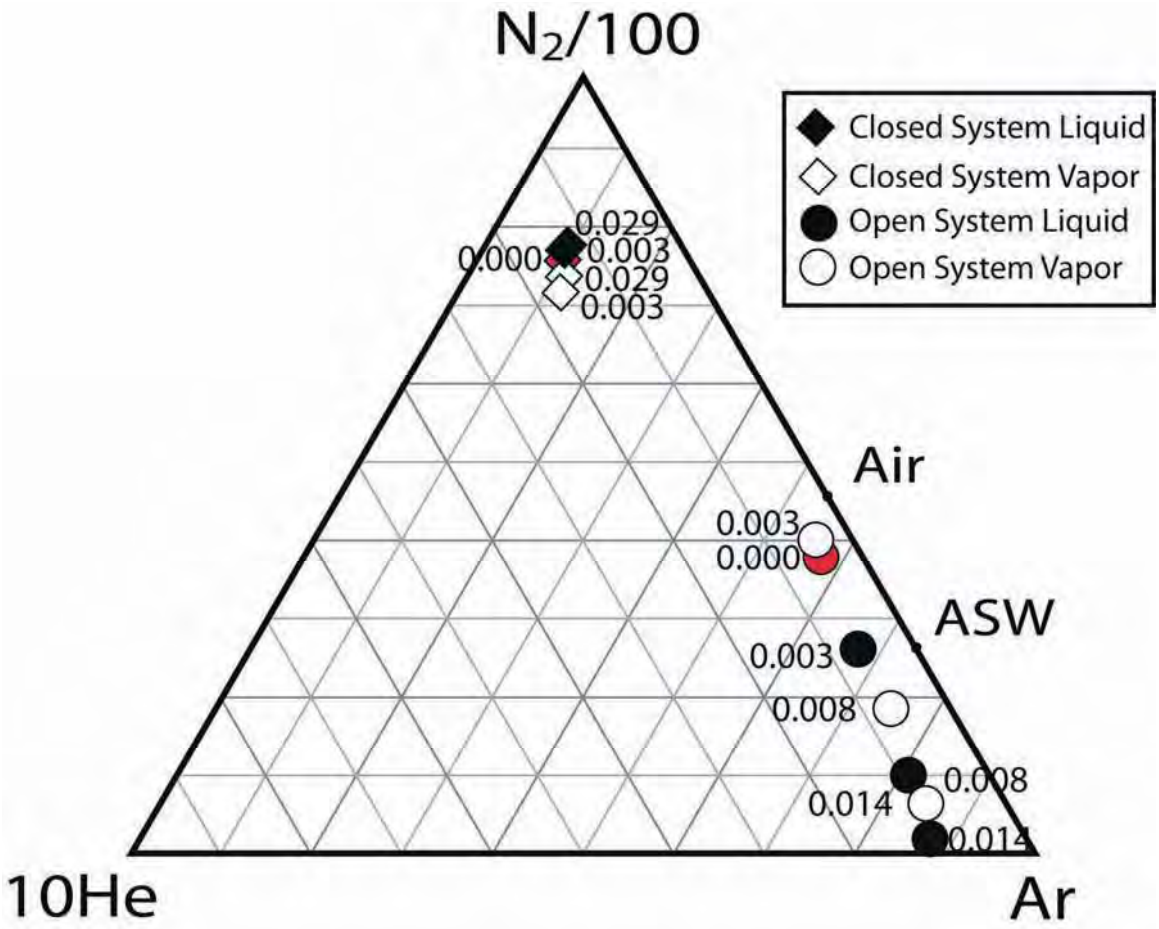

Fig. 1.9. continued. (C) Relative N_2-Ar-He compositional changes associated with closed system and open system boiling. The red symbols represent the initial composition of the fluid. The numbers on the plot are the steam fraction (y) associated with each composition plotted. Upon commencement of boiling (y = 0.003) in an open system, the vapor becomes slightly enriched in N_2 relative to Ar, while the liquid becomes depleted in N_2, moving the composition of the residual liquid to a lower N_2/Ar ratio. With progressive boiling in an open system, N_2 becomes depleted relative to Ar in both the liquid and vapor, and Ar also begins to be depleted relative to He in the liquid (see y=0.008 and y=0.014). Upon initiation of boiling in a closed system (y=0.003), the liquid becomes slightly enriched in N_2 relative to Ar and He, while the vapor becomes slightly depleted in N_2 relative to Ar and He. With progressive boiling in a closed system, the compositions of both liquid and vapor move to higher N_2 than their compositions at y=0.003. The measured y value of the steam and fluid discharged at the wellhead was 0.156 in 1997 and 0.159 in 2009.

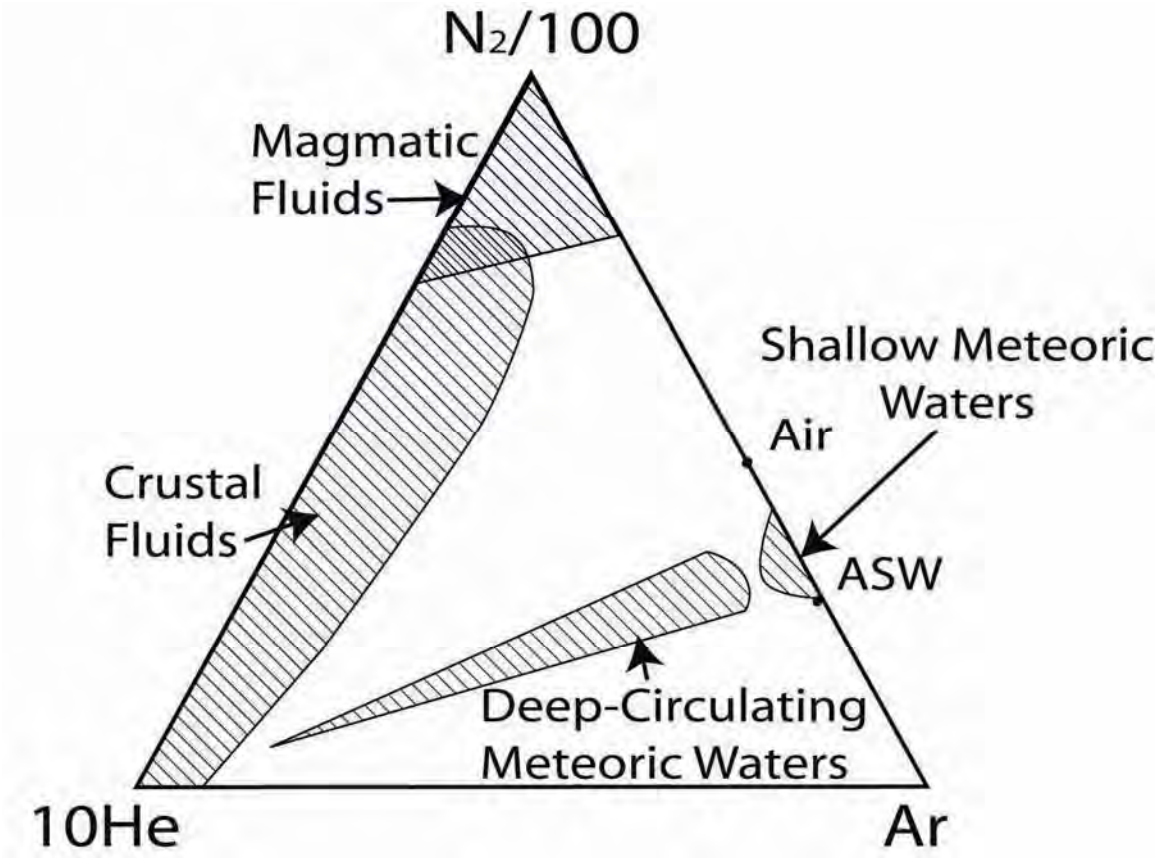

Fig. 1.9. continued. (D) N_2-Ar-He compositional fields for magmatic, crustal, deeply circulated meteoric, and shallow meteoric fluid sources (modified from Norman and Musgrave 1994).

from Goff et al. (2002) are presented on the CO_2-CH_4-H_2 and N_2-Ar-He plots in Figs. 1.8B and 1.9B, respectively. The compositions of 28-33, other Dixie Valley wells, and fumarole gases are all overwhelmingly rich in CO_2 and have similar CO_2-CH_4-H_2 compositions to most of the gas analyses from calcite samples. In contrast, most of the aragonite samples are variably enriched in CH_4 and/or H_2. The gas analyses from the Dixie Valley wells and fumaroles also define a linear trend of He enrichment similar to that defined by the fluid inclusion gas analyses from the aragonite scales (Figs. 1.9B and 1.9A).

Discussion

Mineralogy

The mineral composition, habit, and textural relationships provide a record of the physical and chemical conditions in the well during scale formation. Polyacrylate scale inhibitors, such as Nalco 9354, create chemical conditions that favor the spontaneous nucleation and formation of very small calcite crystals in the fluid (Siega et al., 2005). This could explain the appearance of the calcite crystals found in the mineral scale, but not the presence of large aragonite crystals.

The form of the aragonite crystals is interpreted to reflect the degree of saturation of the fluid at the time of their formation. Gonzales et al. (1992) and Rimstidt (1997) suggest that minerals formed under near equilibrium conditions will show smooth faces on well-developed crystals. With higher degrees of supersaturation, these crystal faces become roughened due to surface nucleation (Liu et al., 1992). Hopper growth, penetration twinning, and radial fiber growth result from the growth rate becoming

diffusion limited. At the highest degrees of supersaturation, colloidal particles form in solution then precipitate as aggregates (in low flow rate systems) or as banded deposits (in high flow rate systems) (Saunders, 1990). If these principles are applied to this geothermal well environment, the observed textures indicate that aragonite was deposited with a moderate degree of supersaturation in the fluid, whereas the calcite was deposited where progressive boiling significantly increased supersaturation of $CaCO_3$. Differences in the morphology of the calcite (cryptocrystalline calcite or coarser grained calcite aggregates) may also reflect variations in the degree of supersaturation of $CaCO_3$. These variations could, in part, be related to changes in well bore conditions dictated by field operations. Operational changes include putting the well on idle, bringing the well back on line, varying flow rates, and periods of unrestricted flow to atmosphere.

Fluid Inclusion Gases

Some of the fluid inclusion gases have higher CH_4 or H_2 (relative to CO_2) and/or higher N_2 (relative to Ar) than gas samples from the well head, other wells, and fumaroles. The formation of CH_4 rich (relative to CO_2) inclusions may reflect: 1) the mixing of a higher CO_2/CH_4 fluid with a lower CO_2/CH_4 fluid and the subsequent trapping of various mixtures of these fluids over time; 2) Fischer-Tropsch reactions (see below) occurring within the inclusion after formation; 3) bacterial production of CH_4 within the inclusion after formation; 4) the consumption of free CO_2 by carbonate mineral formation; and/or 5) the trapping of early steam in the fluid inclusions (vapor will have a CO_2/CH_4 ratio about 1/4 of that in the liquid at temperatures near 250^{o}C (Moore et al., 2000)). The formation of CH_4 through Fischer-Tropsch reactions in a natural system

is controversial (McCollum and Seewald, 2001). Abiogenic formation of CH_4 is postulated at midocean ridges (MOR) and in other high temperature environments where a chemical catalyst may be involved (Fiebig et al., 2004).

$$CO_2+4H_2=CH_4+2H_2O \quad (1.1)$$

Comparisons of the C_{1-6} gases can provide insight into the origins of the CH_4. C_1 and C_2 gases can be used as a geothermometer in geothermal fields. Their relationship to temperature is given by:

$$T^oC=57.8\log(C_1/C_2)+96.8 \quad (1.2)$$

This relationship was developed by Darling (1998) based on data from various hydrothermal systems. This relationship assumes that the thermal decomposition of higher order hydrocarbon chains will be temperature dependent. Excess CH_4 for a given temperature implies the addition of CH_4 from another source, possibly abiogenic production. The calculated temperatures for the Dixie Valley samples using this geothermometer are given in Table 1.3 and range from 42 to 175^{o}C. All but one of the calculated temperatures is lower than the measured production temperatures. This indicates a deficiency of CH_4 with respect to C_2H_6, possibly reflecting the influence of abundant sedimentary hosted organics on these gas compositions (Giggenbach and Corrales, 1992; Darling, 1998). Thus, these geothermometer calculations do not support the formation of CH_4 by abiogenic processes within the inclusion after formation.

N_2-rich (relative to Ar) inclusions can be the result of: 1) decomposition of organic matter providing an additional source of N_2 (Norman and Musgrave, 1994); 2) breakdown of ammonia;

$$2NH_3=2N_2+3H_2 \quad (1.3)$$

or 3) mixing of fluids with different N_2/Ar and the subsequent trapping of various mixtures of these fluids. The breakdown of ammonia would increase N_2 and H_2 in the fluid inclusion gases. However, the reservoir and well temperatures are too low to be conducive to the thermal breakdown of ammonia (Norman and Musgrave, 1994), and there does not seem to be a correlation between increased N_2 and increased H_2 in gas analyses (Table 1.3).

During boiling, CH_4, H_2, N_2, and other light gases preferentially partition into the vapor phase (Henley et al., 1984). Owing to greater solubility, some gases, particularly CO_2 and H_2S, are partially retained in the residual liquid phase. Calculations of the gas content in either the vapor or liquid phase can be made using gas distribution coefficients following the procedures outlined by Giggenbach, (1980) and Henley et al., (1984) as detailed in Appendix A. Vapor-liquid distribution constants (referred to as K_d or B) reported by Fernandez-Prini et al., (2003) were used to calculate the composition of the liquid and vapor phases at different stages of boiling. Both closed and open system boiling end member processes were considered. Example boiling trends are illustrated in Figs. 1.8C and 1.9C. These calculations indicate that boiling can explain the progression in the fluid inclusion gas compositions from high CH_4 and H_2 to high CO_2. Simmons et

al. (2007) observed heterogeneous trapping of coexisting gas and liquid phases as a result of boiling in fluid inclusions from the Broadlands-Ohaaki geothermal system in New Zealand. The measured variations in CH_4 and H_2 to CO_2 in the fluid inclusions analyzed in this study probably reflect heterogeneous trapping of both liquid and vapor phases, as well; therefore, gas compositions of both liquid and vapor phases during progressive boiling were calculated and plotted in Figs. 1.8C and 1.9C. Fluid inclusion analyses with gas contents >1 mol% (Fig. 1.7) also suggest that some of these analyses are sampling predominantly vapor rich fluid inclusions.

However, boiling of a single source fluid cannot produce both the high CH_4 and high H_2 fluid inclusion gas compositions shown in Fig. 1.8A. Boiling also cannot explain the trend of some samples toward higher N_2 (relative to Ar) in shallower samples (Fig. 1.9A), since lower N_2 would be expected with progressive boiling; nor can boiling explain the trend of the variable He contents at near constant N_2/Ar ratio. The pattern of the fluid inclusion gas data indicates that boiling has influenced the variation in the gas compositions, but the data and compositional trends cannot be fully explained by this process.

Alternatively, variation in gas compositions suggests heterogeneity in the composition of the production fluids over time. Various studies have concluded that there is mixing between a deeper circulating geothermal reservoir fluid with a shallower meteoric fluid in the Dixie Valley geothermal field (Bergfeld et al., 2001; Kennedy and van Soest, 2006). Ra values of 0.7-0.76 have been interpreted to indicate the presence of a mantle derived He component (Kennedy and van Soest, 2006). The linear trend of increasing He at near constant N_2/Ar in both fluid inclusion gas analyses (Fig. 1.9A) and

surface gas analyses (Fig. 1.9B) is consistent with variable mixing between deeply circulating meteoric water (reservoir fluid) and shallow meteoric water (Fig. 1.9D) or variation in the input of He from a mantle derived source (Giggenbach, 1986). This trend is also observed in the data from the Dixie Valley well and fumarole gas samples (Fig. 1.9B) and in the well gas sampled from 28-33 (open circles, Fig. 1.9A). The fluid inclusions from depths of 718 and 1100 m (calcite) plot closer to the air or air saturated water end member on the mixing trend. This implies dominance of a shallow source fluid on the composition of gases trapped within this depth interval.

Conclusion

At the Dixie Valley geothermal field, fluid boiling triggered the precipitation of calcite and aragonite scale in concentric bands around tubing inserted into production well 28-33. The trends and ranges in fluid inclusion gas compositions from these mineral scales appear to result from the combined effects of fluid mixing and boiling. The fluid inclusion gas analyses define a linear trend of increasing He at constant N_2/Ar ratios similar to air saturated surface (meteoric) water, a trend consistent with variable mixing of this surface water with deeply circulated meteoric water (deep geothermal reservoir fluid) or variation in the input of He from a mantle derived source. However, the variations in CO_2/CH_4 and CO_2/H_2 in these inclusion gases and the entrapment of gas enriched in CH_4 and/or H_2 relative to the very CO_2 rich gas composition discharged at the wellhead demonstrate the impacts of progressive boiling. Because CO_2 is assumed to be the dominant gas present in geothermal systems based on well gas sampling (Hedenquist and Henley, 1985), the trapping of CH_4 and H_2 in fluid inclusions as a result of initial

boiling has implications for the calculation and interpretation of salinity and redox conditions in both modern and fossil geothermal systems.

Acknowledgments

Funding for this project was provided by the US Department of Energy's Geothermal Program under grant DE-FG36-04GO14292. The author would like to thank Terra-Gen Power, LLC for allowing the collection of the samples and providing data on downhole conditions. The author would also like to thank Jungho Park and David Norman for the fluid inclusion gas analyses, David Langton for his work in collecting the mineral scale samples, Louise Spann for processing and analyzing the samples using X-ray diffractometry. The author would also like to thank A.E. Williams-Jones and Stuart Simmons for their thoughtful review and comments.

References

Benoit, D., 1992. A case history of injection through 1991 at Dixie Valley, Nevada. Geothermal Resources Council Transactions 16, 611-620.

Bergfeld, D., Goff, F.E., Janik, C.J., 2001. Elevated carbon dioxide flux at the Dixie Valley geothermal field, Nevada: relations between surface phenomena and the geothermal reservoir. Chemical Geology 177, 43-66.

Blackwell, D.D., Golan, B., Benoit, D., 2000. Thermal regime in the Dixie Valley geothermal system. Proceedings World Geothermal Congress 2000, 991-997.

Blackwell, D.D., Leidig, M., Smith, R., Johnson, S., Wisian, K.W., 2002 Exploration and development techniques for Basin and Range geothermal systems: examples from Dixie Valley, Nevada. Geothermal Resources Council Transactions 26, 513-518.

Darling, W.G., 1998. Hydrothermal hydrocarbon gases: 1, Genesis and geothermometry. Applied Geochemistry 13, 815-824.

Fernandez-Prini, R., Alvarez, J., Harvey, A., 2003. Henry's constants and vapor-liquid distribution constants for gaseous solutes in H_2O and D_2O at high temperatures. Journal of Physical and Chemical Reference Data 32, 903-916.

Fiebig, J., Chiodini, G., Caliro, S., Rizzo, A., Spangenberg, J., Hunziker, J.C., 2004. Chemical and isotopic equilibrium between CO_2 and CH_4 in fumarolic gas discharges: Generation of CH_4 in arc magmatic-hydrothermal systems. Geochimica et Cosmochimica Acta 68, 2321–2334.

Giggenbach, W.F., 1980. Geothermal gas equilibria. Geochimica et Cosmochimica Acta 44, 2021-2032.

Giggenbach, W.F., 1986. The use of gas chemistry in delineating origin of fluids discharges over the Taupo Volcanic Zone: a review. International Volcanological Congress 5, 47-50.

Giggenbach, W.F., Corrales, R., 1992. The isotopic and chemical composition of water and steam discharges from volcanic-magmatic-hydrothermal systems of Guanacaste Geothermal Province, Costa Rica. Applied Geochemistry 7, 309-332.

Goff, F., Bergfeld, D., Janik, C.J., Counce, D., Murrell, M., 2002. Geochemical data on waters, gases, scales, and rocks from the Dixie Valley region, Nevada (1996-1999). Los Alamos National Laboratory publication LA-13972, 1-80.

Gonzales, L., Carpenter, S.J., Lohmann, K.C., 1992. Inorganic calcite morphology: Roles of fluid chemistry and fluid flow: Journal of Sedimentary Petrology 62, 382-399

Graney, J.R., Kesler, S.E., 1995. Gas composition of inclusion fluid in ore deposits: Is there a relation to magmas? In: Magmas, Fluids and Ore Deposits (ed. JFH Thompson) Mineralogical Association of Canada Short Course Series 23, 221-245.

Hedenquist, J.W., Henley, R.W., 1985. The importance of CO_2 on freezing point measurements of fluid inclusions; evidence from active geothermal systems and implications for epithermal ore deposition. Economic Geology 80, 1379-1406.

Henley, R.W., Truesdell, A.H., Barton, P.B., 1984. Fluid-mineral equilibria in hydrothermal systems. Reviews in economic geology, Society of Economic Geologists, El Paso, TX.

Kennedy, B.M., van Soest, M.C., 2006. A helium isotope perspective in the Dixie Valley, Nevada hydrothermal system. Geothermics 35, 26-43.

Liu, X.Y., Bennema, P., van der Eerden, J.P., 1992. The rough-flat-rough transition at crystal surfaces. Nature 356, 778-780.

Lutz, S.J., Moore, J.N., Benoit, D., 1997. Geologic framework of Jurassic reservoir rocks in the Dixie Valley geothermal field, Nevada: implications from hydrothermal alteration and stratigraphy. Proceedings 22nd Workshop on Geothermal Reservoir Engineering 1997, 131-139.

McCollum, T.M., Seewald, J.S., 2001. A reassessment of the potential for reduction of dissolved CO_2 to hydrocarbons during serpentinization of olivine. Geochimica et Cosmochimica Acta 65, 3769-3778.

Moore, J.N., Powell, T.S., Heizler, M.T., Norman, D.I., 2000. Mineralization and hydrothermal history of the Tiwi geothermal system, Philippines. Economic Geology 95, 1001-1023.

Moore, J.N., Norman, D.I., Kennedy, B.M., 2001. Fluid inclusion gas compositions from an active magmatic-hydrothermal system: a case study of The Geysers geothermal field, USA. Chemical Geology 173, 3-30.

Norman, D.I., Sawkins, F.J., 1987. Analysis of fluid inclusions by mass spectrometer. Chemical Geology 61, 1-10.

Norman, D.I., Musgrave, J.A., 1994. N_2-Ar-He compositions in fluid inclusions: Indicators of fluid source. Geochimica et Cosmochimica Acta 58, 1119-1131.

Norman, D.I., Moore, J.N., Yonaka, B., Musgrave, J., 1996. Gaseous species in fluid inclusions: a tracer of fluids and indicator of fluid processes. Proceedings 21st Workshop on Geothermal Reservoir Engineering 1996, 233-240.

Norman, D.I., Moore, J.N., Musgrave, J., 1997. More on the use of fluid-inclusion gaseous species as tracers in geothermal systems. Proceedings 22nd Workshop on Geothermal Reservoir Engineering 1997, 419-426.

Norman, D.I., Moore, J.N., 1999. Methane and excess N_2 and Ar in geothermal fluid inclusions. Proceedings 24th Workshop on Geothermal Reservoir Engineering 1999, 233-240.

Rietveld, H.M., 1969. A profile refinement method for nuclear and magnetic structures. Journal of Applied Crystallography 2, 65-71.

Rimstidt, J.D., 1997. Gange mineral transport and deposition. In: Geochemistry of Hydrothermal Ore Deposits (ed. HL Barnes) New York, John Wiley and Sons, 487-516.

Saunders, J.A., 1990. Colloidal transport of gold and silica in epithermal precious-metal systems; Evidence from Sleeper deposit, Nevada. Geology 18, 757-760.

Siega, F.L., Herras, E.B., Buning, B.C., 2005. Calcite scale inhibition: the case of Mahanagdong Wells in Leyte geothermal production field, Philippines. Proceedings World Geothermal Congress 2005.

Simmons, S.F., Browne, P.L.R., 2000. Hydrothermal minerals and precious metals in the Broadlands-Ohaaki geothermal system: Implications for understanding low-sulfidation epithermal environments. Economic Geology 95, 971-999.

Simmons, S.F., Christenson, B.W., 1994. Origins of calcite in a boiling geothermal system. American Journal of Science 294, 361-400.

Simmons, S.F., Simpson, M.P., Reynolds, T.J., 2007. The significance of clathrates in fluid inclusions and the evidence for overpressuring in the Broadlands-Ohaaki geothermal system, New Zealand. Economic Geology 102, 127-135.

Speed, R.C., 1976 Geologic map of the Humboldt Lopolith. Geological Society of America Map Chart Series MC-14, 1:81050 scale, 1 sheet.

Weibel, A.F., 1987. An overview of the geology and secondary mineralogy of the high temperature geothermal system in Dixie Valley, Nevada. Geothermal Resources Council Bulletin Sept/Oct, 5-11.

CHAPTER 2

MODELING THE GEOCHEMICAL EFFECTS OF INJECTION AT COSO GEOTHERMAL FIELD, CA; COMPARISON WITH FIELD OBSERVATIONS

Abstract

Decreased performance of injection wells after 5 to 7 years of injection has been documented in several geothermal fields. In this study, the effects of injecting flashed geothermal fluids into the Coso geothermal field, California are investigated by comparing drill cuttings from the original injection wells with samples from wells drilled on the same pads after injectivities in the original wells had declined. At Coso the fluids injected into well 68-20 had silica contents up to 940 ppm and are significantly supersaturated in silica with respect to quartz, the stable silica phase in the reservoir. X-ray diffraction and scanning electron microscope analyses of the reservoir rock penetrated by redrilled injection well 68-20RD indicate that loss of injectivity in 68-20 was caused by the deposition of silica as opal-A accompanied by trace amounts of calcite near the well bore. As the scale deposits mature, the original 2 μm spheres coalesce into larger spheres, up to 10 μm in diameter and plate like sheets. Application of TOUGHREACT one dimensional (1D) reactive transport models (Xu et al., 2004)

predicts the deposition of amorphous silica with minor calcite, leading to a sharp decrease in porosity 1 to 2 years after initiation of injection. These predictions are consistent with field measurements and the observations made from injection well cuttings from Coso pad 68-20. Furthermore, the modeling predicts silica deposition will occur close to the wellbore, consistent with the observation that amorphous silica is found only in the redrilled wells (68-20RD and 68B-20RD) with trajectories closest to a previously drilled injection well.

Introduction

The geochemical effects of injecting fluids into geothermal reservoirs are poorly understood and may be significantly underestimated. Decreased performance of injection wells has been observed in several geothermal fields after only a few years of service, although the reason for these changes has not previously been established. The purpose of this investigation is to predict the geochemical effects of the injection fluids on the reservoir rocks and to test the effects of modifying the injection fluid as a strategy for mitigating mineral precipitation. This study consists of petrologic investigations of the scale mineral assemblages in the cuttings from wells drilled on the 68-20 pad at the Coso geothermal field along with application of TOUGHREACT one dimensional reactive transport models to predict the mineral precipitation observed. The effects of changes to the injected fluid chemistry on the reservoir fluids and rocks were also modeled to further understand the consequences of particular injection strategies.

The Coso Geothermal Field

The Coso geothermal field is developed in Mesozoic granitic rocks of the Sierra Nevada Batholith on the western edge of the Basin and Range (Adams et al., 2000) (Fig. 2.1). The heat driving the geothermal activity is related to shallow intrusions that have given rise to 38 rhyolitic domes during the last million years. The reservoir host rocks range in composition from diorite to granite with varying degrees of alteration and veining (Kovac et al., 2005). Active and fossil fumaroles lie along a northeast to southwest trending belt that extends through Devil's Kitchen and Coso Hot Springs. On the eastern margin of the field, known as the East Flank, fossil sinter and travertine deposits are present (Adams et al., 2000). Installed capacity of the power plant is 240 MWe, and power production has been sustained since 1989. Between 1987 and 1993, six injection wells were drilled on the 68-20 pad and four were drilled on the 67-17 pad in the southern part of the field (Fig. 2.1). Cuttings were examined from wells drilled on both pads, but pad 67-17 is not discussed here because no injection related mineral scale deposits were found in the cuttings of these wells.

Well pad 68-20

Between 1987 and 1993, six injection wells were drilled on the 68-20 pad in the southern part of the field. The trajectories of these wells and lost circulation zones obtained from well logs are shown in Fig. 2.2. Injectivity decreased in well 68-20 from a maximum liquid injection rate of over 1000 kph (kilopounds per hour mass flow) in March, 1989 to a minimum rate of 0 kph in November, 1990 after a steady decline (Fig. 2.3). Mechanical and chemical cleanouts increased injectivity to a one time high of 800

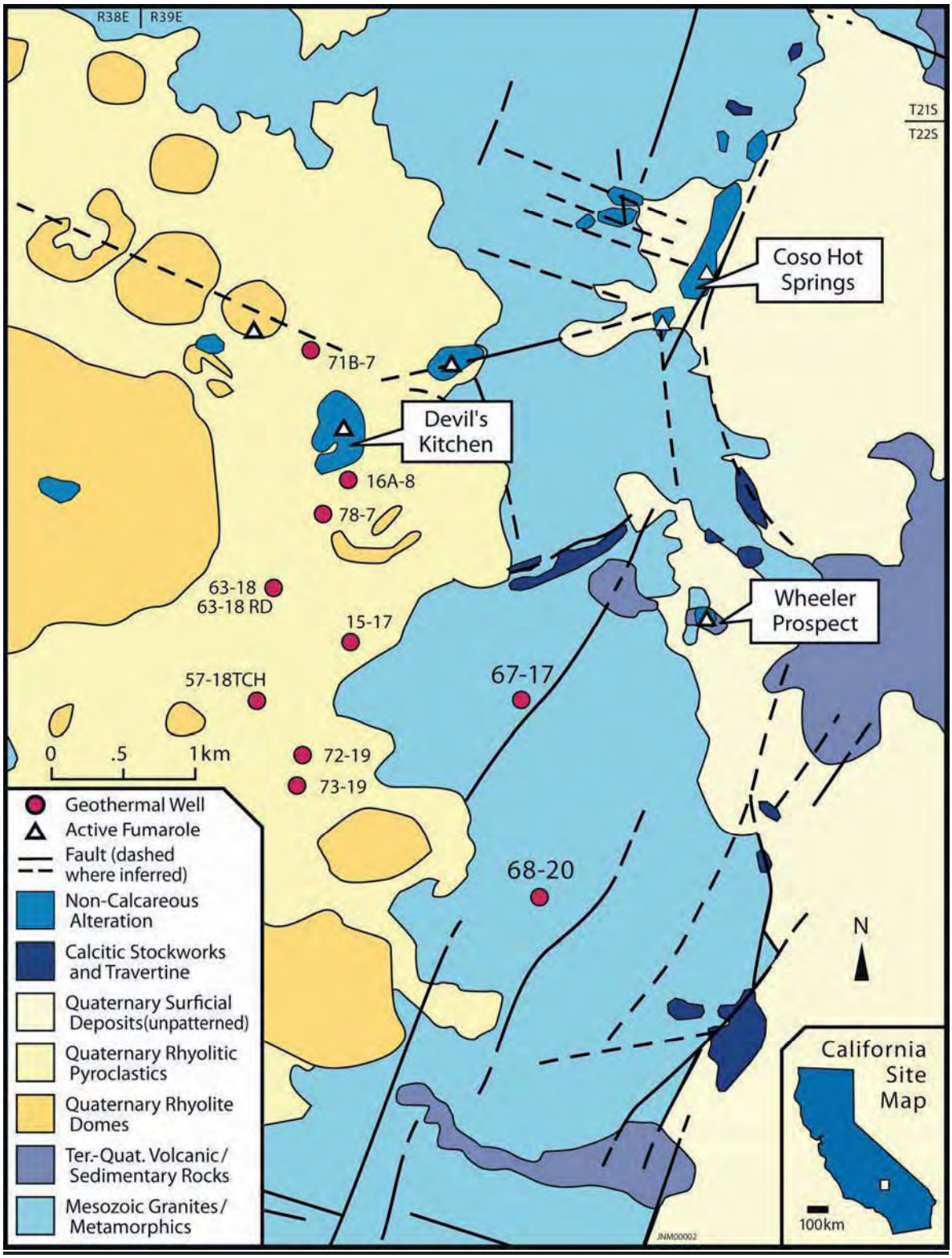

Fig. 2.1. Simplified geologic map of the Coso geothermal field showing the locations of the major thermal features. The 68-20 injection pad is located in the southern part of the field.

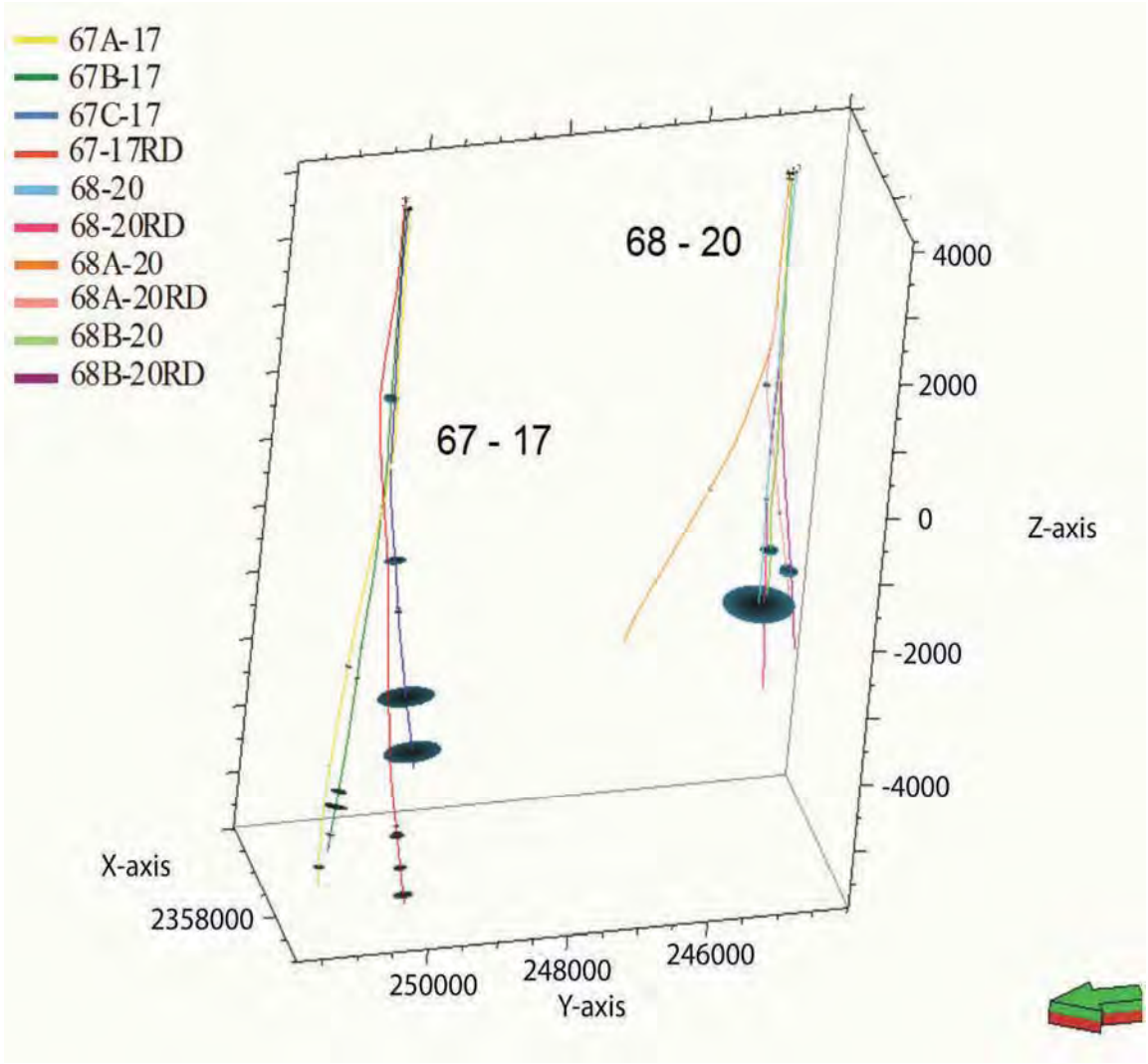

Fig. 2.2. Well trajectories for injection wells drilled in pads 67-17 and 68-20. Locations of lost circulation zones are shown as discs, and the amount of fluid lost is represented by the size of the disc. X and Y axes in UTMs, Z axis in feet.

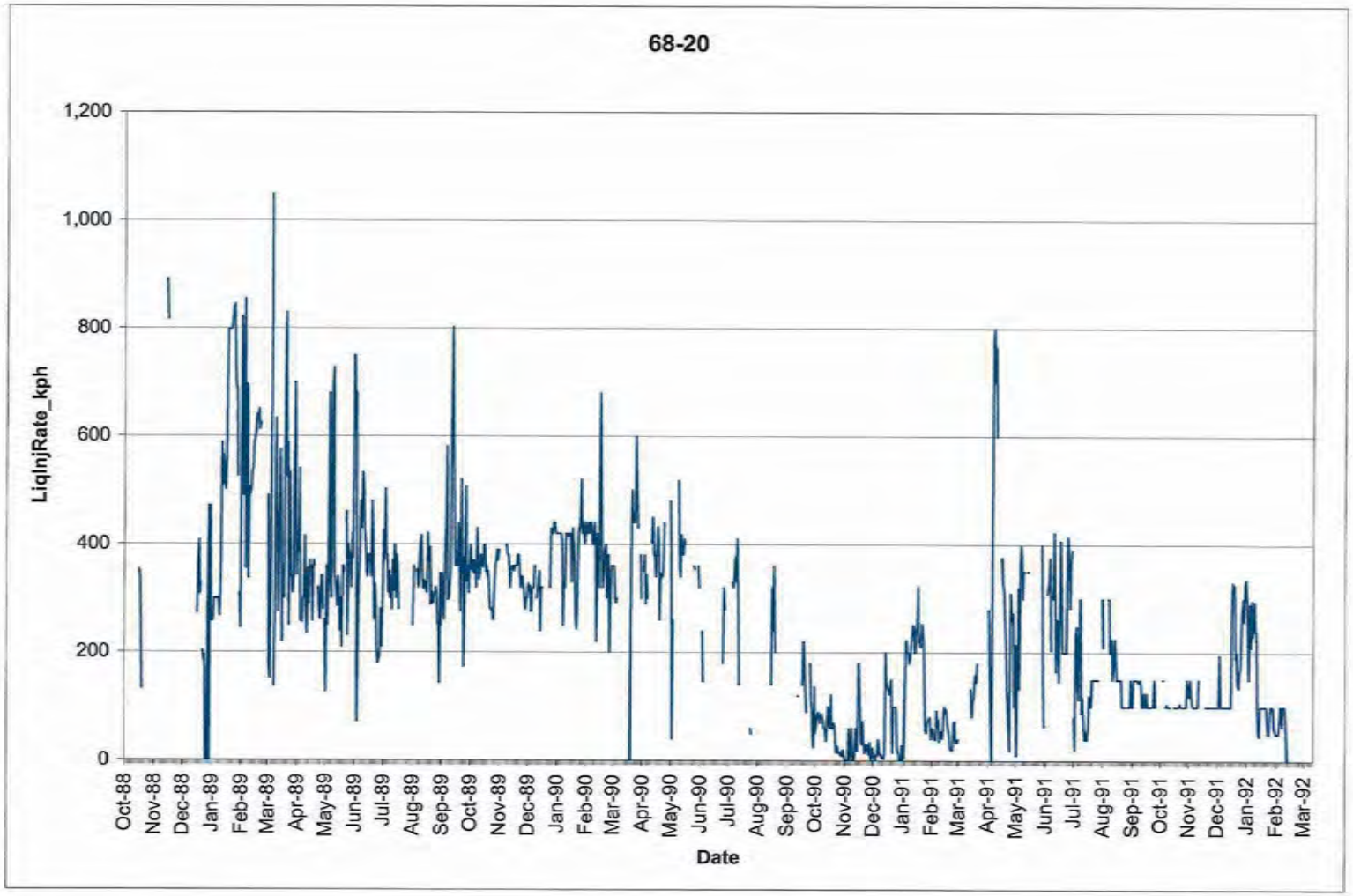

Fig. 2.3. Injection history of well 68-20 from October 1988 to March 1992. (kph=kilopounds per hour)

kph after November, 1990, but never fully recovered, remaining between 0-400 kph through 1992. Redrilled wells also experienced similar injectivity declines.

Reservoir temperatures in this part of the field prior to injection ranged from approximately 205-240^{o}C, but cooling of the reservoir was observed around these wells post injection as seen in temperature logs of subsequent redrills. The temperatures of the injected fluids ranged from 110-120^{o}C. Cuttings from the six injection wells were sampled at 3 m intervals. The reservoir host rocks in these wells ranged from diorite to granite with trace to moderate alteration and veining. Fault breccias were observed in the cuttings, indicating major fault or fracture zones intersected by the wells.

Table 2.1 shows the reported chemistry of injection fluid for well 68-20. There was a wide range in the composition of the injected fluids, showing variation in produced fluids and practices of adding steam condensate back into the injected fluid. The maximum silica content analyzed was 965 mg/L.

Mineral Scale from 68-20RD

Cuttings from Coso injection wells 68-20, the original injection well, and 68-20RD, 68A-20, and 68A-20RD have been examined at 3 m depth intervals. The rock type, the abundance of primary and secondary minerals, and the abundance, mineralogy, and paragenesis of the veins were documented at each interval. Thinly banded opaline silica was observed in the cuttings from 68-20RD and 68B-20RD, but not in the original injection well 68-20 or in wells 68A-20, 68A-20RD, and 68B-20. The banding and textural relationships suggest the silica represents fracture fillings and not alteration of preexisting minerals. The greatest density of silica precipitation was found in cuttings

Table 2.1

Well 68-20 Injected Fluid Chemistry

Chemistry of injected fluid from well 68-20, showing high, low, and average concentrations in mg/kg from 15 analyses. Brines were injected at 110-120°C.

	High	Low	Average
Na^+	4,283	2,897	3,612
K^+	941	362	614
Ca^{2+}	130	19	45
Mg^{2+}	8.7	0	1.1
Fe	84.1	0.1	9.5
Al^{3+}	10.4	0	1.1
$SiO_{2\ (aq)}$	965	97	657
$B(OH)_3$	141.8	83	115.4
Li^+	47	25	34
Sr^{2+}	8.2	2.6	4.4
As_{total}	26.24	2.85	9.54
Ba^{2+}	116	0	9
HCO_3^-	229	77	167
Cl^-	6,958	5,015	6,079
F^-	5.7	1.6	2.5
SO_4^{2-}	99	27	68
TDS	12300	9233	11103
Lab pH	8.3	6.17	7.44

from depths of 869-884 and 1710-1713 m in well 68-20RD. Samples of the precipitate from these two zones were analyzed using a scanning electron microscope and X-ray diffractometer. Additional petrographic images (photomicrographs and SEM images) of silica scale from 68-20RD and 68B-20RD are shown in Appendix B. SEM images and X-ray patterns of scale deposits are separated here by depth for descriptive purposes; however, morphologies and depth are not correlative.

869-884 m Depth

The silica deposits consist of opal-A spheres and plates. Fig. 2.4 shows the morphological progression associated with maturation of deposits. Textural relationships shown in Fig. 2.4A indicate the silica was deposited initially as spheres 1-2 μm in diameter. As the deposit matures, the spheres coalesce to form larger spheres up to 10 μm in diameter (Fig. 2.4B). Further maturation is associated with the formation of plates and sheets. Infilling of the spaces between spheres provides a possible explanation for the dense, smooth surfaces seen in Figs. 2.4B, 2.4C, and 2.4D. This maturation sequence is similar to changes observed in young sinter deposits in New Zealand described by Rodgers et al. (2004) and Lynne and Campbell (2004). Traces of calcite locally coat the amorphous silica, suggesting it represents a later stage in the evolution of the deposits. The X-ray diffraction pattern of hand picked silica rich samples from this depth (Fig. 2.4E) indicate that the deposit consists of opal-A with a broad peak centered at 22^{o} 2-theta. In addition, quartz peaks are present in the X-ray diffraction patterns at 21.5^{o} and 26.8^{o} 2-theta, but quartz was not unambiguously documented in the SEM images. It is possible that traces of quartz were deposited by the injected fluid or through interactions with the amorphous silica. Alternatively, the quartz could represent fragments of the host reservoir rock that were incorporated into the deposits of amorphous silica.

1710-1713 m Depth

SEM images of silica deposits from a depth of 1710-1713 m (Fig. 2.5) show that they display similar textural and mineralogical relationships as those from depths of 869-884 m (Fig. 2.4). Both dense and porous layers of silica are present. Textures shown in

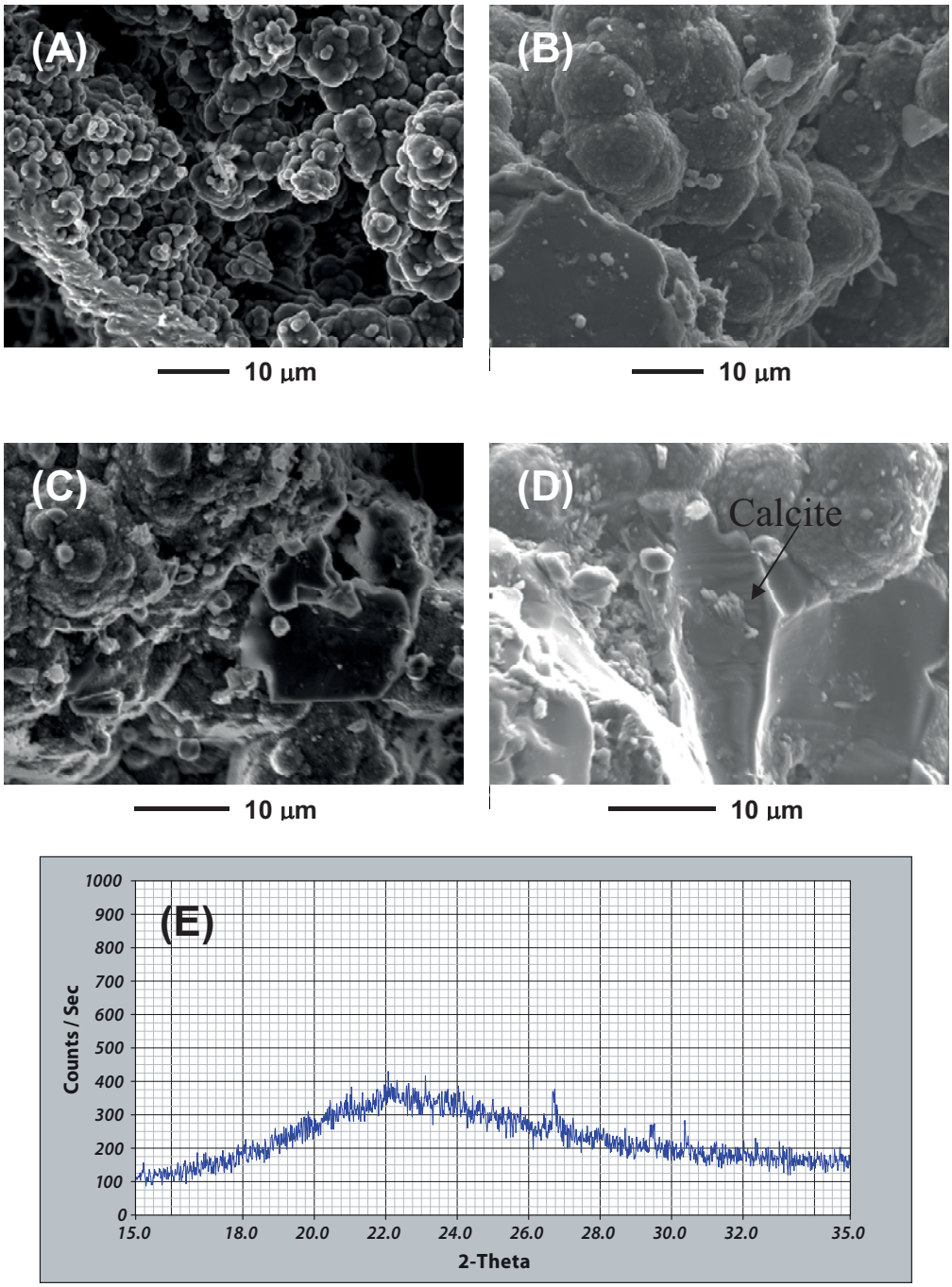

Fig. 2.4. Mineral scale from 68-20RD at 869-884 m depth. (A)-(D) SEM images of samples taken from 68-20RD at 869-884 m depth. Opal-A spheres 1-2 mm in diameter seen in (A) coalesce to form 10 mm spheres and sheets seen in (B), (C), and (D). (E) X-ray diffraction pattern of scale samples taken from the depth interval 869-884 m showing a broad opal-A peak centered at 22^{o} 2-theta and quartz peaks at 21.5^{o} and 26.8^{o} 2-theta.

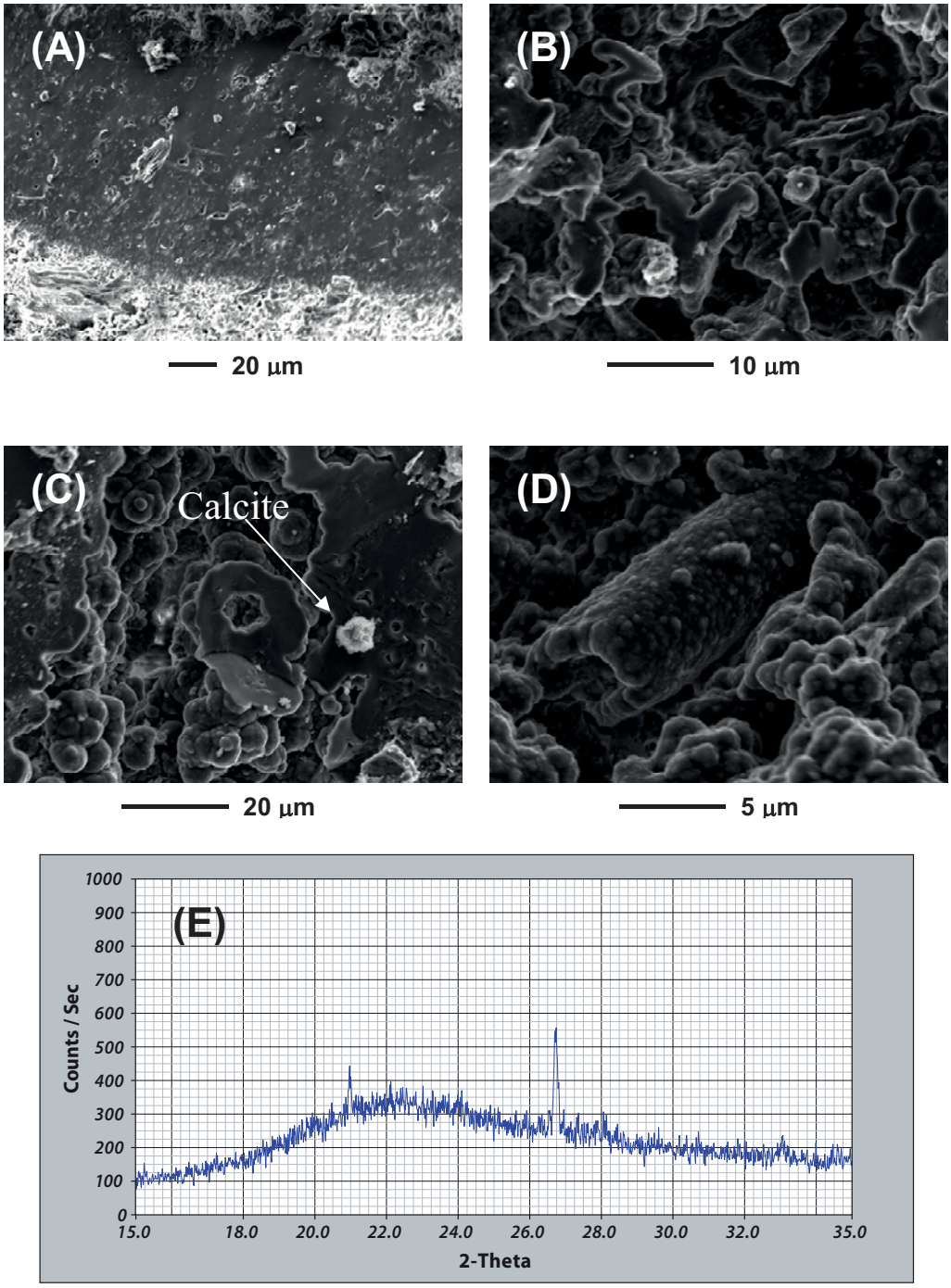

Fig. 2.5. Mineral scale from 68-20RD at 1710 to 1713 m depth. (A)-(D) SEM images of samples taken from 68-20RD at 1710-1713 m depth. (A) Alternating silica layers with varying density and visible porosity. (B), (C) Silica spheres aligning to form fibrils (B) and sheets (C). (D) Tube structure covered with silica spheres. (E) X-ray diffraction pattern of scale samples taken from the depth interval 1710-1713 m showing a broad opal-A peak centered at 22° 2-theta and quartz peaks at 21.5° and 26.8° 2-theta.

Figs. 2.5A, 2.5B and 2.5C suggest that the denser layers develop as the silica spheres form strands and sheets. The formation of strands of small spheres suggests a progression to a more stable silica form. The silica plates in Fig. 2.5C appear to be formed from coalesced opal-A spheres. An unusual tube like structure coated with silica spheres is shown in Fig. 2.5D. Similar features, interpreted as silicified bacteria, have also been observed in sinters from geothermal fields in New Zealand (Rodgers et al., 2004). The X-ray pattern (Fig. 2.5E) of a sample from 1710-1713 m indicates the silica consists of opal-A with a broad peak centered at 22^{o} 2-theta and quartz with peaks at 21.5^{o} and 26.8^{o} 2-theta.

Discussion

Monomeric and polymeric deposition are two mechanisms of silica precipitation (Iler, 1979). Direct deposition of silica molecules onto solid surfaces is referred to as monomeric deposition. The formation of a colloid in solution and its subsequent precipitation is referred to as polymeric deposition. Monomeric deposition tends to form a hard, dense deposit, while polymeric deposition forms a softer, porous silica scale. The textures of silica spheres observed in deposits from Coso well 68-20RD indicate that polymeric deposition is the dominant process of silica deposition. The growth and nucleation stages that accompany the polymerization of amorphous silica are controlled mainly by silica saturation, pH, and salinity (Makrides et al., 1978; Iler, 1979). Precipitation or amorphous silica can be further catalyzed by the presence of iron and aluminum in solution, which reduces the solubility of amorphous silica when these metals are incorporated (Gallup, 1998). At higher degrees of silica supersaturation and

near neutral pH, polymeric deposition is favored (Iler, 1979). As the silica precipitates, the degree of supersaturation in the fluid decreases, favoring monomeric deposition. Also, the chemical composition of the injected fluid is variable (see Table 2.1), including varying degrees of silica saturation. These mechanisms can explain the variety in textures and observed porosity in the amorphous silica scale.

When compared to the maturation sequence observed and documented in geothermal sinter deposits (Rodgers et al., 2004; Lynne and Campbell, 2004; Lynne et al., 2007), several textures observed in the Coso scale indicate a maturation of silica during and/or after deposition. The observed textures include nano and micro spheres (Fig. 2.4A), botryoidal coalesced microspheres (Fig. 2.4A), bumpy microspheres (Fig. 2.4B), sheets (Fig. 2.5A) and aligned chains of amorphous silica (Fig. 2.5B and 2.5C). Maturation of the silica usually leads to increased porosity and permeability when the opal-A phase progresses to opal-CT. However, infilling of spaces within aggregates of colloidal particles that leads to sheet like textures observed at Coso may provide a barrier to further maturation of the silica by depriving contact with fluid necessary to dissolve and re precipitate silica as a more stable phase. This infill could also lead to difficulty in removing this scale as it becomes a barrier to fluid flow over time.

Mineral Scale Summary

Examination of cuttings from redrilled injection wells at the Coso geothermal field has yielded direct evidence for relating injectivity losses to mineral precipitation. Deposits of amorphous silica associated with traces of calcite were found in the reservoir rocks adjacent to the original injection well 68-20. This well had experienced a

significant loss in injectivity within a period of 1 1/2 years. The silica deposits are layered, with individual layers ranging from tens to hundreds of micrometers. Apparent porosities vary from layer to layer with some displaying little visible pore space. Textural relationships indicate that the silica was originally deposited as 1-2 μm spheres of opal-A. The size and uniform diameter of the spheres suggests the silica layers formed as a colloidal precipitate. As the deposits mature, botryoidal, coalesced microspheres and bumpy microspheres up to 10 μm in diameter form. With further maturation, infilling of pore spaces between spheres results in the formation of silica plates and sheets, which could form a barrier to fluid flow that could slow or stop the maturation sequence of the silica.

One Dimensional Reactive Transport Modeling

Modeling Approach

Simulations were carried out using the nonisothermal reactive geochemical transport code TOUGHREACT (Xu and Pruess, 2001; Xu et al., 2004). This code was developed by introducing reactive chemistry into the framework of the existing multiphase fluid and heat flow code TOUGH2 V2 (Pruess et al., 1999, see also http://www-esd.lbl.gov/TOUGHREACT/). Interactions between mineral assemblages and fluids can occur under local equilibrium or kinetic rates. Precipitation and dissolution reactions can change formation porosity and permeability. This simulator can be applied to one, two, and three dimensional porous and fractured media with physical and chemical heterogeneity. Simulations can include any number of species present in the liquid, solid, and gaseous phases. Various thermal, physical, and chemical processes are

considered under conditions of pressure, temperature, water saturation, ionic strength, pH, and Eh. The current models do not consider processes related to certain types of mineral precipitation and maturation kinetics, including nucleation, formation of metastable phases and their transformation to stable phases, and Ostwald ripening (Xu et al., 2007).

Simulation Setup

The conceptual model considers a one dimensional flow path between the injection and production wells, which is a small subvolume of the more extensive three-dimensional reservoir. The initial reservoir conditions were 275^{o}C and 30 MPa pressure. An over pressure of 2 MPa was applied to simulate injection. The model is based on conditions during nearly continuous injection over 7 years. The control case model uses measured, observed, and estimated parameters from data gathered through various studies at Coso (Lutz and Moore, 1997; Kovac et al., 2005; McLin et al., 2006). Further cases are based on hypothetical situations where these parameters are adjusted to determine the sensitivity of the modeling, as well as predict alternative reservoir conditions. The simulations were run to a total time of 7 years. Changes in fluid pH, fracture porosity, fracture permeability, fluid temperature, and changes in mineral abundances were monitored out to a distance of 594 m from the injection well. Mineral abundance changes were reported in terms of changes in volume fraction for the following minerals: quartz, potassium feldspar, chlorite, illite, Na smectite, Ca smectite, calcite, dolomite, anorthite, annite, and amorphous silica. Amorphous silica, calcite, and quartz displayed the most significant changes. Changes in porosity were calculated as a function of mineral

dissolution and precipitation. A porosity increase indicates that mineral dissolution is dominant, while a porosity decrease occurs when precipitation dominates. Changes in permeability were calculated from changes in porosity using a cubic law to calculate the relationship between porosity and permeability.

Fluid and Heat Flow Conditions

The geometry and fluid and heat flow conditions are modeled after those described in Xu and Pruess (2004). A one dimensional MINC (multiple interacting continua) model was used to represent the fractured rock. The MINC method can resolve "global" flow and diffusion of chemicals in the fractured rock and interaction with "local" exchange between fractures and matrix. Details on the MINC method for reactive geochemical transport are described by Xu and Pruess (2001). In the simulations, interactions with 1) a zone representing the relatively impermeable, unaltered host rock, and 2) altered, fractured, and veined host rock were considered. In addition, two different reservoir rock types, diorite and granodiorite, were considered. These are the rock types are the dominant lithologies where amorphous silica deposition has been observed. The hydrologic and thermal parameters used in the models are shown in Table 2.2. Density = 2650 $kg*m^{-3}$, heat capacity = 1000 $J*kg^{-1}K^{-1}$, and diffusivity = 10^{-9} $m^{-2}s^{-1}$ were used for all zones. The cubic law was used to define the porosity-permeability relationship in both zones (Xu et al., 2004). The model generates changes in porosity and permeability based on changes in mineral abundances.

Mineralogical Conditions

The reservoir rocks at a depth of 878 m in 68-20RD are dominated by hornblende-biotite-quartz diorite. Biotite granodiorite dominates at 1710 m. The mineralogical compositions of these rocks were estimated from petrographic observations of samples from 68-20RD and from X-ray and thin section studies of East Flank wells by Kovac et al. (2005) and Lutz and Moore (1997). Both rock types were found to be only weakly altered in 68-20RD. The veining was found to be especially weak in the diorite at 878 m, so the fracture zone was modeled as nearly empty. The deeper granodiorite zone was found to contain quartz, calcite, and chlorite veins. Mineral parameter inputs are shown in Table 2.3.

Table 2.2

Hydrologic and Thermal Parameters

Hydrologic and thermal parameters of rocks used in the models

Parameters	Fracture	Average Weakly Altered Granodiorite	Average Weakly Altered Diorite
Volume (m^3)	0.1	0.9	0.9
Permeability (m^2)	2.0E-12	2.0E-18	2.0E-15
Porosity	0.10	0.02	0.05
Thermal Conductivity ($W^* m^{-1}K^{-1}$)	2.9	3.0	3.0
Tortuosity	0.3	0.1	0.1

Table 2.3

Mineralogical Parameters

Simplified initial mineralogical composition of the two rocks used in the preliminary simulations. A temperature of 275°C was used for the initial rock temperature in the simulations.

	Volume Fraction of Solid Rock			
	1710 m: Granodiorite hosted		878 m: Diorite hosted	
Mineral	Average Weakly Altered Granodiorite	Fracture	Average Weakly Altered Diorite	Fracture
Quartz	0.34	0.05	0.135	
Potassium Feldspar	0.17		0.045	
Chlorite	0.02	0.01	0.010	
Illite	0.03			
Calcite	0.02	0.04	0.025	0.009
Anorthite	0.33		0.038	
Annite	0.06		0.150	

Mineral Kinetic Rates and Parameters

Mineral dissolution and precipitation are considered under kinetic constraints. The general kinetic rate expression is used in TOUGHREACT (Xu et al., 2004) is:

$$r_m = \pm k_m A_m a_{H+}{}^n |1 - Q_m/K_m| \quad (2.1)$$

where m is the mineral index, r_m is the dissolution/precipitation rate, (positive for dissolution, negative for precipitation), k_m is the rate constant (moles per unit mineral surface area and unit time) which is temperature dependent, A_m is the specific reactive surface area per kg of H_2O, a_{H+} is the activity of H^+, and n is an empirical reaction order

accounting for catalysis by H^+ in solution. K_m is the equilibrium constant for the mineral water reaction written for the destruction of one mole of mineral m, Q_m is the ion activity product. The temperature dependence of the reaction rate constant can be expressed as:

$$k = k_{25} \exp[-E_a/R(1/T - 1/298.15)] \quad (2.2)$$

where E_a is the activation energy, k_{25} is the rate constant at 25°C, R is the universal gas constant, and T is absolute temperature. Table 2.4 shows the parameters used in the kinetic rate expression.

Water Chemistry

The composition of the reservoir fluid was estimated from the approximate composition of reservoir fluid taken from an East Flank well (Table 2.4). Initial fluid compositions within the fracture and host rock were calculated by equilibrating the reservoir fluid composition with each rock's mineralogical composition at 275°C. An example injection fluid composition that was calculated from 15 well 68-20 injection fluid analyses as representative injection fluid was chosen as the trial injection water (Table 2.5). The injectate composition was not allowed to change over time within the model.

Results

In the modeled control case for both diorite and granodiorite hosted fracture systems, amorphous silica precipitates soon after injection begins, followed by calcite and a very minor amount of quartz (Figs. 2.6A, 2.6B, 2.6C, and 2.6D), consistent with

Table 2.4

Kinetic Rate Parameters

List of kinetic rate parameters used in Eqns. (1) and (2) for minerals considered in the present paper (Xu and Pruess, 2004; Palandri and Kharaka, 2004). The first line indicates dissolution parameters and the second line precipitation parameters; the same values were used for both where only one line is shown.

Mineral	k_{25} (moles m^{-2} s^{-1})	E_a (KJ/mole)	n (rxn. order)	Surface Area (cm^2/g)
Quartz	1.2589E-14	87.5	0	9.1
Am. Silica	7.3200E-13	60.9	0	1.0E6
	1.0000E-10	0.00	0	1.0E6
K-feldspar	1.0000E-12	57.78	0	9.1
Anorthite	1.0000E-12	57.78	0	9.1
Na smectite	1.0000E-14	58.62	0	108.7
Ca smectite	1.0000E-14	58.62	0	108.7
Illite	1.0000E-14	58.62	0	108.7
Annite	2.5119E-15	66.20	1	9.1
	2.5119E-15	66.20	0	9.1
Calcite	6.9183E-2	18.98	1	9.1
	6.4565E-7	62.76	0	9.1
Dolomite	1.0233E-3	20.90	1	9.1
	4.4668E-10	62.76	0	9.1
Chlorite	2.5119E-12	62.76	0	9.1

Table 2.5

Fluid Chemistry

Composition of a reservoir fluid from an East Flank well at 275°C, the temperature used in the simulations, and average injection fluid composition at 120°C temperature based on 15 samples.

Chemical Component	Reservoir (Mol/kg)	Injection (Mol/kg)
SiO_2	1.30E-2	9.96E-03
$B(OH)_3$	8.42E-3	1.01E-02
Na^+	9.50E-2	1.46E-01
K^+	1.20E-2	1.42E-02
Li^+	2.45E-3	4.44E-03
Ca^{2+}	9.55E-4	1.07E-03
Mg^{2+}	4.12E-6	2.22E-2
Sr^{2+}	3.60E-5	5.00E-2
Cl^-	1.10E-1	1.60E-01
F^-	1.47E-4	1.15E-04
HCO_3^-	1.10E-3	2.48E-03
SO_4^-	3.12E-4	6.97E-04
HS^-	3.02E-5	
CH_4	6.25E-10	
pH	6.84	6.47
As		1.16E-04

observed mineral scale deposits in the injection well 68-20RD (Figs. 2.7A and 2.7B). Amorphous silica deposition did not occur in a case where silica concentration was decreased in the injected fluid by an order of magnitude (Figs. 2.6A and 2.6D).

In both the diorite and granodiorite hosted cases, the majority of amorphous silica precipitates within a few meters of the well and within the first year of the simulation (Fig. 2.8 A and C). Minor calcite precipitation is also precipitated rapidly within the first few meters (Fig. 2.8 B and D). Modeled porosity and permeability decreases are also predicted within a few meters of the well over the same time period.

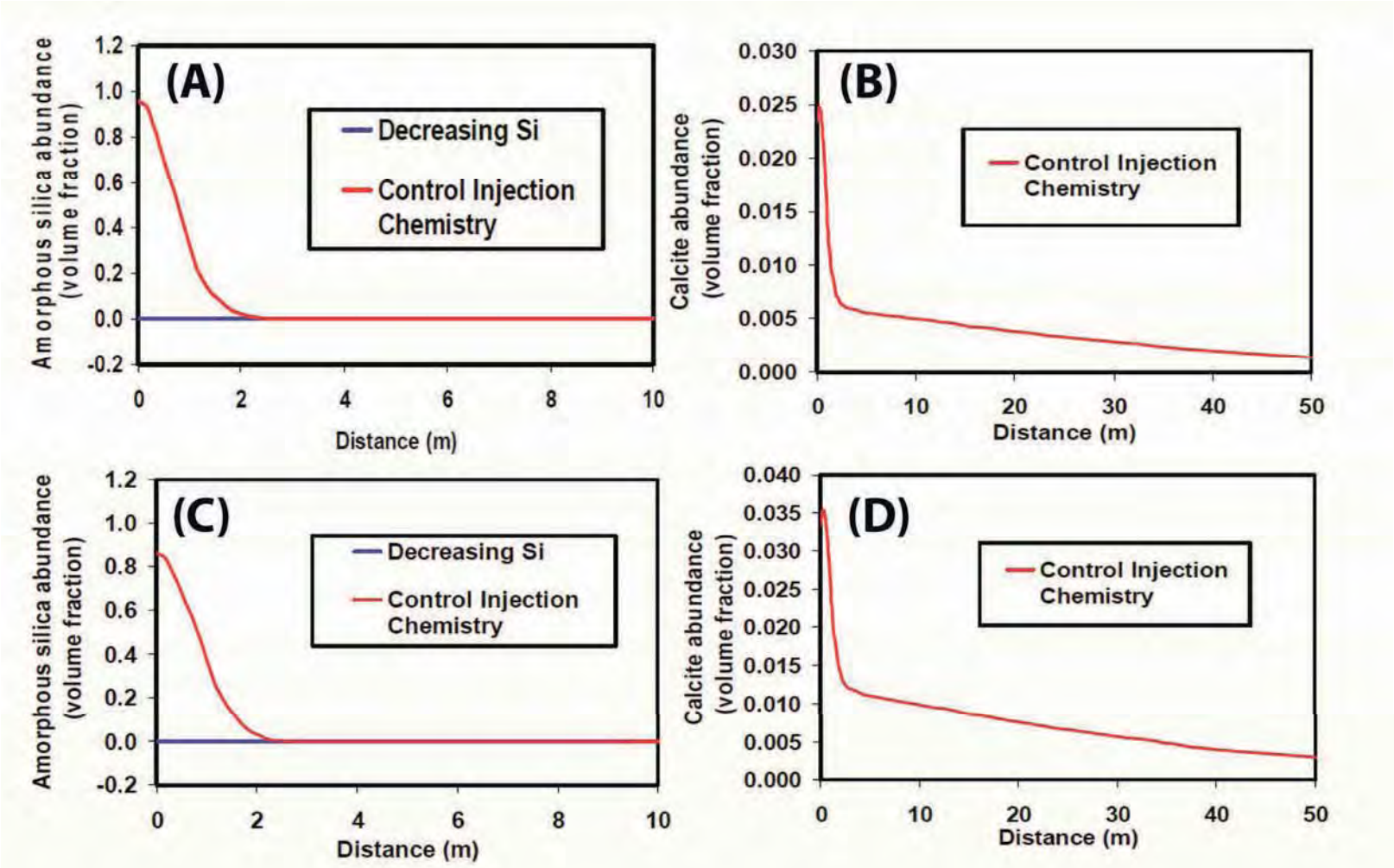

Fig. 2.6 Results of TOUGHREACT models. (A) and (B) Modeled results for the diorite hosted case showing amorphous silica (A) and calcite (B) as a function of distance in meters at t = 7 years. (C) and (D) Modeled results for the granodiorite hosted case showing amorphous silica (C) and calcite (D) as a function of distance in meters at t = 7 years.

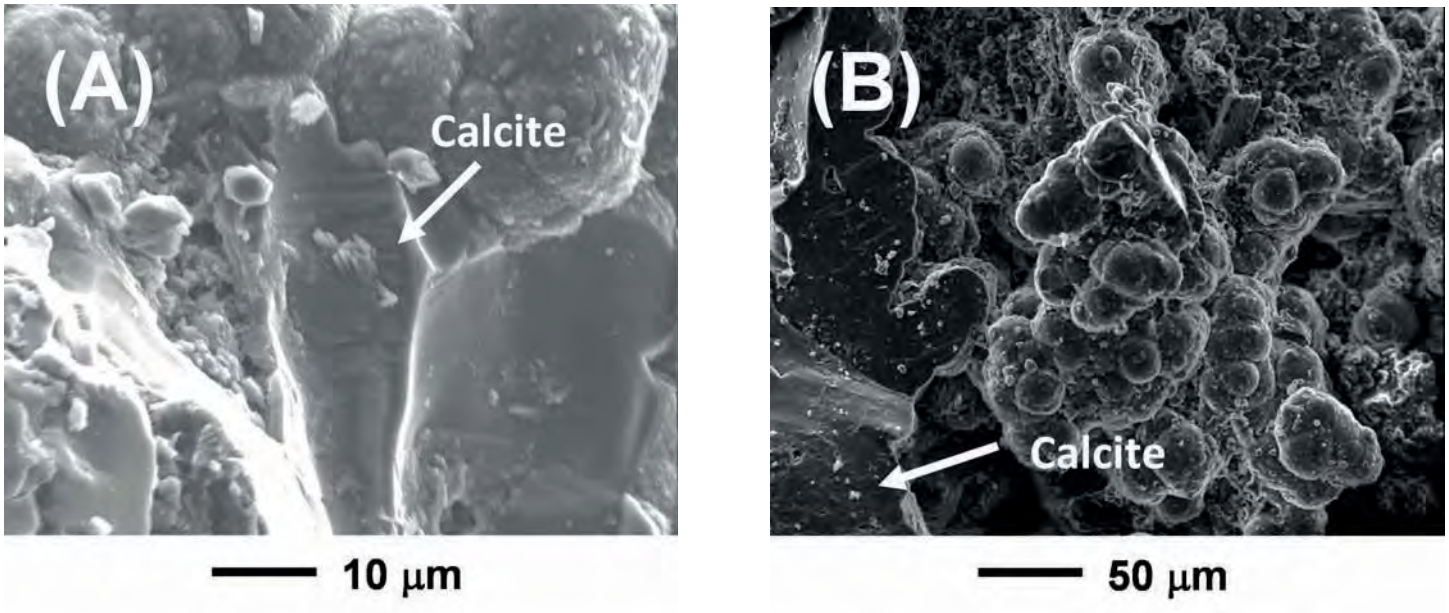

Fig. 2.7. SEM images showing calcite in scale. (A) SEM image of opal-A and calcite from the depth interval 869-884 m. (B) SEM image of opal-A with small white calcite crystals from the depth interval 1710-1713 m.

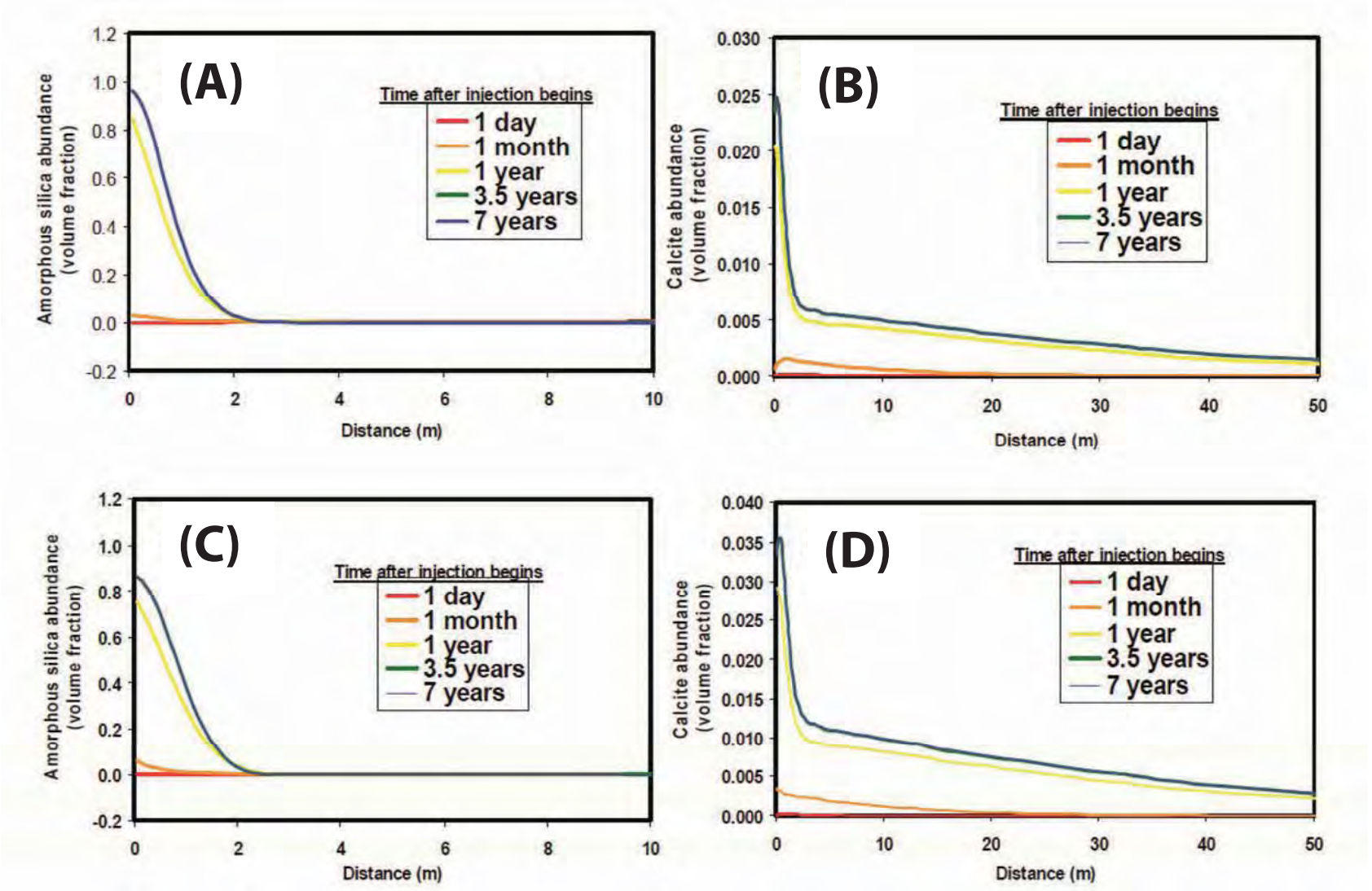

Fig. 2.8. Modeled results using the control injection chemistry for the diorite hosted case ((A) and (B)) and the granodiorite hosted case ((C) and (D)) showing amorphous silica and calcite as a function of distance in meters for various time periods over seven years.

Well 68-20, the first well drilled on the 68-20 pad, experienced a sharp decline in injectivity within months of initiation of injection. Significant amorphous silica scale deposits have only been observed in two of the subsequently drilled injection wells studied on the 68-20 pad, wells 68-20RD and 68B-20RD. The trajectory of 68-20RD lies only several meters from the original well 68-20. The trajectory of 68B-20RD lies near that of 68A-20RD. In contrast, the trajectories of wells 68A-20 and 68A-20RD place them hundreds of meters from the trajectories of previously drilled injection wells. Although the trajectory of 68B-20 is close to that of both 68-20 and 68-20RD, no scale was observed in the cuttings from this well.

Conclusions and Future Work

The modeled results closely simulate the observed mineral paragenesis and abundances based on observations made on cuttings from injection well 68-20RD. Future investigations will consider the effects of varying the composition of the injected fluid and changing temperatures. Temperatures profiles were measured for wells 68-20 and 68-20RD. Lower temperatures measured in 68-20RD indicate that the surrounding rock has cooled over time due to the injection of cooler fluids into 68-20 over the period of four and a half years. Attempts are being made at many geothermal fields, including Coso, to increase the solubility of silica in injected fluids by decreasing the pH. It is not yet known what effect acidifying the injected fluid will have on the system. Future modeling will attempt to predict the effect of pH modifications on mineral deposition and dissolution within the reservoir.

References

Adams, M.C., Moore, J.N., Bjornstad, S., Norman, D.I., 2000. Geologic history of the Coso geothermal system. Geothermal Resources Council Transactions 24, 205-209.

Iler, R.K., 1979. The Chemistry of Silica-Solubility, Polymerization, Colloid, and Surface Properties, and Biochemistry. John Wiley & Sons, Inc., New York.

Kovac, K.M., Moore, J.N., Lutz, S.J., 2005. Geologic framework of the East Flank, Coso geothermal field: Implications for EGS Development. Proceedings, 30th Workshop on Geothermal Reservoir Engineering.

Lutz, S.J., Moore, J.N., 1997. Petrographic and x-ray diffraction study of 130 cuttings samples from six wells in the Coso geothermal area, California. Unpublished CalEnergy Corporation Report.

Lynne, B.Y., Campbell, K.A., 2004. Morphologic and mineralogic transitions from opal-A to opal-CT in low-temperature siliceous sinter diagenesis, Taupo Volcanic zone, New Zealand. Journal of Sedimentary Research 74, 561-579.

McLin, K.S., Moore, J.N., Hulen, J., Bowman, J.R., Berard, B., 2006. Mineral characterization of scale deposits in injection wells; Coso and Salton Sea geothermal fields, CA. Proceedings 31st Workshop on Geothermal Reservoir Engineering.

Palandri, J.L., Kharaka, Y.K., 2004. A compilation of rate parameters of water-mineral interaction kinetics for application to geochemical modeling. U.S. Geological Survey Open File Report 2004-1068.

Pruess, K., Oldenburg, C., Moridis, G., 1999. TOUGH2 user's guide, Version 2.0. Lawrence Berkeley Laboratory Report LBL-43134.

Rodgers, K.A., Browne, P.R.L., Buddle, T.F., Cook, K.L., Greatrex, R.A., Hampton, W.A., Herdianita, N.R., Holland, G.R., Lynne, B.Y., Martin, R., Newton, Z., Pastars, D., Sannazarro, K.L., Teece, C.I.A., 2004. Silica Phases in sinters and residues from geothermal fields of New Zealand. Earth Science Reviews 66, 1-61.

Xu, T., Pruess, K., 2004. Numerical simulation of injectivity effects of mineral scaling and clay swelling in a fractured geothermal reservoir. Geothermal Resources Council Transactions 28, 269-276.

Xu, T., Sonnenthal, E., Spycher, N., Pruess, K., 2004. TOUGHREACT user's guide: A simulation program for non-isothermal multiphase reactive geochemical transport in variably saturated geologic media. Lawrence Berkley National Laboratory publication LBNL-55460.

Xu, T., Pruess, K., 2001. Modeling multiphase non-isothermal fluid flow and reactive geochemical transport in variably saturated fractured rocks: 1. Methodology. American Journal of Science 301, 16-33.

CHAPTER 3

MODELING THE GEOCHEMICAL EFFECTS OF INJECTING pH MODIFIED FLUIDS AT COSO GEOTHERMAL FIELD, CA

Abstract

Decreased performance of injection wells has been documented in several geothermal fields after very short periods of injection. At the Coso, CA geothermal field, the fluids injected into wells on pad 68-20 were supersaturated with respect to amorphous silica. Examination of drill cuttings from the original and five redrilled injection wells on pad 68-20 indicated that opal-A, accompanied by trace amounts of calcite, was precipitating near the well bore, causing the observed declines in injectivity. Injection fluids at Coso are now modified with H_2SO_4 to decrease fluid pH as a method of reducing the deposition of amorphous silica scale by reducing the kinetic rate of silica polymerization. One dimensional (1D) models were constructed using the reactive transport code TOUGHREACT (Xu et al., 2004) to assess amorphous silica precipitation and the long term effects of injecting acidic fluid into the geothermal reservoir at Coso. These simulations predict that injection of fluid supersaturated with respect to amorphous silica will cause rapid declines in injectivity due to precipitation of opal-A, consistent with observations of amorphous silica scaling in cuttings from injection wells drilled on

pad 68-20 at Coso. The modeling results also predict that an optimal injection fluid pH of 4 would virtually eliminate amorphous silica and calcite deposition within fractures and therefore maintain porosity and permeability. The fracture fluid pH is buffered rapidly upon injection into the reservoir rock due to silicate mineral reactions and SiO_2(aq) in solution. Although changes to porosity and permeability of the fracture or reservoir rock are not predicted by these models, mineral dissolution and precipitation are predicted to occur. Porosity and permeability of the fracture and reservoir rock are maintained by equal volume dissolution and precipitation of minerals in these models, but processes that are not considered by the models, such as preferential precipitation in pore throats and pressure solution at grain contacts, may still change porosity and permeability along the flow path from injection to production well.

Introduction

The geochemical effects of injecting fluids into geothermal reservoirs are poorly understood and may be significantly underestimated. Decreased performance of injection wells has been observed in several geothermal fields after only a few years of service, including the six injection wells on pad 68-20 in the Coso, CA geothermal system. Rock cuttings from original and redrilled injection wells drilled on pad 68-20 at Coso were used to characterize the mineral and geochemical changes that occur as a result of injection. Samples from the original well 68-20 at Coso were used to establish the mineral assemblages and their geochemical characteristics prior to injection. Amorphous silica scale deposits were found in two of the five subsequently drilled injection wells on

pad 68-20. Based on these initial studies, McLin et al., (2006a) identified that precipitation of amorphous silica led to declining injectivity in these wells.

Because amorphous silica scale is difficult to remove once it has precipitated, modifications to the injected fluid are made to prevent this precipitation. Silica scale control methods used in geothermal operations include injecting at higher temperature, dilution with condensate or cool surface or groundwater, reduction of fluid pH to slow polymerization kinetics, and a variety of treatments with scale inhibitors (Gallup, 1998). Of these options, reduction of fluid pH is often the most practical and economic solution due to the expense of inhibitors and the lack of fresh water for injection at many sites. H_2SO_4 is commonly used to reduce the pH (Gallup and Kitz, 1998; Gallup, 1997). The target range for injection in a geothermal field is typically between pH=5.25 and pH=4.75 to minimize both silica scale precipitation and corrosion (Darrell Gallup, personal communication). Although pH modification is a commonly employed practice, including at Coso, the effects of these modifications on the reservoir fluids and rocks are poorly understood and should be examined. Reactive transport modeling is an ideal geochemical method for predicting the effects of injecting flashed brine and brine modified with H_2SO_4 on the reservoir fluids and rocks at the Coso geothermal field.

Because it is difficult to measure directly the effects of H_2SO_4 injection on the reservoir rocks and fluids, models can provide valuable insight into the consequences of acid injection on the productivity of the Coso geothermal field. In this study, the results of previous petrological investigations of amorphous silica scale deposition in Coso reservoir rock (McLin et al., 2006a) and reactive transport modeling of amorphous silica precipitation in fractured Coso reservoir rock (McLin et al., 2006b) were used to

constrain numerical modeling of fluid-rock interactions and mineral changes with H_2SO_4 injection in the near well bore and downstream reservoir environments. The objectives of this study were to evaluate the geochemical and mineralogical impacts of fluid injection and of reducing silica scale precipitation with H_2SO_4 injection on reservoir rocks and fluids.

Study Area

The Coso geothermal field is developed in Mesozoic granitic rocks of the Sierra Nevada Batholith on the western edge of the Basin and Range (Adams et al., 2000) (Fig. 3.1). The heat driving the geothermal activity is related to shallow intrusions that have given rise to 38 rhyolitic domes during the last million years. The reservoir host rocks range in composition from diorite to granite with varying degrees of alteration and veining (Kovac et al., 2005). Active and fossil fumaroles lie along a northeast to southwest trending belt that extends through Devil's Kitchen and Coso Hot Springs. On the eastern margin of the field, known as the East Flank, fossil sinter and travertine deposits are present (Adams et al., 2000). The alteration mineral assemblage identified in East Flank wells related to the current geothermal system consists of calcite veins with minor quartz, chlorite, pyrite, and hematite at shallow depths and epidote, chlorite, quartz, adularia, and wairakite in the deepest portions (Kovac et al., 2005). Geothermal power production has been sustained since 1989 with an installed capacity of 240 MWe at the power plant.

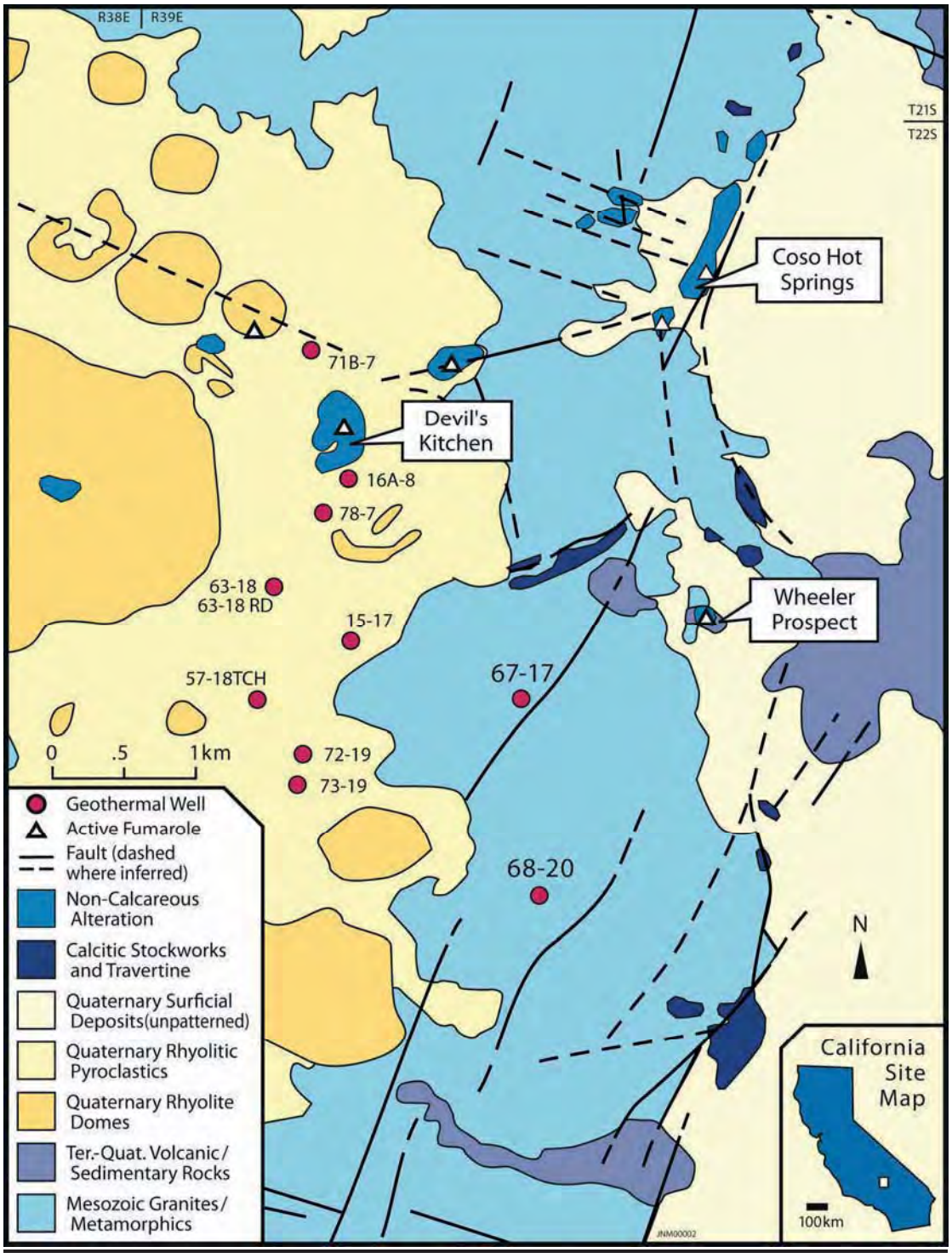

Fig. 3.1. Simplified geologic map of the Coso geothermal field showing the locations of the major thermal features. The 68-20 injection pad is located in the southern part of the field.

Well pad 68-20

Between 1987 and 1993, six injection wells were drilled on the 68-20 pad in the southern part of the field. The trajectories of these wells and lost circulation zones obtained from well logs are shown in Fig. 3.2. Injectivity decreased in well 68-20 from a maximum liquid injection rate of over 1000 kph (kilopounds per hour mass flow rate) in March, 1989 to a minimum rate of 0 kph in November, 1990 after a steady decline. Cleanouts increased injectivity to a one time high of 800 kph after November, 1990, but never fully recovered, remaining between 0-400 kph through 1992. Redrilled wells also experienced similar injectivity declines.

Although one well on the East Flank reaches nearly 350^{o}C at depth, reservoir temperatures in the part of the field near pad 68-20 prior to injection ranged from approximately 205-240^{o}C. Cooling of the reservoir was observed around these wells post injection as seen in temperature logs of subsequent redrills. The temperatures of the injected fluids ranged from 110-120^{o}C. Cuttings from the six injection wells were sampled at 3 m intervals. The reservoir host rocks in these wells ranged from diorite to granite with trace to moderate alteration and veining. Fault breccias were observed in the cuttings, indicating major fault or fracture zones intersected by the wells.

Table 3.1 shows the reported chemistry of injection for well 68-20. There was a wide range in the composition of the injected fluids, resulting from variation in produced fluids and practices of adding steam condensate back into the injected fluid. The maximum silica content analyzed was 941 mg/L. The minimum silica concentration of 97 mg/L corresponds to mixing produced fluid with steam condensate.

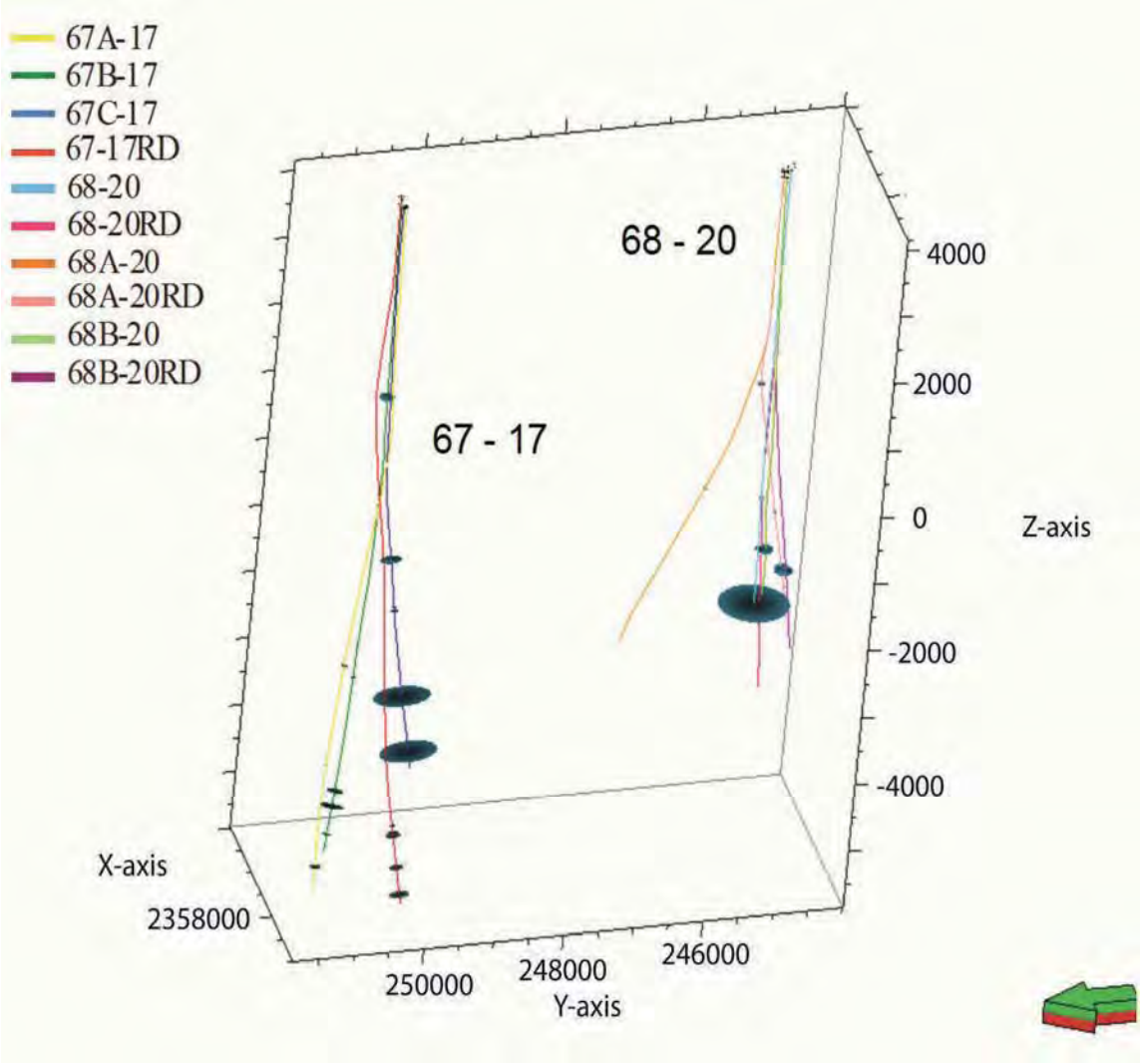

Fig. 3.2. Well trajectories for injection wells drilled in pads 67-17 (not discussed in this paper) and 68-20. Locations of lost circulation zones are shown as discs, and the amount of fluid lost is represented by the size of the disc. X and Y axes in UTMs, Z axis in feet. The green and red arrows point north.

Table 3.1

Chemistry of Injected Fluid, Well 28-20

Injected fluid chemistry from well 68-20, showing concentrations in mg/kg from 15 analyses. Brines were injected at 110-120°C.

Date (mm/dd/yy)	Na	K	Ca	Mg	Fe	Al	SiO_2	B	Li	As	HCO_3	Cl	F	SO_4	TDS	Lab pH
06/27/88	3340	725	78	8.7	33	10	555	100	37	9.2	229	5570	2.4	73	10900	6.7
10/04/88	3520	941	64	0.27	0.49	>0.61	965	116	47	11	77	6600	2.8	27	12300	7.2
03/30/89	2897	362	19	0.08	0.30	0.37	617	88	25	8.3	156	5015	2.3	80	9233	6.8
06/15/89	2993	465	22	0.09	0.13	0.56	678	83	41	11	195	5465	2.2	90	nr	7.3
09/27/89	3652	501	29	0.14	0.01	0.25	174	119	33	10	178	6440	1.7	95	11237	7.5
11/13/89	3470	580	25	0.12	2.53	0.63	698	114	31	6.9	168	5165	1.6	71	nr	6.8
01/07/90	3540	590	24	0.15	1.88	0.39	826	129	35	8.0	225	6018	2.3	44	nr	6.7
04/20/90	4283	633	36	0.65	84.1	1.6	747	127	35	26	142	5698	5.7	90	nr	6.7
08/19/90	4010	739	32	0.14	2.85	0.50	936	142	40	7.2	151	6958	3.0	27	nr	7.3
10/12/90	3908	672	38	0.15	0.33	0.33	701	121	37	8.8	161	6618	2.1	47	nr	8.2
02/03/91	3774	595	47	0.46	0.12	>0.61	545	109	31	6.7	161	6340	2.5	99	11550	8.2
05/07/91	3480	605	37	>0.16	0.88	>0.02	593	113	28	2.9	174	6070	2.2	87	11000	8.3
08/03/91	4192	590	130	3.94	6.5	1.0	620	130	30	11	185	6855	2.8	53	nr	8.2
11/21/91	3508	601	46	0.14	0.30	0.43	546	125	31	6.1	143	6100	1.9	72	11500	8.3
12/13/96	876	147	18	nd	1.7	nd	97	36	6.8	1.9	7.5	1412	nd	59	2766	6.2

nd=not detected, nr=not recorded

Note: Fluid analysis from 12/13/96 is representative of a mixture of flashed production fluid and condensed steam.

Observations from Well Cuttings

Thinly banded opaline silica was observed in the cuttings from 68-20RD (McLin et al., 2006a) and 68B-20RD, but not in the original injection well 68-20, 68A-20, 68A-20RD, or 68B-20. The banding and textural relationships suggest the silica represents fracture fillings and not alteration of preexisting minerals. The greatest density of silica precipitation in well 68-20RD was found in cuttings from depths of 869-884 and 1710-1713 m. The zone from 1710-1713m depth corresponds to the depth of a zone of lost circulation in well 68-20.

Scanning electron microscopy (SEM) was used to examine the textures of the amorphous silica scale. Figs. 3.3A-E are SEM images that show the morphological progression associated with deposition and maturation of the silica scale deposits. The deposits consist of opal-A deposited as colloidal particles of nano and microspheres (Fig. 3.3A), indicating that silica homogeneously nucleated in solution to form polymeric particles (Iler 1979). Several textures related to the evolution of these deposits, including coalesced (Fig. 3.3B) and botryoidal (Fig. 3.3C) microspheres, fibrils (Fig. 3.3D), and sheets (Fig. 3.3E) are observed. Textural relationships indicate the silica was deposited initially as spheres 1-2 μm in diameter (Fig. 3.3A). As the deposits mature, the spheres coalesce to form larger spheres up to 10 μm in diameter (Fig. 3.3B and C). Further maturation is associated with the formation of fibrils and sheets (Fig. 3.3D and E) through infilling. Traces of calcite are found deposited on the amorphous silica, suggesting it represents a later stage in the evolution of the deposits. Fig. 3.3F shows an interesting feature that has been interpreted as a silicified bacterium.

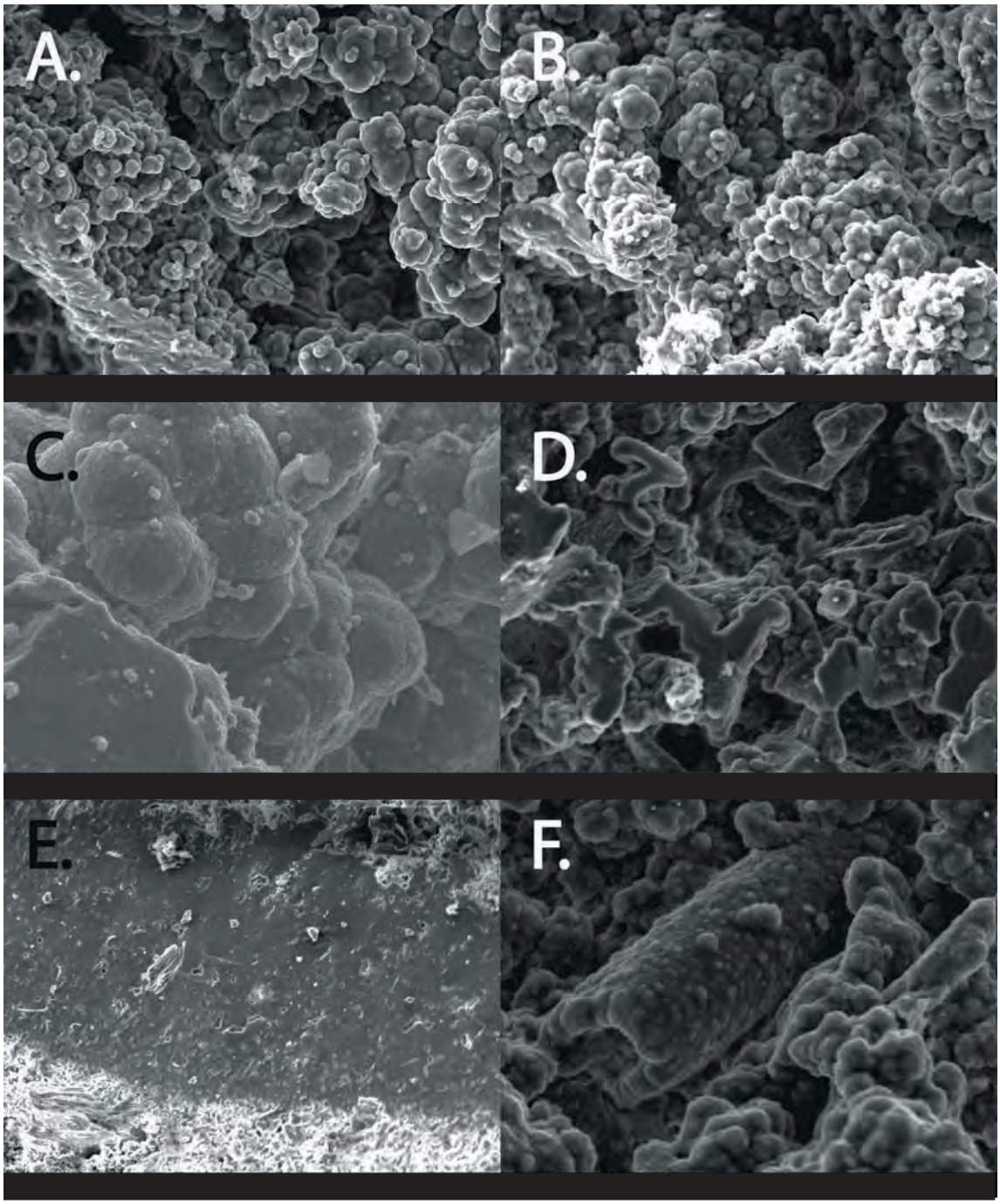

Fig. 3.3. SEM images of amorphous silica scale deposits from well 68-20RD. (A) Micro and nanoparticles of silica. (B) Coalesced particles of silica. (C) Botryoidal microspheres. (D) Fibrils of silica. (E) Sheet of amorphous silica. (F) Possible silicified bacterium.

When compared to the maturation sequence observed and documented in geothermal sinter deposits (Rodgers et al., 2004; Lynne and Campbell, 2004; Lynne et al., 2007), several textures observed in the Coso scale indicate a maturation of opal-A during and/or after deposition. Maturation of the silica usually leads to increased porosity and permeability when the opal-A phase progresses to opal-CT. However, infilling of spaces in colloidal particle deposits that leads to sheet like textures observed at Coso may provide a barrier to further maturation of the silica by depriving contact with fluid necessary to dissolve and reprecipitate silica as a more stable phase. This infill could also lead to difficulty in removing this scale as it becomes a barrier to fluid flow over time.

The X-ray diffraction patterns of the amorphous silica scale samples are characterized by a broad peak centered at 22^{o} 2-theta representing opal A, and peaks at 21.5^{o} and 26.8^{o} 2-theta representing quartz Fig. 3.4. Although quartz was not documented in the SEM images, it is possible that it represents fragments of the host reservoir rock. Alternatively, it is possible, but less likely, that the quartz represents maturation of the opal-A to a higher degree of crystallinity. Although quartz is common in mature sinter deposits at other geothermal fields (Lynne et al., 2004), there is no evidence from the SEM or X-ray diffraction studies of stages in silica maturity beyond opal-A in the Coso scale deposits.

Previous Coso Modeling Studies

Prior to examination of the cuttings from the wells on pad 68-20, Adams et al. (2005) examined the geochemical consequences of injecting groundwater at Coso

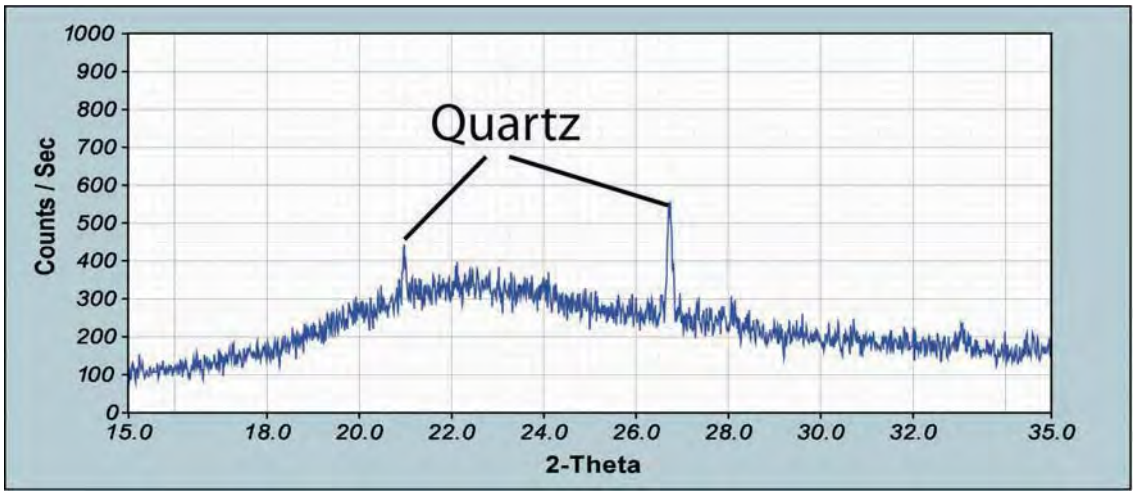

Fig. 3.4. X-ray diffraction pattern of amorphous silica scale from 1710-1713 m depth.

geothermal field as a strategy for minimizing precipitation of amorphous silica in the near-wellbore environment. The modeling code REACT (Bethke, 1996) was used to calculate saturation states of minerals to predict fluid-rock interactions with this injection strategy. With the addition of Mg^{2+} and Ca^{2+} rich groundwater, the precipitation of anhydrite + dolomite or anhydrite + calcite and a magnesium silicate was predicted.

Following the examination of cuttings from wells 68-20 and 68-20 RD, a small set of initial models were run using the nonisothermal reactive transport code TOUGHREACT (Xu et al., 2004) to examine the precipitation of amorphous silica during injection (McLin et al., 2006b). An injection fluid based on the 15 analyses of injection fluid from well 68-20 was used, and fluid was injected into a one dimensional, 594 m long flow path that consisted of a zone of fractures and a zone of altered host rock (either granodiorite or diorite). Based on data from Adams et al. (2005), the reservoir temperature used for these simulations was 275^{o}C. In the modeled cases using injection fluid with 650 ppm SiO_2(aq), amorphous silica precipitated and significantly reduced

porosity of the fracture within the first meter of the flow path within the first year. Modeled silica precipitation was followed by calcite and a very minor amount of quartz in the near wellbore environment, consistent with observed mineral deposits in the injection well cuttings. These results are consistent with the rapid decline in injectivity experienced by well 68-20. Amorphous silica scale is only found in redrilled injection wells that have a trajectory very close to that of a previously drilled well, and amorphous silica was predicted to deposit only within a few meters of the original well. Thus the modeled results closely simulated the observed mineral paragenesis and abundances based on analyses of the cuttings.

The effects of modifying the pH of the injection fluid, from acidic to basic, to mitigate the effects of silica deposition were investigated by Park et al. (2006). Acid injection reduces the kinetic rate of silica precipitation by reducing the rate of silica polymerization (Iler, 1979; Rothbaum et al., 1979; Klein, 1995). Park et al. (2006) constructed a one dimensional reactive transport model to investigate the consequences of injection of acid or alternating acid and base on the reservoir rocks and fluids. Park et al. (2006) explain that injection of a basic solution will lead to SiO_2 undersaturation and dissolution by the increased activity of $H_3SiO_4^-$ and the formation of $NaHSiO_3(aq)$. The models predicted that with acid injection SiO_2 deposition was mitigated in the immediate vicinity of the injection well, but deposition of SiO_2 was predicted at greater distances. Injection of base also mitigated SiO_2 precipitation, but the precipitation of calcite was predicted. Thus alternating the pH of the injected fluid to prevent mineral scale, as well as to maintain neutral fluid pH in the reservoir near production wells over time, was predicted to enhance permeabilities at Coso. However, the acid fluids modeled for

injection were very low pH (pH=2.26), and thus could cause extensive corrosion of equipment and well casing. Therefore, injection of fluid at this pH is not practical.

Modeling Approach

The current simulations were carried out using the nonisothermal reactive geochemical transport code TOUGHREACT (Xu and Pruess, 2001; Xu et al., 2004). This code was developed by introducing reactive chemistry into the framework of the existing multiphase fluid and heat flow code TOUGH2 V2 (Pruess et al., 1999, see also http://www-esd.lbl.gov/TOUGHREACT/). Interactions between mineral assemblages and fluids can occur under local equilibrium or kinetic rates. Precipitation and dissolution reactions can change formation porosity and permeability. This simulator can be applied to one, two, and three dimensional porous and fractured media with physical and chemical heterogeneity. Simulations can include any number of species present in the liquid, solid, and gaseous phases. Various thermal, physical, and chemical processes are considered under conditions of pressure, temperature, water saturation, ionic strength, pH, and Eh. However, the current models do not consider processes related to certain types of mineral precipitation and maturation kinetics, including nucleation, formation of metastable phases and their transformation to stable phases, and Ostwald ripening (Xu et al., 2007).

Simulation Setup

The conceptual model considers a one dimensional flow path between the injection and production wells, which is a small subvolume of the more extensive three

dimensional reservoir. The geometry and fluid and heat flow conditions of the model were based on those of Xu and Pruess, (2004). The thermodynamic database provided with the TOUGHREACT program, modified from the EQ3/6 database (Wolery, 1992) as described by Xu et al., (2004), was used. The initial reservoir conditions were 220^{o}C and 30 MPa pressure. The decrease in model reservoir temperature from that used in previous models is based on temperature surveys from well 68-20 and better reflects the initial reservoir temperature prior to injection. An over pressure of 2 MPa was applied at the boundary of the flow path to simulate fluid injection. The model is based on conditions during continuous injection over seven years.

The initial models use measured, observed, and estimated parameters from data gathered through various studies at Coso (Lutz and Moore, 1997; Lutz et al., 1999; Kovac et al., 2005; McLin et al., 2006a, 2006b). Further cases are based on hypothetical situations where these parameters are adjusted to determine the sensitivity of the modeling, as well as to predict the effects of alternative reservoir conditions. Finally, injection of H_2SO_4 modified fluid is modeled for mixtures of injectate with 98% H_2SO_4 at pH=3, 4, and 5. The simulations were each run to a total time of 7 years. Changes in fluid pH, fracture porosity, fracture permeability, fluid temperature, and changes in mineral abundances were monitored out to a distance of 594 m from the injection well. Mineral abundance changes were reported in terms of changes in volume fraction for the following minerals: quartz, potassium feldspar, chlorite, illite, Na smectite, Ca smectite, calcite, dolomite, albite, oligoclase, anorthite, annite, phlogopite, clinozoisite, anhydrite, and amorphous silica. Changes in porosity were calculated as a function of mineral dissolution and precipitation. A porosity increase indicates that mineral dissolution is

dominant, while a porosity decrease occurs when precipitation dominates. Changes in permeability were calculated from changes in porosity using a cubic law to calculate the relationship between porosity and permeability (as discussed in Xu et al., 2004).

Fluid and Heat Flow Conditions

The geometry and fluid and heat flow conditions are modeled after those described in Xu and Pruess (2004). A one dimensional MINC (multiple interacting continua) model was used to represent the fractured rock. The MINC method can resolve mass transport from "global" flow and diffusion of chemical species within the fractured rock from transport by "local" exchange between fluid within fractures and the minimally permeable rock matrix. Details on the MINC method for reactive geochemical transport are described by Xu and Pruess (2001). In the simulations, interactions with 1) a zone representing the relatively impermeable, unaltered host rock, and 2) a fracture zone within the host rock were considered. The model allows these two zones in the flow column to have individually assigned porosity and permeability. The fluid can flow in and chemically interact with rock both zones. Mass fluxes and reaction progress within each zone will be a function of the assigned parameters. The parameters used in the models are shown in Table 3.2. Density = 2650 $kg*m^{-3}$, heat capacity = 1000 $J*kg^{-1}K^{-1}$, and diffusivity = 10^{-9} $m^{-2}s^{-1}$ were used for both fracture and reservoir rock zones. The cubic law was used to define the porosity-permeability relationship in both zones (Xu et al., 2004). The model generates changes in porosity and permeability based on changes in mineral abundances.

Mineralogical Conditions

Mineral modes used for the simulations are shown in Table 3.3. The reservoir rocks at depths of 878 m and 1710 m in 68-20RD are dominated by hornblende biotite quartz diorite and biotite granodiorite, respectively. These are the two depths were the most amorphous silica scale was observed in the cuttings. Because lost circulation was associated with 1710 m depth, the majority of the models are based on injection into granodiorite.

The mineralogical compositions of the granodiorite and diorite were estimated from petrographic observations of samples from 68-20RD and from X-ray and thin section studies of East Flank wells by Kovac et al. (2005), Lutz et al. (1999), and Lutz and Moore (1997). Initially, anorthite was used as the composition of the plagioclase feldspar in the reservoir rock. This composition served as a noncalcite source of calcium, and the alteration mineralogy observed by Kovac et al. (2005) is an alteration product of Ca rich feldspar in the presence of CO_2. However, the composition of the feldspar in the initial granodiorite is likely more albite rich (e.g., oligoclase), and feldspar near fractures is likely already altered to a Na rich feldspar composition from prior interaction with reservoir fluids. Both rock types were found to be only weakly altered in 68-20RD. The veining was found to be especially weak in the diorite at 878 m. The granodiorite was found to contain quartz, calcite, and chlorite veins.

Due to mineralogical variations and uncertainties, sensitivity studies were conducted for a range of mineralogical compositions of the rocks, including diorite as the reservoir host rock, different composition of plagioclase feldspar in the reservoir rock (anorthite (an), albite (al), and oligoclase (olig)), and increased mafic minerals biotite

Table 3.2

Hydrologic and Thermal Parameters

Hydrologic and thermal parameters of rocks used in the models

Parameters	Fracture	Weakly Altered Reservoir Rock
Volume (m^3)	0.1	0.9
Permeability (m^2)	2.0E-12	2.0E-18
Porosity	0.10	0.02
Thermal Conductivity ($W^* m^{-1}K^{-1}$)	2.9	3.0
Tortuosity	0.3	0.1

(represented by annite and phlogopite) and epidote (represented by clinozoisite) in the reservoir rock. For three models, low albite was allowed to precipitate. These sensitivity studies were constructed to explore the effects of these differing mineralogical compositions on the fluid chemistry and mineral precipitation within the system.

Mineral Kinetic Rates and Parameters

Mineral dissolution and precipitation are considered under kinetic constraints. A general kinetic rate expression is used in TOUGHREACT (Xu et al., 2004):

$$r_m = \pm k_m A_m a_{H^+}{}^n |1 - Q_m/K_m| \quad (3.1)$$

where m is the mineral index, r_m is the dissolution/precipitation rate, (positive for dissolution, negative for precipitation), k_m is the rate constant (moles per unit mineral

Table 3.3

Mineralogical Parameters

Initial mineralogical composition of the rock types used in the preliminary simulation and mineralogical sensitivity studies. A temperature of 220°C was used for the initial rock temperature in the simulations.

	Rock Mineralogical Composition					
Mineral	Granodiorite (an)	Diorite (an)	Granodiorite (olig)	Granodiorite (ab)	Diorite (60% mafic)	Fracture
Albite				0.33		
Anorthite	0.33	0.50			0.12	
Oligoclase			0.33			
Quartz	0.34	0.18	0.34	0.34	0.12	0.05
K Feldspar	0.17	0.07	0.17	0.17	0.06	
Illite	0.03		0.03	0.03	0.01	
Chlorite	0.02	0.01	0.02	0.02	0.04	0.01
Calcite	0.02	0.02	0.02	0.02	0.02	0.04
Annite	0.06	0.20	0.02	0.02	0.20	
Phlogopite			0.02	0.02	0.20	
Clinozoisite			0.02	0.02	0.20	

an=anorthite, olig=oligoclase, ab=albite

surface area and unit time) which is temperature dependent, A_m is the specific reactive surface area per kg of H_2O, a_{H+} is the activity of H^+, and n is an empirical reaction order accounting for catalysis by H^+ in solution. K_m is the equilibrium constant for the mineral-water reaction for the dissolution or precipitation of one mole of mineral m, Q_m is the ion activity product. The temperature dependence of the reaction rate constant can be expressed as:

$$k = k_{25} \exp[-E_a/R(1/T - 1/298.15)] \quad (3.2)$$

where E_a is the activation energy, k_{25} is the rate constant at 25°C, R is the universal gas constant, and T is absolute temperature. Table 3.4 shows the parameters used in the kinetic rate expression.

Because precipitation rate data do not exist for most minerals, parameters for neutral pH dissolution were used to calculate precipitation rates for those minerals without precipitation rate data. The processes, different from dissolution, that are not considered in the calculation of precipitation rates include nucleation, crystal growth and Ostwald ripening processes, as well as the calculation of changes to the reactive surface area.

Amorphous silica will homogeneously nucleate, polymerize, and precipitate as a colloidal particle at near neutral pH, as observed in cuttings from the Coso geothermal system, and the code does not provide for a pH dependent impact on the polymerization of silica. A surface area of 10^6 cm^2/g was used for calculation of the rate of amorphous silica precipitation for injection fluid pH above 5 to account for these nucleation and polymerization processes within the framework of the code. This large surface area value takes into account the very small size of amorphous silica particles in solution (Parks, 1990; Xu et al., 2004) and can approximate precipitation rates that match observations of rapid injectivity declines in wells on pad 68-20. To approximate and simulate the reduced rate of polymerization with lower pH (Iler, 1979), the amorphous silica surface area term

Table 3.4

Kinetic Rate Parameters

List of kinetic rate parameters used in Eqns. (3.1) and (3.2) for minerals considered in this study(Xu and Pruess, 2004; Palandri and Kharaka, 2004; Xu et al., 2007). The same values were used for both dissolution and precipitation, except for amorphous silica where the first line indicates dissolution parameters and the second indicates precipitation parameters.

Mineral	A (cm^2/g)	Parameters for kinetic rate law: Neutral Mechanism k^{25} ($mol/m^2/s$)	Neutral Mechanism E (kJ/mol)	Acid Mechanism k^{25} ($mol/m^2/s$)	Acid Mechanism E (kJ/mol)	Acid Mechanism n (H^+)	Base Mechanism k^{25} ($mol/m^2/s$)	Base Mechanism E (kJ/mol)	Base Mechanism n (H^+)
Quartz	9.1	1.023E-14	87.7						
Illite	108.7	1.660E-13	35	1.047E-11	23.6	0.34	3.020E-17	58.9	-0.4
Oligoclase	9.1	1.445E-12	69.8	2.138E-10	65	0.457			
Albite	9.1	2.745E-13	69.8	6.918E-11	65	0.457	2.512E-16	71	-0.572
Low albite	9.1	2.754E-13	69.8	6.918E-11	65	0.457	2.512E-16	71	-0.572
Anorthite	9.1	7.586E-10	17.8	3.162E-4	16.6	1.411			
K-feldspar	9.1	3.890E-13	38	8.710E-11	51.7	0.5	6.310E-12	94.1	-0.823
Chlorite	9.1	3.02E-13	88	7.762E-12	88	0.5			
Na smectite	108.7	1.660E-13	35	1.047E-11	23.6	0.34	3.020E-17	58.9	-0.4
Ca smectite	108.7	1.660E-13	35	1.047E-11	23.6	0.34	3.020E-17	58.9	-0.4
Calcite	9.1	1.549E-6	23.5	5.012E-1	14.4	1.000			
Dolomite	9.1	2.951E-8	52.2	6.457E-4	36.1	0.5			
Annite	9.1	2.818E-13	22	1.445E-10	22	0.525			
Phlogopite	9.1	3.981E-13	29						
Clinozoisite	9.1	1.023E-12	70.7	2.512E-11	71.1	0.338	4.677E-18	79.1	-0.556
Am. Silica	9.1 or 10^6	4.900E-13	76						
		3.800E-10	49.8						
Anhydrite	9.1	6.457E-4	14.3						

was reduced to 9.1 cm^2/g for injection fluid pH less than 5. Sensitivity of this amorphous silica surface area term was investigated in a series of models with granodiorite host rock (Granodiorite (an)) and injection fluid pH=6.5.

Water Chemistry

The composition of the reservoir fluid was estimated from the approximate composition of reservoir fluid produced from an East Flank well and was calculated by equilibrating the East Flank fluid composition with the granodiorite mineralogical composition at 220°C in batch calculations (shown in Table 3.5). An injection fluid composition that was calculated from 15 analyses of injection fluid from well 68-20 was chosen as the trial injection water (Table 3.5). Injection of H_2SO_4 modified fluid was modeled for mixtures of injectate with 98% H_2SO_4 at pH=3, 4, and 5 calculated with batch equilibrations. The composition of the injectate was constant over time within each model simulation.

Results

The initial model considers the injection of fluid supersaturated with respect to amorphous silica into a fracture zone in a granodiorite host rock (Granodiorite (an), Table 3.3). Several minerals dissolve and precipitate within the fracture and the altered reservoir rock. Amorphous silica precipitates in the fracture (Fig. 3.5), with the majority of the precipitation occurring within the first year of the model and within the first few meters of the flow path. Precipitation of amorphous silica fills greater than 80% of the fracture pore volume within the first meter of the flow path after seven years of injection

Table 3.5

Fluid Chemistry

Composition of a reservoir fluid from a produced fluid from Coso East Flank well 38B-9 in equilibrium with Granodiorite (an) at 220°C and injection fluid composition at 110°C based on 15 analyses of fluid injected into well 68-20.

Chemical Component	Reservoir (Mol/kg)	Injection (Mol/kg)
SiO_2	4.44E-3	9.96E-3
$B(OH)_3$	3.88E-2	1.01E-2
Na^+	6.82E-2	1.46E-1
K^+	3.70E-3	1.42E-2
Li^+	1.63E-3	4.44E-3
Ca^{2+}	9.55E-4	1.07E-3
Al^{3+}	1.44E-5	8.49E-7
Mg^{2+}	3.23E-4	1.52E-5
Sr^{2+}	3.60E-5	5.00E-2
Cl^-	8.42E-2	1.60E-1
F^-	1.07E-4	1.15E-4
HCO_3^-	8.84E-2	2.48E-3
SO_4^{2-}	1.83E-4	6.97E-4
HS^-	3.02E-5	
CH_4	6.25E-10	
pH	6.50	6.50

(Fig. 3.5). Trace quartz precipitates in the fracture and rock. No dissolution of K-feldspar is observed. However, trace dissolution of anorthite is observed in the rock. Trace illite and smectite precipitate in the rock. There is both trace dissolution and trace precipitation of chlorite within the fracture, with only trace dissolution in the rock. Calcite and trace dolomite precipitate within the fracture. Trace calcite also precipitates in the rock. Trace chlorite dissolves in the fracture and rock, and then it precipitates in the fracture. These results are consistent with the rapid decline in injectivity experienced with well 68-20 and

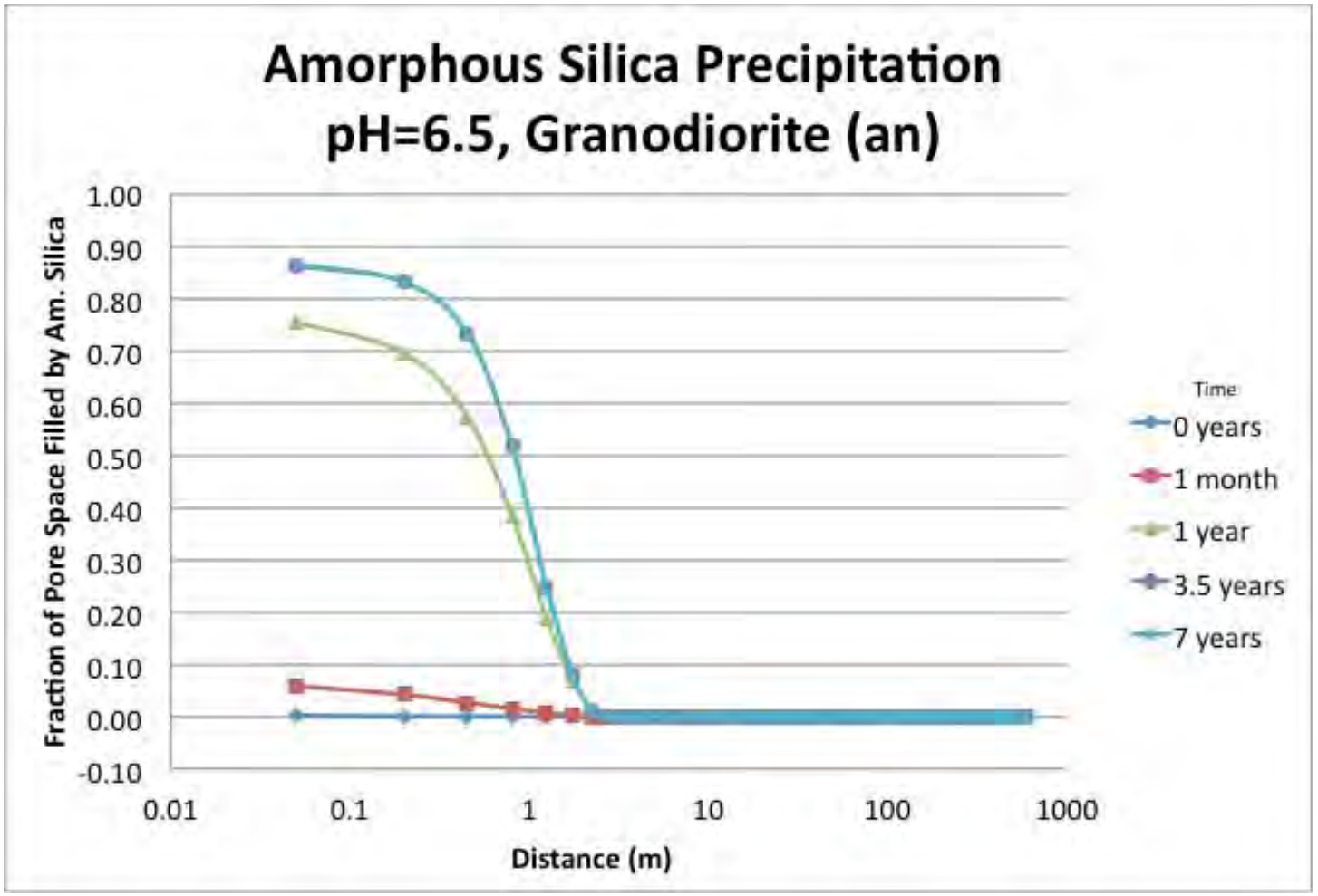

Fig. 3.5. Precipitation of amorphous silica in the fracture zone for simulation with Granodiorite (an). Amorphous silica surface area is $10^6 cm^2/g$.

the observed scale mineralogy. These results are also consistent with the observation that amorphous silica scale was only found in wells 68-20RD and 68B-20RD, as these are the two wells with trajectories very near those of previously drilled wells. However, amorphous silica may be transported farther in the fractures than predicted by these models because the models do not account for the transport of suspended colloidal amorphous silica particles once they have formed.

Surface Area Sensitivity Test

To test model sensitivity to the surface area input for amorphous silica, several models were run with fluid injected into Granodiorite (an) for amorphous silica surface areas between 9.1 and 10^6 cm^2/g (Fig. 3.6). As the surface area is reduced from 10^6, amorphous silica precipitation decreases slightly, and precipitation of amorphous silica occurs farther along the flow path. The largest change in the volume of amorphous silica precipitation is between surface area of 10^2 and 9.1 cm^2/g. Precipitation of amorphous silica is virtually eliminated when the surface area of amorphous silica is modeled as 9.1 cm^2/g.

Differing Reservoir Rock Mineral Compositions

Varying the mineral composition has no effect on amorphous silica precipitation within the fracture when modeling an unmodified injection fluid (pH=6.5). However, the fracture fluid pH varies significantly when the unmodified fluid (pH=6.5) is injected into reservoir rocks of differing mineralogical compositions (Fig. 3.7). The fracture fluid pH

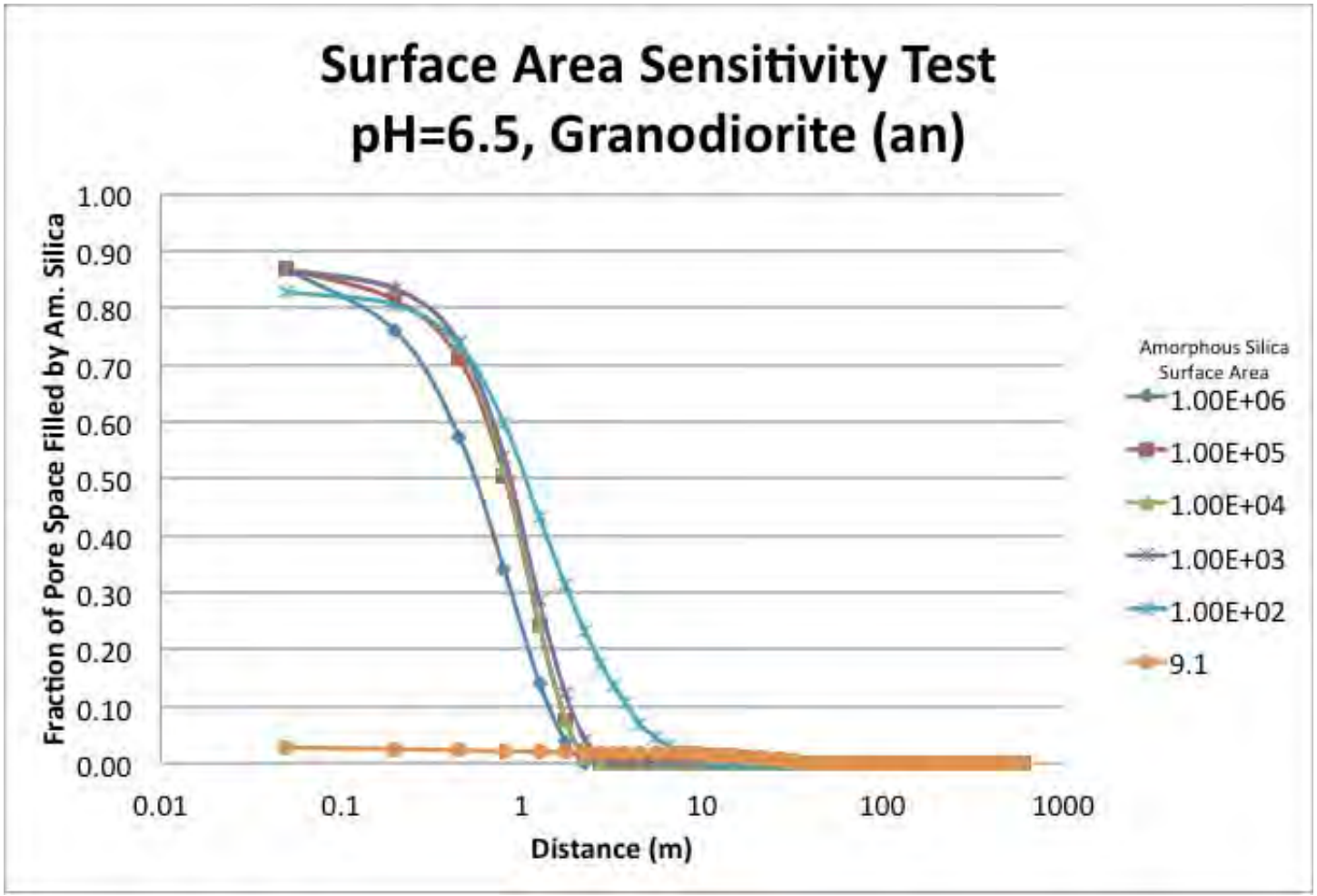

Fig. 3.6. Amorphous silica precipitation in fracture zone for simulations with Granodiorite (an) and varying amorphous silica surface area. Surface area units are cm^2/g.

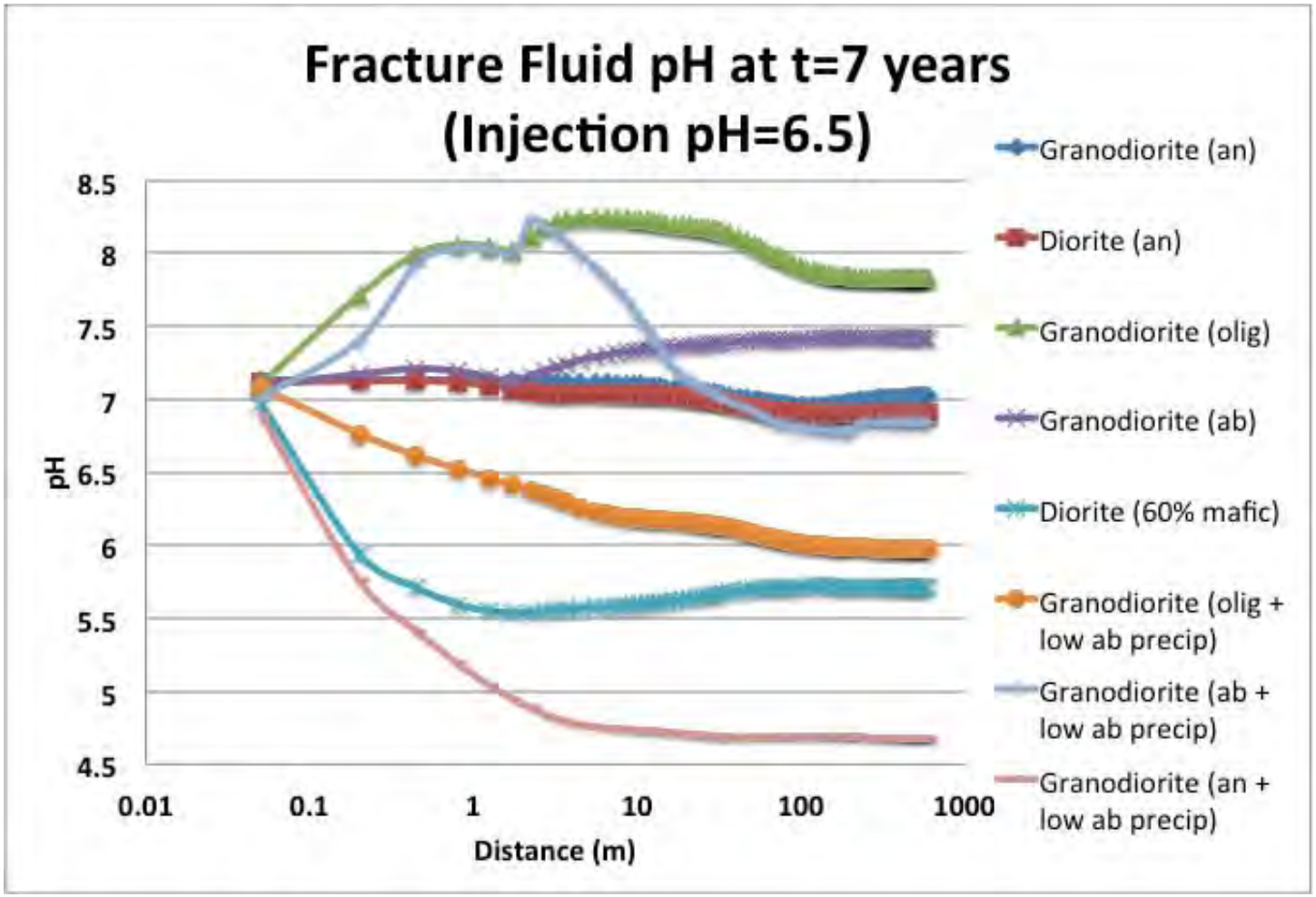

Fig. 3.7. Fracture fluid pH at t=7 years for the different reservoir rock mineralogical compositions (injection fluid pH=6.5).

values with reservoir rocks Granodiorite (an) and Diorite (an) do not vary considerably. These two reservoir rock types differ in the amounts of anorthite, K-feldspar, quartz, and annite in their starting compositions (Table 3.3). When the plagioclase feldspar in the reservoir rock is albite (Granodiorite (ab)), the pH of the fluid is slightly higher than that of the reservoir rock with anorthite (Granodiorite (an)). Granodiorite with oligoclase as the plagioclase feldspar yields the highest predicted fluid pH. With the addition of mafic minerals phlogopite and clinozoisite to reservoir rock (Diorite (60% mafic)), the predicted fracture fluid pH is reduced significantly. Allowing the precipitation of low albite in the simulation involving granodiorite with oligoclase (Granodiorite (olig + low ab precip)) and the granodiorite case with anorthite (Granodiorite (an + low ab precip)) reduces the predicted fracture fluid pH below those of the other granodiorite simulations. When the precipitation of low albite is allowed in the granodiorite with albite case, the pH is initially high in the first 10 m of the flow path. The pH then decreases below that of the other granodiorite cases where low albite is not allowed to precipitate.

Figs. 3.8, 3.9, and 3.10 show the Na^+, Ca^{2+}, and AlO_2^- in the fracture fluid at t=7 years for each of these reservoir rock mineralogies. Na+ declines most dramatically in the fracture fluid in the granodiorite cases with oligoclase and anorthite when low albite is allowed to precipitate. Na+ also declines initially in the fracture fluid in the granodiorite case with albite when low albite is allowed to precipitate, but then increases again farther along the flow path. Ca^{2+} in the fracture fluid is highest in the granodiorite case with anorthite where low albite is allowed to precipitate, followed by the granodiorite cases with albite (with and without low albite precipitation) and the granodiorite case with oligoclase where low albite is allowed to precipitate. The AlO_2^- is highest in the

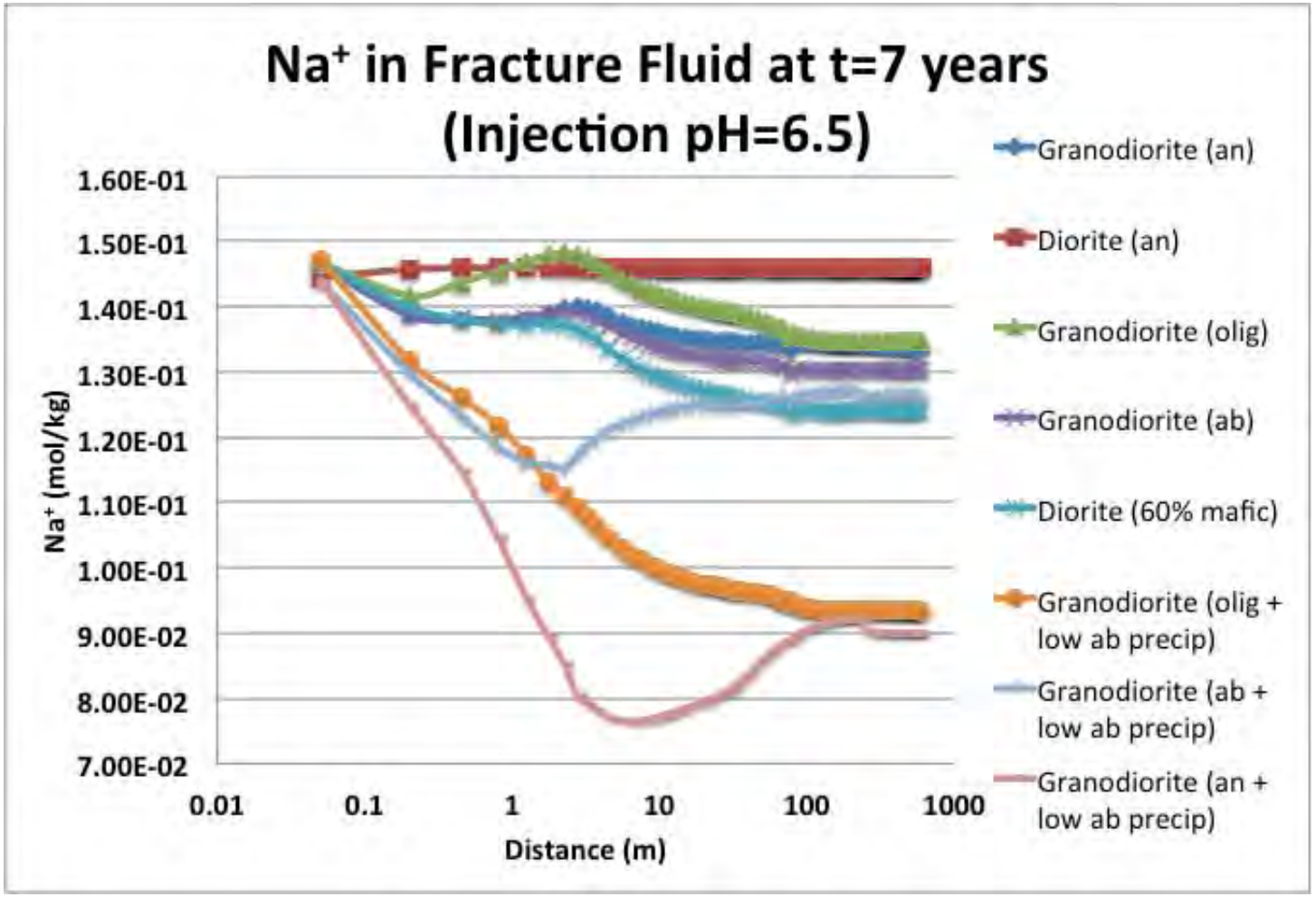

Fig. 3.8. Na^+ in the fracture fluid at t=7 years for the different reservoir rock mineralogical compositions (injection fluid pH=6.5).

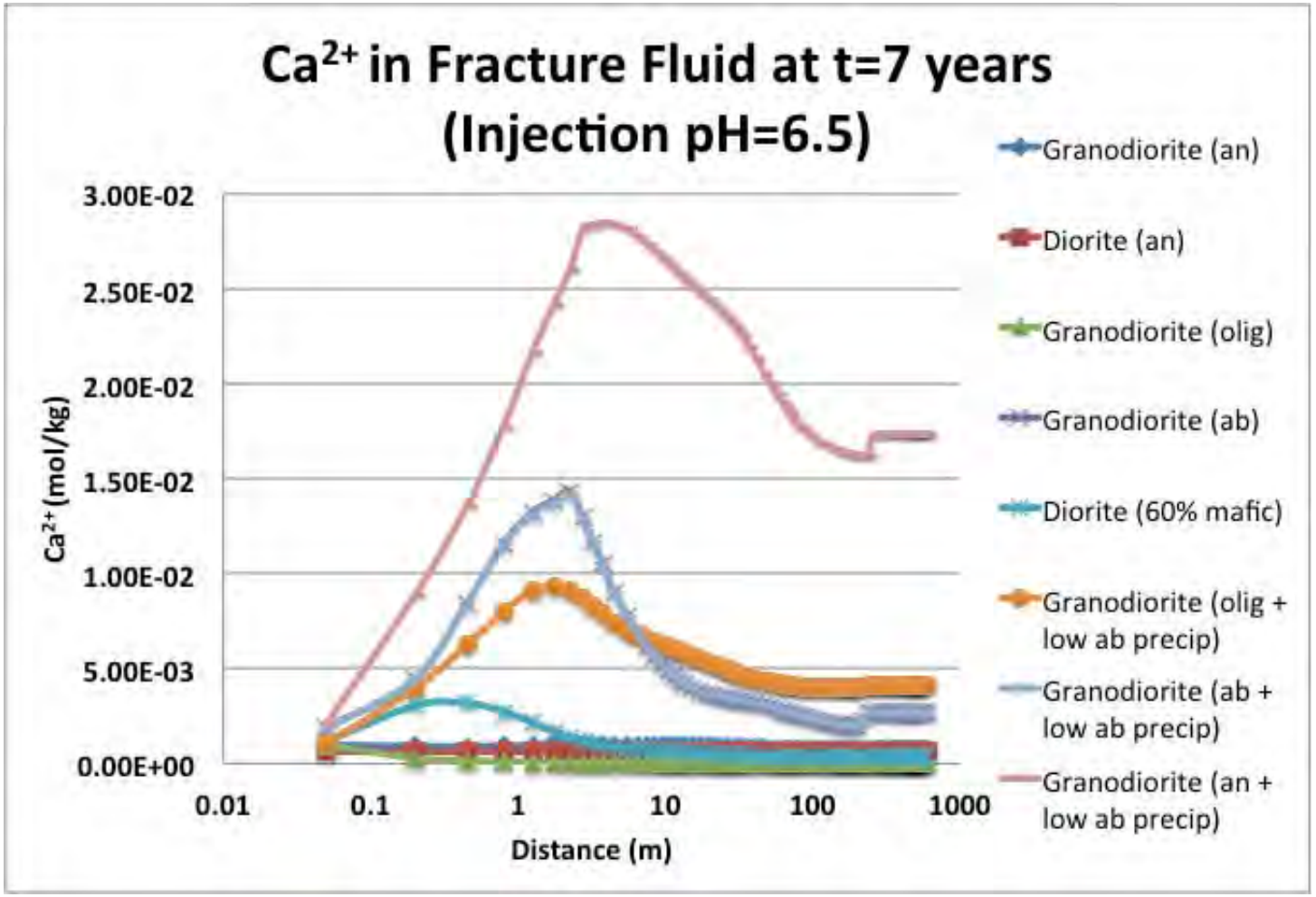

Fig. 3.9. Ca^{2+} in the fracture fluid at t=7 years for the different reservoir rock mineralogical compositions (injection fluid pH=6.5).

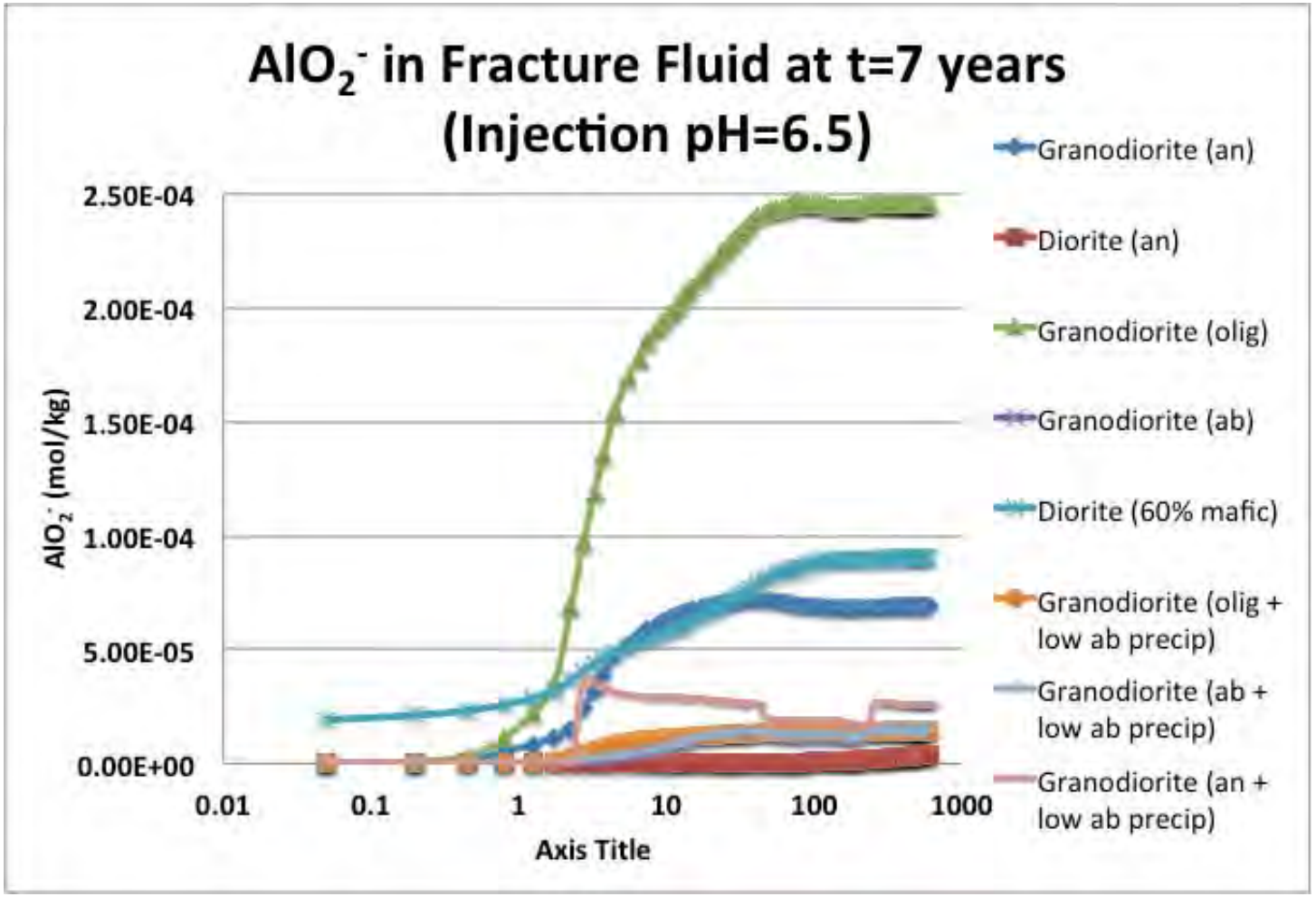

Fig. 3.10. AlO_2^- in the fracture fluid at t=7 years for the different reservoir rock mineralogical compositions (injection fluid pH=6.5).

granodiorite case with oligoclase, followed by the diorite case with 60% mafic minerals and the granodiorite case with anorthite.

Modeling pH Modification of Injection Fluid

Injected fluid was modified to pH=3, 4, and 5 to predict the effects of injecting fluid modified with H_2SO_4 into reservoir rocks at the Coso geothermal field. The fluid injected in these simulations was modified by mixing 98% H_2SO_4 with the injection fluid from Table 3.5 at 110^oC until the desired pH was achieved. SO_4^{2-} contents for pH=3, 4, and 5 were 7.40E-4, 7.30E-4, and 7.00E-4 respectively. Amorphous silica surface area was 9.1 cm^2/g for these models.

Amorphous silica precipitation was significantly reduced in the simulations involving each of these lower pH fluids, mainly due to the decrease in the surface area term used in the calculation of the kinetic rate of precipitation (which represents a reduction in the rate of silica polymerization). Precipitation of amorphous silica for the injection fluid with pH=4 and an amorphous silica surface area of 9.1 cm^2/g is shown in Fig. 3.11. With an injection fluid pH=4, the model predicts that amorphous silica precipitation will fill less than 2% of pore space by seven years of injection. Calcite precipitation varies with injection fluid pH (Fig. 3.12). Between injection pH=5 and 4, calcite precipitation declines significantly within the first meter of the flow path (decrease from 14% to 3% of the fracture volume filled). However, in all cases where injected fluid pH=3, 4, or 5, fracture porosity is not predicted to increase or decrease more than 3% by volume in the overall rock volume (fracture and reservoir rock) because the volume of minerals dissolved is roughly equivalent to the volume of minerals precipitated.

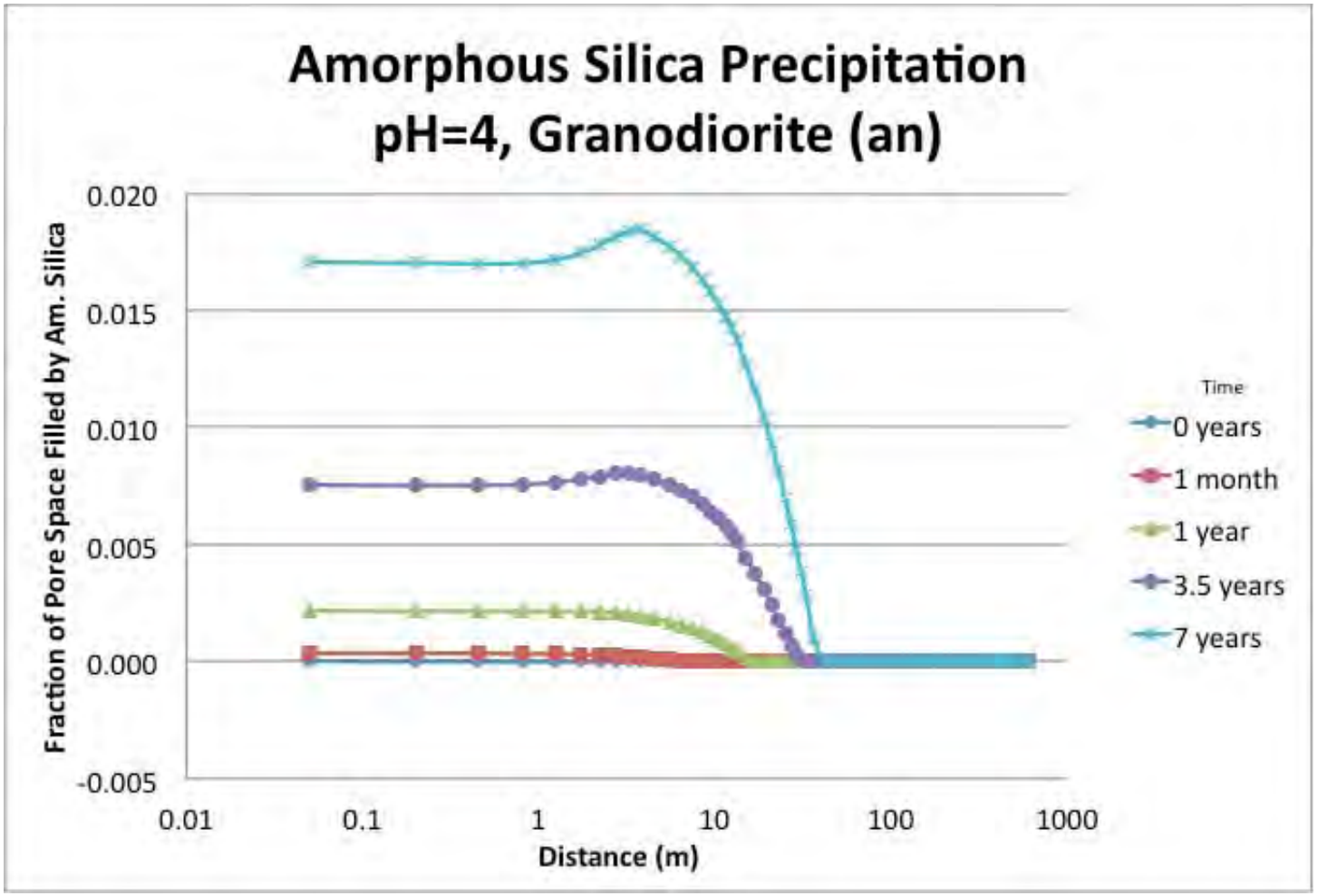

Fig. 3.11. Amorphous silica precipitation in fracture zone for Granodiorite (an) with injection pH=4 and amorphous silica surface area of 9.1 cm^2/g. Note the contrast in scale for fraction of pore space filled between this figure and Figs. 3.5 and 3.6.

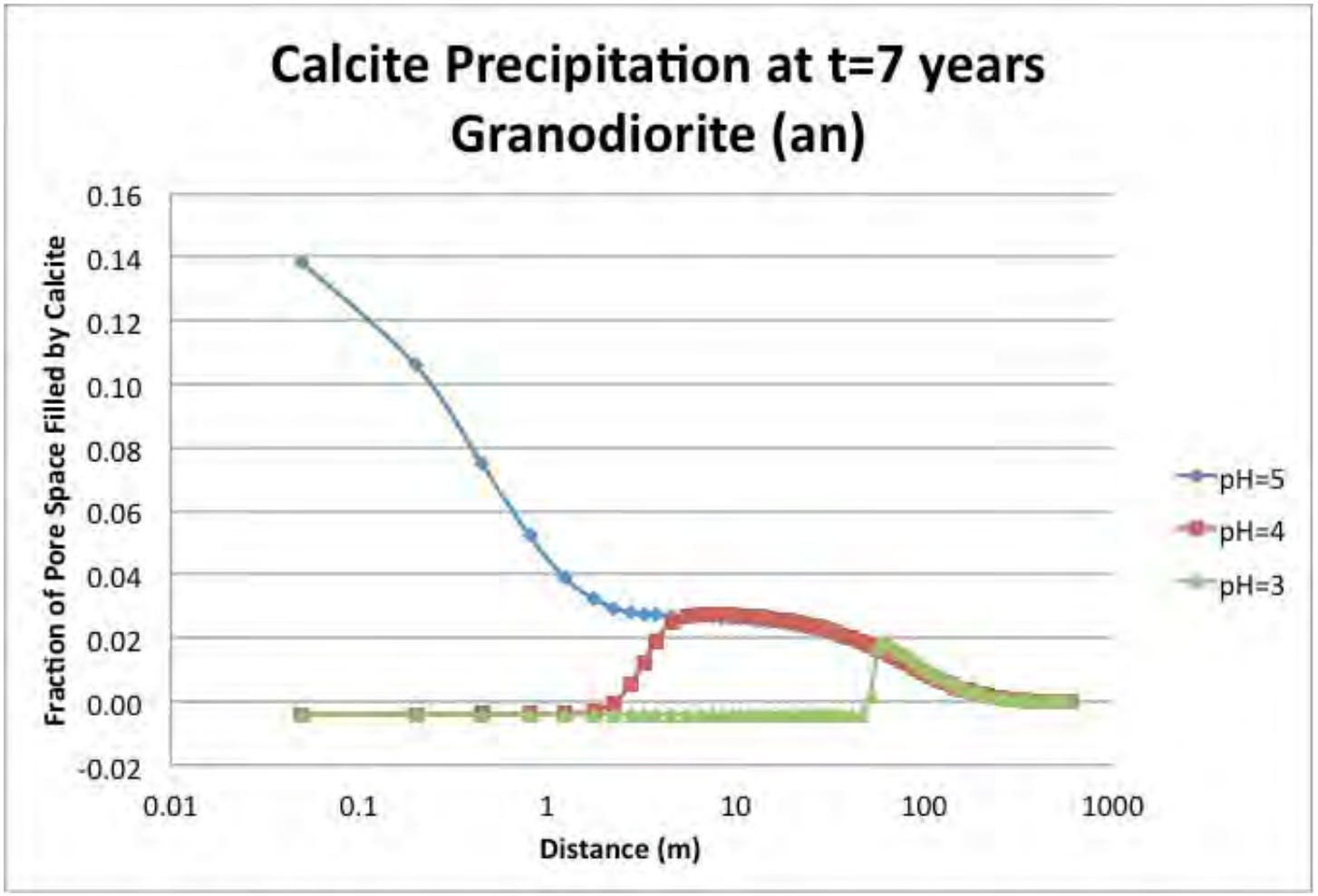

Fig. 3.12. Calcite precipitation in the fracture zone for Granodiorite (an) at t=7 years for injection fluid pH=3, 4, and 5 (amorphous silica surface area is 9.1 cm^2/g).

However, this prediction does not accurately represent the complexity of the effects of mineral dissolution and precipitation on porosity and permeability.

Fracture Fluid pH with pH Modification

Fracture fluid pH predictions for various injection fluid pH values are plotted in Fig. 3.13 for Granodiorite (an) and in Fig. 3.14 for Granodiorite (olig + low ab precip). With injection fluid pH=6 and 7, the two cases diverge in the predicted fracture fluid pH, with Granodiorite (olig + low ab precip) having a lower predicted fracture fluid pH. With injection pH=3, 4, and 5, the predicted fracture fluid pH for Granodiorite (an) and Granodiorite (olig + low ab precip) are very similar to each other.

Discussion

These simulations provide insight into the geochemical consequences of injecting fluid supersaturated with respect to amorphous silica and H_2SO_4 modified fluid into a geothermal reservoir. However, because there are limitations to the current models, it is important to discuss the implications of such limitations for the predictions presented. For example, because there are only empirical data available on the impact of pH reduction on the rate of silica polymerization in this temperature range, the surface area term in the rate equation for silica precipitation is reduced to simulate the reduced rate of silica polymerization in the simulations involving the injection of lower pH fluids. While the input for the surface area term of amorphous silica is modified depending on the initial injection pH, feedback modifications to the surface area term based on pH after reaction

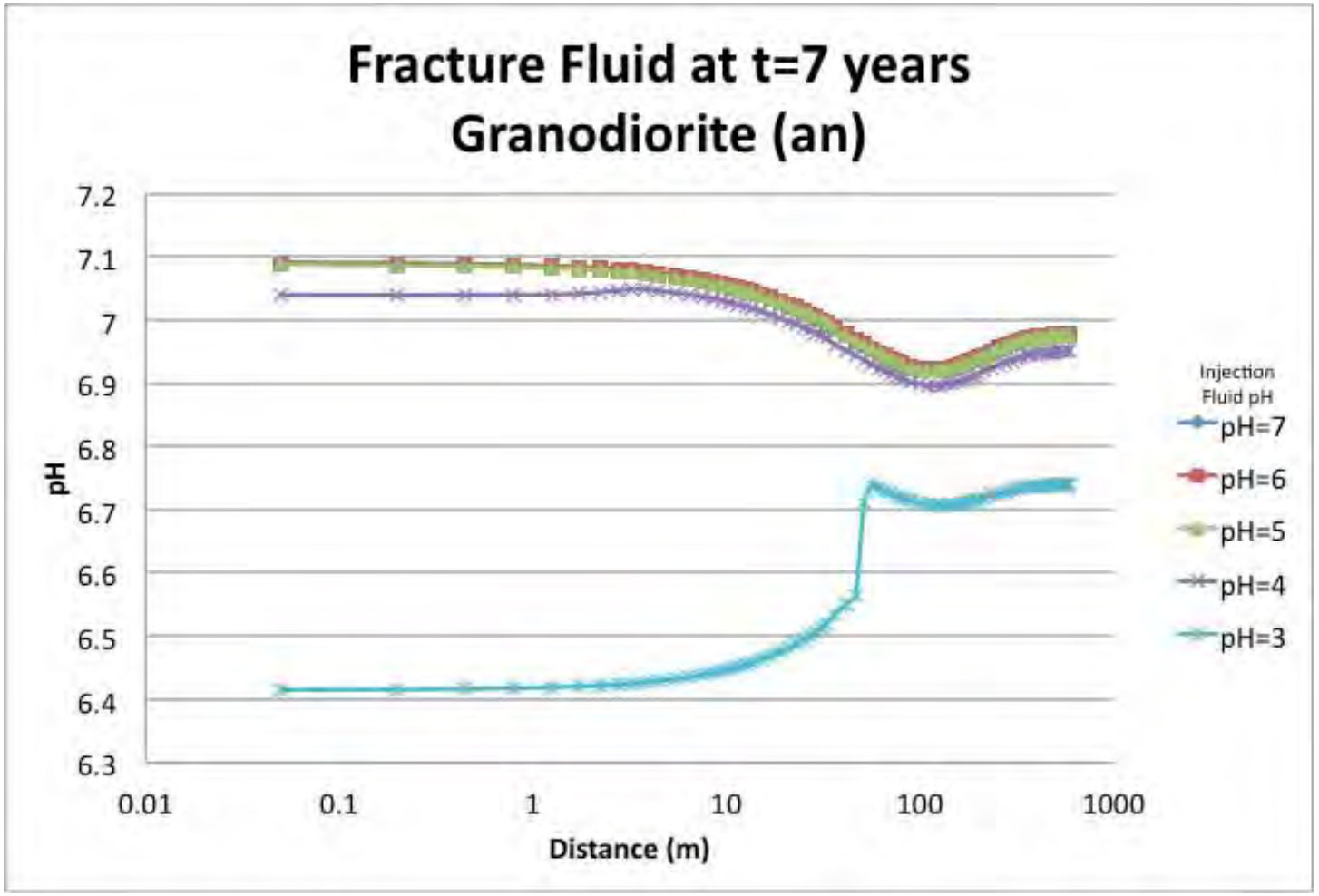

Fig. 3.13. Fracture fluid pH for Granodiorite (an) at t=7 years for injection fluid pH=3, 4, 5, 6, and 7. Amorphous silica surface area is 10^6 cm^2/g for injection fluid pH=6 and 7 and 9.1 cm^2/g for injection fluid pH=3, 4, and 5.

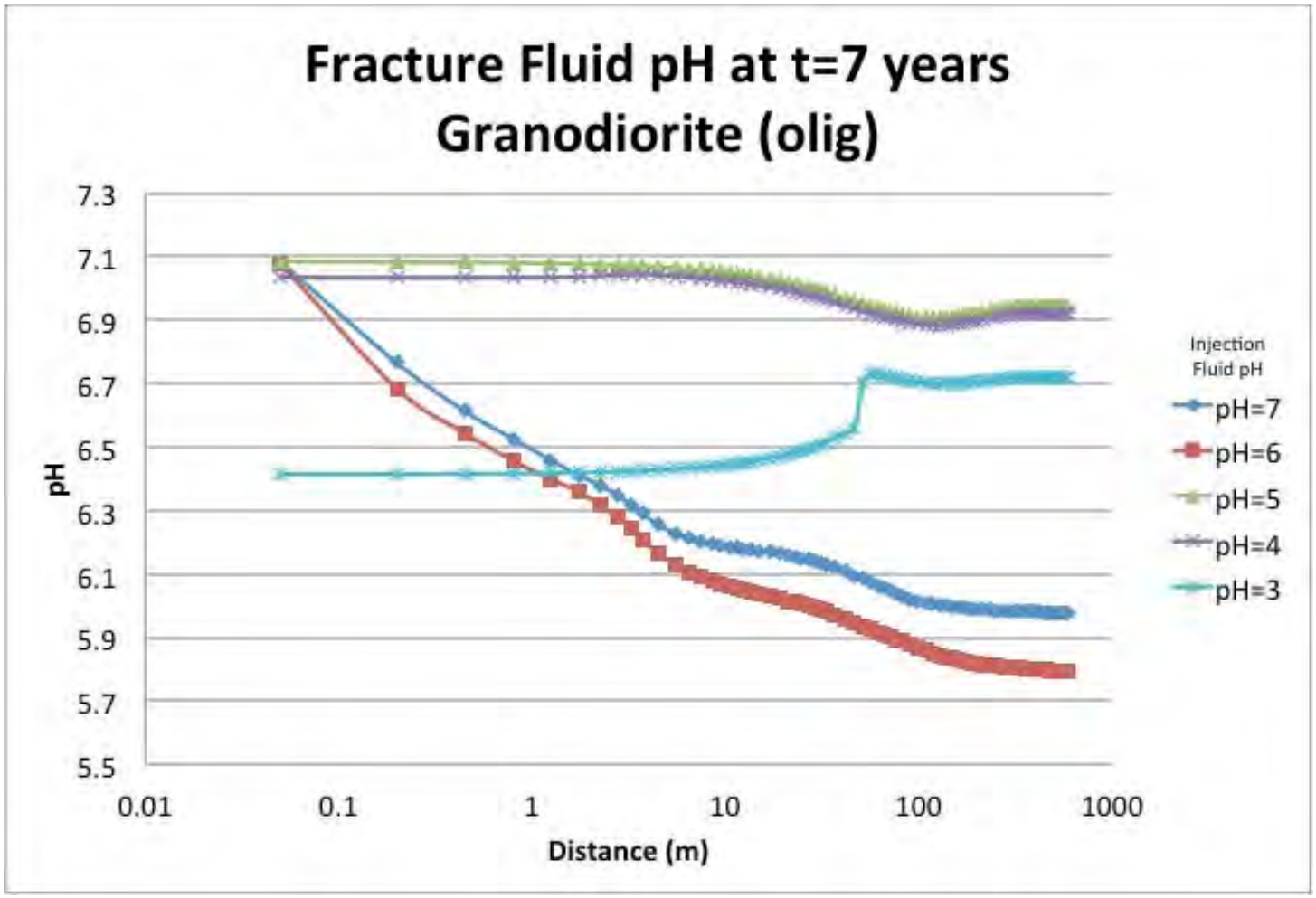

Fig. 3.14. Fracture fluid pH for Granodiorite (olig + low ab precip) at t=7 years for injection fluid pH=3, 4, 5, 6, and 7. Amorphous silica surface area is 10^6 cm^2/g for injection fluid pH=6 and 7 and 9.1 cm^2/g for injection fluid pH=3, 4, and 5.

of the fluid with the host rock are not allowed. Also, the models do not consider processes related to nucleation, growth, and maturation of silica particles.

The models predict that an injection pH of 4 would be optimal at Coso geothermal field to inhibit the majority of both amorphous silica and calcite precipitation. Dissolution and precipitation of minerals is not predicted to dramatically impact porosity and permeability over time with continued injection of fluid with pH=3 to 5. However, due to the limitations of the model, it is important to consider that minerals will not dissolve and precipitate exactly in their original locations, and other aspects of mineral dissolution and precipitation should be considered as a possible means for modification of porosity and permeability over time (i.e., preferential mineral precipitation in pore throats or preferential dissolution at mineral contacts due to pressure solution). The predicted changes in fracture fluid pH over time will also have a possible impact on whether or not silica will remain in solution long enough to be heated in the reservoir, where high temperature removes homogeneous nucleation and polymerization as major factors in the precipitation of amorphous silica (Iler, 1979).

In geothermal systems, reactions involving carbonates and feldspars typically exert the most control on the fluid pH through alteration phase equilibria (Giggenbach, 1981). The variation in pH of the fluid produced at Coso may also be related to reactions with reservoir rocks of differing mafic content, as there is significant variation in the abundance of mafic minerals in the reservoir rocks observed in drill cuttings and cores from the Coso geothermal field. Salinity has an impact on the ionic strength of the fluid, and therefore on the activity of H^+ (Henley et al., 1984). These reactions may be very

important controls on the production fluid pH at Coso and may also be important controls on the pH of injected fluid in fractures at Coso.

The $P(CO_2)$ will also influence the pH of the fracture fluid. The difference in the two most recent alteration mineral assemblages observed on the East Flank at Coso (Kovac et al., 2005) is directly related to the $P(CO_2)$ of the system at the time of the alteration (Giggenbach, 1981). However, variations in the $P(CO_2)$ of the injected fluid are not considered in these models because CO_2 is typically removed when the produced fluid has been flashed through boiling and deposition of carbonate minerals. Interactions between the fluid and carbonate minerals after injection will determine the $P(CO_2)$ of the injected fluid, and therefore influence the pH of the fracture fluid and the type of alteration minerals that would likely be observed.

These pH control mechanisms are important factors in determining the changes in pH of the reservoir fluid with the addition of H_2SO_4 into the injected fluid, and thus the precipitation rate and mechanism of amorphous silica deposition within the reservoir. The models indicate that the effect of pH-modified fluid on the reservoir rock will also be dependent on the mineral assemblage, mineral solubility, and assemblage buffering capabilities.

The calculated pH of the fluid in the fracture at t=7 years varies depending on the input reservoir rock mineralogy for injection fluid pH=6.5 (Fig. 3.7). The calculated pH of the fracture fluid varies with the type of plagioclase mineral used in the reservoir rock in the model (an, olig, ab). Models using granodiorite reservoir rock with oligoclase as the plagioclase feldspar predict a higher fracture fluid pH than the models with anorthite or albite as the plagioclase. The oligoclase is predicted to dissolve and add Na^+ to the

fracture fluid. This increases the ionic strength of the fracture fluid, decreasing the activity of H^+ and increasing the fluid pH. In the case where anorthite is the plagioclase feldspar, anorthite is predicted to dissolve, but the Ca^{2+} can precipitate out in the form of calcite. Thus dissolution of anorthite does not affect the ionic strength of the fluid significantly. The injection fluid is already saturated with albite and K-feldspar at 110^{o}C (log(Q/K)=0.64 and 1.38, respectively), indicating that the injection fluid had already exchanged extensively with both feldspars in the Coso geothermal reservoir. Hence the models predict low dissolution rates (Table 3.4) and that neither albite nor K-feldspar will dissolve. In contrast, oligoclase and anorthite are compositionally and structurally out of equilibrium with the injection fluid, and the models predict high dissolution rates (Table 3.4) for both of these higher temperature (igneous) feldspars. When low albite is allowed to precipitate in the granodiorite cases with oligoclase or albite feldspar, the low albite precipitation removes the Na^+ from the fracture fluid, reducing the ionic strength of the fluid and increasing the activity of H^+. However, fracture fluid pH cannot be explained simply with the concentration of Na^+ in the fluid for the other cases, as the fluid pH is dependent on many mineral reactions. The saturation of the injection fluid used in the model with albite and K-feldspar and the predicted dissolution of oligoclase and anorthite in the models indicate that the structure and composition of the feldspars in the reservoir rocks that the fluids flow through at Coso are likely closer to those of a hydrothermal albite or low albite and K-feldspar than to those of oligoclase or anorthite.

The fracture fluid pH also declines with the addition of the mafic minerals phlogopite and clinozoisite in the initial reservoir rock (Diorite (60% mafics)). The pH does not vary considerably relative to the amount of plagioclase feldspar (an), quartz,

annite, or K-feldspar, as seen by comparing the Granodiorite (an) and the Diorite (an) cases. Increasing the mafic mineral percentage to 60% of the rock volume with the addition of phlogopite and clinozoisite (Diorite (60% mafic)) yields a significantly lower fracture fluid pH. The precipitation of clinozoisite in the reservoir rock releases H+ into the fluid in these models.

The injectivity of wells at Coso geothermal field is currently maintained by injecting H_2SO_4 modified fluid. The target pH is near pH=5, and precipitation of amorphous silica scale does not appear to be a problem when the pH modified fluid is injected. The current simulations predict the deposition of amorphous silica when there is a very large available surface area for amorphous silica precipitation. However, the fracture fluid pH is predicted to neutralize very quickly in Granodiorite (an) and Granodiorite (olig + low ab precip) reservoir rocks when the injection fluid pH is between pH=3 to 5 (Fig. 3.14). Of particular interest is the predicted fracture fluid pH in Granodiorite (olig + low ab precip). When the surface area of amorphous silica is 10^6 cm^2/g (as in models where injection pH= 6 or 7) and low albite is allowed to precipitate from the fluid (removing Na^+), the fracture fluid pH is predicted to decrease below pH=6. When amorphous silica does not precipitate (pH=3, 4, or 5 and amorphous silica surface area is 9.1 cm^2/g), $SiO_2(aq)$ will likely complex with H^+, buffering the solution to higher pH. Hence, the predicted fracture fluid pH is strongly related not only to silicate mineral reactions but to the amount of $SiO_2(aq)$ in solution. The relative impact of these two processes on the pH of the fracture fluid therefore will be a function of the pH of the injection fluid.

Because the kinetic rate of amorphous silica precipitation is dependent upon pH, the predicted pH of the fracture fluid is important in determining if amorphous silica will precipitate at some point along the flow path between injection and production wells at Coso. The kinetic rate of deposition will also be dependent on the temperature of the fluid within the reservoir. As observed in subsequent injection wells drilled on pad 68-20 after the initial injection well, the temperature of the reservoir rocks is declining in the near wellbore with injection over time. When amorphous silica does not precipitate and inhibit the flow of injection fluids into the reservoir, there is the possibility that this temperature decline may be accelerated in certain portions of the reservoir. The current models predict a decline of fracture fluid temperature related to the maintenance of porosity and permeability with inhibition of amorphous silica precipitation (Fig. 3.15). The neutralization of the pH of the fracture fluid, as well as the possible declines in temperature along the flow path may lead to the need for increasing the amount of H_2SO_4 in the injection fluid over time to keep amorphous silica from precipitating.

The models predict that the addition of H_2SO_4 to the injection fluid may lead to an increase in anhydrite precipitation further into the flow path as fluid heated. The models, however, do not predict the deposition of anhydrite with the addition of quantities of H_2SO_4 calculated for the injection fluid to reach pH=3, 4 or 5. An increase in SO_4^{2-} to 10^{-3} in the injection fluid (corresponding to an injection fluid pH >2 reduced from 6.5) would correspond to a 10^{-5}% increase in the volume of anhydrite in distant portions of the flow path. Therefore, the precipitation of anhydrite is not predicted to be significant for additions of H_2SO_4 required to reduce the pH of the injection fluid from 6.5 to >3. However, if the pH of the injection fluid is higher before modification and more H_2SO_4 is

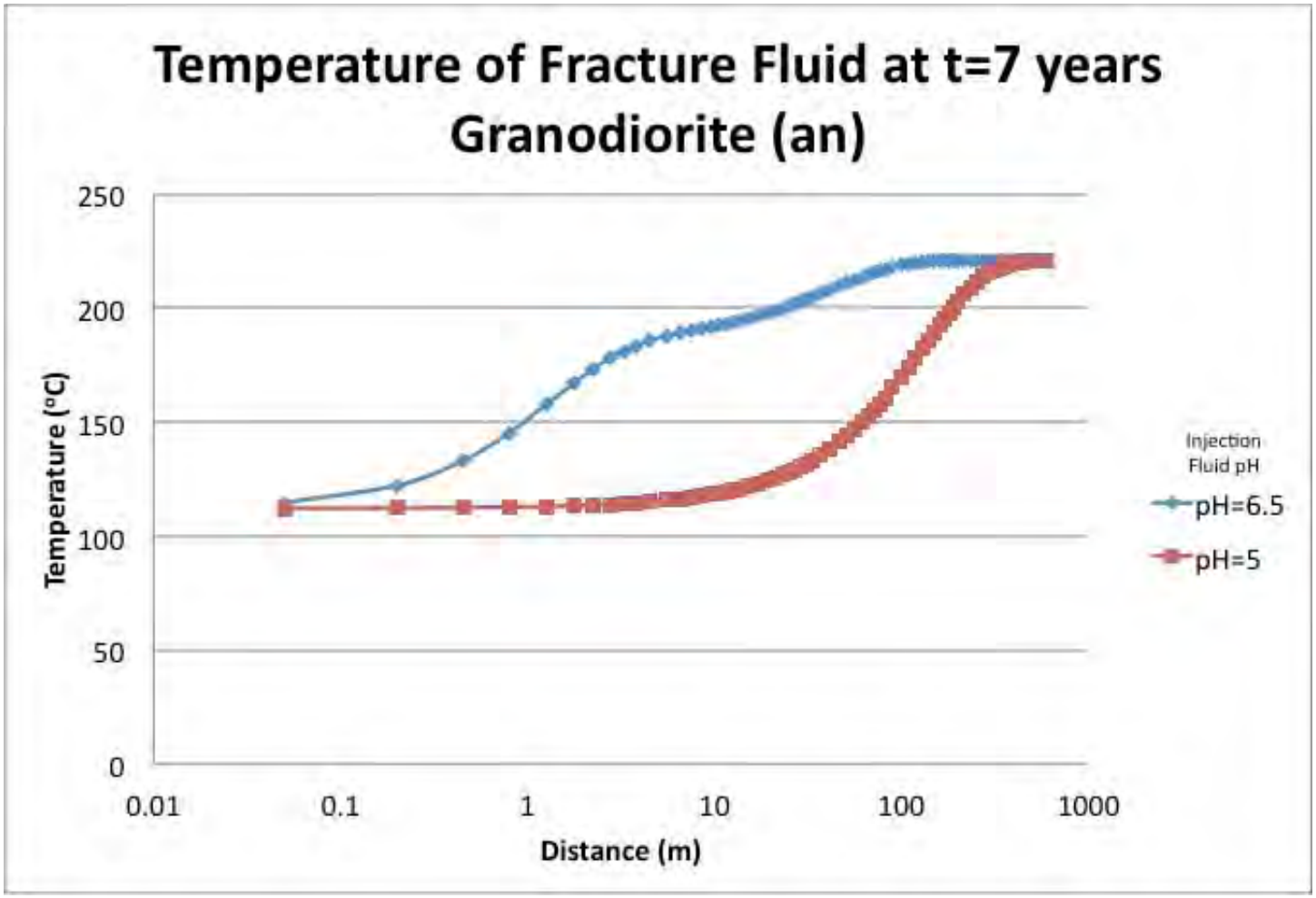

Fig. 3.15. Temperature of fracture fluid for Granodiorite (an) at t=7 years for injection fluid pH=6.5 and 5. Amorphous silica surface area is 10^6 cm^2/g for injection fluid pH=6.5 and 9.1 cm^2/g for injection fluid pH=5. The temperature decline progresses farther when significant amounts of amorphous silica do not precipitate.

required to reduce the pH, there may be an increased amount of anhydrite precipitation in fractures.

Conclusions

Although there are limitations to the models, reactive transport models using the program TOUGHREACT provide insight into the consequences of injecting post production reservoir fluid and H_2SO_4 modified fluid at the Coso geothermal field. These simulations predict that injection of fluid supersaturated with respect to amorphous silica will cause rapid declines in injectivity due to precipitation of opal-A, consistent with observations of amorphous silica scale in cuttings from injection wells drilled on pad 68-20 at Coso. The TOUGHREACT model was then used to predict the effects of injection of pH modified fluid on reservoir rocks and fluids. An optimal injection pH of 4 is predicted to prevent significant precipitation of amorphous silica. The models predict that the pH of this fluid will be buffered within the reservoir as a result of silicate mineral reactions and SiO_2(aq) in the fluid. Mineralogy of the reservoir rock may have a significant effect on the pH of the fluid after it has been injected, which in turn will have a significant effect on the polymerization kinetics of amorphous silica. Significant changes in porosity and permeability of fractures or reservoir host rock are not predicted for injection fluid with lower pH (3 to 5) from the addition of H_2SO_4. However, minor mineral dissolution and precipitation are predicted, which could cause declines in porosity and permeability within the reservoir through processes that the models do not consider, such as pressure solution and preferential precipitation in pore throats. With

decreased mineral precipitation, increased injectivity may lead to more rapid declines in temperature in portions of the reservoir.

References

Adams, M.C., Moore, J.N., Bjornstad, S., Norman, D.I., 2000. Geologic history of the Coso geothermal system. Geothermal Resources Council Transactions 24, 205-209.

Adams, M.C., Moore, J.N., Bjornstad, S., McCulloch, J., Buck, C., 2005. Fluid-mineral equilibria and injection in EGS - effect of injecting groundwater. Proceedings, 30th Workshop on Geothermal Reservoir Engineering.

Bethke, C., 1996. GWB reaction modeling guide: a user's guide to react and gtplot. Hydrogeology Program, University of Illinois.

Gallup, D.L., 1997. The interaction of silicic acid with sulfurous acid scale inhibitor. Geothermal Resource Council Transactions 21, 49-53.

Gallup, D.L., 1998. Aluminum silicate scale formation and inhibition (2): scale solubilities and laboratory field inhibition tests. Geothermics 27, 485-501.

Gallup, D.L., Kitz, K., 1998. On-site production and usage of sulfurous acid for scale inhibition. Proceedings 19th PNOC-EDC Geothermal Conference, 191-198.

Giggenbach, W.F., 1981. Geothermal mineral equilibria. Geochimica et Cosmochimica Acta 45, 393-410.

Henley, R.W., Truesdell, A.H., Barton, Jr. P.B., 1984. Fluid-Mineral Equilibria in Hydrothermal Systems. Reviews in Economic Geology, 267 p.

Iler, R.K., 1979. The Chemistry of Silica-Solubility, Polymerization, Colloid, and Surface Properties, and Biochemistry. John Wiley & Sons, Inc., New York.

Klein, C., 1995. Management of fluid injection in geothermal wells to avoid silica scaling at low levels of silica oversaturation. Geothermal Resources Council Transactions 19, 503-511.

Kovac, K.M., Moore, J.N., Lutz, S.J., 2005. Geologic framework of the East Flank, Coso geothermal field: Implications for EGS Development. Proceedings 30th Workshop on Geothermal Reservoir Engineering.

Lutz, S.J., Moore, J.N., 1997. Petrographic and x-ray diffraction study of 130 cuttings samples from six wells in the Coso geothermal area, California. Unpublished CalEnergy Corporation Report.

Lutz, S.J., Moore, J.N., Adams, M.C., Norman, D.I., 1999. Tracing fluid sources in the Coso geothermal system using fluid-inclusion gas chemistry. Proceedings 24th Workshop on Geothermal Reservoir Engineering.

Lynne, B.Y., Campbell, K.A., 2004. Morphologic and mineralogic transitions from opal-A to opal-CT in low-temperature siliceous sinter diagenesis, Taupo Volcanic zone, New Zealand. Journal of Sedimentary Research 74, 561-579.

Lynne, B.Y., Campbell, K.A., James, B.J., Browne, P.R.L., Moore, J.N., 2007. Tracking crystallinity in siliceous hot spring deposits. American Journal of Science 307, 612-641.

McLin, K.S., Moore, J.N., Hulen, J., Bowman, J.R., Berard, B., 2006a. Mineral characterization of scale deposits in injection wells; Coso and Salton Sea geothermal fields, CA. Proceedings 31st Workshop on Geothermal Reservoir Engineering.

McLin, K.S., Kovac, K.M., Moore, J.N., Adams, M.C., Xu, T., 2006b. Modeling the Geochemical Effects of Injection at Coso Geothermal Field, CA; Comparison with Field Observations. Proceedings 31st Workshop on Geothermal Reservoir Engineering.

Palandri, J.L., Kharaka, Y.K., 2004. A compilation of rate parameters of water-mineral interaction kinetics for application to geochemical modeling. U.S. Geological Survey Open File Report 2004-1068.

Park, J., Norman, D., McLin, K., Moore, J., 2006. Modeling amorphous silica precipitation: a strategy to reduce silica precipitation near Coso injection wells. Proceedings 29th Workshop on Geothermal Reservoir Engineering.

Parks, G.A., 1990. Surface energy and absorption at mineral-water interfaces: an introduction. Reviews in Mineralogy and Geochemistry 23, 133–175.

Pruess, K., Oldenburg, C., Moridis, G., 1999. TOUGH2 user's guide, Version 2.0. Lawrence Berkeley National Laboratory Report LBL-43134.

Rodgers, K.A., Browne, P.R.L., Buddle, T.F., Cook, K.L., Greatrex, R.A., Hampton, W.A., Herdianita, N.R., Holland, G.R., Lynne, B.Y., Martin, R., Newton, Z., Pastars, D., Sannazarro, K.L., Teece, C.I.A., 2004. Silica Phases in sinters and residues from geothermal fields of New Zealand. Earth Science Reviews 66, 1-61.

Rothbaum, H.P., Anderton, B.H., Harrison, R.F., Rohde, A.G., Slatter, A., 1979. Effect of silica polymerisation and pH on geothermal scaling. Geothermics 8, 1-20.

Wolery, T.J., 1992. EQ3/6: Software package for geochemical modeling of aqueous systems: Package overview and installation guide (version 7.0). Lawrence Livermore National Laboratory Report UCRLMA-110662 PT I.

Xu, T., Apps, J.A., Pruess, K., 2004. Mineral Sequestration of Carbon Dioxide in a Sandstone-Shale System. Lawrence Berkeley National Laboratory Report LBNL-55818.

Xu, T., Apps, J.A., Pruess, K., Yamamoto, H., 2007. Numerical modeling of injection and mineral trapping of CO_2 with H_2S and SO_2 in a sandstone formation. Chemical Geology 242, 319-346.

Xu, T., Pruess, K., 2004. Numerical simulation of injectivity effects of mineral scaling and clay swelling in a fractured geothermal reservoir. Geothermal Resource Council Transactions 28, 269-276.

Xu, T., Pruess, K., 2001. Modeling multiphase non-isothermal fluid flow and reactive geochemical transport in variably saturated fractured rocks: 1. Methodology. American Journal of Science 301, 16-33.

Xu, T., Sonnenthal, E., Spycher, N., Pruess, K., 2004. TOUGHREACT user's guide: A simulation program for non-isothermal multiphase reactive geochemical transport in variably saturated geologic media. Lawrence Berkley National Laboratory publication LBNL-55460.

CHAPTER 4

MODELING THE GEOCHEMICAL EFFECTS OF INJECTION AT THE SALTON SEA GEOTHERMAL FIELD, CA: COMPARISON WITH FIELD OBSERVATIONS

Abstract

Mineral deposition has reduced the injection rates in an injection well at the Salton Sea geothermal field. Scanning electron microscope images combined with semiquantitative energy dispersive analyses show that the scale deposits found in cuttings from the Elmore IW3 RD-2 redrilled well consist of layers of barite and fluorite and minor anhydrite, amorphous silica and copper arsenic sulfides. Geochemical modeling using TOUGHREACT has been initiated to further assess the behavior of the injection fluids and their effects on well performance. A one dimensional model is used to simulate injection into sandstone containing a fracture zone with 95% porosity. Initial models predict that barite is the mineral responsible for porosity declines when silica and bicarbonate are removed from the injection fluid. This prediction is consistent with the observed mineral relationships.

Introduction

Direct evidence has been observed for relating injectivity losses in the Salton Sea geothermal system to mineral precipitation (McLin et al., 2006). In order to mitigate the effects of mineral deposition, the geochemistry and mineralogy of these deposits, as well as fluid-fluid and fluid-rock interactions must be understood. In this chapter, the effects of injecting flashed geothermal fluids into Salton Sea injection well Elmore IW3 RD-1 are investigated by comparing field observations from drill cuttings with modeled results. The effects of changes in fluid chemistries are also modeled.

Salton Sea Geothermal Field

The Salton Sea geothermal system is developed in Quaternary deltaic sandstones and shales of the Salton Trough, the northern landward extension of the tectonic regime of the Gulf of California (Hulen and Pulka, 2001) (Fig. 4.1). The sediments, which are located above continental spreading centers, serve as thermal insulators. Quaternary volcanoes are exposed at Obsidian Butte, Rock Hill, Red Island and Mullet Island and several of the wells have encountered older rhyolite (Hulen and Pulka, 2001). Injection well Elmore IW3 RD-1 was drilled in 1988 and used for injection until 1997. Fluids injected into Elmore IW3 RD-1 were hypersaline (TDS exceeds 220,000 mg/kg) and metal-rich, but low in silica, which was removed prior to injection. The well was deepened in 1997 from 2308 to 2405 m depth due to declining performance and renamed Elmore IW3 RD-2.

Fig. 4.1. Generalized map of the Salton trough (modified from McLin et al., 2006, Hulen et al., 2001).

Observations

A variety of scale deposits have been recognized in the cuttings from Elmore IW3 RD-2 based on their mineralogy and textures. Concentrations of scale occur primarily at the top of the redrill at a depth of approximately 2308 and sporadically at greater depths (Fig. 4.2). Petrologic, scanning electron microscope (SEM), and semiquantitative energy dispersive x-ray (EDX) analyses were used to determine the mineralogy and texture of the scale deposits found in the cuttings. Fluid inclusions were studied in associated euhedral calcite crystals to determine their petrogenesis.

Photomicrographs of scale deposits show distinct mineral banding that range from tens to hundreds of micrometers in thickness (Fig. 4.3; McLin et al., 2006). SEM and EDX analyses demonstrate that the scale deposits consist of layers of barite and fluorite associated with minor anhydrite, amorphous silica and copper arsenic sulfides. Some bands of barite show strong Ti peaks in the EDX spectra, whereas amorphous silica bands show strong Fe peaks in the spectra. No differences in the chemistries of adjacent barite bands, was observed, suggesting that factors other than fluid chemistry control barite deposition. The anhydrite coats the barite, whereas the amorphous silica was found deposited on the copper arsenic sulfide scale.

Secondary fluid inclusions were studied in euhedral calcite crystals from a depth of 2308 m. Only two-phase liquid rich inclusions were observed. The homogenization temperatures of thirty inclusions ranged from 337^{o} to 357^{o}C. These temperatures represent the minimum trapping temperatures. Ice melting temperatures indicate salinities between 23 and 25 weight percent NaCl-$CaCl_2$ equivalent. These homogenization temperatures indicate that the calcite crystals were not formed as scale

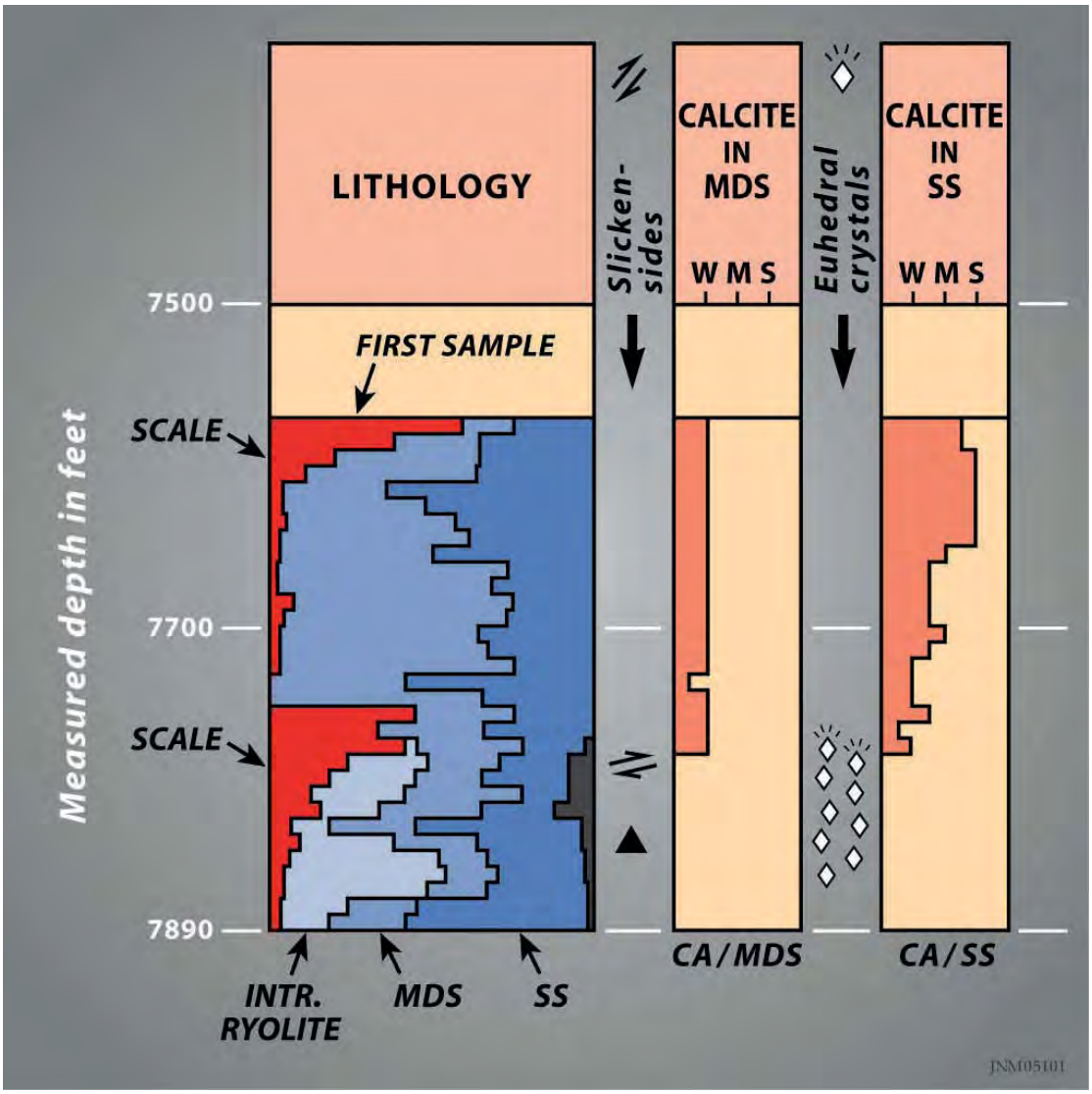

Fig. 4.2. Lithology of cuttings from Elmore IW3 RD-2 and calcite concentration, as well as the location of euhedral crystals and slickensides (as described by Jeff Hulen). MDS is mudstone, SS is sandstone, and CA is calcite.

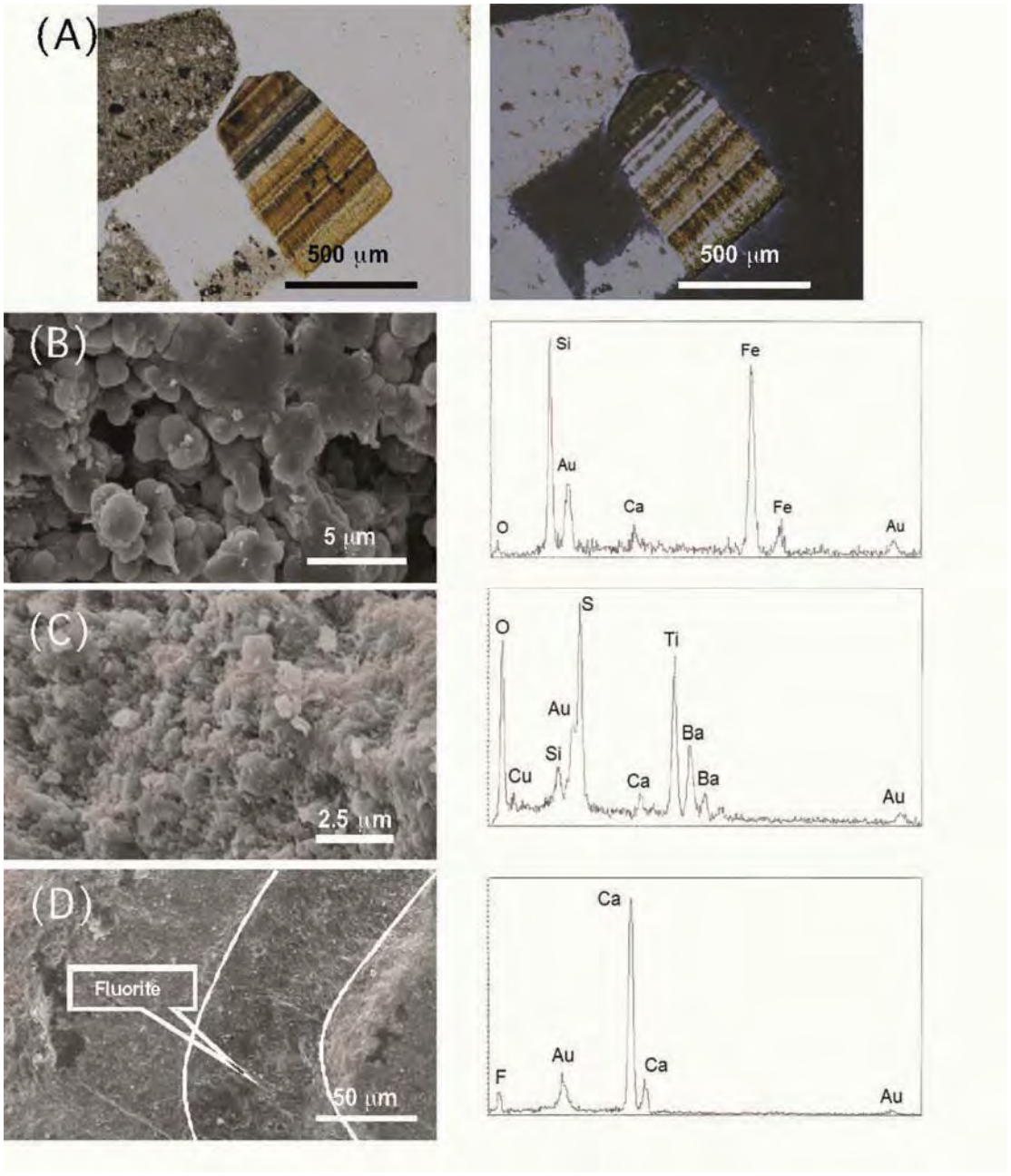

Fig. 4.3. Photomicrographs and SEM images of scale from Elmore IW3 RD2. (A) Photomicrographs of scale deposits from Elmore IW3 RD2 sampled from 2308-2405 m depth. Images taken under plane polarized light (left) and under crossed nicols (right). (B), (C), (D) SEM and corresponding EDX spectra for (B) amorphous silica (C) barite and (D) fluorite from scale deposits.

deposits, as these temperatures are much higher than the 110°C and 258°C temperatures of the injected fluid and the reservoir respectively.

Modeling Approach

Simulations were carried out using the nonisothermal reactive geochemical transport code TOUGHREACT (Xu and Pruess, 2001; Xu et al., 2004). This code was developed by introducing reactive chemistry into the framework of the existing multiphase fluid and heat flow code TOUGH2 V2 (Pruess et al., 1999). Additional information on TOUGHREACT can be found on the site http://www-esd.lbl.gov/TOUGHREACT/. Interactions between mineral assemblages and fluids can occur under local equilibrium or kinetic rates. The gas phase can be chemically active. Precipitation and dissolution reactions can change formation porosity and permeability, and can also modify the unsaturated flow properties of the rock. This simulator can be applied to one, two, and three dimensional porous and/or fractured media with physical and chemical heterogeneity. Any number of species may present in liquid, solid, and gaseous phases in these simulations.

Simulation Setup

Fluid and Heat Flow Conditions

The flow geometry and conditions of fluid and heat flow are modeled after those described in Xu and Pruess (2004). A one dimensional MINC (multiple interacting continua) model was used to represent the fractured rock. The MINC method can resolve "global" flow and diffusion of chemicals in the fractured rock and interaction of fluids

with “local” exchange between fractures and matrix. Details on the MINC method for reactive geochemical transport are described by Xu and Pruess (2001). Two different domains are considered in the model; one representing the relatively impermeable, unaltered host rock and the second representing the relatively permeable fractures. The physical characteristics of the two domains are provided in Table 4.1. The host rock is considered to be a weakly to moderately altered calcite cemented sandstone, based on petrographic studies of the well cuttings. Few veins were found in the well. To account for the lack of veining, the fractures were modeled as containing only trace amounts of anhydrite and smectite (Table 4.2). A density of 2650 $kg*m^{-3}$, heat capacity of 1000 $J*kg^{-1}K^{-1}$, and diffusivity of 10^{-9} $m^{-2}s^{-1}$ were used for both domains. The cubic law was used to define the porosity-permeability relationship in both cases (Xu et al., 2004). The model generates changes in porosity and permeability based on changes in mineral abundances.

Mineral Kinetic Rates and Parameters

Mineral dissolution and precipitation are considered under kinetic constraints. The general kinetic rate expression used to calculated mineral precipitation and dissolution rates is given by

$$r_m = \pm k_m A_m a_{H+}^{\ n} |1 - Q_m/K_m| \qquad (4.1)$$

where m is the mineral index, r_m is the dissolution/precipitation rate, (positive for dissolution, negative for precipitation), k_m is the rate constant (moles per unit mineral surface area and unit time) which is temperature dependent, A_m is the specific reactive

Table 4.1

Hydrologic and Thermal Parameters

Hydrologic and thermal parameters for the flow regimes.

Parameters	Fracture	Average Moderately Altered Sandstone
Volume	0.1	0.6
Permeability (m^2)	2.0E-12	2.0E-15
Porosity	0.95	0.10
Thermal Conductivity ($W^* m^{-1}K^{-1}$)	2.9	3.0
Tortuosity	0.3	0.1

surface area per kg of H_2O, a_{H+} is the activity of H^+, and n is an empirical reaction order accounting for catalysis by H^+ in solution (Xu et al., 2004):. K_m is the equilibrium constant for the mineral-water reaction written for the destruction of one mole of mineral m, Q_m is the ion activity product. The temperature dependence of the reaction rate constant can be expressed as:

$$k = k_{25} \exp[-E_a/R (1/T – 1/298.15)] \quad (4.2)$$

where E_a is the activation energy, k_{25} is the rate constant at 25°C, R is the universal gas constant, and T is absolute temperature. Table 4.3 shows the parameters used in the kinetic rate expression.

Table 4.2

Mineralogical Parameters

Simplified initial mineralogical composition of solid rock from the two domains used in the preliminary simulations. These estimations were made using data from the petrologic and petrographic studies. Initial rock temperature for both zones used was 258^{o}C in the preliminary simulations.

	Volume Fraction of Solid Rock	
Mineral	Fracture Mineralogy	Moderately Altered Sandstone
Quartz		.470
Potassium Feldspar		.080
Chlorite		.015
Illite		.015
Calcite		.015
Anorthite		.260
Annite		.100
Na smectite	.333	
Ca smectite	.333	
Anhydrite	.333	.020
Calcite		.015
Dolomite		.010

Table 4.3

Kinetic Rate Parameters

List of kinetic rate parameters used in Eqns. (4.1) and (4.2) for minerals considered in the present paper (Xu and Pruess, 2004; Palandri and Kharaka, 2004). The first line indicates dissolution parameters and the second line precipitation parameters; the same value was used for both dissolution and precipitation where only one line is shown.

Mineral	k_{25} (moles m^{-2} s^{-1})	E_a (KJ/mole)	n (rxn. order)	Surface Area (cm^2/g)
Quartz	1.2589E-14	87.50	0	9.8
Am. Silica	4.9000E-13	76.00	0	1.0E6
	3.8000E-10	49.80	0	1.0E6
K-feldspar	1.0000E-12	57.78	0	9.8
Anorthite	1.0000E-12	57.78	0	9.8
Na smectite	1.0000E-14	58.62	0	151.63
Ca smectite	1.0000E-14	58.62	0	151.63
Illite	1.0000E-14	58.62	0	151.63
Annite	2.5119E-15	66.20	1	9.8
	2.5119E-15	66.20	0	9.8
Calcite	6.9183E-02	18.98	1	9.8
	6.4565E-07	62.76	0	9.8
Dolomite	1.0233E-03	20.90	1	9.8
	4.4668E-10	62.76	0	9.8
Chlorite	2.5119E-12	62.76	0	151.63
Barite	1.3000e-08	30.80	0	9.8
Fluorite	1.6218e-14	73.00	0	9.8
Anhydrite	6.4565e-04	14.30	0	9.8

Water Chemistry

The composition of the reservoir fluid was estimated based on the approximate composition of production fluids from the Unit 6 Obsidian Butte Well (Table 4.4). The fluid has an ionic strength of 2.2 M. Iron and magnesium values were estimated based on values from Hulen et al. (2004). Initial fluid compositions were calculated by equilibrating the reservoir fluid composition with sandstone at 258°C, the initial reservoir temperature. The injectate composition was not allowed to change over time.

Table 4.4

Fluid Chemistry

Example approximate composition of reservoir fluid from Salton Sea Unit 6 Obsidian Butte well at 258°C temperature as used in the simulations.

Chemical Component	mol/kg
SiO_2	0.9962E-2
Na^+	0.1957
K^+	0.3325
Ca^{2+}	0.6137E-1
Mg^{2+}	0.1781E-5
Cl^-	3.944
F^-	0.1053E-2
HCO_3^-	0.1506E-2
SO_4^-	0.1040E-2
Fe^{+2}	0.2586E-6
Mg^{+2}	0.1781E-5
Ba^{+2}	0.1310E-2
pH	4.5

Results

The publicly available TOUGHREACT version, using an extended Debye-Huckel equation after Helgeson et al. (1981) for calculating activity of aqueous species, was used in this study. Our conceptual model considers a one dimensional flow tube beginning at the injection well and extending outward 500 m. The simulations were run for a total of 7 years. Changes in fluid pH, fracture porosity, fracture permeability, fluid temperature, and changes in mineral abundances were monitored. Mineral abundance changes are reported in terms of changes in volume fraction for the following minerals: quartz, potassium feldspar, chlorite, illite, sodium smectite, calcium smectite, calcite, dolomite, anorthite, biotite, amorphous silica, anhydrite, barite and fluorite. Calcite, barite, fluorite, anhydrite, quartz and amorphous silica displayed the most significant changes. Changes in porosity were calculated as a function of mineral dissolution and precipitation. Porosity increases when mineral dissolution is dominant, whereas porosity decreases when precipitation dominates. Changes in permeability are calculated from changes in porosity as described above.

For the initial model, the injection fluid chemistry is equivalent to the production fluid chemistry. The model results indicate that, with this chemistry, the deposition of amorphous silica, calcite, and quartz would be responsible for the porosity declines in Elmore IW3 RD. Barite and fluorite are minor precipitates, whereas anhydrite dissolves in this scenario. As in the following models, fluorite precipitation continues after deposition of barite ceases. This model does not fit the observed mineralogy of the scales. In the second modeled run, the concentration of silica in the injection fluid was reduced to 10^{-22}, reflecting precipitation of silica prior to injection. In this case, amorphous silica

does not precipitate, but a minor amount of quartz dissolves and precipitates. Thus, the amorphous silica must be carried in the injection fluid and could not be derived through dissolution of the reservoir rock. In contrast to the initial model, Fig. 4.4 shows that significant barite and calcite and minor fluorite precipitate. However, barite precipitation reaches a maximum at a later time, compared to the initial model.

Fig. 4.5 shows the results of reducing both silica and HCO_3^- concentrations in the injection fluid. Reducing HCO_3^- in the modeled injection fluid to trace amounts eliminates calcite from the precipitate, consistent with the observed scale mineralogy. In this model, barite and fluorite are the dominant phases precipitated, with fluorite deposition continuing after barite deposition ceases. Thus, this model best explains the observed mineral banding of the scale deposits.

Conclusions

The modeled results closely simulate the observed mineral deposits based on observations made on cuttings from injection well Elmore IW3 RD-2 when silica and bicarbonate are reduced to trace amounts in the injection fluid. Because minor amounts of amorphous silica are found in the scale deposits, the model indicates that amorphous silica must at times be present in the injection fluid. The Pitzer ionic interaction model described by Xu et al. (2005) should be used in future investigations and compared to results from this study. Future investigations should also include variations in the composition of the injection fluid, such as the addition of condensate and the effects of steam loss. Reductions in injection fluid temperature should be considered to determine if injectivity increases are predicted by injecting cooler fluids.

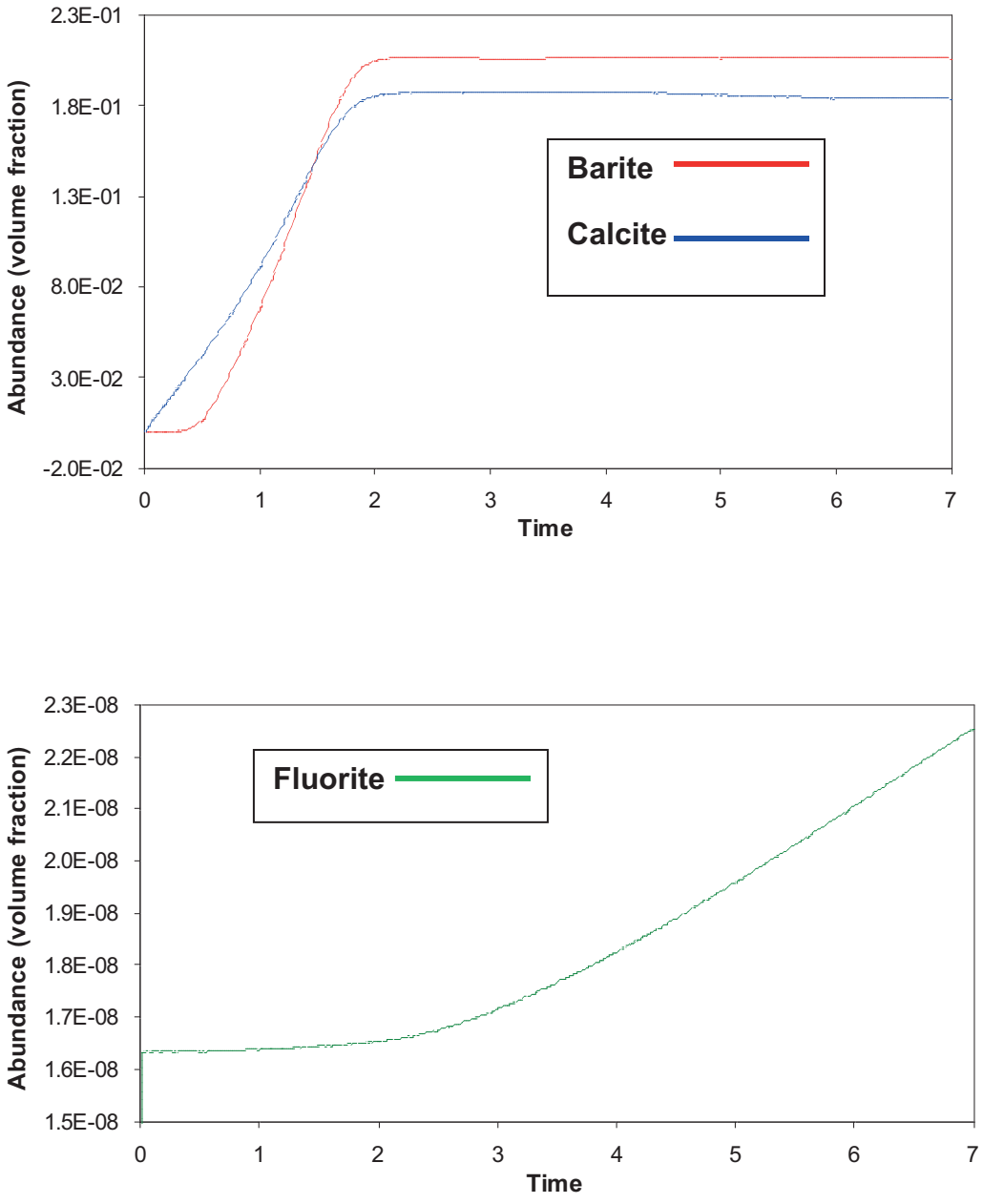

Fig. 4.4. Graphs showing barite, calcite, and fluorite precipitation in fracture over time for the model with silica removed from the injection fluid (t=0 to 7 years).

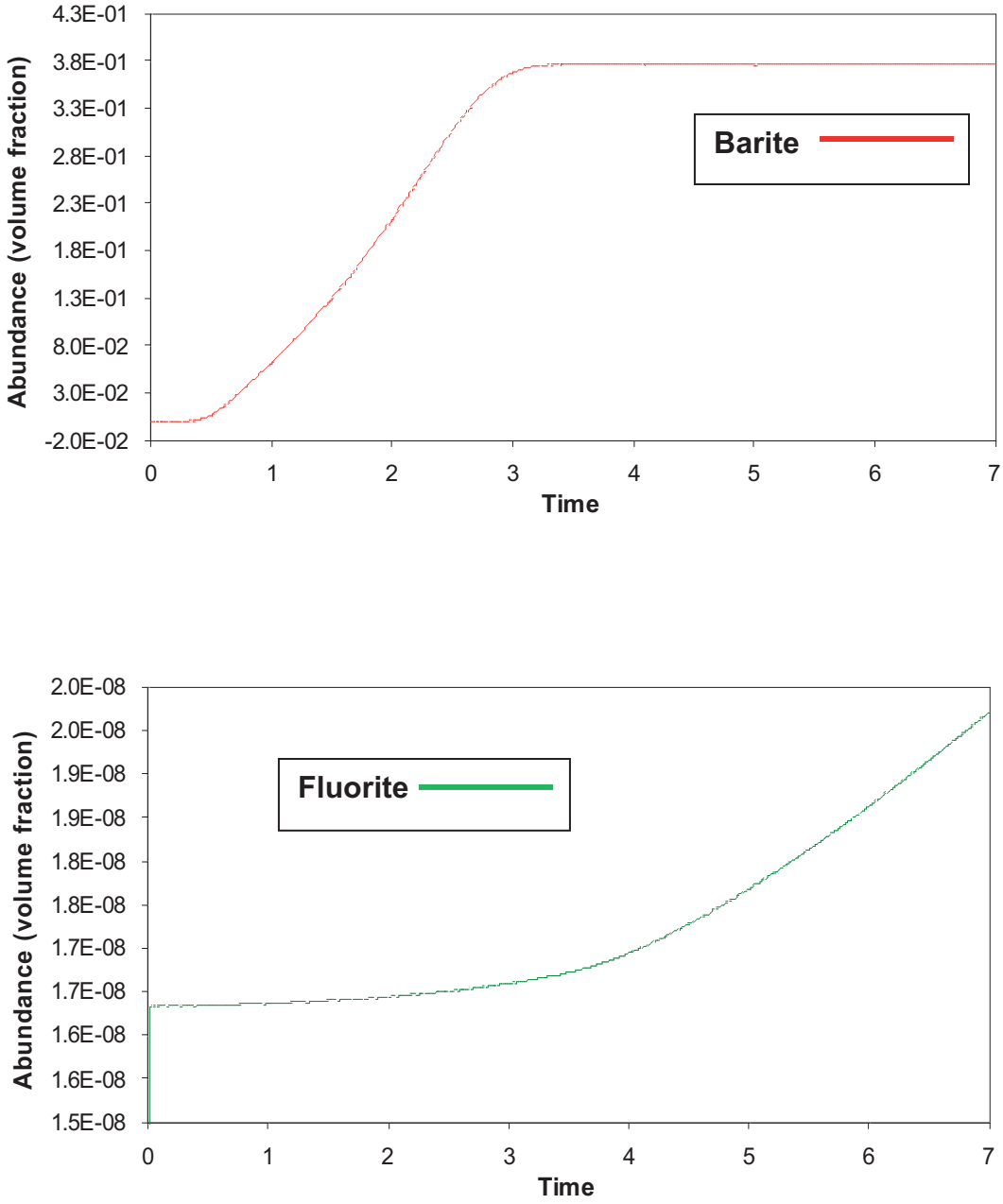

Fig. 4.5. Graphs showing barite and fluorite precipitation in fracture over time for the model with silica and bicarbonate removed from the injection fluid (t=0 to 7 years).

References

Helgeson, H.C., Kirkham, D.H., Flowers, D.C., 1981. Theoretical prediction of the thermodynamic behavior of aqueous electrolytes at high pressures and temperatures: IV. Calculation of activity coefficients osmotic coefficients, and apparent molal and standard and relative partial molal properties to 600^{o}C and 5 kb. American Journal of Science 281, 1249-1516.

Hulen, J.B., Pluka, F.S., 2001. Newly-discovered, ancient extrusive rhyolite in the Salton Sea geothermal field, Imperial Valley, California. Proceedings 26th Workshop on Geothermal Reservoir Engineering.

Hulen, J.B., Norton, D.L., Moore, J.N., Kaspereit, D., 2004. Epithermal vein-hosted and stratabound Pb-Zn mineralization in an active hydrothermal system: the southern Salton Sea geothermal field, California. Geothermal Resources Council Transactions 28, 415-424.

McLin, K.S., Moore, J.N., Hulen, J., Bowman, J.R., Berard, B., 2006. Mineral characterization of scale deposits in injection wells; Coso and Salton Sea geothermal fields, CA. Proceedings 31st Workshop on Geothermal Reservoir Engineering.

Pruess, K., Oldenburg, C., Moridis, G., 1999. TOUGH2 user's guide, Version 2.0. Lawrence Berkeley Laboratory Report LBL-43134.

Xu, T., Pruess, K., 2001. Modeling multiphase non-isothermal fluid flow and reactive geochemical transport in variably saturated fractured rocks: 1. Methodology. American Journal of Science 301, 16-33.

Xu, T., Pruess, K., 2004. Numerical simulation of injectivity effects of mineral scaling and clay swelling in a fractured geothermal reservoir. Geothermal Resources Council Transactions 28, 269-276.

Xu, T., Sonnenthal, E., Spycher, N., Pruess, K., 2004. TOUGHREACT user's guide: A simulation program for non-isothermal multiphase reactive geochemical transport in variably saturated geologic media. LBNL publication LBNL-55460.

Xu, T., Zhang, G., Pruess, K., 2005. Use of TOUGHREACT to simulate effects of fluid chemistry on injectivity in fractured geothermal reservoirs with high ionic strength fluids. Proceedings 30th Workshop on Geothermal Reservoir Engineering.

CHAPTER 5

GEOCHEMICAL MODELING OF WATER-ROCK-PROPPANT INTERACTIONS

Abstract

Enhanced geothermal system (EGS) reservoir fracture creation and management may require the use of proppants to maintain fracture conductivity. The most commonly used proppants, which remain in hydraulically created fractures to keep them open, include silica sand, ceramic, and sintered bauxite. In geothermal systems, proppant will need to withstand high temperatures, acidified fluids, acid treatments, and cleanouts while maintaining the porosity and permeability of the fracture. Geochemical modeling of water-rock-proppant interactions was conducted in conjunction with static experiments to extrapolate experimental observations to the reservoir scale. PHREEQC was used to examine the chemical stability of silica and bauxite proppants in equilibrium with fluids of varying composition. TOUGHREACT was used to model one dimensional flow of these fluids through a granite reservoir with fractures filled with silica or bauxite proppant. The models predict that amorphous silica would precipitate in quartz sand propped fractures. The models also predict that dissolution and reprecipitation of aluminum minerals from the bauxite proppant would occur when the porosity was high enough (50%) for a sufficient water/rock ratio, allowing the hydration of corundum to

diaspore. This predicted hydration reduced the fracture porosity by increasing the volume of the aluminum bearing mineral.

Introduction

In the oil and gas industry, hydraulic fracturing is often accompanied by the addition of proppants. Proppants are sized particles that are added to fracturing fluids and remain in the fracture to physically hold the newly created fracture open while maintaining conductivity within the fracture. A variety of proppants are available, and the most commonly used proppants consist of silica sand, ceramic and resin coated sands, and bauxite. In enhanced geothermal systems (EGS), proppant will need to withstand high temperatures, acidified fluids, acid treatments, and cleanouts while maintaining the porosity and permeability of the fracture. However, proppant particles may act as nucleation sites and promote precipitation, or they may dissolve, consequently affecting fracture performance by increasing or decreasing permeability. Thus, the performance of proppants in geothermal reservoirs must be understood to avoid costly mistakes in the creation and maintenance of EGS reservoirs. The goal of this investigation is to develop improved methods for maintaining permeable fracture volumes in EGS reservoirs by experimentally evaluating the performance of proppants (natural and manufactured) under conditions found within geothermal environments and determining the effects of mineral deposition and dissolution on propped fractures.

Previous Studies

There have been few geothermal applications of proppants. In the Northeast German Basin at Schoenbech, high strength ceramic proppant was used in a well at 4080-4190 m depth and 140^{o}C (Legarth et al., 2003). Propped fractures were created, and inflow performance of the well was significantly enhanced. Even so, post fracture productivity was not as high as predicted. The possible reasons given for this discrepancy are chemical and mechanical processes during well shut in or undersized and poorly connected fractures. Sand proppant was used during stimulation of production wells at Raft River, Idaho in the late 1970's and early 1980's (Hanold, 1982). Sand proppant was substantially produced from well RRGP-4 for ten days following stimulation (Verity, 1980).

Previous studies from the oil and gas industry have reported that sintered bauxite proppant is resilient in high stress environments (Cooke, 1977). When formation stresses are high, these proppants deform, rather than crush. This deformation allows for the increase of contact area between proppant grains or between proppant and the wall rock. Quartz sand has been shown to crush, decreasing porosity and permeability in the fracture (Cooke, 1977). Significant conductivity loses were reported after flow-through testing with sintered bauxite in fractured sandstone at temperatures between 93 and 287^{o}C (Weaver et al., 2009). These loses were partially attributed to geochemical interactions of the fluid, proppant, and formation rock.

McLin et al. (2010) and Brinton et al. (2011) show dissolution of proppant and precipitation of minerals in static experiments. Proppant and a proppant-granite mixture were reacted with various fluids for up to two months at 200-230^{o}C. Dissolution textures

were observed on the surface of the bauxite proppant in several experiments. The precipitated minerals included aluminosilicates (possibly wairakite), zeolites, aluminum oxides/hydroxides, and amorphous silicates. The main mechanisms for precipitation of the minerals appear to be related to the experimental methodology. Fluid leakage concentrated the dissolved components in solution, and cooling the reactor for extended periods of time allowed lower temperature mineral assemblages to become stable and precipitate.

Batch Model Setup

Bauxite proppant consists mainly of corundum (Al_2O_3). The stability of corundum was examined using the Geochemist's Workbench (Bethke, 2008) with the Lawrence Livermore National Laboratory (LLNL) database and PHREEQC (Parkhurst and Appelo, 1999) with the LLNL and THERMODDEM (TDEM) databases. For these models, corundum is dissolved when equilibrated with deionized water. The saturation of gibbsite, boehmite, and diaspore were calculated for temperatures ranging from 0 to 300^{o}C.

PHREEQC was used to model batch equilibration of fluid with proppant and granite. The LLNL database was used. These simulations were constructed to model the experiments conducted by McLin et al. (2010) and Brinton et al. (2011). Deionized water and fluid with a composition based on the production fluid from Raft River well RRG-7 were reacted with granite and proppant. Simulations were run for both quartz and corundum proppants. Temperatures between 100 and 250^{o}C were used for these simulations. The quartz and corundum proppants were allowed to dissolve to saturation,

and mineral saturations were calculated based on these dissolved mineral concentrations. Outputs include pre and post reaction fluid chemistries and mineral saturation indexes.

Flow Model Setup

The flow simulations were carried out using the nonisothermal reactive geochemical transport code TOUGHREACT (Xu and Pruess, 2001; Xu et al., 2004). This code was developed by introducing reactive chemistry into the framework of the existing multiphase fluid and heat flow code TOUGH2 V2 (Pruess et al., 1999, see also http://www-esd.lbl.gov/TOUGHREACT/). Interactions between mineral assemblages and fluids can occur under local equilibrium or kinetic rates. The gas phase can be chemically active. Precipitation and dissolution reactions can change formation porosity and permeability, as well as modify the unsaturated flow properties of the rock. This simulator can be applied to one, two, and three dimensional porous and fractured media with physical and chemical heterogeneity. Any number of species can be present in the liquid, solid, and gaseous phases within this program.

Fluid and Heat Flow Conditions

The geometry and fluid and heat flow conditions are modeled after those described in Xu and Pruess (2004) and are similar to those used by McLin et al. (2006). A one dimensional MINC (multiple interacting continua) model was used to represent the fractured rock. The MINC method can resolve “global” flow and diffusion of chemicals in the fractured rock and interaction with “local” exchange between the fractures and matrix. Details on the MINC method for reactive geochemical transport are described by

Xu and Pruess (2001). In the simulations we considered interactions with: 1) a zone representing the relatively impermeable, unaltered host rock; and 2) altered host rock containing fractures filled with either corundum or quartz proppant. Granite was used as the host rock for these models. The flow distance was 698 meters, and the simulation monitored changes in temperature, fluid chemistry, porosity, permeability, and mineral volume fractions through t = 7 years. The parameters used in the models are shown in Table 5.1. Density = 2650 kg*m^{-3}, heat capacity = 1000 J*$kg^{-1}K^{-1}$, and diffusivity = 10^{-9} $m^{-2}s^{-1}$ were used for all zones. The cubic law was used to define the porosity-permeability relationship in both zones (Xu et al. 2004). The model generates changes in porosity and permeability based on changes in mineral abundances.

Table 5.1

Hydrologic and Thermal Parameters

Hydrologic and thermal parameters of rocks used in the models

Parameters	Fracture	Granite
Volume (m^3)	0.1	0.9
Permeability (m^2)	1.0E-13	2.0E-18
Porosity	0.30-0.50	0.02
Thermal Conductivity ($W* m^{-1}K^{-1}$)	2.9	3.0
Tortuosity	0.3	0.1

Mineralogical Conditions

The mineralogical composition of the reservoir rock is an estimated composition of granite. The fractures were given the porosity (30%), permeability, and tortuosity of a typical sandstone (as used in Xu et al., 2007). A higher porosity (50%) situation was also considered for the bauxite propped fracture. The type of proppant used in the simulation determined the mineralogy of the fracture zone. The bauxite proppant was simulated as mostly corundum with a few mineral contaminants, such as quartz, calcite, and clay minerals. Mineralogical compositions of the host rock and fractures are presented in Table 5.2.

Table 5.2

Mineralogical Parameters

Mineralogical composition of the granite used in the simulations. A temperature of 200^{o}C was used for the initial rock temperature in the simulations.

Mineral	Granite	Fracture (bauxite proppant)	Fracture (quartz proppant)
Quartz	0.22	0.06	0.90
Potassium Feldspar	0.22		
Chlorite	0.10	0.01	0.01
Illite	0.10	0.01	0.01
Calcite	0.03	0.04	0.05
Smectite		0.03	0.03
Anorthite	0.29		
Annite	0.06		
Amorphous Silica			
Corundum		0.85	

Mineral Kinetic Rates and Parameters

Mineral dissolution and precipitation are considered under kinetic constraints, with the exception of corundum, gibbsite, boehmite, and diaspore because good kinetic data were not available for all aluminum oxides/hydroxides. The general kinetic rate expression used in TOUGHREACT (Xu et al., 2004) is:

$$r_m = \pm k_m A_m a_{H+}^{\ n} |1 - Q_m/K_m| \quad (5.1)$$

where m is the mineral index, r_m is the dissolution/precipitation rate, (positive for dissolution, negative for precipitation), k_m is the rate constant (moles per unit mineral surface area and unit time), which is temperature dependent, A_m is the specific reactive surface area per kg of H_2O, a_{H+} is the activity of H^+, and n is an empirical reaction order accounting for catalysis by H^+ in solution. K_m is the equilibrium constant for the mineral-water reaction written for the destruction of one mole of mineral m, Q_m is the ion activity product. The temperature dependence of the reaction rate constant can be expressed as:

$$k = k_{25} \exp[-E_a/R(1/T - 1/298.15)] \quad (5.2)$$

where E_a is the activation energy, k_{25} is the rate constant at 25°C, R is the universal gas constant, and T is the absolute temperature. Table 5.3 shows the parameters used in the kinetic rate expression.

Table 5.3

Kinetic Rate Parameters

List of kinetic rate parameters used in Eqns. (5.1) and (5.2) for minerals considered in the present paper (Palandri and Kharaka, 2004 and Xu et al., 2007). The first line indicates dissolution parameters and the second line precipitation parameters; the same values were used for both where only one line is shown. Only the neutral mechanism was considered.

Mineral		Neutral Mechanism	
	A (cm^2/g)	k_{25} (mol m^{-2} s^{-1})	E_a (kJ/mol)
Quartz	9.1	1.023E-14	35
Am.	9.1	4.900E-13	76
Silica	9.1	3.800E-10	49.8
K-feldspar	9.1	3.890E-13	38
Anorthite	9.1	7.586E-10	17.8
Smectite	108.7	1.660E-13	35
Illite	108.7	1.660E-13	35
Annite	9.1	2.512E-15	66.20
Calcite	9.1	6.457E-07	18.98
	9.1	6.457E-07	62.76
Chlorite	9.1	3.020E-13	88

Water Chemistry

Initial fluid compositions within the fracture and host rock were calculated by equilibrating production fluid from Raft River well RRG-7 with granite at 200^{o}C. The injection fluid was taken from an analysis of production fluid from Raft River well RRG-7 (Table 5.4). The composition of injectate was not allowed to change over time.

Table 5.4

Fluid Chemistry

Composition of the reservoir at 200°C, the temperature used in the simulations, and injection fluid composition at 109°C, based on an analysis of produced fluid from the Raft River well RRG-7.

Chemical Component	Reservoir (mol/kg)	Injection (mol/kg)
SiO_2	3.549E-3	8.694E-3
Fe^{2+}	1.130E-8	6.689E-9
AlO_2^-	5.986E-4	1.185E-5
Na^+	5.849E-2	3.701E-2
K^+	2.617E-3	6.317E-3
Ca^{2+}	8.424E-3	8.697E-3
Mg^{2+}	2.393E-4	2.188E-5
Cl^-	9.368E-2	1.229E-1
HCO_3^-	4.082E-5	2.014E-3
SO_4^-	3.279E-6	5.696E-3
pH	6.56	7.82

Results

Tables 5.5-7 show the saturation of gibbsite, boehmite, and diaspore from 0°-300°C when corundum proppant was dissolved to saturation in the simulation. None of the aluminum oxides or hydroxides are significantly saturated at 200 to 300°C. These models are consistent with the observed experimental results (Brinton et al., 2011) at 230°C showing dissolution of the corundum proppant. PHREEQC predicted supersaturation of several minerals in simulations with both corundum and quartz

Table 5.5

Gibbsite Saturation

Gibbsite saturation calculated for 0-300°C using the Geochemist's Workbench and PHREEQC with the LLNL and TDEM databases.

T (°C)	Log Q/K (GWB LLNL)	Log Q/K (PHREEQC LLNL)	Log Q/K (PHREEQC TDEM)
0	3.2575		
25	2.7316	1.41	1.41
60	2.0956	0.87	0.91
100	1.4791	0.28	0.41
200	0.2924	-1.10	-0.56
300	-0.5648	-2.34	

Table 5.6

Boehmite Saturation

Boehmite saturation calculated for 0-300°C using the Geochemist's Workbench and PHREEQC with the LLNL and TDEM databases.

T (°C)	Log Q/K (GWB LLNL)	Log Q/K (PHREEQC LLNL)	Log Q/K (PHREEQC TDEM)
0	1.2512		
25	1.0958	1.60	1.52
60	0.9109	1.23	1.23
100	0.7324	0.75	0.95
200	0.3811	-0.61	0.41
300	0.1083	-2.04	

Table 5.7

Diaspore Saturation

Diaspore saturation calculated for 0-300°C using the Geochemist's Workbench and PHREEQC with the LLNL and TDEM databases.

T (°C)	Log Q/K (GWB LLNL)	Log Q/K (PHREEQC LLNL)	Log Q/K (PHREEQC TDEM)
0	2.2359		
25	1.9402	2.00	2.28
60	1.5942	1.58	1.90
100	1.2688	1.04	1.53
200	0.6588	-0.42	0.82
300	0.2186	-1.92	

proppant at 200°C. These minerals included anthophyllite, antigorite, talc, tremolite, grossular-andradite, and several zeolites. At lower temperatures, these minerals become undersaturated with the exception of the zeolites. The zeolites become more supersaturated in the 100°C simulations. Because the water to rock ratio was low for these simulations, the initial minerals present dissolved to saturation at each temperature.

TOUGHREACT flow models predicted declines in porosity and permeability over a short time for the quartz proppant filled fractures. The quartz proppant served as a nucleation site for amorphous silica, calcite, and minor quartz, illite, and smectite. The injection fluid serves as a source for the silica that has precipitated. Fig. 5.1 shows the porosity of the quartz sand propped fracture. In the simulation with bauxite proppant and 30% porosity, nothing precipitated or dissolved in the fracture. There was minor dissolution and precipitation of minerals in the granite. However, when porosity was

increased to 50%, the corundum dissolved and reprecipitated as diaspore in the first 10 meters of the flow path (Fig. 5.2). The increased volume of diaspore led to the decline in porosity and permeability. There is minor dissolution and precipitation of other minerals, but these reactions do not seem to significantly affect the porosity and permeability of the propped fracture.

Discussion

Although supersaturation of several minerals, such as grossular, talc, and antigorite, is predicted with batch equilibrations at 200°C, these minerals were not identified in the experiments conducted by Brinton et al. (2011). Even if these minerals are present, the concentration of magnesium in solution is so low that the amount of magnesium silicate minerals precipitated will be minute. Furthermore, kinetic precipitation of these minerals may be slow, and the minerals may not precipitate within the time frame of the experiment. Brinton et al. (2011) report that zeolites precipitated in one experiment, along with aluminum oxides/hydroxides and amorphous silicates in this same and another experiment. Fluid leakage and prolonged cooling of the reaction vessels probably allowed the precipitation of these minerals. The lower temperature simulations confirm that the temperatures of the reactors were probably much lower than 200°C when these minerals precipitated. In recent static experiments with modified methods to prevent leakage, dissolution of the bauxite proppant is observed, along with possible minor dissolution of the granite at 230°C (Brinton et al., 2011).

In flow models where the reservoir temperature was 200°C, there was no dissolution of corundum when the porosity was 30% in the bauxite propped fracture. In

the model that allowed a higher fluid flux through the sintered bauxite proppant (porosity of 50%), corundum dissolved and reprecipitated as diaspore. This reaction occurred in the cooler part of the flow path where injection had lowered the temperature of the fluid and rock in the flow path. In static experiments conducted with Raft River geothermal fluid, granite, and quartz sand proppant at 230^{o}C, the quartz proppant had dissolved (Brinton et al., 2011). No precipitation was observed on the proppant or granite after these experiments. In flow simulations with quartz proppant, mineral precipitation decreases fracture porosity and permeability in the first few meters of the flow path. Any mineral precipitation that was predicted in these simulations was predicted to occur in the cooler initial portion of the flow path.

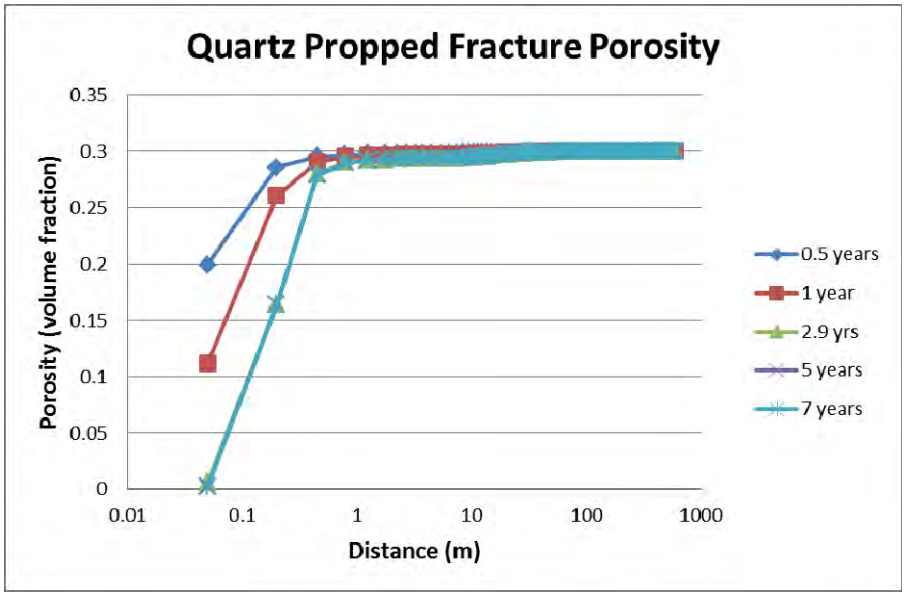

Fig. 5.1. Porosity along the flow path (quartz sand propped fracture) at t = 0.5 to 7 years. The initial porosity for the entire flow path (at t=0) is 30%.

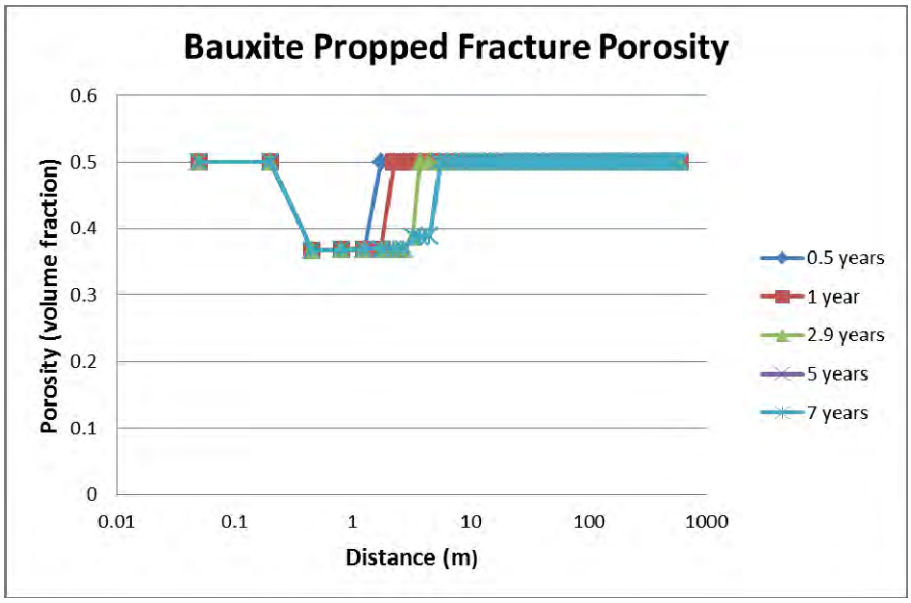

Fig. 5.2. Porosity along the flow path (sintered bauxite propped fracture) at t = 0.5 to 7 years. The initial porosity for the entire flow path (at t=0) is 50%.

Conclusions

It is possible that proppants will be: 1) chemically stable; 2) dissolve and reprecipitate; or 3) serve as nucleation sites in propped fractures under different chemical conditions. Fluid flow/reaction models (TOUGHREACT) predict that amorphous silica would precipitate in quartz sand propped fractures. These models also predict dissolution and reprecipitation of aluminum minerals from the bauxite proppant would occur when the porosity was high enough (50%) for a sufficient fluid flux to allow the hydration of corundum to diaspore. This predicted hydration reduced the fracture porosity by increasing the volume of the aluminum bearing mineral.

Future TOUGHREACT simulations should investigate the chemical stability of quartz and bauxite proppants under pH modified conditions, with different reservoir and injection temperatures, and with different injection fluid chemistries. These simulations,

along with future experiments, will allow better predictions of in-situ chemical stability of proppants in geothermal reservoirs.

Acknowledgements

This study is funded by the U.S. Department of Energy under grant DE-FG36-08GO18189.

References

Bethke, C.M., 2008. Geochemical and Biogeochemical Reaction Modeling, Cambridge University Press, 543 p.

Brinton, D., McLin, K., Moore, J., Jones, C., 2011. Effects of simulated geothermal conditions on proppants. Proceedings 36th Workshop on Geothermal Reservoir Engineering.

Cooke Jr., C.E., 1977. Fracturing with a high-strength proppant. Journal of Petroleum Technology, 1222-1226.

Hanold, R.J., 1982. Induced fractures: well simulation through fracturing. Los Alamos National Laboratories report LA-UR-82-1971.

Legarth, B., Tischner, T., Huenges, E., 2003. Simulation experiments in sedimentary, low-enthalpy reservoirs for geothermal power generation, Germany. Geothermics 32, 487-495.

McLin, K., Brinton, D., Mandalaparty, P., Jones, C., Moore, J., 2010. The chemical and thermal stability of proppants under geothermal conditions. Geothermal Resources Council Transactions 34.

McLin, K., Kovac, K., Moore, J., Adams, M., Xu, T., 2006. Modeling the geochemical effects of injection at Coso Geothermal Field, CA; Comparison with field observations. Proceedings 31st Workshop on Geothermal Reservoir Engineering.

Pruess, K., Oldenburg, C., Moridis, G., 1999. TOUGH2 user's guide, Version 2.0. Lawrence Berkeley Laboratory Report LBL-43134.

Palandri, J.L, Kharaka, Y.K., 2004. A compilation of rate parameters of water-mineral interaction kinetics for application to geochemical modeling. U.S. Geological Survey Open File Report 2004-1068.

Parkhurst, D.L., Appelo, C.A.J., 1999. User's guide to PHREEQC (Version2)—A computer program for speciation, batch-reaction, one-dimensional transport, and inverse geochemical calculations. U.S. Geological Survey Water-Resources Investigations Report 99-4259.

Verity, R.V., 1980. Planning and execution of Raft River stimulation treatments. Proceedings of the Geothermal Reservoir Well Stimulation Symposium 1980, 140-154.

Weaver, J., Rickman, R., Luo, H., 2009. Formation mineralogy, proppant characteristics drive conductivity. E&P, Hart Energy Publishing, http://www.epmag.com

Xu, T., Apps, J., Pruess, K., Yamamoto, H., 2007. Numerical modeling of injection and mineral trapping of CO_2 with H_2S and SO_2 in a sandstone formation. Chemical Geology 242, 319-346.

Xu, T., Pruess, K., 2004. Numerical simulation of injectivity effects of mineral scaling and clay swelling in a fractured geothermal reservoir. Geothermal Resources Council Transactions 28, 269-276.

Xu, T., Sonnenthal, E., Spycher, N., Pruess, K., 2004. TOUGHREACT user's guide: A simulation program for non-isothermal multiphase reactive geochemical transport in variably saturated geologic media. LBNL publication LBNL-55460.

Xu, T., Pruess, K., 2001 Modeling multiphase non-isothermal fluid flow and reactive geochemical transport in variably saturated fractured rocks: 1. Methodology. American Journal of Science 301, 16-33.

CHAPTER 6

EVALUATING FLUID-ROCK REACTIONS IN THE TALC ZONE OF THE ALTA CONTACT AUREOLE

Abstract

In the talc zone of the Alta stock outer aureole, the presence of talc does not define a regular isogradic surface parallel to the inner tremolite, forsterite, and periclase isograds. At a given distance from the stock, the distribution and abundance of talc in the outer Alta aureole is heterogeneous on several scales, and is in large part stratigraphically controlled, despite the ubiquitous presence of dolomite + quartz. The implication is that pore fluid $X(CO_2)$ may also have been heterogeneous as a function of stratigraphy at several scales. Possible explanations for these heterogeneities include: multiple, possibly non-contemporary, hydrothermal circulation cells, bedding-controlled variations in fluid flow and reaction progress, and fluid immiscibility. Understanding the P-T-X_{fl} stability of talc and fluid immiscibility in the CaO-MgO-SiO_2-H_2O-CO_2-$NaCl$ system is important for evaluating these alternative processes. Calculations using Perple_X 07 (Connolly, 1990) and the Mathematica based computer programs of Matthias Gottschalk (Personal communication, 2008) show that with increasing salinity, the stability field of talc is shifted to higher temperature and lower $X(CO_2)$. Phase equilibria were calculated for 400,

425, and 450°C and for pressures of 100, 125, 150, and 200 Mpa. These phase equilibria predict that under certain T, P, and Xfl conditions, an H_2O rich fluid that flows down-temperature (and possibly down-pressure) away from the Alta Stock can either remain miscible or become immiscible. For example, a down-T flowing fluid can stay single phase, as demonstrated by phase equilibria, for a decrease in temperature from 450 to 400°C and for a pressure decrease from 200 to 100 Mpa for certain starting fluid compositions. This single phase fluid may equilibrate with the observed sequence of mineral assemblages (tremolite + dolomite, talc + calcite and dolomite + quartz) in the outer aureole on a down-T and down-P path, depending on the composition of the fluid, pressure, and temperature. Other starting fluid compositions may be immiscible at 450°C and 200 Mpa, or they may be single phase and become immiscible with decreases in temperature and/or pressure from 450°C and 200 Mpa. These phase equilibria calculations show that the talc + calcite and fluid immiscibility fields intersect only at temperatures below 425°C and pressures below 125 MPa. The fluids that form when the parent fluid becomes immiscible may also become immiscible with further decrease in temperature and/or pressure. This could lead to the formation of several H_2O and CO_2-rich fluids. Future data collected from the Alta Aureole can be considered within these constraints in order to understand the formation of the talc zone.

Introduction

Although important, the formation of the outermost portions of contact aureoles remains understudied. Evaluating fluid-rock interactions in the outer portion of contact aureoles could provide insight into processes and reactions taking place in a wide variety

of shallow crustal environments, ranging from low-grade metamorphism to diagenesis in deep sedimentary basins. The low-grade systems developed in carbonate rocks are of particular interest because these systems record production, transport, and storage of CO_2 at time scales of 10^3-10^5 years (Bowman et al., 1994; Cook et al., 1997; Cook and Bowman, 2000; Pollington et al., 2005). The outer portion of the Alta Aureole provides an opportunity to study the onset of metamorphism, particularly the parameters controlling the onset of metamorphism, which are not well understood. The talc zone of the Alta Stock thermal aureole is a system where the geology and exposures allow observations on the outer aureole and its transition into country rocks. In addition, the impact of NaCl-bearing fluids on fluid immiscibility in lower temperature metamorphic environments is potentially important (Sisson et al., 1981; Trommsdorff and Skippen, 1987; Heinrich et al., 2004) but has also been understudied. Development of computer codes, such as the Mathematica based program of Matthias Gottschalk (Personal communication, 2008), allows the quantitative evaluation of phase equilibria, including fluid immiscibility, within the CaO-MgO-SiO_2-H_2O-CO_2-$NaCl$ system down to T=400^oC and P=50 Mpa.

Geologic Setting and Metamorphism in the Alta Aureole

The Alta Stock is a mid-Tertiary age granodiorite pluton in the central Wasatch Range of Utah (Crittenden et al., 1973). Precambrian and Paleozoic sedimentary rocks were intruded and contact metamorphosed by the stock (Moore and Kerrick, 1976; Cook and Bowman, 2000). These rocks consist mainly of quartzite and carbonates with a single

pelitic unit separating the quartzites from the overlying carbonate section. The carbonate units are principally dolostone, and many of these units contain chert nodules.

The contact aureole is defined by several isograds defining a prograde sequence of talc, tremolite, forsterite, clinohumite, and periclase zones that formed during reactions of rocks with H_2O-rich fluids (Moore and Kerrick, 1976) (Fig. 6.1). Metamorphism extends up to about 2 km from the intrusive contact in the southern portion of the aureole (Cook and Bowman 2000). Thermal conditions, reaction progress, and fluid infiltration in the inner aureole (periclase, forsterite zones) have been well documented in a series of previous studies (Bowman et al., 1994; Cook and Bowman, 1994; Cook et al., 1997; Cook and Bowman, 2000). The estimated lithostatic pressure during the emplacement of the Alta Stock, based on stratigraphic measurements and mineral assemblages, is between 100 to 200 Mpa (Wilson, 1961; Cook and Bowman, 1994). Temperatures during contact metamorphism from application of calcite-dolomite geothermometry are >570^{o}C for the periclase zone, 490-570^{o}C for the forsterite zone, and 400-450^{o}C for the tremolite zone (Cook and Bowman, 1994). Cook and Bowman (2000) measured reaction progress and spatial patterns of $^{18}O/^{16}O$ depletion in carbonates. These results provide evidence for the development of the inner aureole (periclase and forsterite zones) by infiltration and sub-horizontal flow of large fluxes (~3000 m^3/m^2) of H_2O-rich fluids down-temperature and laterally away from the igneous contact.

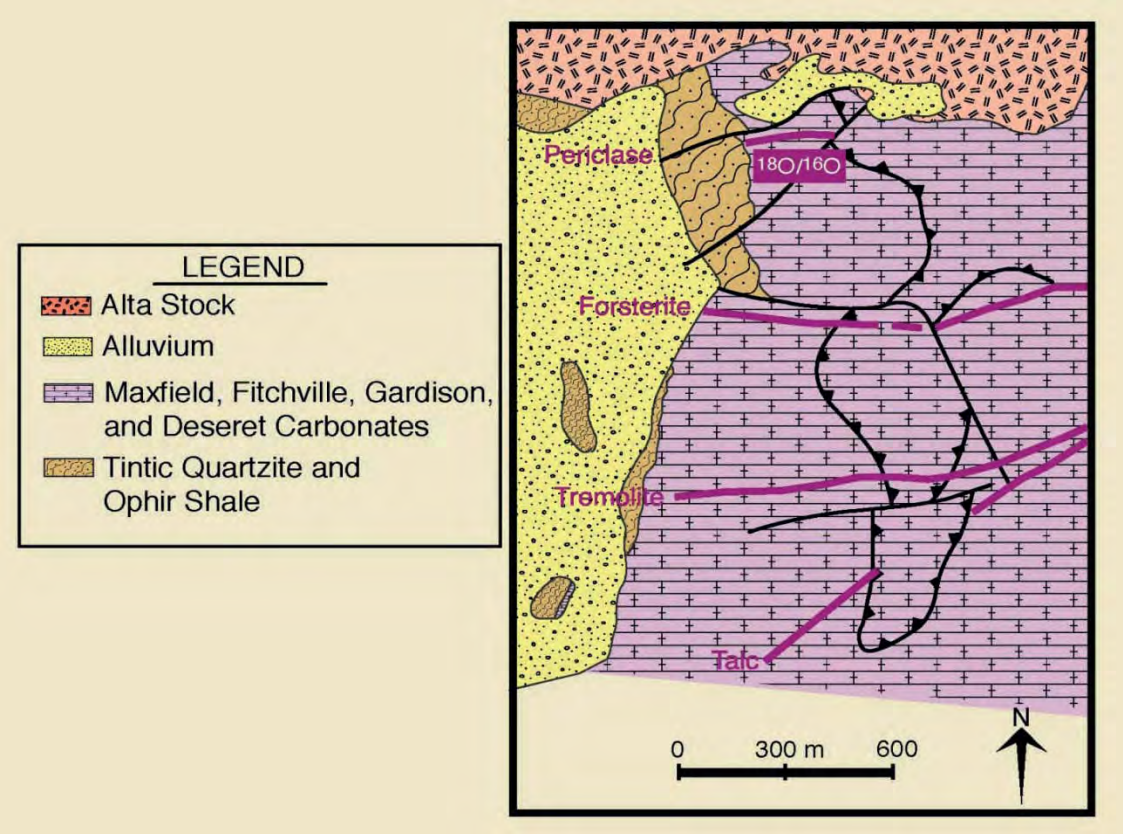

Fig. 6.1. Map of the southern portion of the Alta Stock and thermal aureole modified by J. Bowman from Moore and Kerrick, (1976), showing the location of the periclase, forsterite, tremolite, and talc isograds. Although the periclase, forsterite, and tremolite isograds approximately parallel the boundary of the stock, the talc isograd does not. The band labeled $^{18}O/^{16}O$ denotes the location of the transition between the $^{18}O/^{16}O$-depleted marbles of the inner aureole and the undepleted marbles and dolostone protoliths of the outer aureole.

Previous studies (Bowman et al., 2004; Pollington et al., 2005; Bowman, unpublished results) have shown that the distribution and abundance of talc in the outer Alta aureole (Fig. 6.2) is heterogeneous at several scales and is not controlled by variation in the bulk composition of the rock. Where present, talc + calcite forms a reaction rim surrounding chert nodules in the nodular dolomite (Cook and Bowman, 2000). This reaction rim separates the nodule from the surrounding dolomite matrix. At any given location, the exposed strata in the talc zone (Fig. 6.3) alternate between talc-bearing and talc-absent compositions (both containing chert nodules), and the talc-bearing and talc-absent strata are in direct contact (Figs. 6.4 and 6.5). Hence, the presence of talc does not define a regular isogradic surface, in contrast with the tremolite, forsterite, and periclase isograds in the inner aureole (Fig. 6.1). At a number of locations, the talc-bearing strata have a greater density and frequency of veins than the talc-absent strata (Fig. 6.5). Figs. 6.6, 6.7, and 6.8 show scanning electron microscope (SEM) images of the talc in the reaction rim of a sample taken from site 1 (see Fig. 6.2). The talc is generally fibrous, with few flattened tabular crystals, and fine grained (generally < 100 μm long). Dolomite and calcite are both found in contact with talc crystals.

At Alta, previous isotope analyses presented by Pollington et al., (2005) and unpublished data from John Bowman at the University of Utah show that the $\delta^{18}O$ values of calcite in talc reaction rims around chert nodules are much lower than the $\delta^{18}O$ values of the matrix dolomite, and thus are out of equilibrium with matrix dolomite. These analyses also indicate that the $\delta^{18}O$ values of a small suite of chert nodules (n=6) range from 8.2 to 24 permil and are also out of exchange equilibrium with the matrix dolomite. The results from Pollington et al. (2005) are shown in Table 6.1.

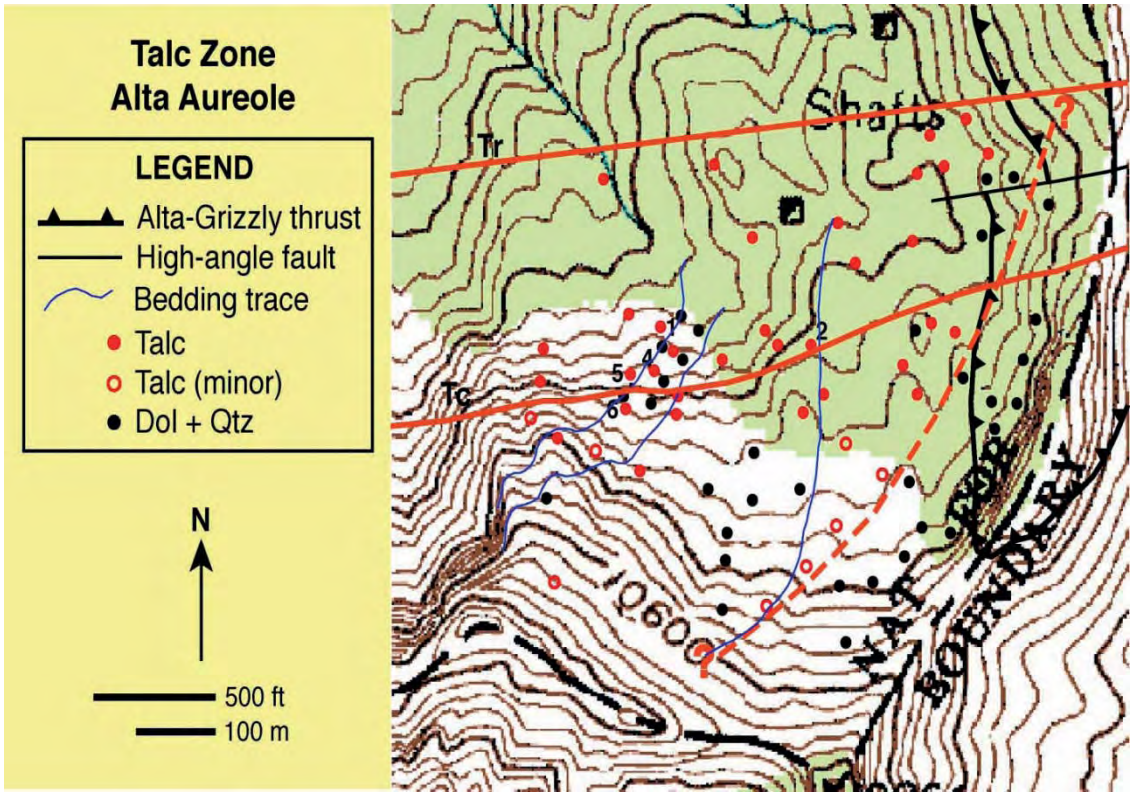

Fig. 6.2. Map of the talc zone showing the heterogeneity of the distribution of talc within the outer portion of the Alta Aureole (J. Bowman, personal communication).

Fig. 6.3. Exposed strata in the talc zone at Alta. Talc-bearing (t) and talc-absent (n) strata alternate in this area. The numbers (1, 4, and 6) represent sites where samples were taken and observations were made for previous and ongoing studies. (Photo: J. Bowman)

Fig. 6.4: Exposed strata in the talc zone at Alta at site 4 (shown in Fig. 6.3). The bracketed section shows a layer where talc is present (note the whiter color) between overlying and underlying, talc-absent layers. Note that the talc-bearing horizon is stratigraphically concordant within the outcrop. (Photo: J. Bowman)

Fig. 6.5. Vein and nodule distribution in talc-bearing (right) strata in direct contact with overlying, talc-absent strata (left) in the outer portion of the Alta Aureole.

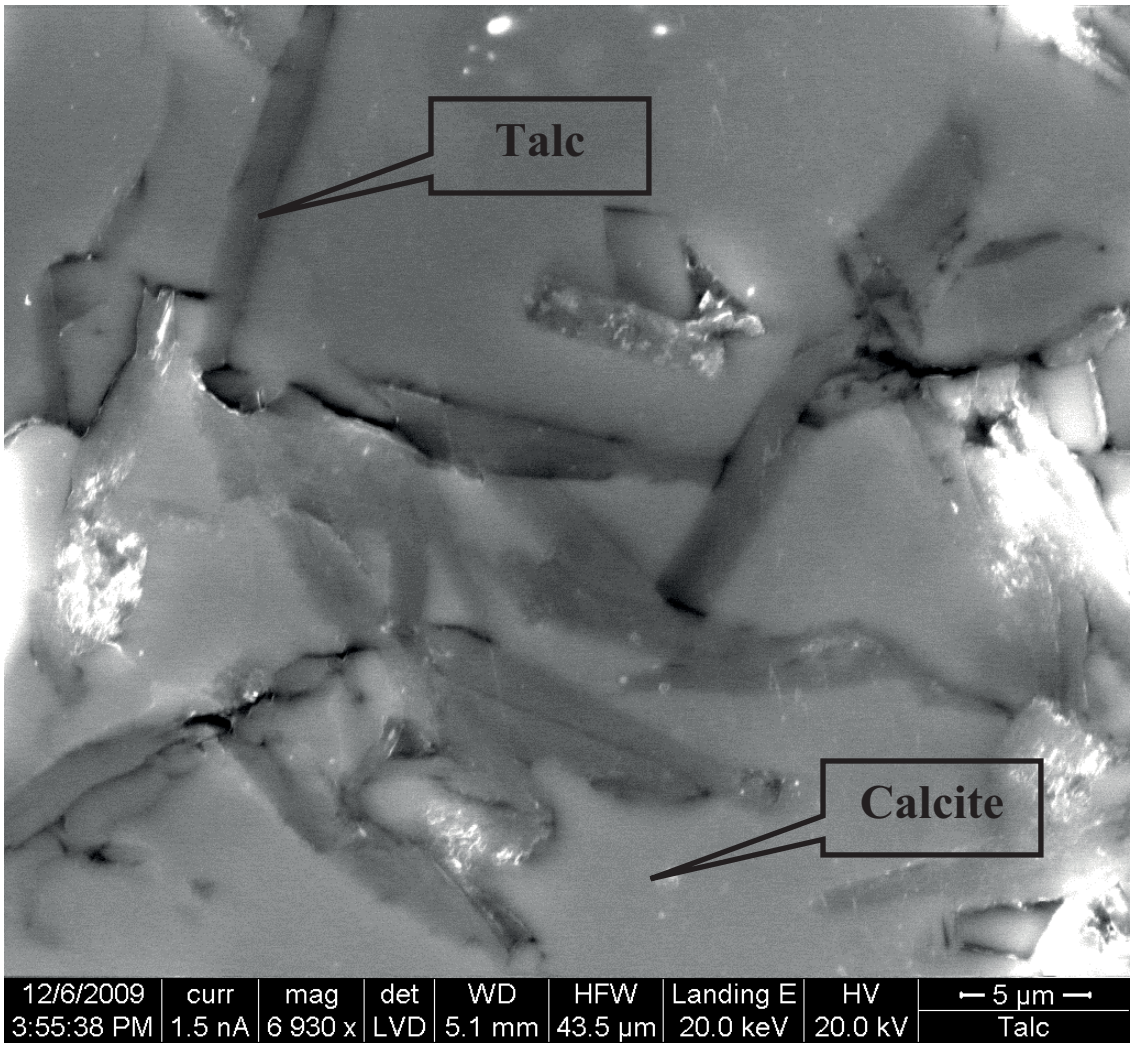

Fig. 6.6. SEM image of a sample taken from talc-bearing strata at site 1 (see Fig. 6.3). Talc crystals appear darker within the matrix.

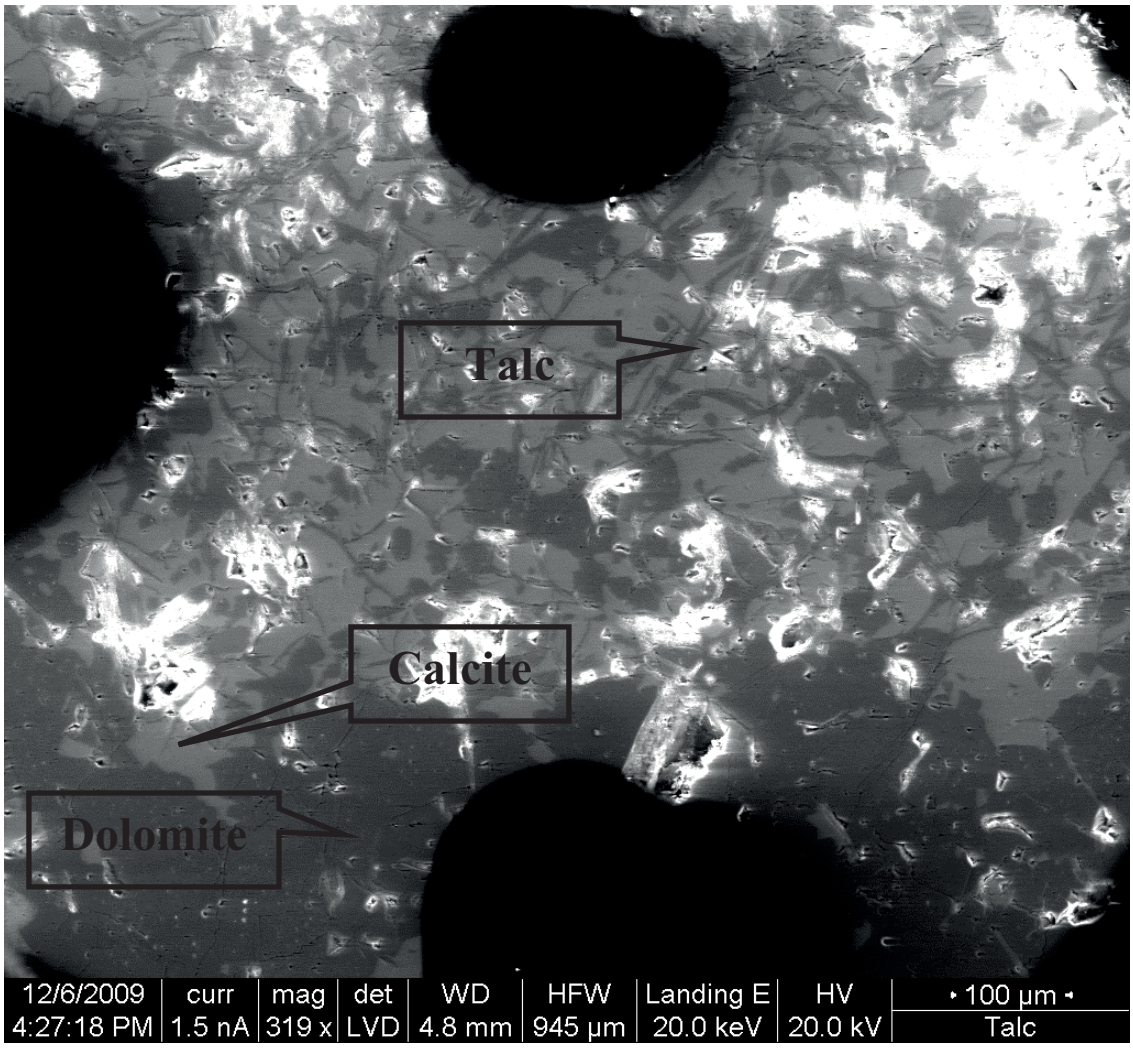

Fig. 6.7. SEM image of sample taken from talc-bearing strata at site 1 (see Fig. 6.3) showing fibrous talc forming in the reaction front between a chert nodule and dolomite matrix.

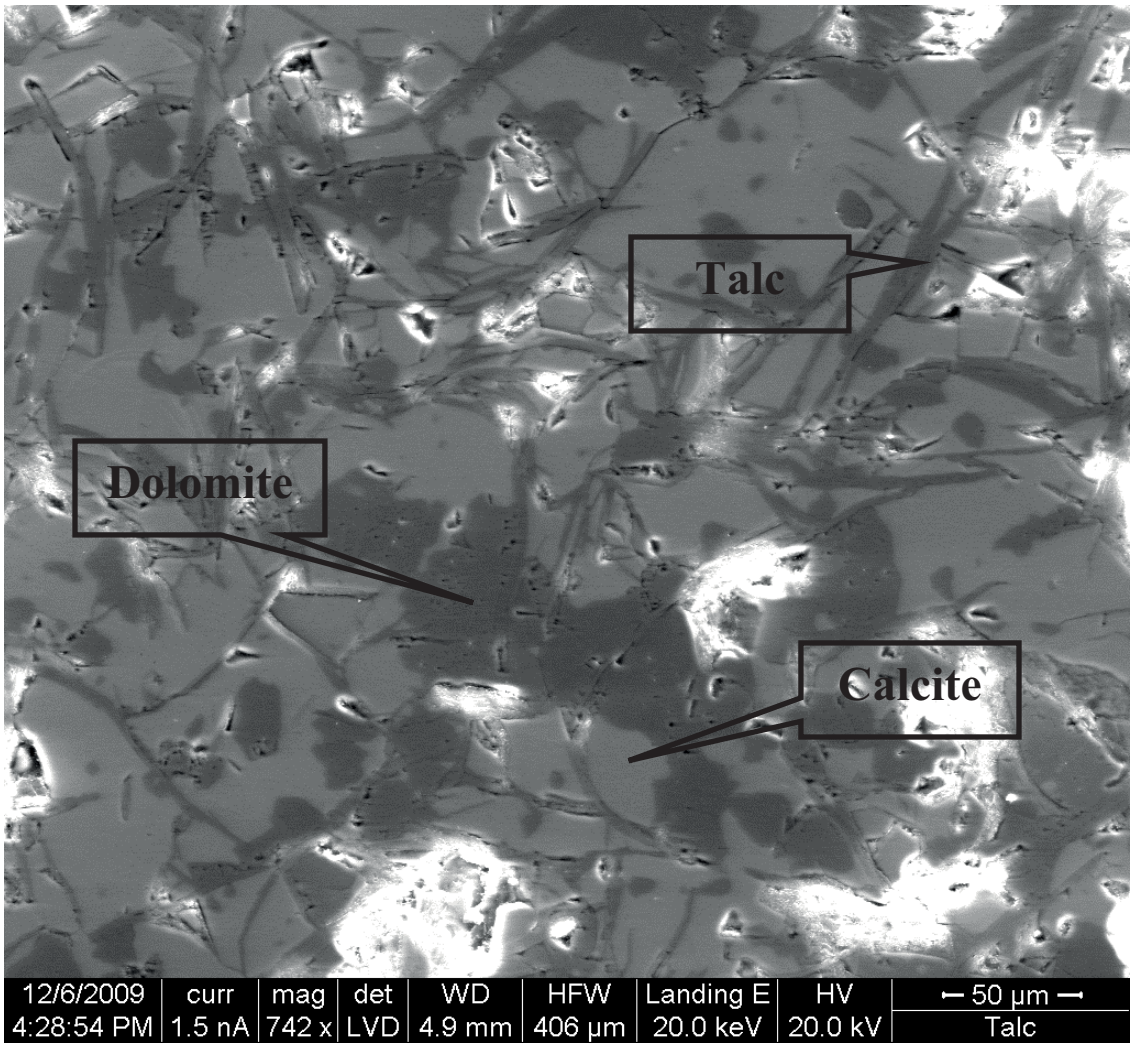

Fig. 6.8. Close-up of a portion of Fig. 6.7, SEM image showing distribution of fibrous talc and textural relationship to calcite and dolomite.

Table 6.1

Stable Isotope Analysis

$\delta^{18}O$ values of reaction rim calcite and matrix dolomite from 5 samples (Pollington et al. 2005).

Sample	Dolomite	Calcite
1-1	27.76	19.60
1-2b	28.50	19.20
1-2c	27.30	19.80
2-1a	27.46	13.36
	14.30	
2-3c	26.53	13.38
	28.74	

Fluid inclusions in skarn minerals from the inner aureole were previously investigated to determine the NaCl content of fluids that formed the skarns and inner aureole mineral zones. Cook (1982) reported that early stage inclusions from contact skarns in the Alta aureole were highly saline (31.7 to 43.0 wt% NaCl), while later stage inclusions exhibit lower salinities (1.9 to 10.4 wt% NaCl). Kemp (1985) suggested the possibility of entrapment of a two phase fluid based on fluid inclusion data gathered from additional Al(Fe)-Ca-Mg-Si contact skarns along the margins of the Alta Stock. The early stage fluids documented by Cook (1982) may then represent the high-density saline liquid phase resulting from fluid immiscibility.

Scenarios for the Development of the Outer Alta Aureole

The heterogeneous distribution of talc in the outer aureole indicates spatial heterogeneity in the $X(CO_2)$ values of pore fluids at several scales that are not related to the distance from the igneous contact. This implies that heterogeneities in pore fluid composition are more important than temperature and bulk composition in determining the distribution of talc in the outer aureole. The processes and mechanisms responsible for these heterogeneities may be fundamentally different from those controlling fluid compositions and mineral reactions in the inner aureoles of contact metamorphic systems (Baumgartner and Ferry, 1991; Ferry, 1994; Ferry et al., 2002) including the inner Alta Aureole (Cook and Bowman, 2000; Cook et al., 1997; Bowman et al., 2009).

Three possible scenarios for the formation of the talc zone can explain the observed spatial heterogeneity in the talc occurrences and resulting spatial heterogeneity in fluid composition. At least one of these scenarios considers the possibility that the outer Alta aureole did not form contemporaneously with the inner aureole, nor from the same hydrothermal system.

Scenario 1: The first scenario is a single hydrothermal circulation cell. In this scenario, the talc zone forms as part of the same down-temperature flow system responsible for the development of the inner aureole. The variations in $X(CO_2)$ values of fluids entering the talc zone would result from variations in the extent of decarbonation reaction progress at higher metamorphic grades and/or variations in the flux of H_2O rich fluids. Fluids in this system are considered compositionally heterogeneous but single phase.

Scenario 2: A second scenario is the existence of multiple hydrothermal circulation cells within the outer aureole. Stratigraphic layer controlled variations in permeability within the talc zone would allow the preferential influx of H_2O-rich fluids flowing toward the igneous contact (e.g., up-temperature flow) into higher-permeability (e.g., talc-bearing) zones. This up-temperature flowing system could either coexist with the down-temperature flowing cell responsible for the inner aureole or operate later in time. The down-temperature flowing fluids would have higher values of $X(CO_2)$ as a result of the contribution of CO_2 from higher grade decarbonation reactions operating in the inner aureole. High $X(CO_2)$ would favor the persistence of dolomite + quartz over the formation of talc. However, talc could form in stratigraphic layers preferentially infiltrated by these up-temperature flowing H_2O rich fluids.

Scenario 3: The third scenario, and most complex, is a single circulation cell in which fluid immiscibility occurs. In this scenario, two fluids, one H_2O-rich, the other CO_2-rich, are generated by fluid immiscibility as CO_2-bearing fluids from the inner aureole flow outward from the igneous contact, cool, and/or decrease in fluid pressure (down-temperature flow). The separation and/or differential flow of these phases could be responsible for the heterogeneity in the talc distribution.

To test the possible scenarios for the formation of the talc zone at Alta, it is necessary to have a quantitative understanding of talc stability and fluid immiscibility at the predicted P-T-X_{fl} conditions in the outer portion of the Alta Aureole.

Fluid Immiscibility

Fluid immiscibility in the H_2O-CO_2-NaCl system has been documented at metamorphic pressures and temperatures in a number of fluid inclusion studies (e.g. Sisson et al., 1981; Trommsdorff et al., 1985; Heinrich and Gottschalk, 1994; Fernandez-Caliani et al., 1996). To calculate the effects of immiscible fluids on the mineral reactions in metamorphic rocks, Bowers and Helgeson (1983a, b) developed a modified Redlich-Kwong (MRK) equation of state to predict the fugacities of H_2O and CO_2 as well as fluid immiscibility fields. They showed that the stability field of talc is affected by the NaCl content of the fluid. The talc stability field moves to higher H_2O/CO_2 with increasing NaCl and can intersect the field of fluid immiscibility when NaCl is present. This equation of state, however, cannot accurately predict fugacities near solvus boundaries and at moderate to high salinities (Duan et al., 1995; Heinrich et al., 2004). The equation of state for the H_2O-CO_2-NaCl system introduced by Duan et al. (1995) calculates activities of fluids in good agreement with experimental results for fluids with up to 30 wt% NaCl and with less accuracy for fluids with up to 50 wt% NaCl. This equation of state was used by Heinrich et al. (2004) to predict the influence of fluid immiscibility on phase relations and reaction progress in metamorphosed rocks in the CaO-MgO-SiO_2-H_2O-CO_2-NaCl system.

Modeling Approach

Previous studies have examined phase equilibria in the CaO-MgO-SiO_2-H_2O-CO_2-NaCl system (eg. Bowers and Helgeson, 1983b; Labotka, 1991; Heinrich et al., 2004; Heinrich, 2007), but this study focuses more intently on the stability field of talc at

the conditions predicted for the outer portion of the Alta Aureole. To calculate talc stability in the H_2O-CO_2-NaCl system and determine the influence of fluid immiscibility on the talc stability field, both Perple_X (Connolly, 1990) and a Mathematica based phase equilibrium calculation program, written and provided by Matthias Gottschalk of GeoForschungsZentrum, were used. Both programs calculate phase equilibria by minimizing Gibbs' free energy.

With Perple_X, phase equilibria were calculated using the unpublished H_2O-CO_2-NaCl equation of Aranovich and Haefner and several databases available within the program, including the Holland and Powell (1991) and the Gottschalk (1997) databases. The equation of Aranovich and Haefner was based on experimental data and does not calculate fluid immiscibility.

The Mathematica based program of Gottschalk implements a corrected version of the Duan et al. (1995) equation of state for the H_2O-CO_2-NaCl system (Gottschalk 2007) and an internally consistent thermodynamic database for solids (Gottschalk 1997). Using this program, both mineral stability and fluid immiscibility fields can be calculated as a function of P-T-X_{fl}. The program should not be used to calculate phase equilibria for temperatures below 400^{o}C and pressures below 50 Mpa (Matthias Gottschalk, personal communication, 2008).

The starting rock composition for the models consists of dolomite and quartz in a molar ratio of 4:3, the stoichiometry of these minerals in the talc-forming reaction:

$$4Dol + 3Qz + H_2O = Tc + 3Cc + 3CO_2 \qquad (6.1)$$

These calculations were made for temperatures of 400, 425, and 450°C and for pressures of 100, 125, 150, and 200 Mpa.

Results

There are many ways to illustrate the calculated mineral stability and fluid immiscibility fields in the H_2O-CO_2-NaCl system. Isobaric T-X(CO_2) pseudo-sections are typically presented when discussing phase equilibria in metamorphic systems such as Alta (e.g. Bowers and Helgeson, 1983b; Cook et al., 1997; Heinrich, 2007). Phase stabilities were calculated with Perple_X for 300-700°C at 200 Mpa using the thermodynamic database of Gottschalk (1997) and the unpublished equation of state of Aranovitch and Haefner for the H_2O-CO_2-NaCl system. These stability fields were plotted as a T-X(CO_2) pseudo-section to examine the effects of NaCl on the stability fields of talc, tremolite, and forsterite (Figs. 6.9 and 6.10). Salinities of 0, 10, and 20 wt% were used to calculate the stability fields shown. The inset in Fig. 6.9 is enlarged and presented as Fig. 6.10. With increasing salinity, the talc stability field moves to higher H_2O/CO_2 and higher temperatures at constant pressure. Invariant points I, II, and III (Fig. 6.9) also shift to higher H_2O/CO_2 and higher temperature with increasing salinity. Fluid immiscibility cannot be calculated in Perple_X, so no information on the intersection of the fluid immiscibility field with the talc stability field was obtained. As shown in Figs. 6.9 and 6.10, talc can be stable at higher temperatures with increased salinity of the fluid. The stability field of talc also narrows and moves to higher H_2O/CO_2 with increasing NaCl.

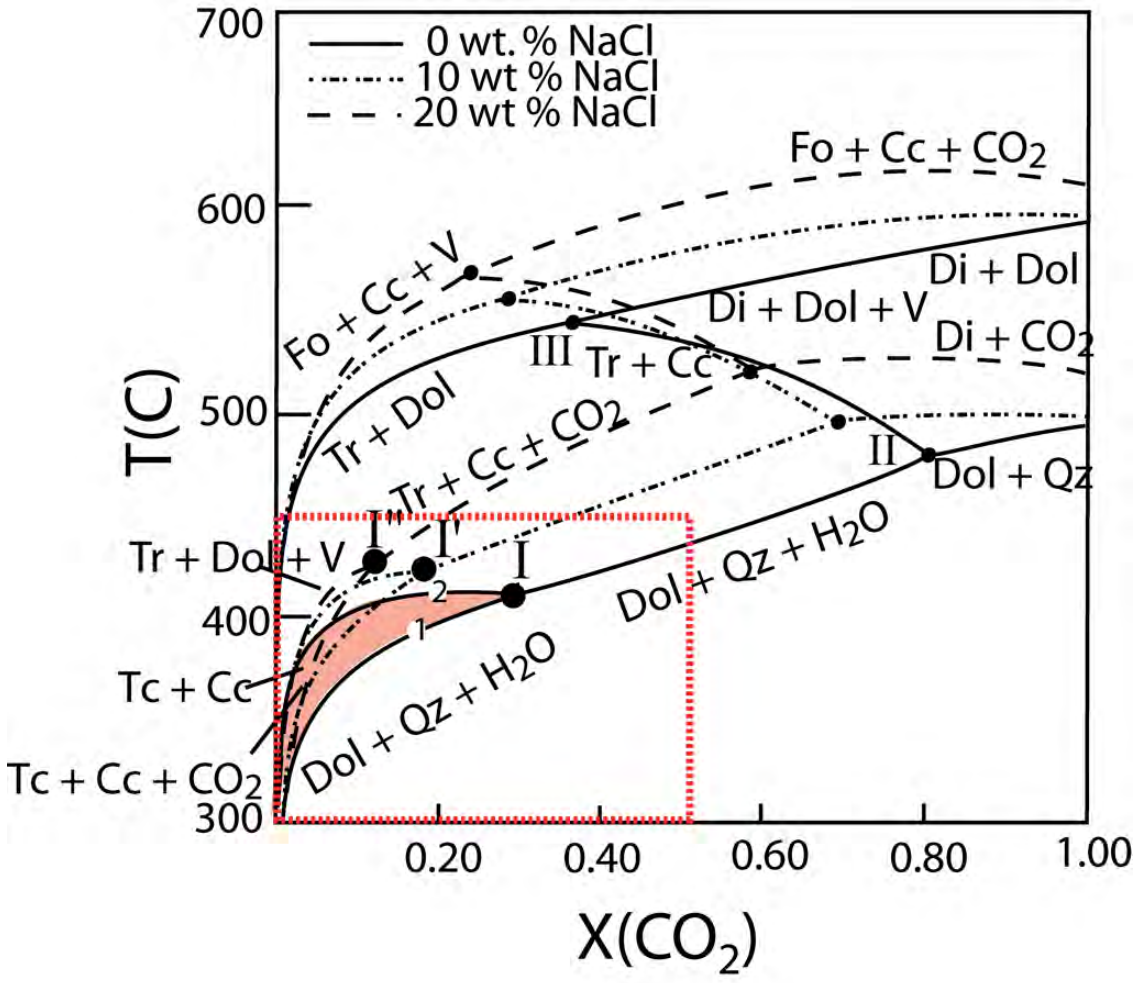

Fig. 6.9. T-X(CO_2) pseudo-section showing the mineral stability fields and the location of invariant points I, II, and III for 0, 10, and 20 wt% NaCl. The talc stability field for a 0 wt% salinity fluid is highlighted in orange. With progressively higher salinity, invariant point I moves to I' and I" which are higher temperature and lower X(CO_2). Inset is enlarged and presented in Fig. 6.10.

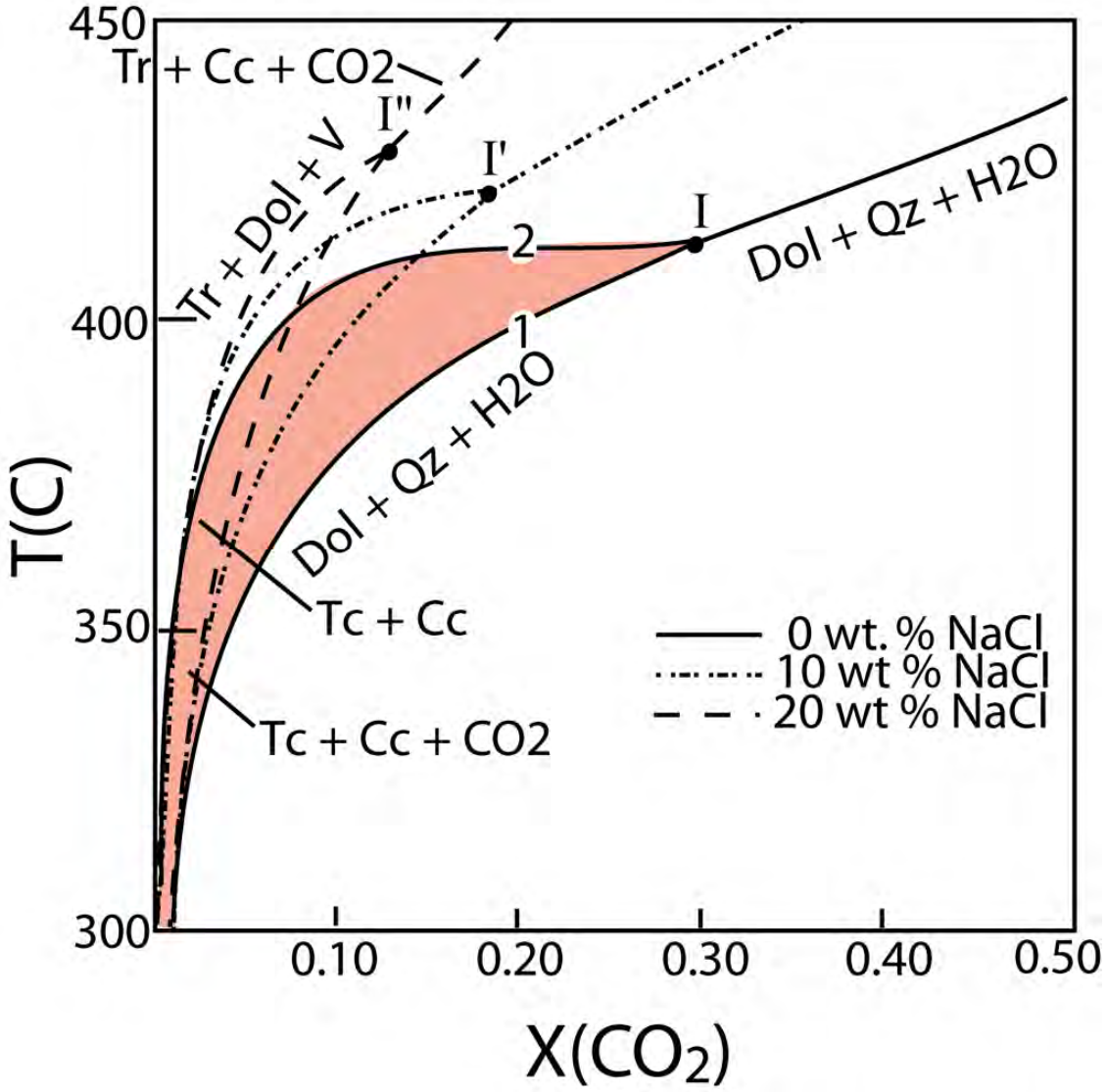

Fig. 6.10. Inset from Fig. 6.9 showing the effect of salinity on the talc stability field (pink) and the invariant point I.

Although calculations of phase equilibria made with Gottschalk's program could also be presented as T-X(CO_2) pseudo-sections, it is useful to present the phase equilibria as isobaric, isothermal H_2O-CO_2-NaCl ternary plots (eg. Tromsdorff and Skippen, 1987; Heinrich et al., 2004). This presentation allows the full range of X_{fl} to be represented in each plot and better illustrates the phase equilibria in the H_2O-CO_2-NaCl system. The stability fields are constructed from over 500 data points for each ternary plot. Calculations were concentrated in the high H_2O portion of the diagram. The mineral stability, two fluid, two fluid plus halite, and one fluid plus halite fields were drawn in the ternary plot for each of the twelve pressure and temperature combinations examined and are presented in Figs. 6.11-13. The components are plotted as mol%.

As shown in Figs. 6.11-13, the shapes and locations of both the talc stability (Tc + Cc + Dol) and the fluid immiscibility (L + V) fields are affected by T, P, and X_{fl} at the temperatures and pressures investigated. The range of the talc stability field expands with respect to H_2O/CO_2 with decreasing temperature, decreasing salinity, and in some cases (T=400^oC, Fig. 6.11) with an isothermal decrease in pressure. Increased salinity moves the talc stability field to higher H_2O/CO_2 and with a narrower range of H_2O/CO_2. Decreasing pressure from 200 Mpa in the 400^oC and 425^oC cases brings the talc stability field closer to the fluid immiscibility field, especially at lower (but non-zero) salinities. The fluid immiscibility field also changes shape with different pressures and temperatures. Talc stability and fluid immiscibility fields intersect only at 400^oC and 100 Mpa (Fig. 6.11). Fluid immiscibility and tremolite stability (Tr + Cc + Dol) fields also intersect at T=425^oC and P=100 and 125 Mpa and T=450^oC and P=100, 125, and 150 Mpa (Figs. 6.11-13). At T=400^oC and P=125, 150, and 200 Mpa, T=425^oC and P=150

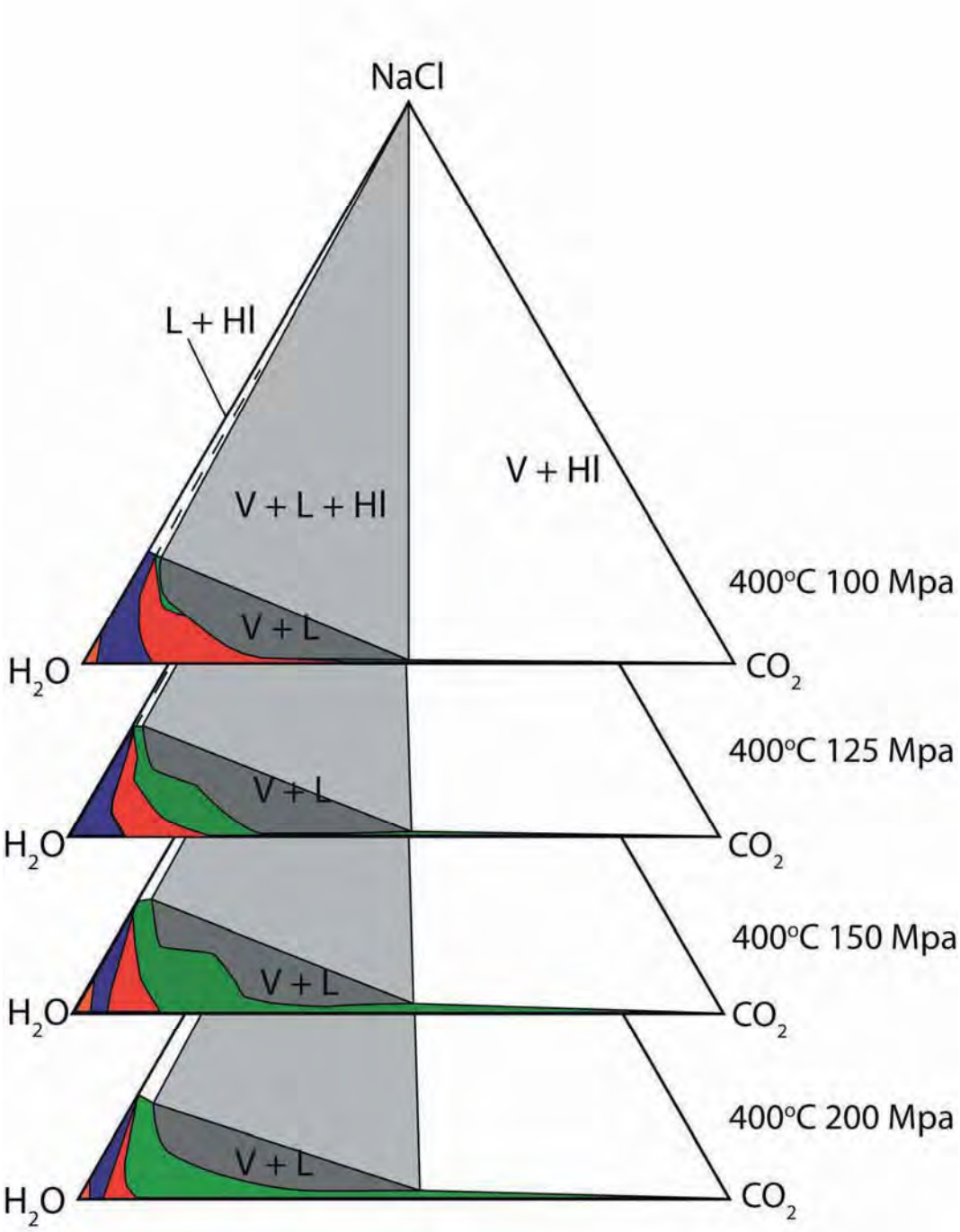

Fig. 6.11. H_2O-CO_2-NaCl plots for 400°C and 100-200 Mpa. The stability field for Antigorite + Tremolite + Calcite (Atg + Tr + Cc) is shown in orange, for Tremolite + Dolomite + Calcite (Tr + Cc + Dol) in blue, for Talc + Calcite + Dolomite (Tc + Cc + Dol) in red, and for Quartz + Dolomite (Qz + Dol) in green. The two phase fluid immiscibility field is shown as V + L (L is H_2O-rich fluid, and V is CO_2-rich fluid). Halite (Hl) is observed in L + Hl, V + Hl, and V + L + Hl fields. The V + L field only intersects the Tc + Cc + Dol field at 400°C and 100 Mpa.

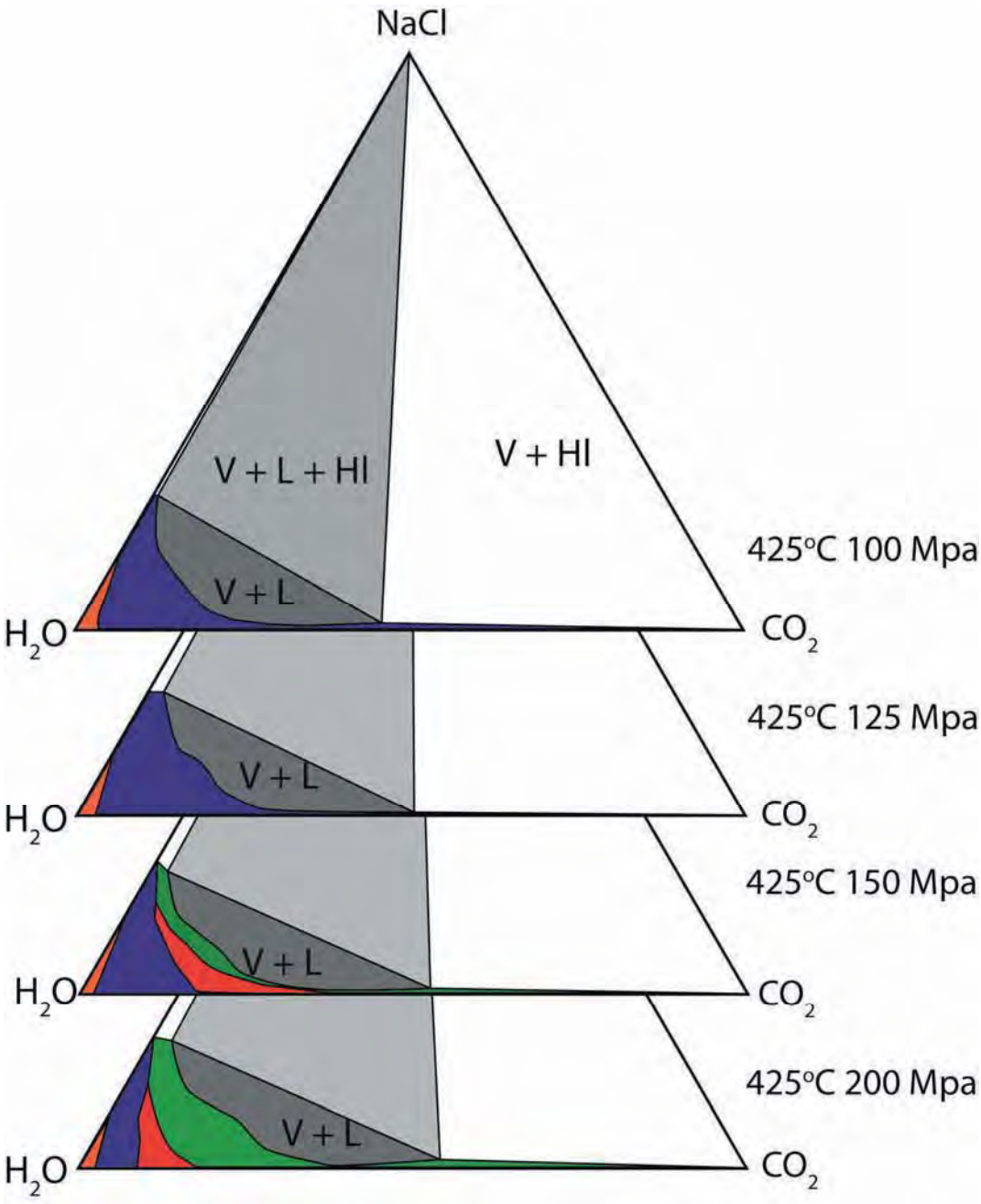

Fig. 6.12. H_2O-CO_2-NaCl plots for 425°C and 100-200 Mpa. The stability field for Antigorite + Tremolite + Calcite (Atg + Tr + Cc) is shown in orange, for Tremolite + Dolomite + Calcite (Tr + Cc + Dol) in blue, for Talc + Calcite + Dolomite (Tc + Cc + Dol) in red, and for Quartz + Dolomite (Qz + Dol) in green. The two phase fluid immiscibility field is shown as V + L (L is H_2O-rich fluid, and V is CO_2-rich fluid). Halite (Hl) is observed in L + Hl, V + Hl, and V + L + Hl fields.

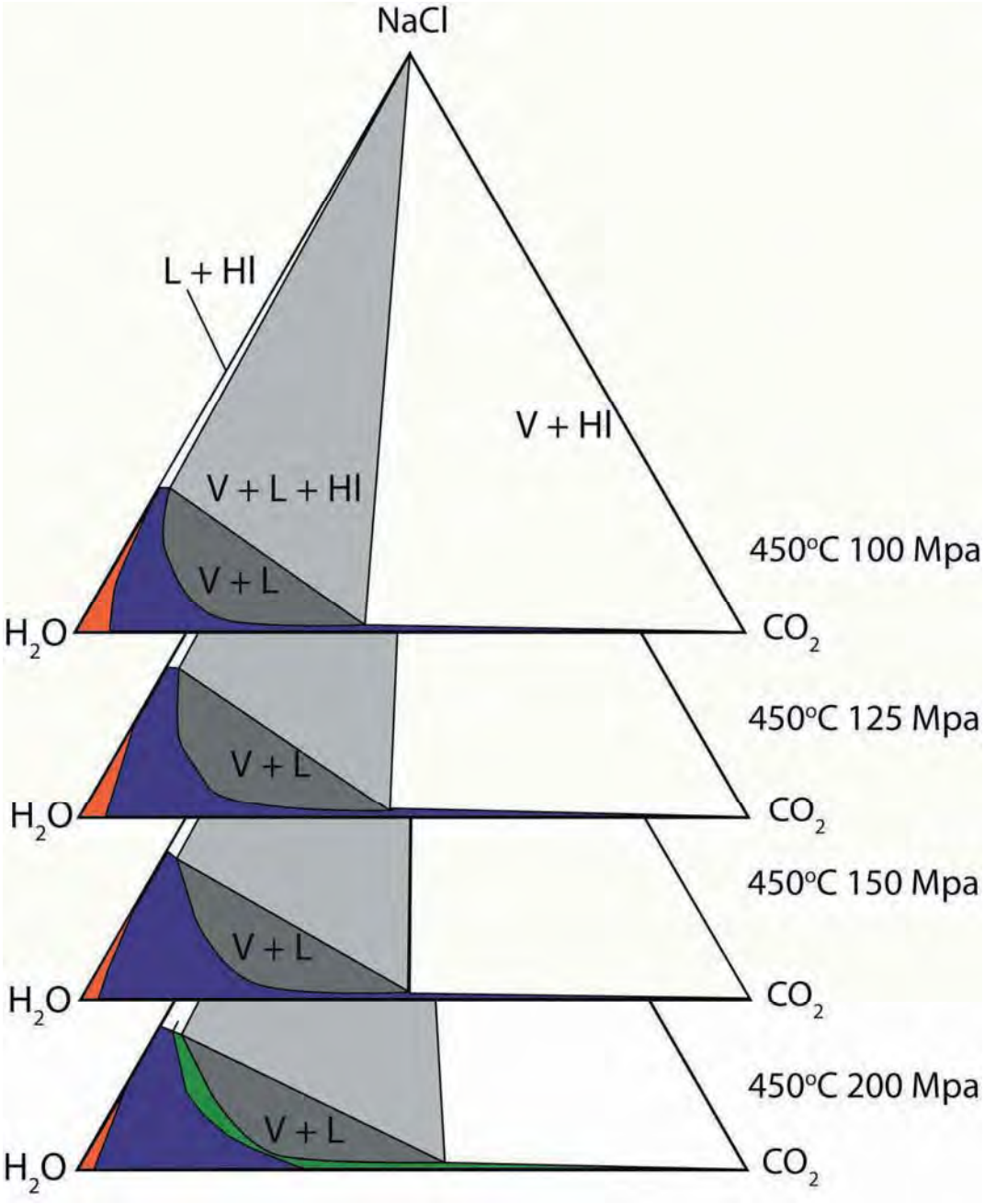

Fig. 6.13. H_2O-CO_2-NaCl plots for 450°C and 100-200 Mpa. The stability field for Antigorite + Tremolite + Calcite (Atg + Tr + Cc) is shown in orange, for Tremolite + Dolomite + Calcite (Tr + Cc + Dol) in blue, for Talc + Calcite + Dolomite (Tc + Cc + Dol) in red, and for Quartz + Dolomite (Qz + Dol) in green. The two phase fluid immiscibility field is shown as V + L (L is H_2O-rich fluid, and V is CO_2-rich fluid). Halite (Hl) is observed in L + Hl, V + Hl, and V + L + Hl fields.

and 200 Mpa, and T=450°C and P=200 Mpa, only the stability field of quartz and dolomite (Qz + Dol) is intersected by fluid immiscibility (Figs. 6.11-13).

Discussion: Fluid Evolution

The phase equilibria calculated in this study provide insight into the feasibility of the three scenarios presented as possible explanations for the formation of talc in the outer aureole at Alta. All three scenarios include a down-temperature component of fluid flow, and these phase equilibria can be used to address the evolution of the fluid as it flows down temperature away from the intrusion. Periclase formation at Alta is restricted to very H_2O rich fluids as determined by phase equilibria and calcite-dolomite geothermometry (Cook and Bowman, 2000). Because there is evidence that this fluid is H_2O rich in the periclase zone in the inner aureole, only the evolution of a down-temperature flowing, initially H_2O-rich fluid will be considered. Fluid inclusions in skarn minerals adjacent to the contact exhibit highly variable salinities, requiring that the evolution of fluids of varying salinities be considered. The $X(CO_2)$ of the fluid will be dependent on the extent of decarbonation reactions as the periclase, forsterite, and tremolite reaction fronts progress, as well as the flux of H_2O-rich fluids flowing into the system. Either the fluid will remain single phase, or it will become immiscible at some point along the flow path, depending on the T, P, and X_{fl} conditions. Talc is not stable in the evaluated temperature and pressure ranges for salinities above 25 mol% (Figs. 6.11-12), so only salinities below this threshold are examined here. In the following cases, the conditions required for single phase or immiscible fluid evolution from a lower salinity (X(NaCl)=2.5 mol%) H_2O-rich parent fluid and a higher salinity (X(NaCl)=15 mol%)

H_2O rich parent fluid are evaluated. All observations for each case are based on the data in Figs. 6.11-13. The fluid evolution in each case is illustrated in condensed versions of these plots in Figs. 6.14-19. Although the stability fields are not all specifically labeled in Figs. 6.14-19 for simplicity, the color scheme is the same as for Figs. 6.11-13 (for Antigorite + Tremolite + Calcite (Ant + Tr + Cc) the stability field is shown in orange; for Tremolite + Dolomite + Calcite (Tr + Cc + Dol) in blue; for Talc + Calcite + Dolomite (Tc + Cc + Dol) in red; and for Quartz + Dolomite (Qz + Dol) in green). Two lines at constant X(NaCl) are shown in the phase equilibria in Figs. 6.14-19. The lower line represents X(NaCl)=2.5 mol%, and the upper line represents X(NaCl)=15 mol%. The blue circle represents a starting fluid composition on the X(NaCl)=15 mol% line, and the yellow circle represents a starting fluid composition on the X(NaCl)=2.5 mol% line in Figs. 6.14-21. When the blue circle or yellow circle lies within a fluid immiscibility field, the parent fluid will separate into two separate, compositionally distinct fluids: the white circle represents the H_2O-rich fluid, and the pink circle represents the CO_2-rich fluid in Figs. 6.19-21.

Down-Temperature Flow of a Single Phase Fluid

In this scenario, H_2O-rich fluid flows down temperature and possibly down-pressure away from the Alta Stock and remains single phase. Fig. 6.14 illustrates two example fluid compositions that will remain single phase. As shown in Fig. 6.14, these single phase fluid compositions will equilibrate with a variety of mineral stability fields as temperature and/or pressure decrease, depending on the initial temperature and pressure of the fluid. For example, a single phase fluid with the higher salinity

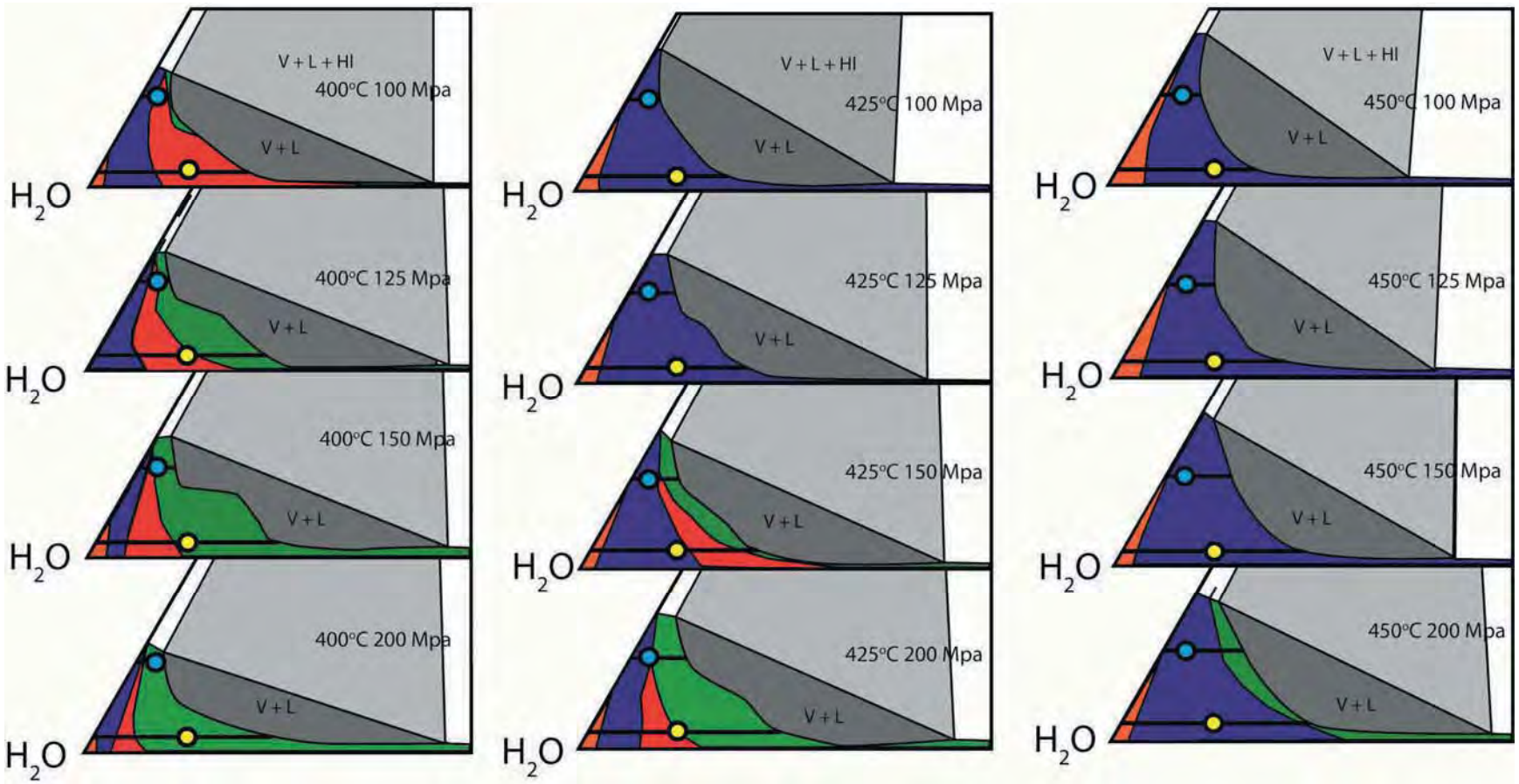

Fig. 6.14. Abbreviated H_2O-CO_2-NaCl plots for T=400-450°C and P=100-200 Mpa. Two lines at X(NaCl)=15 and 2.5 mol% are shown; the blue and the yellow circles represent starting fluids with these X(NaCl) values, respectively, as discussed in the text. As shown, these fluids can remain single phase with decreases in either or both temperature and pressure from 450°C and 200 Mpa, respectively. These decreases in temperature and/or pressure can result in fluids of constant X_{fl} equilibrating with different mineral assemblages.

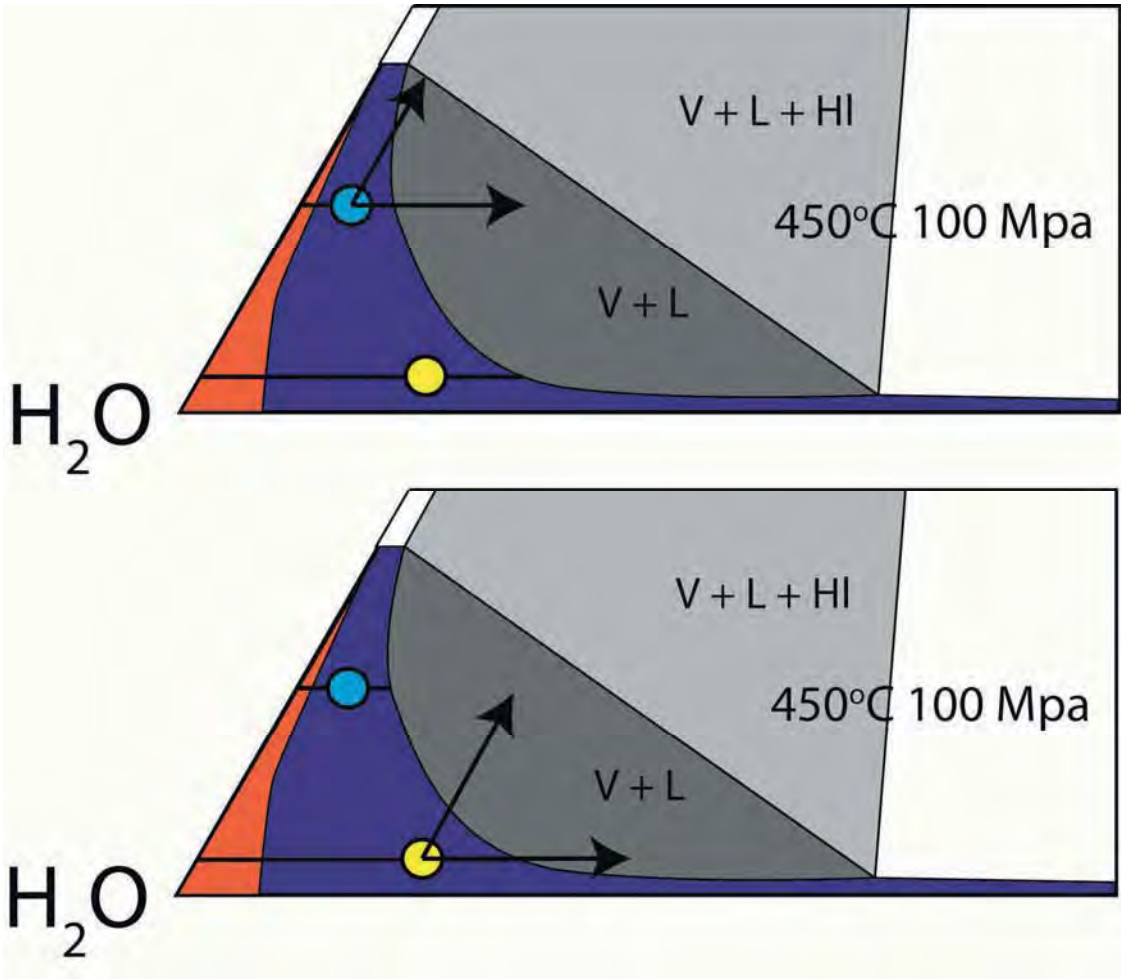

Fig. 6.15. Abbreviated H_2O-CO_2-NaCl plots for T=450°C and P=100 Mpa. At constant T and P, a fluid of a composition represented by either the blue or yellow circle can become immiscible with changes in $X(CO_2)$ and/or X(NaCl) relative to $X(H_2O)$. Arrows indicate the direction of the required compositional evolution of the fluid with either an increase in $X(CO_2)$ (lower arrow) or X(NaCl) (upper arrow).

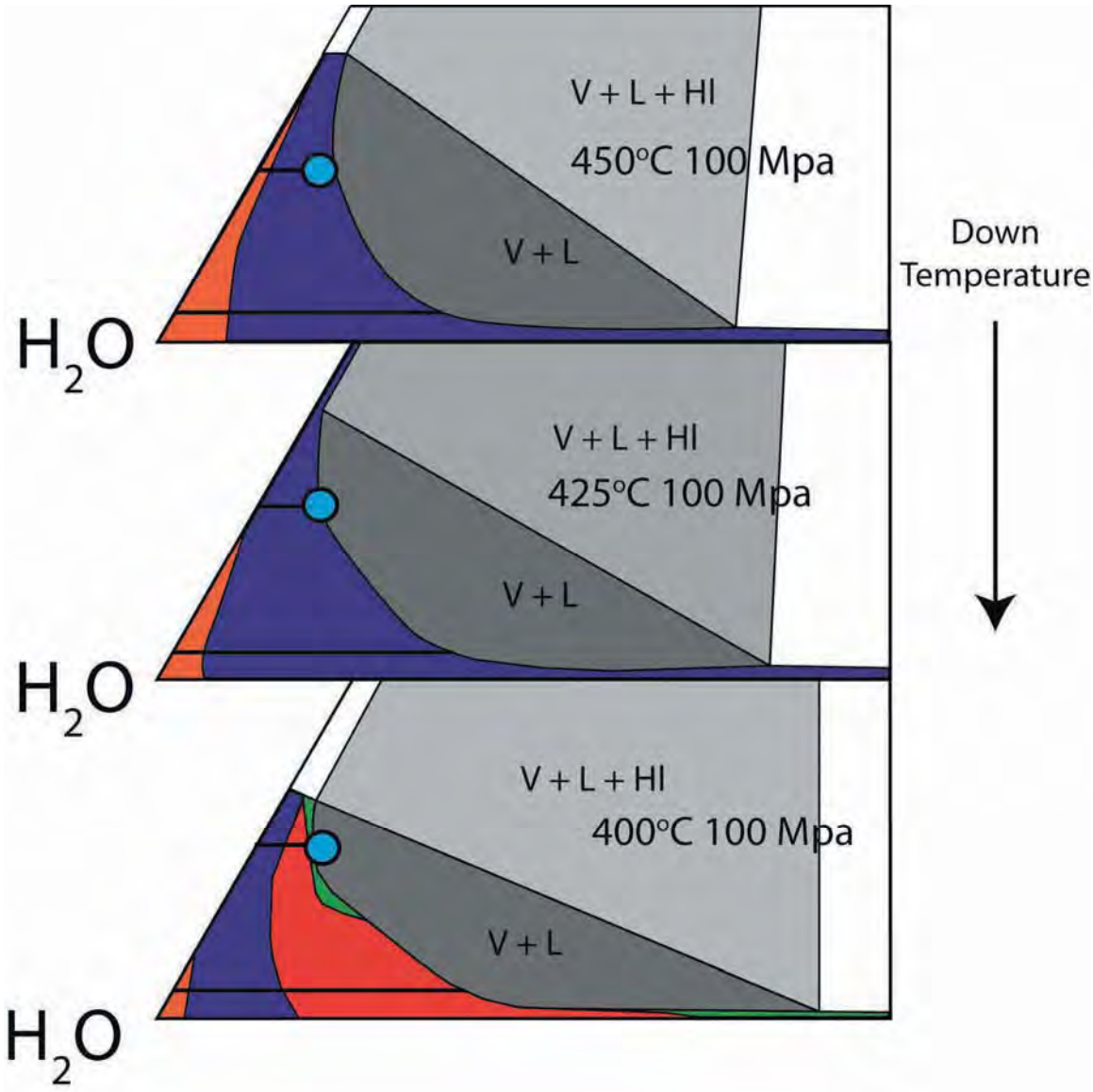

Fig. 6.16. Abbreviated H_2O-CO_2-NaCl plots for T=400-450°C and P=100 Mpa. A fluid with a composition represented by the blue circle could enter the two phase field of V + L with an isobaric decrease in temperature. The arrow is used to illustrate the decline in temperature.

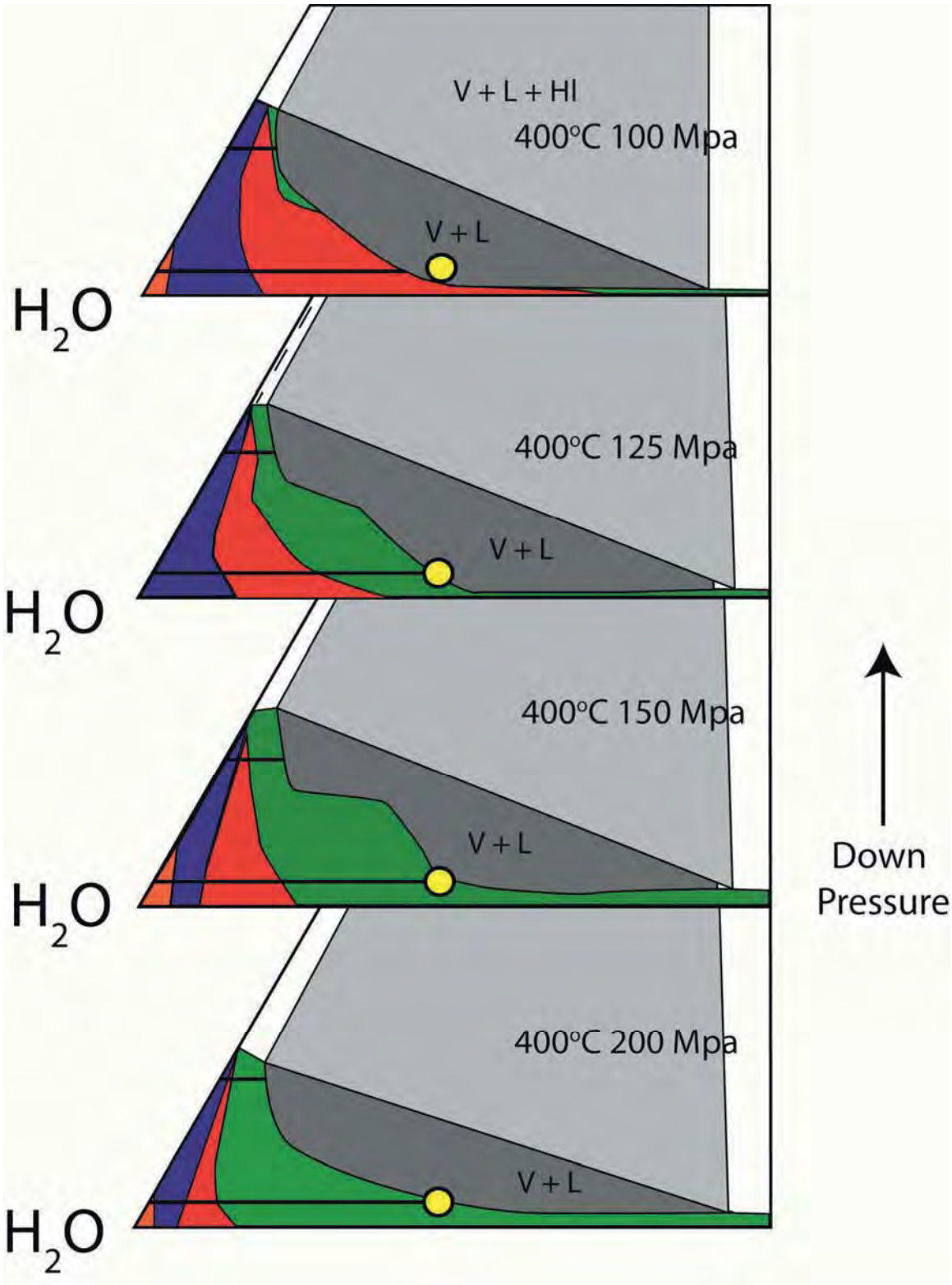

Fig. 6.17. Abbreviated H_2O-CO_2-NaCl plots for T=400°C and P=100-200 Mpa. A fluid with a composition represented by the yellow circle could enter the two phase field of V + L with an isothermal decrease in pressure. The arrow is used to illustrate the decline in pressure.

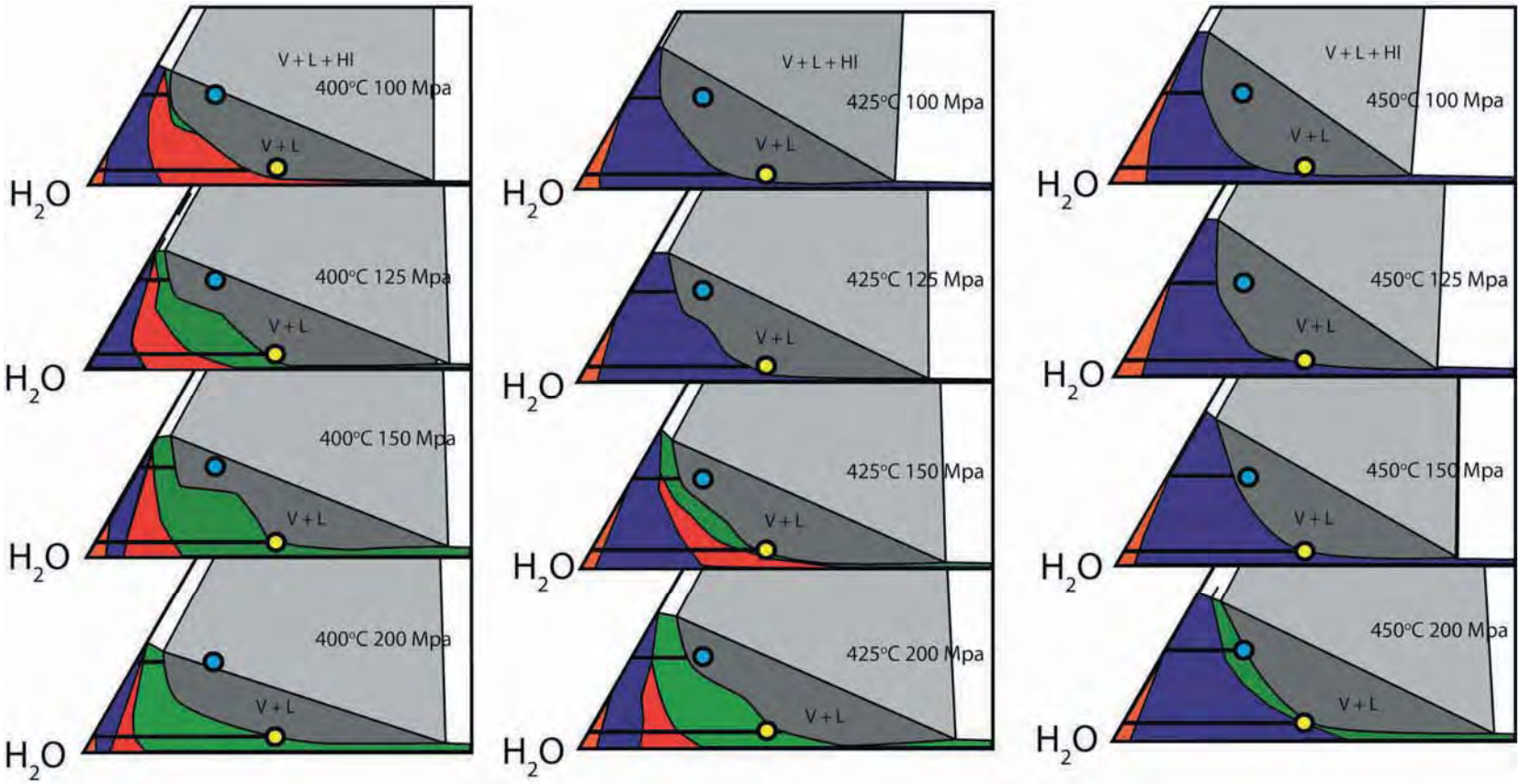

Fig. 6.18. Abbreviated H_2O-CO_2-NaCl plots for T=400-450°C and P=100-200 Mpa. The blue circle represents a fluid with X(NaCl)=15 mol%, and the yellow circle represents a fluid with X(NaCl)=2.5 mol%. The blue and yellow circles show that fluids of different but constant composition will equilibrate with different fluid immiscibility (V + L and V + L + Hl) fields with changes in P and T.

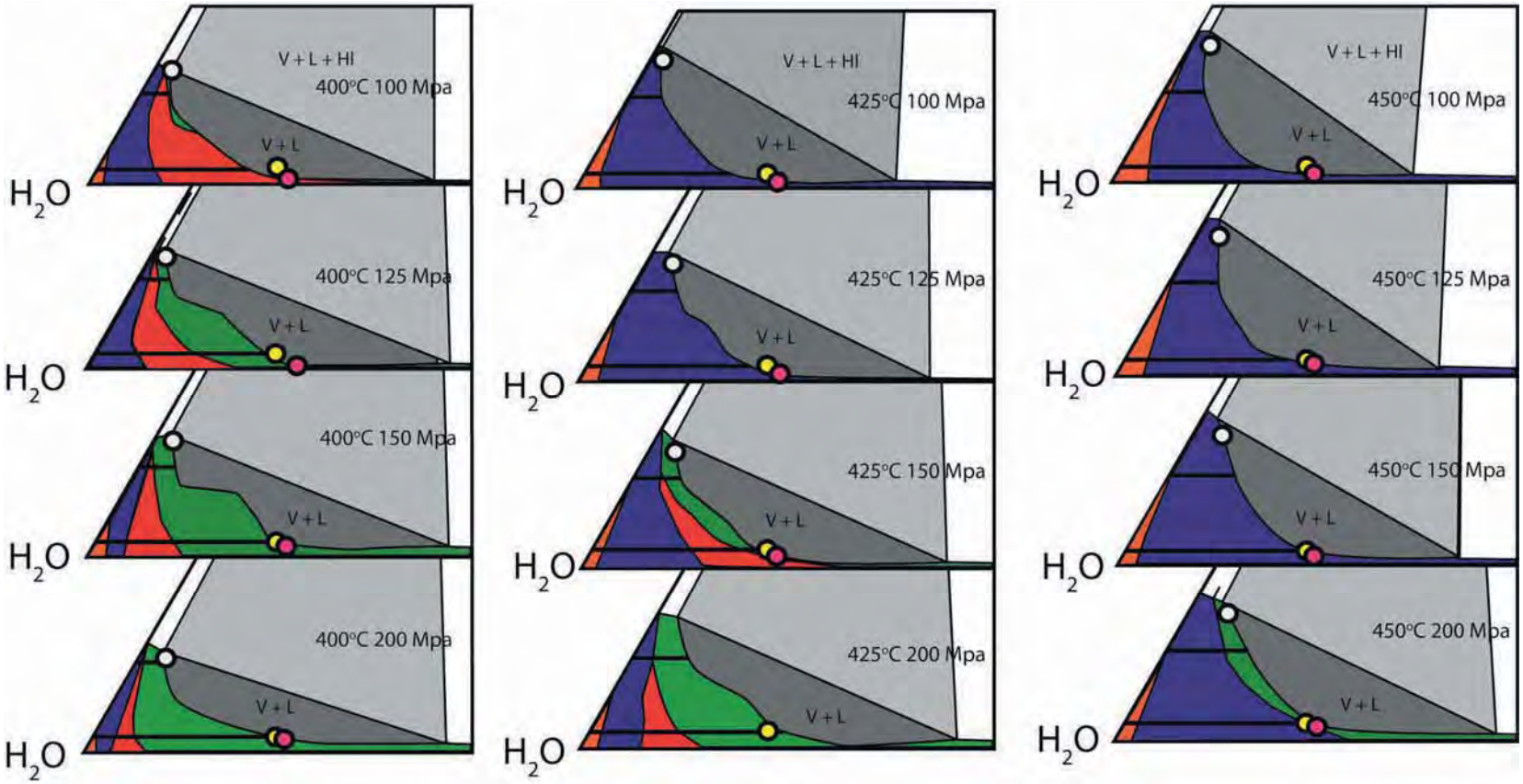

Fig. 6.19. Abbreviated H_2O-CO_2-NaCl plots for T=400-450°C and P=100-200 Mpa. The yellow circle represents an initial parent fluid with X(NaCl)=2.5 mol%. The white circle represents the H_2O-rich fluid and the pink circle represents the CO_2-rich fluid that result from the unmixing of this parent fluid (yellow circle). Note: the initial fluid is immiscible in all cases except for T=425°C and P=200 Mpa.

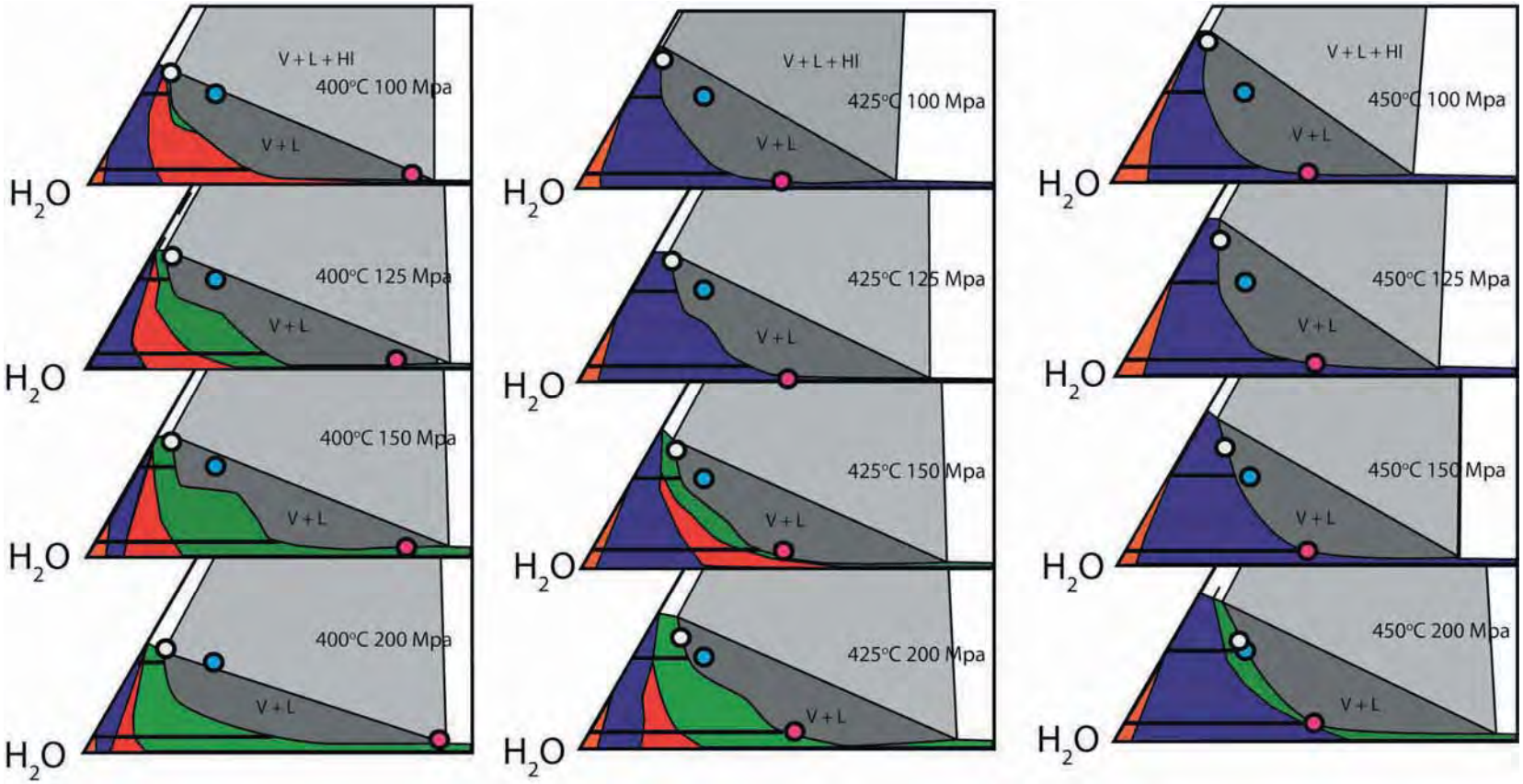

Fig. 6.20. Abbreviated H_2O-CO_2-NaCl plots for T=400-450°C and P=100-200 Mpa. The blue circle represents an initial parent fluid with X(NaCl)=15 mol%. The white circle represents the H_2O-rich fluid and the pink circle represents the CO_2-rich fluid that result from the unmixing of this parent fluid (blue circle).

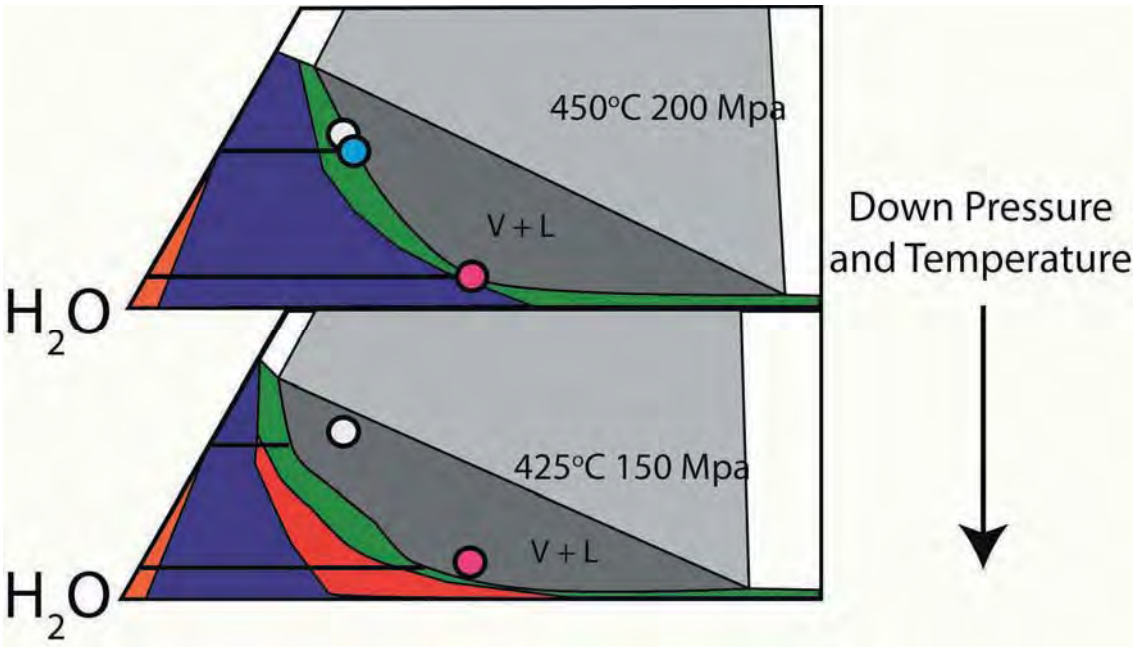

Fig. 6.21. Abbreviated H_2O-CO_2-NaCl plots for T=425°C and P=150 Mpa and T=450°C and P=200 Mpa. This figure illustrates how an initial fluid at T=450°C and P=200 Mpa (blue circle) can become immiscible, forming the fluids with compositions represented by the white (H_2O-rich) and pink (CO_2-rich) circles. With a drop in temperature and pressure to T=425°C and P=150 Mpa, as illustrated by the arrows, these two fluids become immiscible themselves. This process could lead to multiple compositionally distinct H_2O- and CO_2-rich fluids within the system.

composition illustrated by the blue circle (Fig. 6.14) will stay entirely within the tremolite stability field as T decreases from 450 to 425°C and as P decreases to 100 Mpa. If this fluid cools further to 400°C but remains at P≥150 Mpa, it will equilibrate with Qz + Dol and bypass the Tc + Cc stability field. This high salinity fluid composition will equilibrate with Tc + Cc only by decreasing further in pressure to P≤125 Mpa. A single phase fluid with the composition illustrated by the yellow circle (Fig. 6.14) will also remain entirely within the stability field of tremolite during an isothermal (450° C) decrease in P or with cooling to 425° C accompanied by pressure decreasing to and below 150 Mpa. If a single phase fluid with 2.5 mol% NaCl (yellow circle, Fig. 6.14) at P=200 Mpa and T=450° C cooled isobarically to 400°C, it would equilibrate successively with Tr + Dol, Tc + Cc, and Qz + Dol. If this same fluid (initially at 450° C and 200 Mpa in equilibrium with Tr + Dol) cooled to 400° C and also dropped in pressure to or below 150 Mpa, it would equilibrate with the Tc + Cc stability field and remain as a single phase.

It is apparent from the phase diagrams (Fig. 6.14) that a variety of starting single phase fluid compositions could experience these same down-temperature down-pressure flow path scenarios and equilibrate with the same sequences of mineral stability fields as just demonstrated for these two example fluid compositions. Alternatively, compositional changes experienced by either of the starting fluids discussed here could also lead to these fluids entering alternative mineral stability fields during down-T down-P flow.

Down-T Flow Where Fluid Becomes Immiscible

In this significantly more complex scenario, H_2O-rich fluid flows down temperature and possibly down-pressure away from the Alta Stock and becomes

immiscible at some temperature at or below 450°C. Changes in pressure, temperature, or fluid composition can cause a fluid to become immiscible. For example, Fig. 6.15 illustrates how the same two fluid compositions discussed in the previous section would have to change compositionally to enter the fluid immiscibility field (V + L) at 450°C and 100 Mpa. For isothermal isobaric flow, both fluids illustrated in Fig. 6.15 (blue and yellow circles) would have to experience an increase in either or both $X(CO_2)$ and X(NaCl) relative to $X(H_2O)$ to become immiscible (illustrated by arrows in Fig. 6.15). Analogous changes would be required for these same two starting fluids to become immiscible at all temperatures and pressures evaluated in this study. Fig. 6.16 illustrates how a fluid of constant composition (as represented by the blue circle) can become immiscible with no compositional change and an isobaric decrease in temperature from 450 to 400°C at P=100 Mpa. Fig. 6.17 illustrates how a fluid of another composition (as represented by the yellow circle) can become immiscible with no compositional change and an isothermal decrease in pressure from 200 Mpa at T=400°C. Although only three examples of the impact of changes in P-T-X_{fl} are given, it is apparent from the phase diagrams (Figs. 6.15-17) that there are a multitude of alternative scenarios where fluid immiscibility might occur due to changes in P-T-X_{fl}.

Fig. 6.18 illustrates how two different fluids of constant composition, represented by the blue and yellow circles, could undergo changes in phase stability with changes in temperature and pressure of the system. For example, at T=450°C and P=200 Mpa, the blue circle lies on the boundary of fluid immiscibility. With a decrease in temperature to 425°C, the blue circle lies well within the V + L field. The blue circle lies within the V +

L + Hl field when the temperature is further decreased to 400°C, producing solid halite and a two-phase fluid.

When a single phase fluid becomes immiscible, the composition of the resulting H_2O-rich and CO_2-rich fluids will depend on the composition of the parent fluid, as well as the P-T conditions of unmixing, as shown in Figs. 6.19 and 6.20. Fig. 6.19 illustrates the compositions of H_2O- and CO_2-rich fluids that form from the parent fluid with X(NaCl)=2.5 mol%, and Fig. 6.20 illustrates the fluid compositions that form from the X(NaCl)=15 mol% parent fluid. Further complicating this scenario, the H_2O- and CO_2-rich fluids formed when a fluid becomes immiscible may themselves become immiscible, as illustrated in Fig. 6.21. This could lead to multiple compositionally heterogeneous H_2O- and CO_2-rich fluids in the system.

Conclusions

The heterogeneities in the distribution of talc in the outer Alta Aureole require spatially variable fluid $X(CO_2)$. These variations can be the result of fluctuations in the H_2O-CO_2-NaCl composition of a single phase fluid or result from the complex evolution of immiscible fluids with down-temperature flow. The sequence of tremolite + dolomite to talc + calcite to dolomite + quartz observed out from the Alta stock can be produced in all three scenarios considered under certain P-T-X_{fl} conditions. The phase equilibria calculations presented here constrain the conditions necessary for the behavior of the down-temperature flowing fluid in each of the scenarios. For example, a down-T flowing fluid can remain single phase with a decrease in temperature from 450 to 400°C and a pressure decrease from 200 to 100 Mpa for certain starting fluid compositions. Other

starting fluid compositions may be immiscible at 450°C and 200 Mpa, or they may be single phase and become immiscible with decreases in temperature and/or pressure from 450°C and 200 Mpa. These phase equilibria calculations show that the talc +calcite and fluid immiscibility fields intersect only at temperatures below 425°C and pressures below 125 MPa. The fluids that form when the parent fluid becomes immiscible may also become immiscible with further decrease in temperature and/or pressure. This could lead to the formation of several compositionally distinct H_2O- and CO_2-rich fluids. Future data collected from the Alta Aureole can be considered within these constraints in order to understand the formation of the talc zone.

References

Baumgartner, L.P., Ferry, J.M., 1991. A model for coupled fluid-flow and mixed-volatile mineral reactions with applications to regional metamorphism. Contributions to Mineralogy and Petrology 106, 273-285.

Bowers, T.S., Helgeson, H.C., 1983a. Calculation of the thermodynamic and geochemical consequences of nonideal mixing in the system H_2O-CO_2-NaCl on phase relations in geologic systems: equation of state for H_2O-CO_2-NaCl fluids at high pressures and temperatures. Geochimica Cosmochimica Acta 47, 1247-1275.

Bowers, T.S., Helgeson, H.C., 1983b. Calculation of the thermodynamic and geochemical consequences of nonideal mixing in the system H_2O-CO_2 -NaCl on phase relations in geologic systems; metamorphic equilibria at high pressures and temperatures. American Mineralogist 68, 1059-1075.

Bowman, J.R., Willet, S.D., Cook, S.J., 1994. Oxygen isotopic transport and exchange during fluid flow: one-dimensional models and applications. American Journal of Science 294, 1-55.

Bowman, J.R., Valley, J.W., Kita, N.T., 2009. Mechanisms of oxygen isotopic exchange and isotopic evolution of $^{18}O/^{16}O$-depleted periclase zone marbles in the Alta aureole, Utah - Insights from ion microprobe analysis of calcite. Contributions to Mineralogy and Petrology 157, 77-93.

Connolly, J.A.D., 1990. Multivariable phase-diagrams - an algorithm based on generalized thermodynamics. American Journal of Science 290, 666-718.

Cook, S.J., 1982. The physical-chemical conditions of contact skarn formation at Alta, Utah. M.Sc. Thesis, University of Utah, 169p.
Cook, S.J., Bowman, J.R., 1994. Contact metamorphism surrounding the Alta stock: thermal constraints and evidence of advective heat transport from calcite + dolomite geothermometry. American Mineralogist 79, 513-525.

Cook, S.J., Bowman, J.R., Forster, C.B., 1997. Contact metamorphism surrounding the Alta Stock: finite element model simulation of heat and $^{18}O/^{16}O$ mass-transport during prograde metamorphism. American Journal of Science 297, 1-55.

Cook, S.J., Bowman, J.R., 2000. Mineralogical evidence for fluid-rock interaction accompanying prograde contact metamorphism of siliceous dolomites: Alta Stock Aureole, Utah, USA. Journal of Petrology 41, 739-757.

Crittenden, M.D., Stuckless Jr., J.S., Kistler, R.W., Stern, T.W., 1973. Radiometric dating of intrusive rocks in the Cottonwood area, Utah. US Geological Survey Journal of Research 1, 173-178.

Duan, Z., Moller, N., Weare, J.H., 1995. Equation of state for the $NaCl-H_2O-CO_2$ system: prediction of phase equilibria and volumetric properties. Geochimica Cosmochimica Acta 59, 2869-2882.

Ferry, J.M., 1994. Role of fluid flow in the contact metamorphism of siliceous dolomitic limestones. American Mineralogist 79, 719-736.

Ferry, J.M., Wing, B.A., Penniston-Dorland, S.C., Rumble, D., 2002. The direction of fluid flow during contact metamorphism of siliceous carbonate rocks: new data for the Monzoni and Predazo aureoles, northern Italy, and a global review. Contributions to Mineralogy and Petrology 142, 679-699.

Fernandez-Caliani, J.C., Casquet, C.E., Galan, E., 1996. Complex multiphase fluid inclusions in wollastonite from the Merida, Spain, contact-metamorphic deposit: evidence for rock/HCl-rich fluid interaction. European Journal of Mineralogy 8, 1015-1026.

Gottschalk, M., 1997. Internally consistent thermodynamic database for rock-forming minerals in the system $SiO_2-TiO_2-Al_2O_3-Fe_2O_3-CaO-MgO-FeO-K_2O-Na_2O-H_2O-CO_2$: an alternative approach. European Journal of Mineralogy 9, 175-223.

Gottschalk, M., 2007. Equations of state for complex fluids. Reviews in Mineralogy and Geochemistry 65, 49-97.

Heinrich, W., Churakov, S.S., Gottschalk, M., 2004. Mineral-fluid equilibria in the system CaO-MgO-SiO_2-H_2O-CO_2-NaCl and the record of reactive fluid flow in contact metamorphic aureoles. Contributions to Mineralogy and Petrology 148, 131-149.

Heinrich, W., 2007. Fluid immiscibility in metamorphic rocks. Reviews in Mineralogy and Geochemistry 65, 389-430.

Heinrich, W., Gottschalk, M., 1994. Fluid flow patterns and infiltration isograds in melilite marbles from Bufa del Diente contact metamorphic aureole, north-east Mexico. Journal of Metamorphic Geology 12, 345-359.

Holland, T.J.B., Powell, R., 1991. An internally consistent data set for phases of petrological interest. Journal of Metamorphic Geology 16, 309-343.

Jaeger, J.C., 1964. Thermal effects of intrusions. Reviews in Geophysics, Space Physics 2, 443-466.

Kemp, W.M. III., 1985. A stable isotope and fluid inclusion study of the contact Al(Fe)-Ca-Mg-Si skarns in the Alta Stock Aureole, Alta, Utah. M.S. Thesis, University of Utah, 65 pp.

Labotka, T.C., 1991. Chemical and physical properties of fluids. Review in Mineralogy and Geochemistry 26, 43-104.

Moore, J.N., Kerrick, D.M., 1976. Equilibria in siliceous dolomites of the Alta aureole, Utah. American Journal of Science 276, 502-524.

Pollington, A.D., Bowman, J.R., Kaszuba, J.P., 2005. Heterogeneous fluid flow, reaction progress, and isotope disequilibrium in the talc zone, outer Alta Aureole, UT. Geological Society of America Abstracts with Programs 37, 227.

Sisson, V.B., Crawford, M.L., Thompson, P.H., 1981. CO_2-brine immiscibility at high temperatures: evidence from calcareous metasedimentary rocks. Contributions to Mineralogy and Petrology 78, 371-378.

Trommsdorff, V., Skippen, G., 1987. Metasomatism involving fluids in CO_2-H_2O-NaCl. In: Helgeson, H.C. (ed.) Chemical transport in metasomatic processes. Nato ASI series C: Mathematical and Physical Sciences 218, 113-152.

Wilson, J.W., 1961. Geology of the Alta stock. Ph.D. Thesis, California Institute of Technology, Pasadena.

APPENDIX A

METHOD OF CALCULATING LIQUID AND VAPOR CONCENTRATIONS OF GASES WITH BOILING

The method detailed by Henley et al. (1984) to calculate the concentration of gas in the liquid and vapor phases during boiling was used in creating Figs. 1.8C and 1.9C. This appendix details this method.

The mass balance equation is:

$$C_o = C_l(1-y) + C_v(y)$$

where C_o is the initial pre-boiling concentration of gas in the fluid, C_l is the concentration of gas in the liquid phase, C_v is the concentration of gas in the vapor phase, and y is the steam fraction.

The concentration of a gas in the liquid and vapor phases during closed system boiling, also called single step steam separation, is calculated with the mass balance equation and the following equation:

$$C_o/C_l = 1+y(B-1)$$

where C_o is the initial pre-boiling concentration of a gas in the fluid, C_l is the concentration of that gas in the liquid phase, y is the steam fraction separated, and B is the partition coefficient of the gas. The concentration of a gas in the liquid and vapor phases during open system boiling, also called continuous steam separation, is calculated with the mass balance equation and the following Rayleigh-type equation:

$$C_l/C_o=e^{-B'}$$

where C_o is the initial pre-boiling concentration of a gas in the fluid, C_l is the concentration of that gas in the liquid phase, y is the cumulative steam fraction removed, and B' is the average partition coefficient of the gas for the small temperature interval considered.

The vapor-liquid distribution constants reported by Fernandez-Prini et al. (2003) were used for B in these calculations.

APPENDIX B

PHOTOMICROGRAPHS OF AMORPHOUS SILICA SCALE SAMPLES FROM COSO WELLS 68-20RD AND 68B-20RD

This appendix consists of photomicrographs of amorphous silica scale samples found in cuttings from Coso wells 68-20RD and 68B-20RD. There are 23 images taken with a petrographic microscope (all with plain polarized light) and 19 images taken with a Leo 440 scanning electron microscope (SEM) with a tungsten filament electron source. An energy dispersive x-ray (EDX) was used for elemental analysis with the SEM.

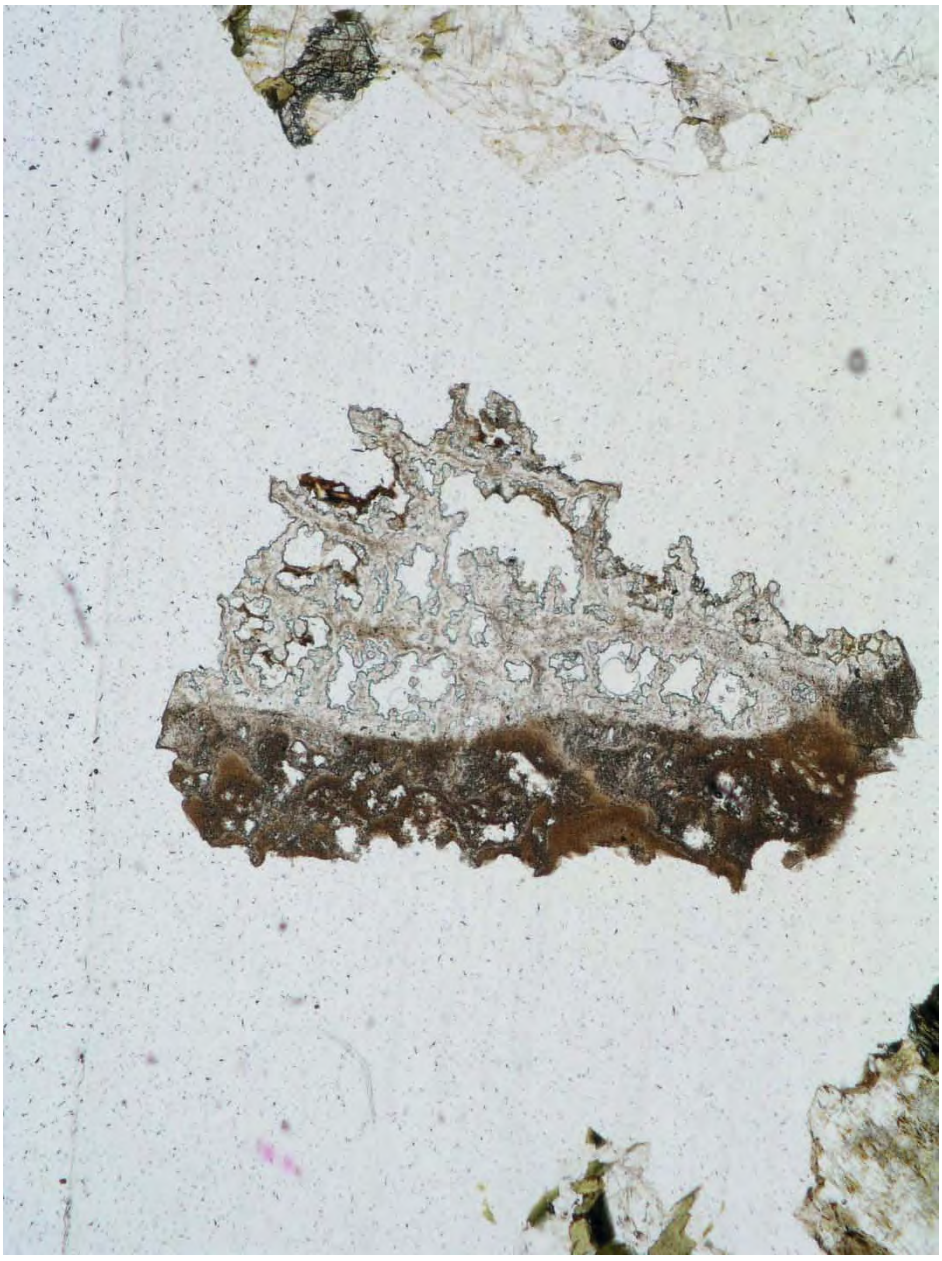

Fig. B.1. Amorphous silica scale from well 68-20RD (847-850 m depth). Horizontal width is 2.15 mm.

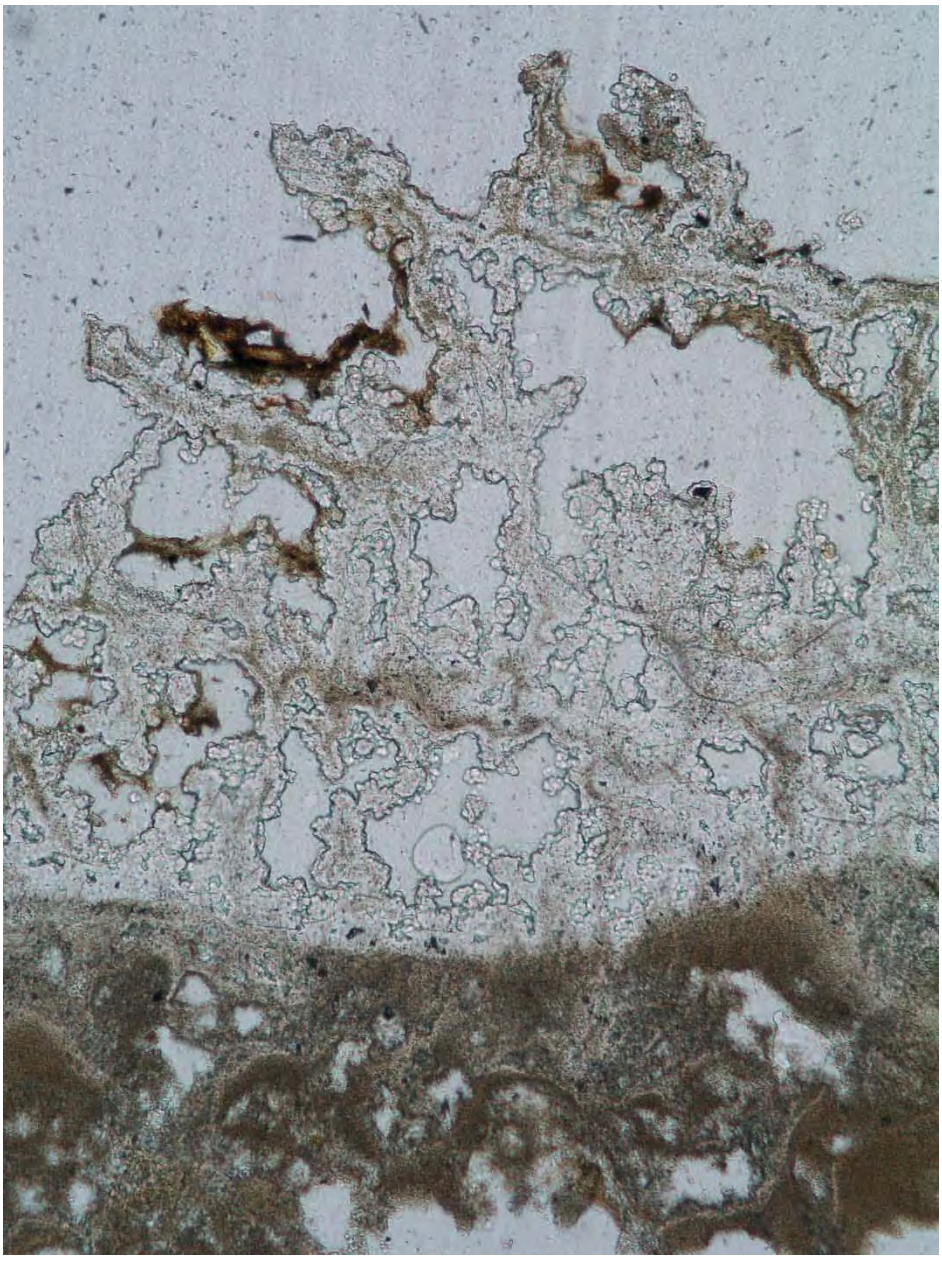

Fig. B.2. Amorphous silica scale from well 68-20RD (847-850 m depth). Horizontal width is 0.86 mm.

Fig. B.3. Amorphous silica scale (center) from well 68-20RD (850-853 m depth). Horizontal width is 2.15 mm.

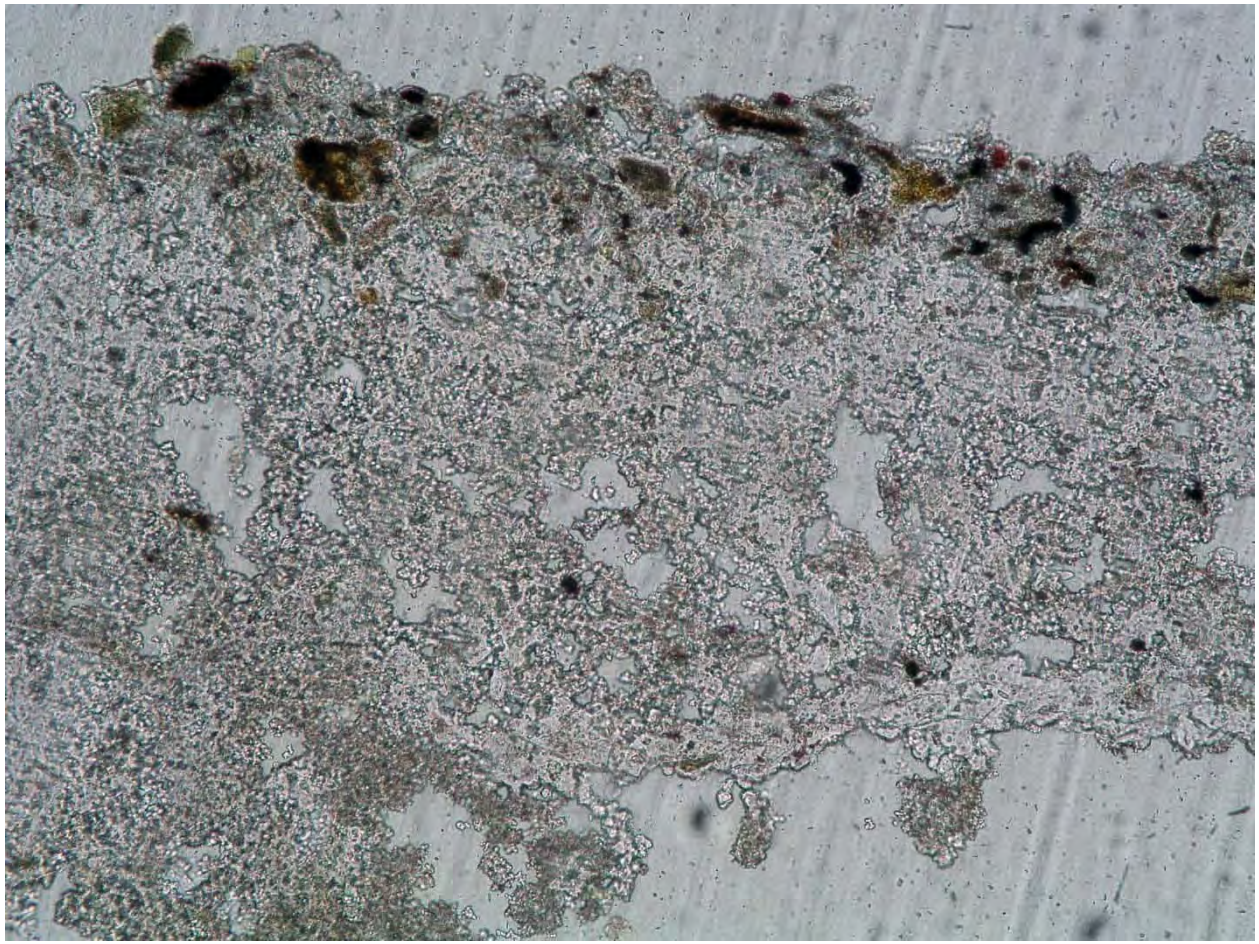

Fig. B.4. Detail of amorphous silica scale from well 68-20RD (850-853 m depth) showing entrapped mineral fragments. Horizontal width is 0.86 mm.

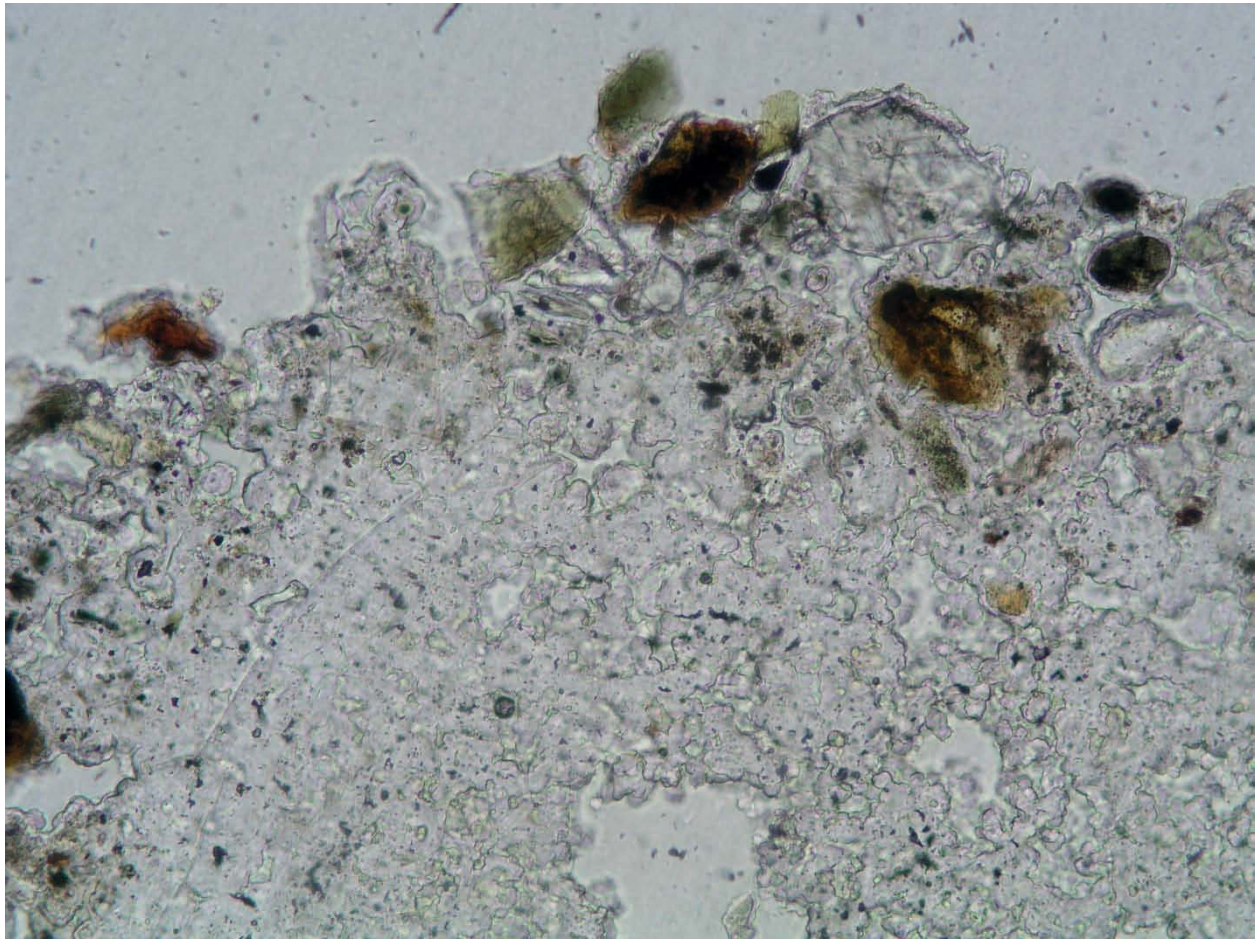

Fig. B.5. Detail of amorphous silica scale from well 68-20RD (850-853 m depth) showing entrapped mineral fragments. Horizontal width is 0.43 mm.

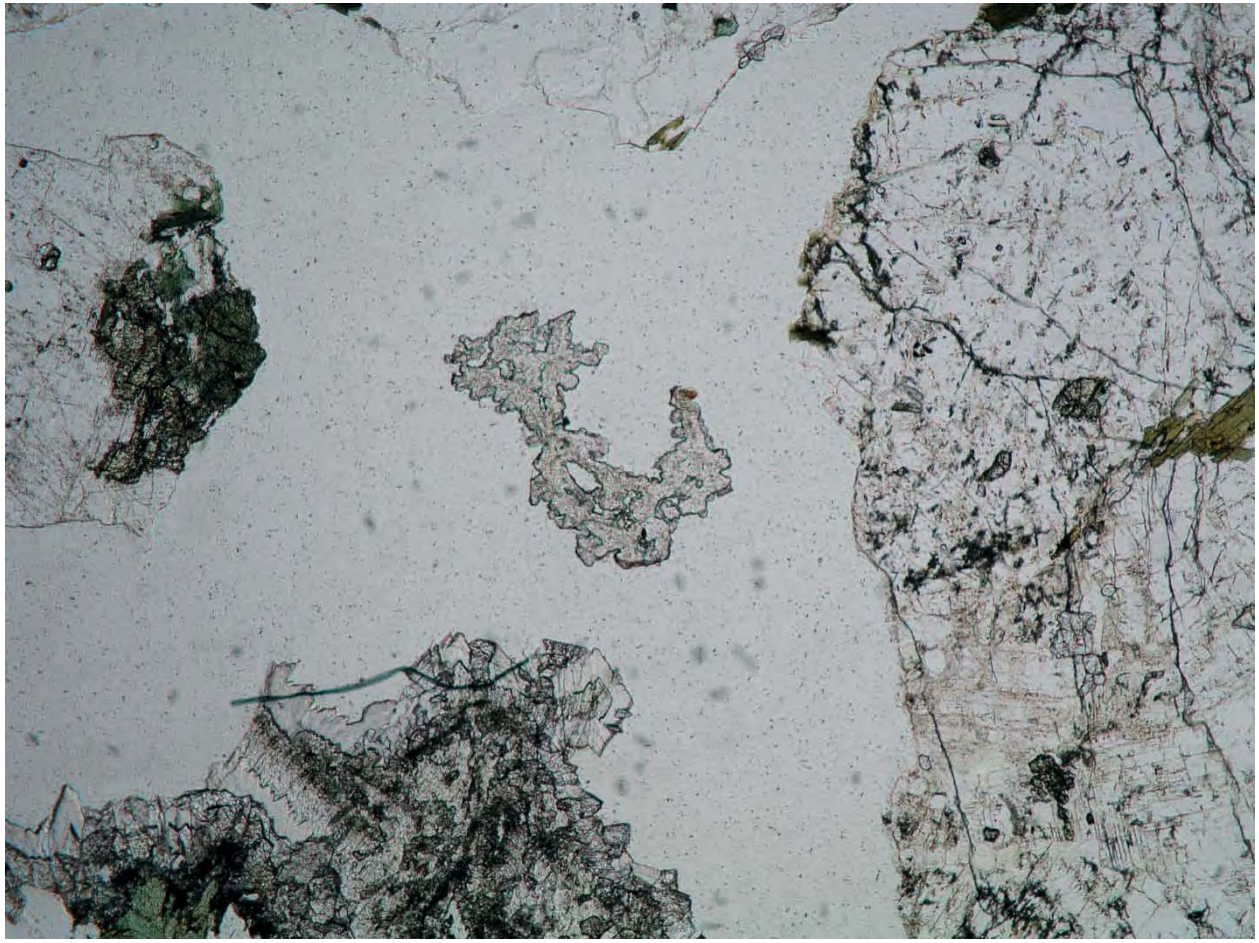

Fig. B.6. Amorphous silica scale (center) from well 68-20RD (853-856 m depth) showing entrapped mineral fragments. Horizontal width is 2.15 mm.

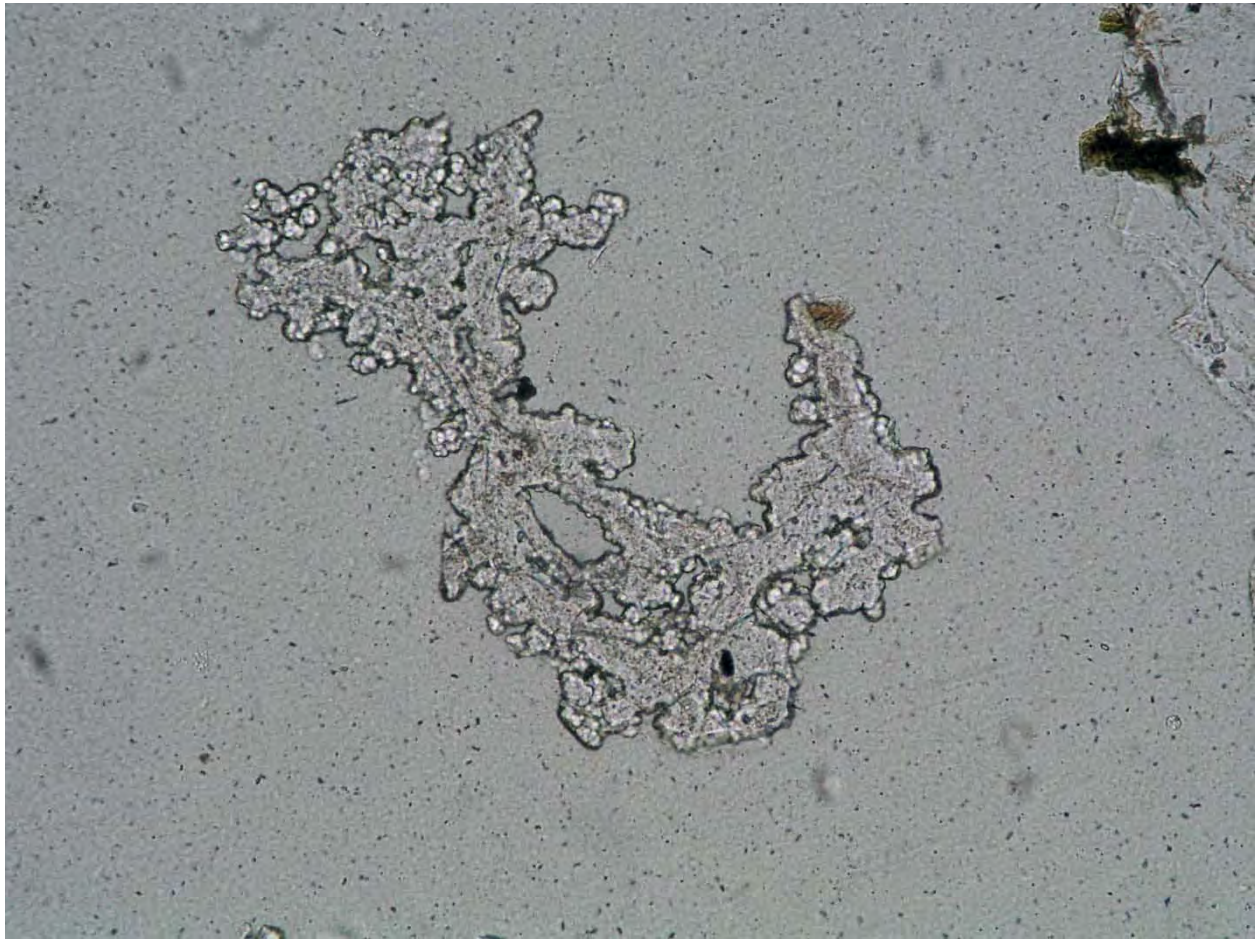

Fig. B.7. Detail of amorphous silica scale from well 68-20RD (853-856 m depth) showing texture and entrapped mineral fragments. Horizontal width is 0.86 mm.

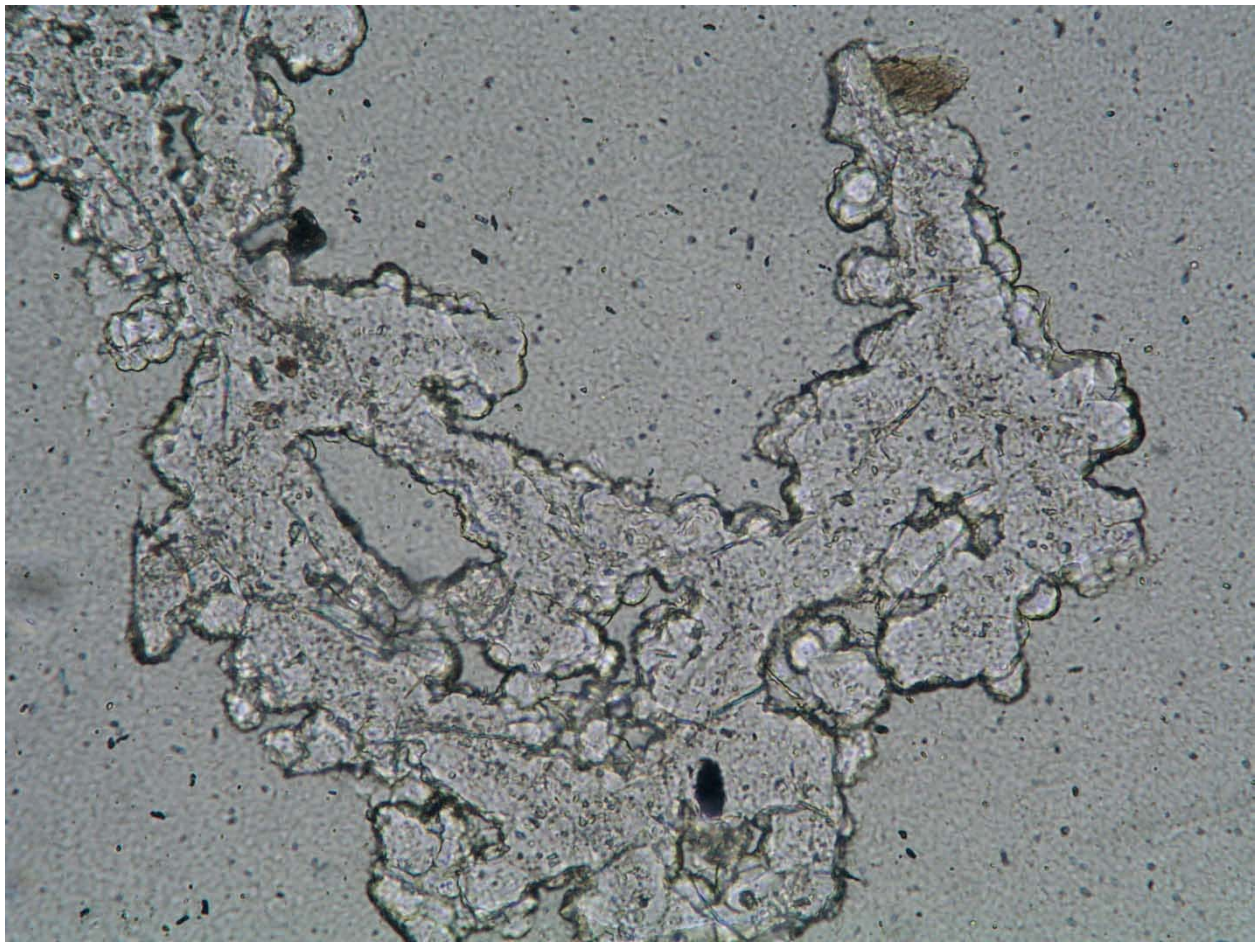

Fig. B.8. Detail of amorphous silica scale from well 68-20RD (853-856 m depth) showing colloidal texture and entrapped mineral fragments. Horizontal width is 0.43 mm.

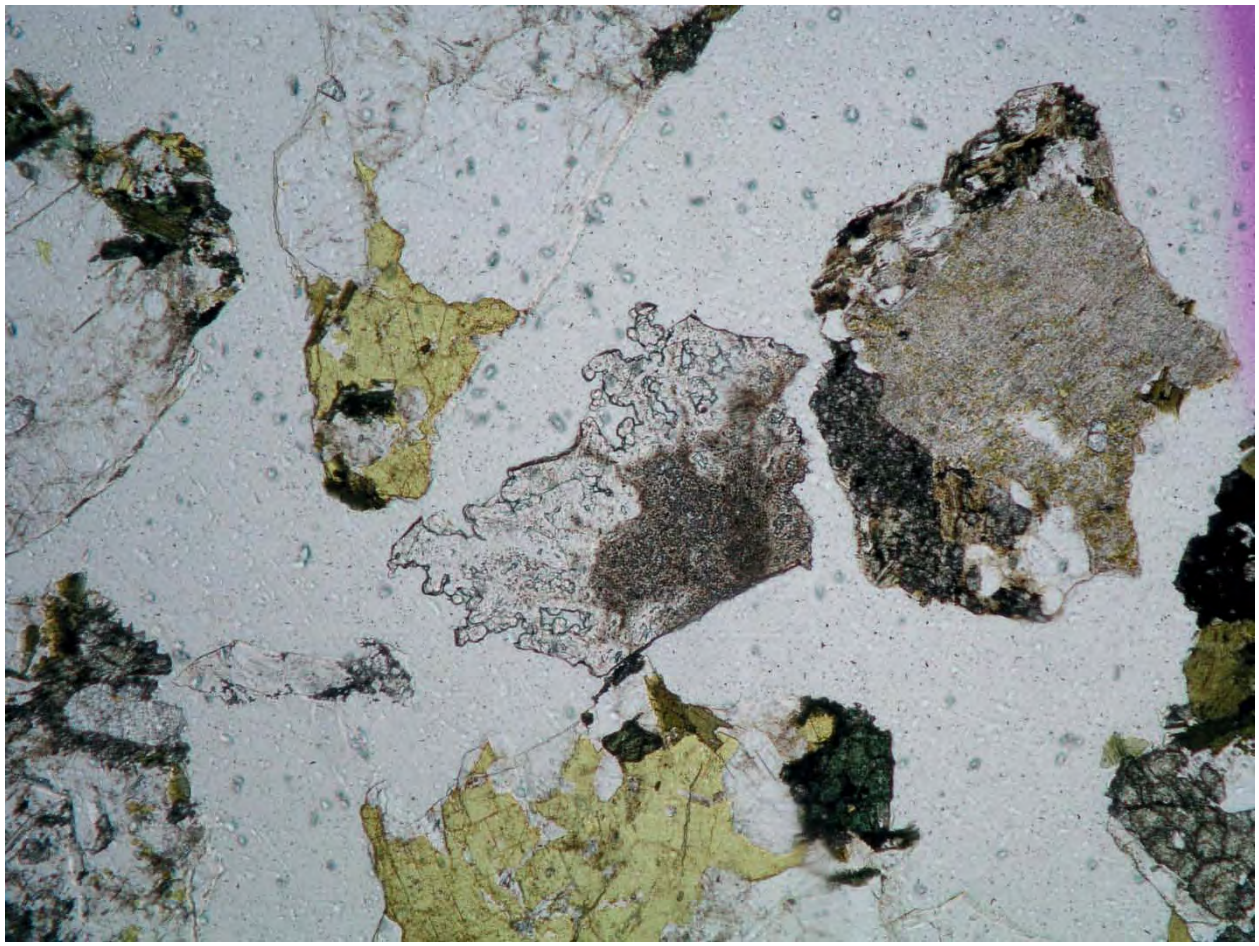

Fig. B.9. Amorphous silica scale (center) from well 68-20RD (853-856 m depth) showing variation in texture. Horizontal width is 2.15 mm.

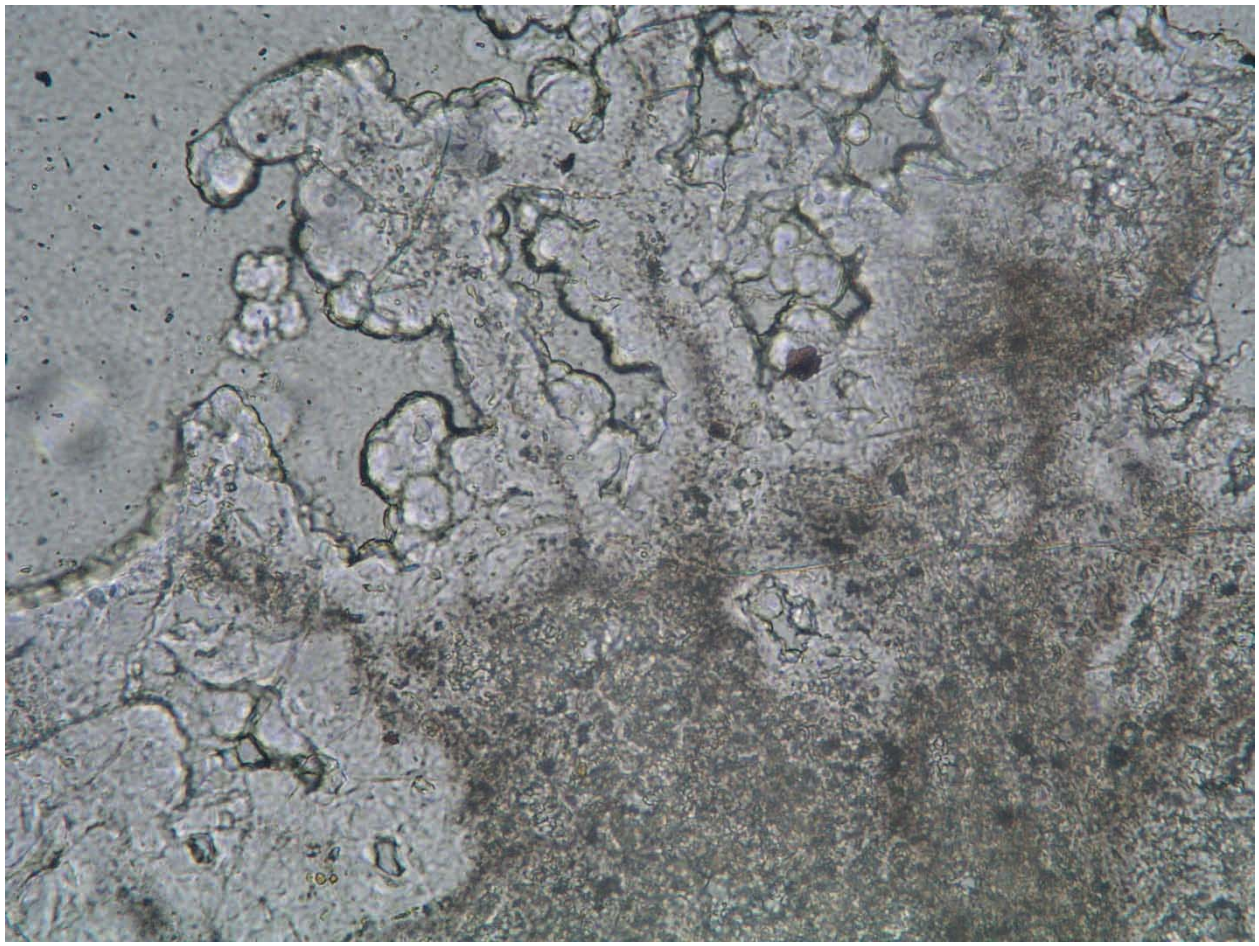

Fig. B.10. Detail of amorphous silica scale from well 68-20RD (853-856 m depth) showing variation in texture. Horizontal width is 0.43 mm.

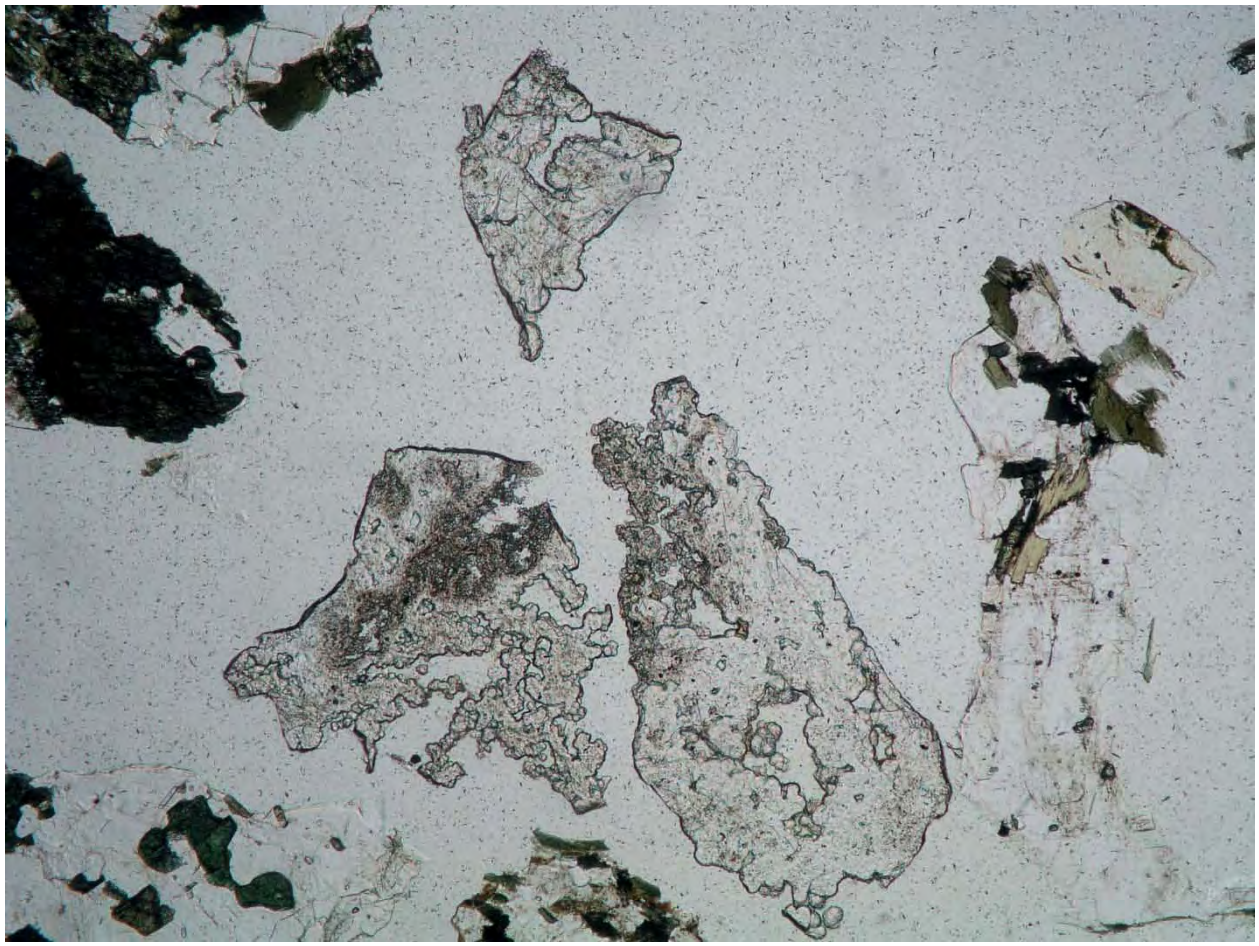

Fig. B.11. Three pieces of amorphous silica scale (center) from well 68-20RD (856-859 m depth) showing variation in texture. Horizontal width is 2.15 mm.

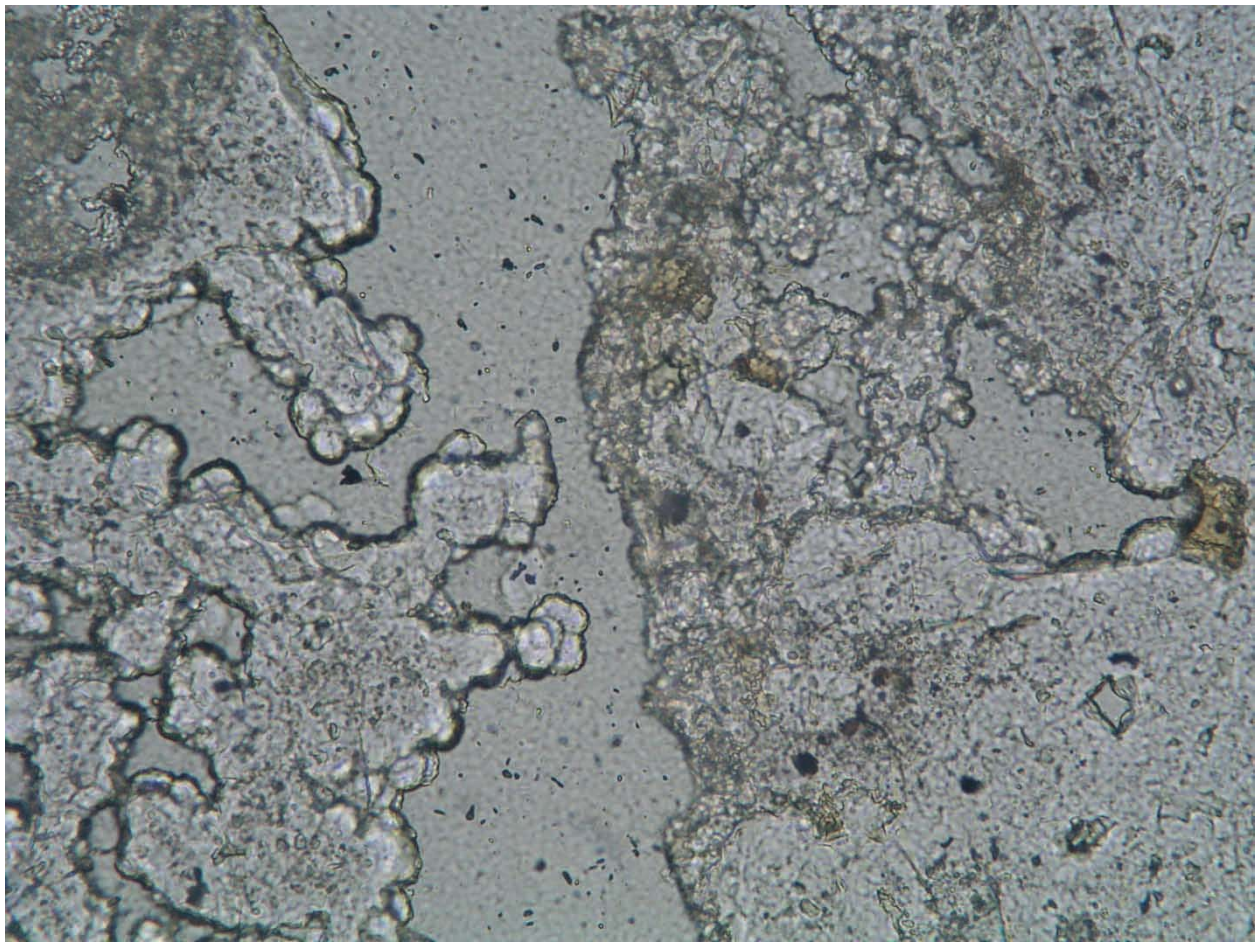

Fig. B.12. Detail of amorphous silica scale from well 68-20RD (856-859 m depth) showing variation in texture and entrapped mineral fragments. Horizontal width is 0.43 mm.

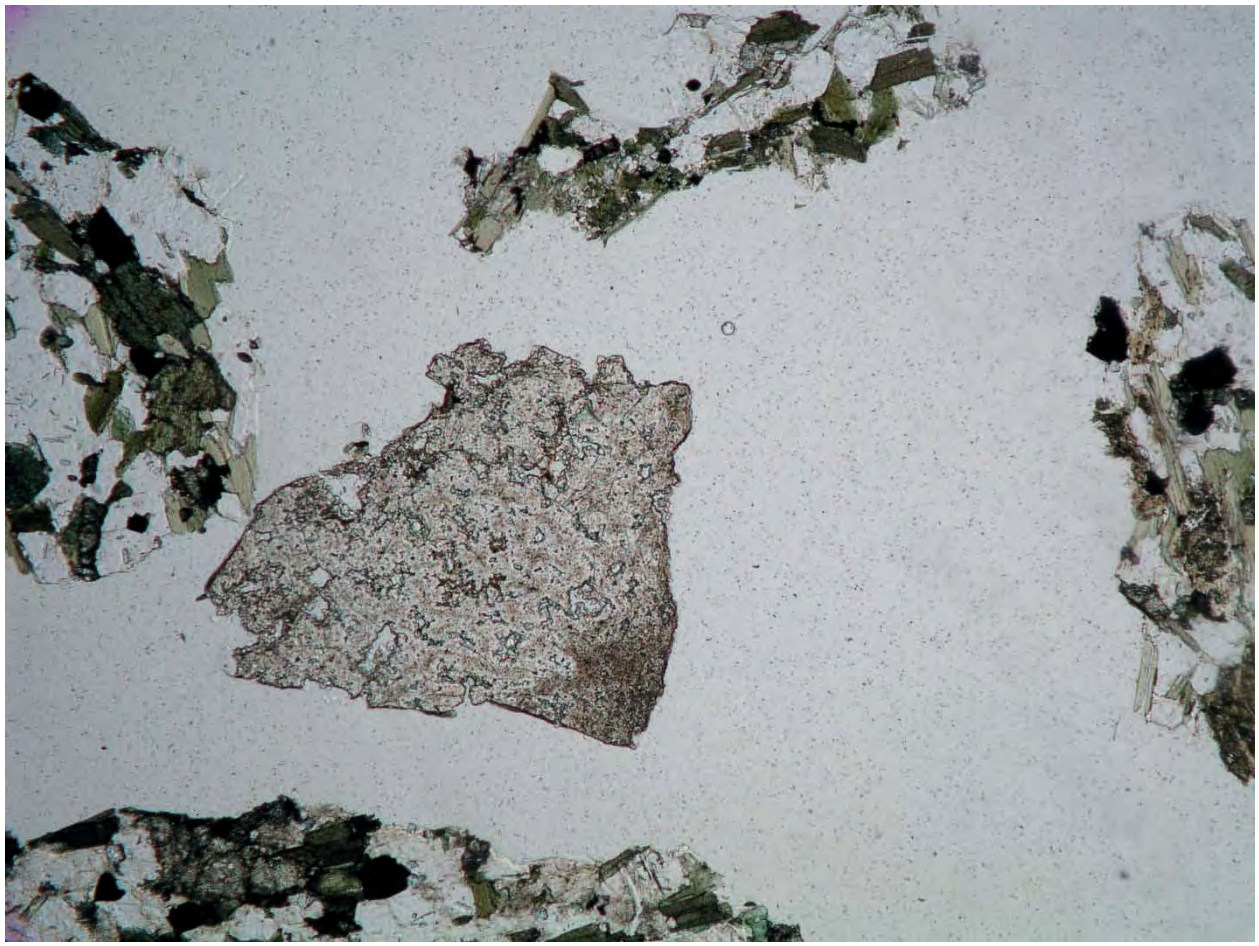

Fig. B.13. Amorphous silica scale (center) from well 68-20RD (866-869 m depth) showing a denser variation in texture. Horizontal width is 2.15 mm.

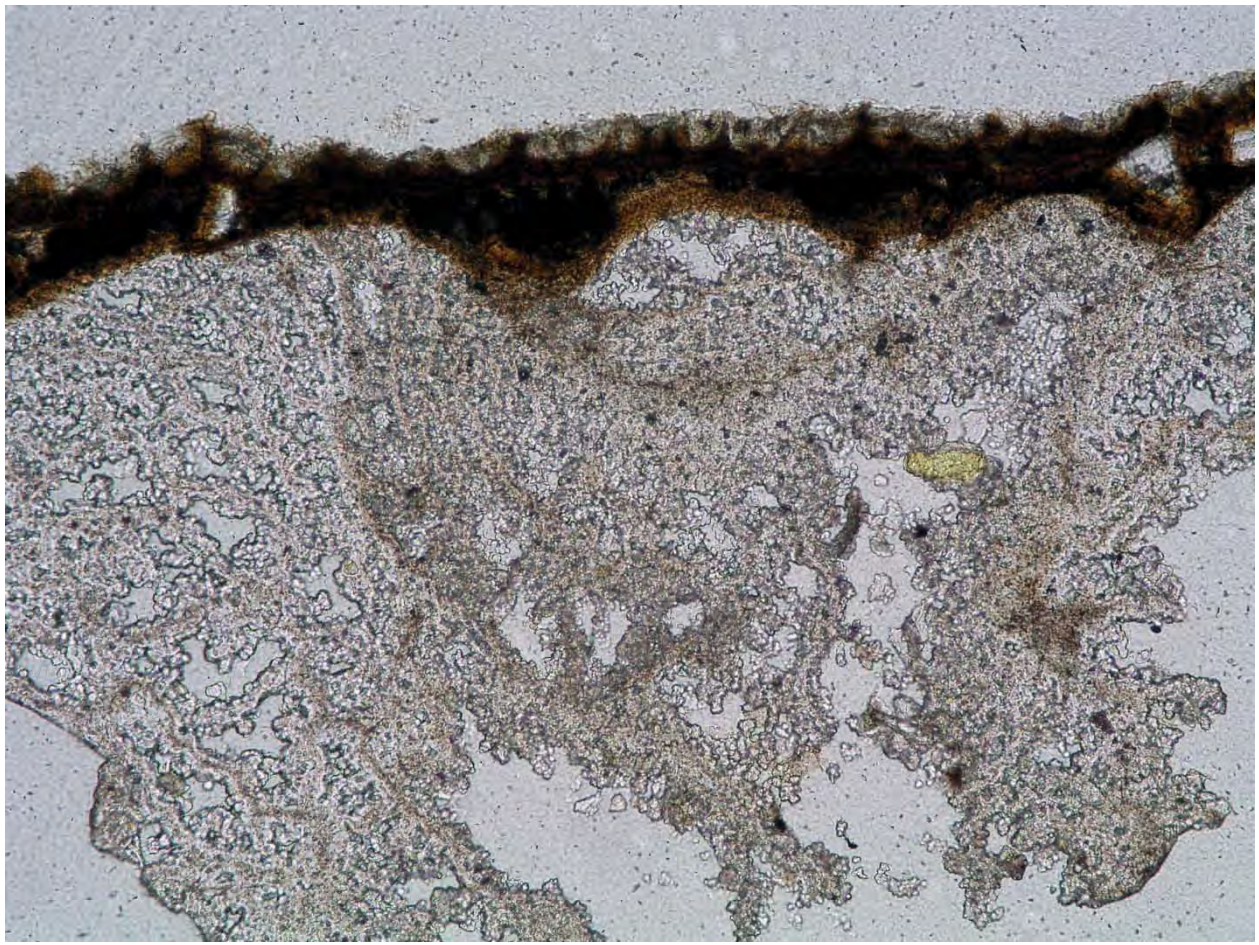

Fig. B.14. Amorphous silica scale from well 68-20RD (878-881 m depth) showing colloidal texture, entrapped mineral fragments, and a dark mineral rind. Horizontal width is 0.86 mm.

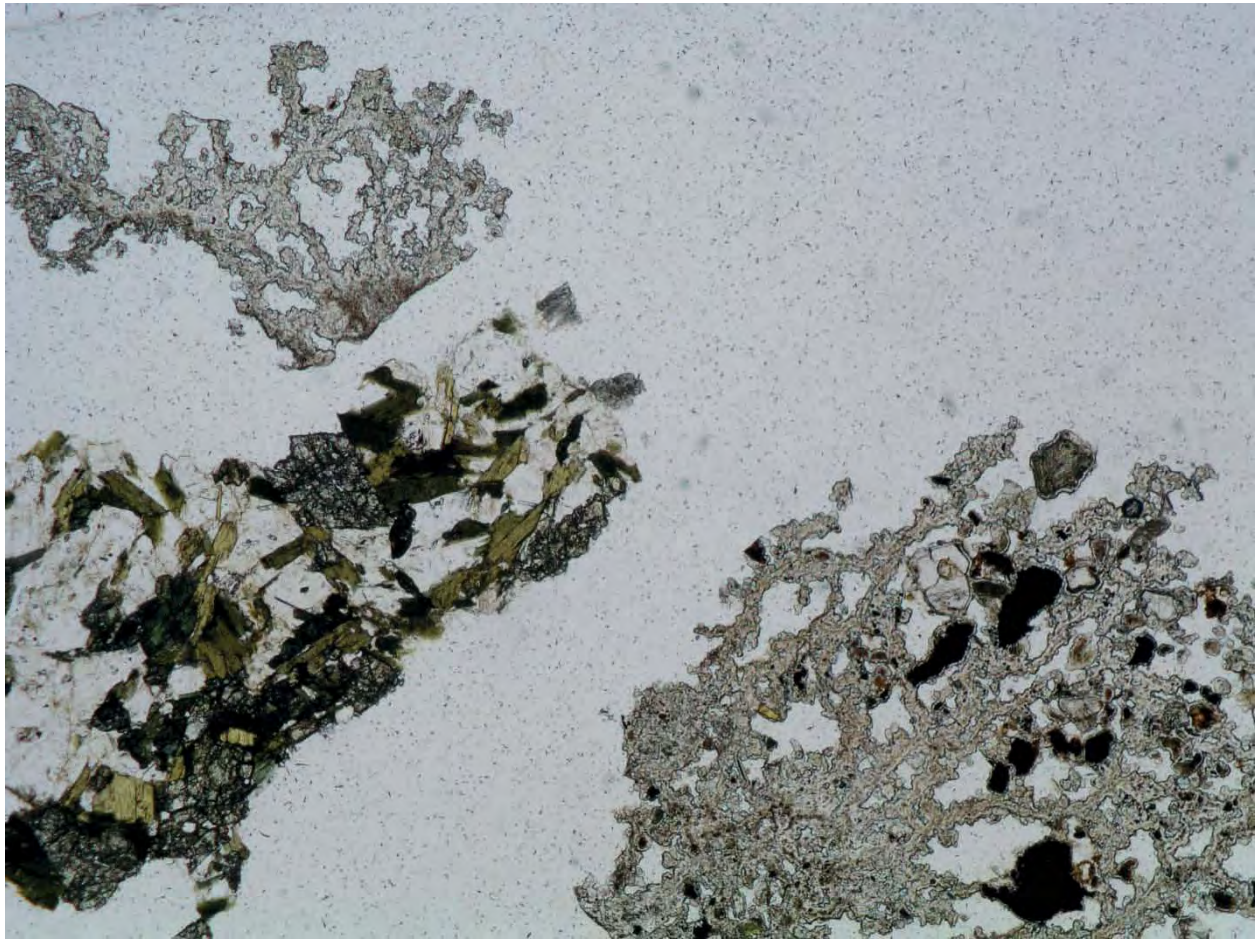

Fig. B.15. Amorphous silica scale (upper left and lower right) from well 68-20RD (896-899 m depth) showing a more open network of spheres and entrapped mineral fragments. Horizontal width is 2.15 mm.

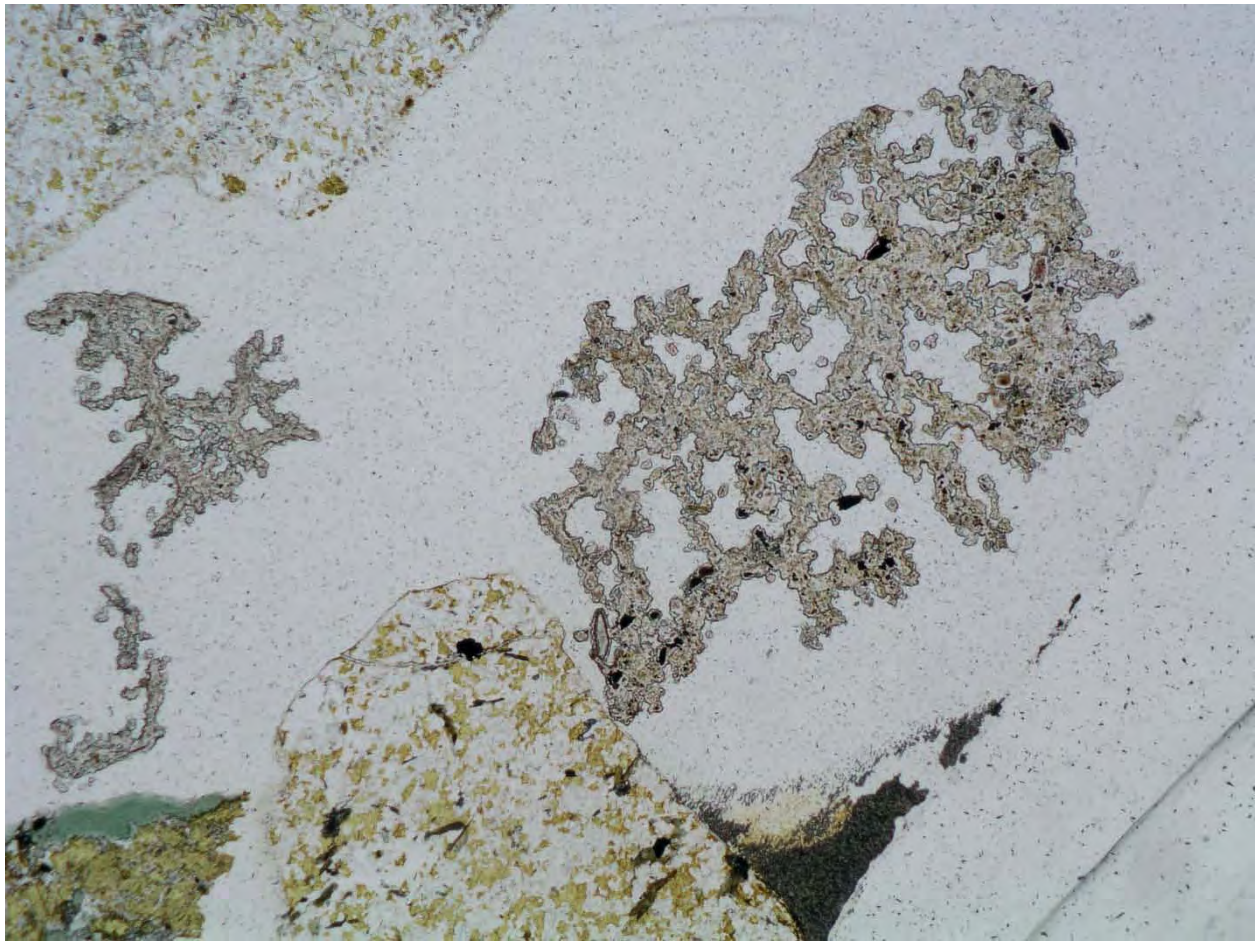

Fig. B.16. Amorphous silica scale (center left and right) from well 68-20RD (896-899 m depth) showing a more open network of spheres and entrapped mineral fragments. Horizontal width is 2.15 mm.

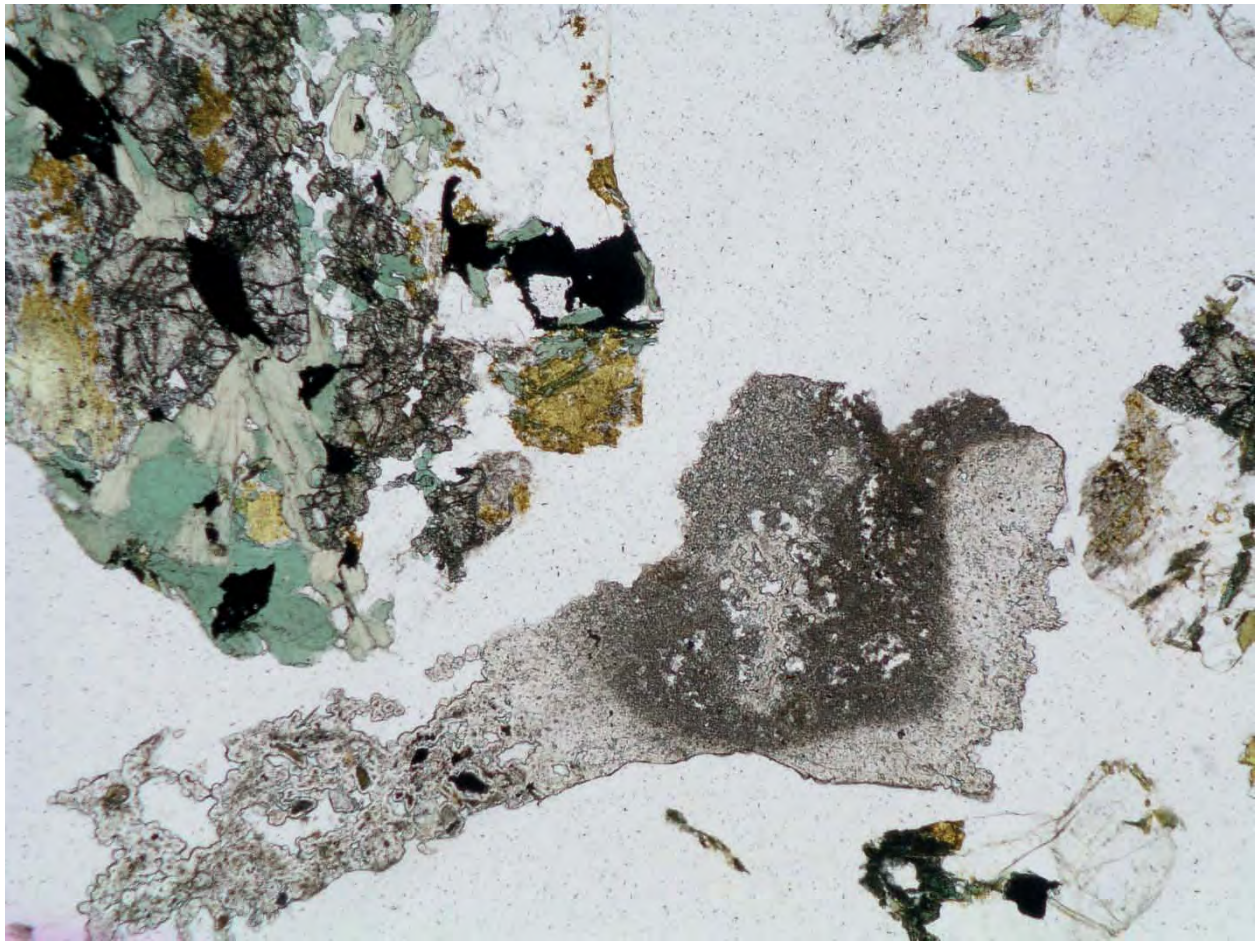

Fig. B.17. Amorphous silica scale (lower left to center) from well 68-20RD (896-899 m depth) showing a more open network of spheres alongside a denser texture. Entrapped mineral fragments can also be seen, with larger fragments trapped in the more open network of spheres. Horizontal width is 2.15 mm.

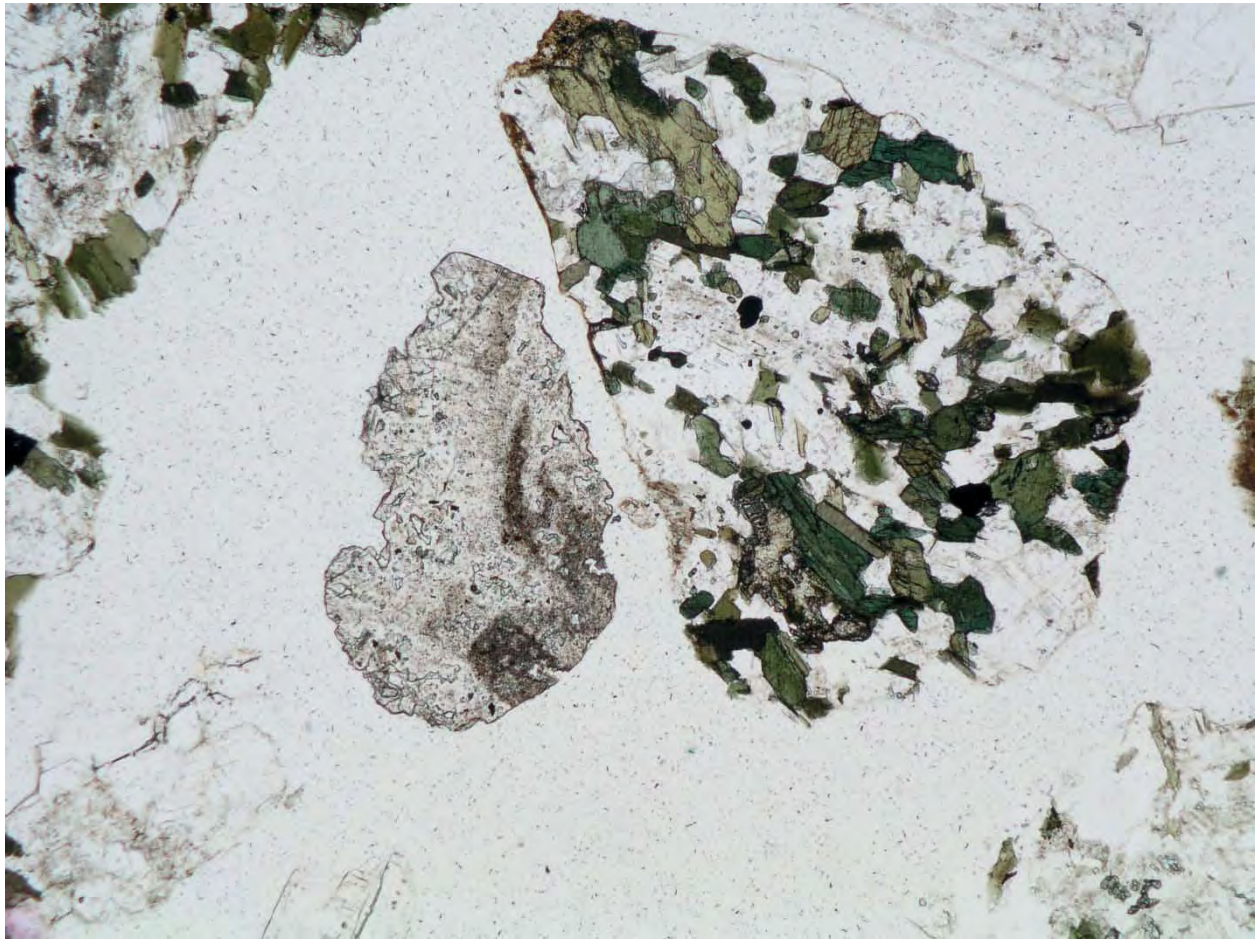

Fig. B.18. Amorphous silica scale (left of center) from well 68-20RD (896-899 m depth) showing a denser texture and entrapped mineral fragments. Horizontal width is 2.15 mm.

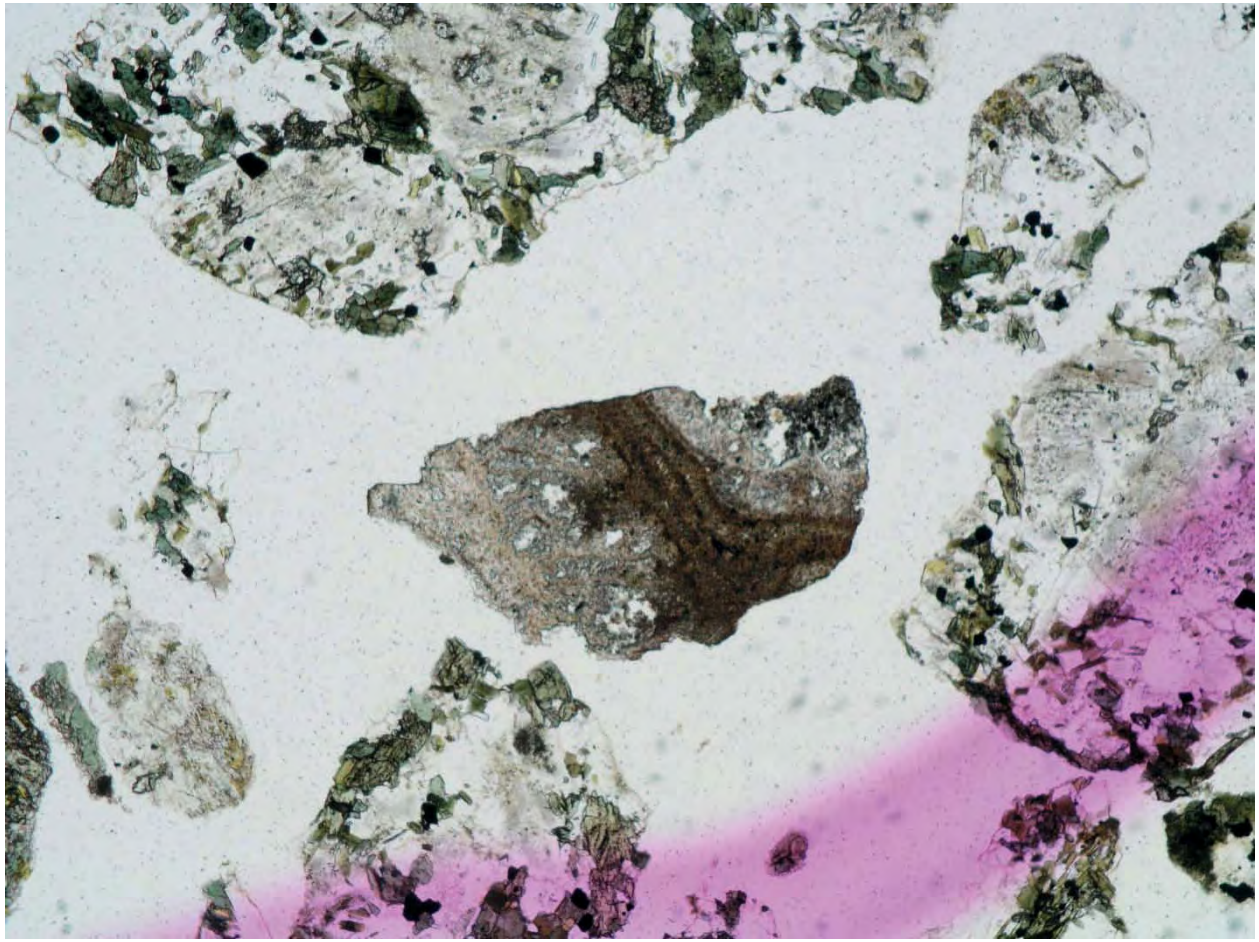

Fig. B.19. Amorphous silica scale (center) from well 68-20RD (939-942 m depth) showing a denser texture with banding and a more open texture to either side of the banding. Horizontal width is 2.15 mm.

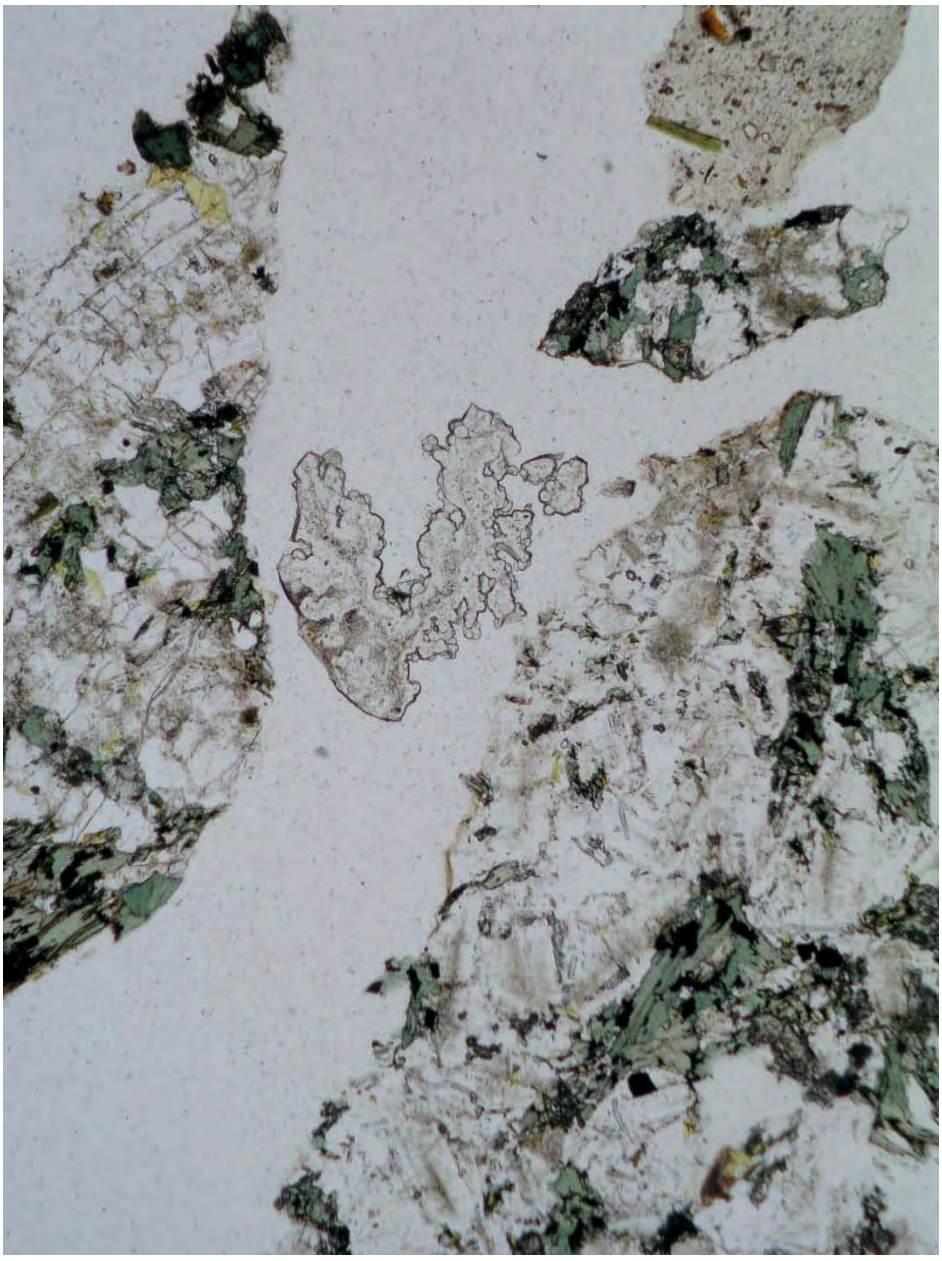

Fig. B.20. Amorphous silica scale (center) from well 68-20RD (942-945 m depth). Horizontal width is 2.15 mm.

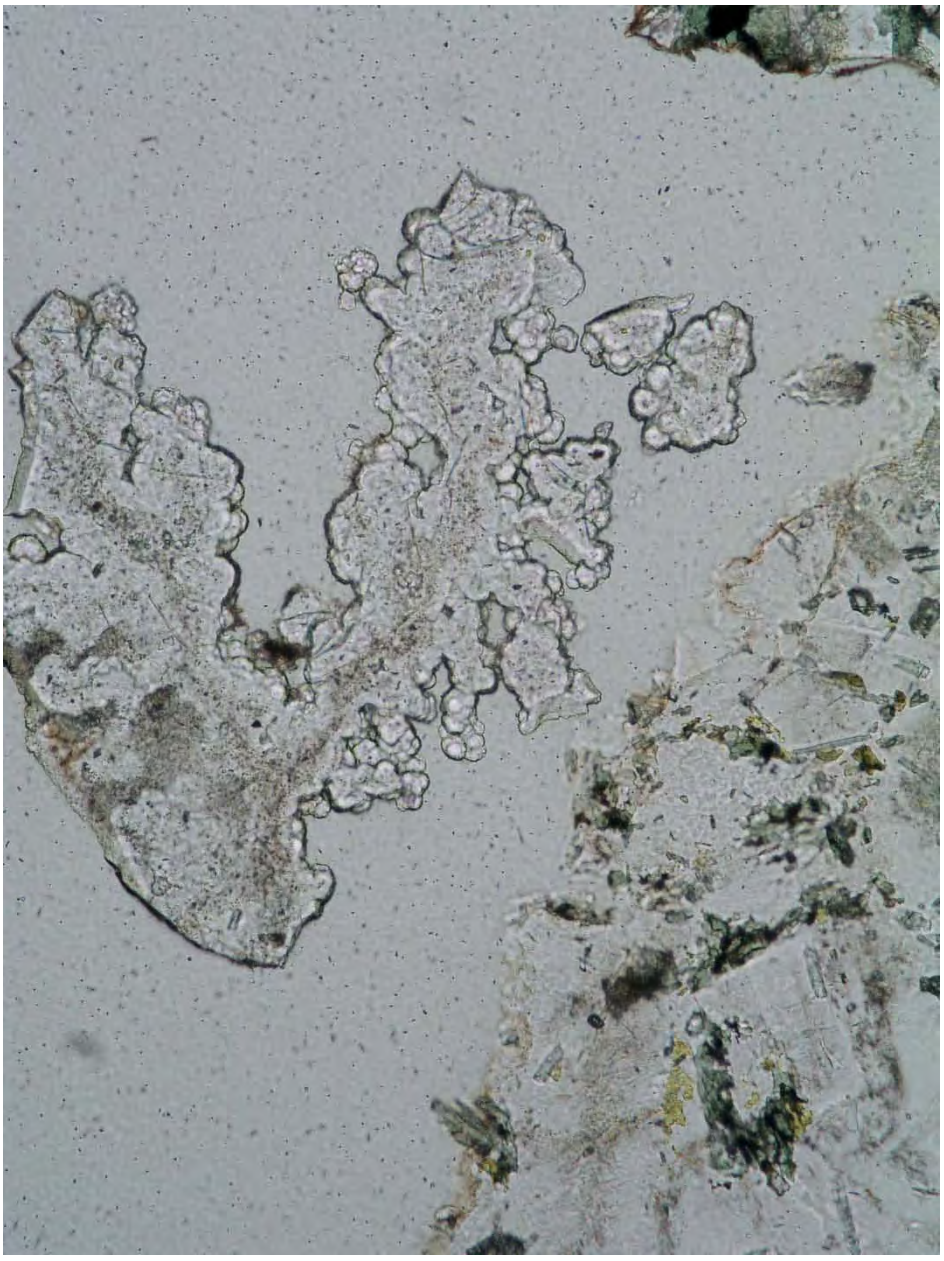

Fig. B.21. Detail of amorphous silica scale (top) from well 68-20RD (942-945 m depth). Horizontal width is 0.86 mm.

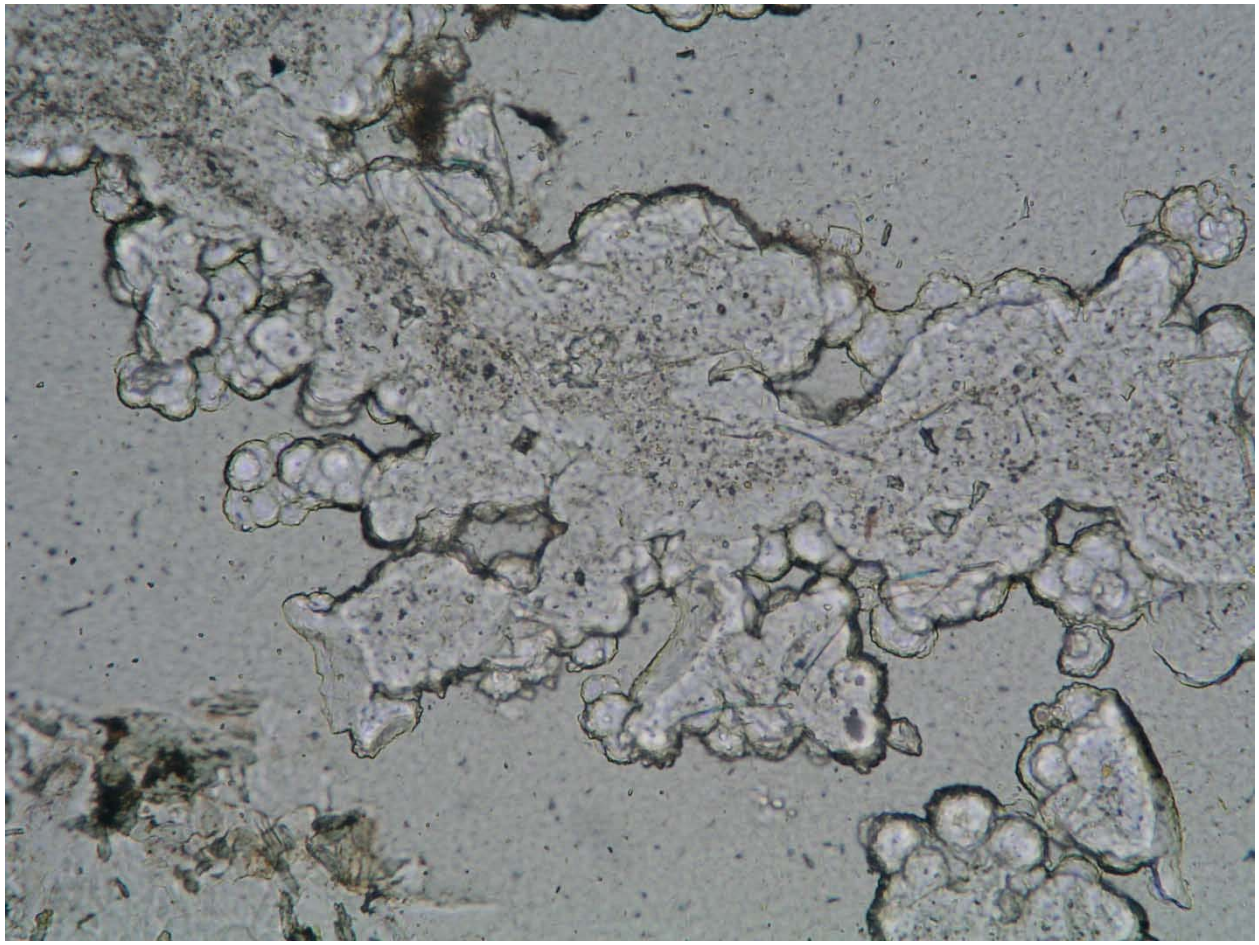

Fig. B.22. Detail of amorphous silica scale from well 68-20RD (942-945 m depth) showing botryoidal coalesced spheres and bumpy microspheres. Horizontal width is 0.43 mm.

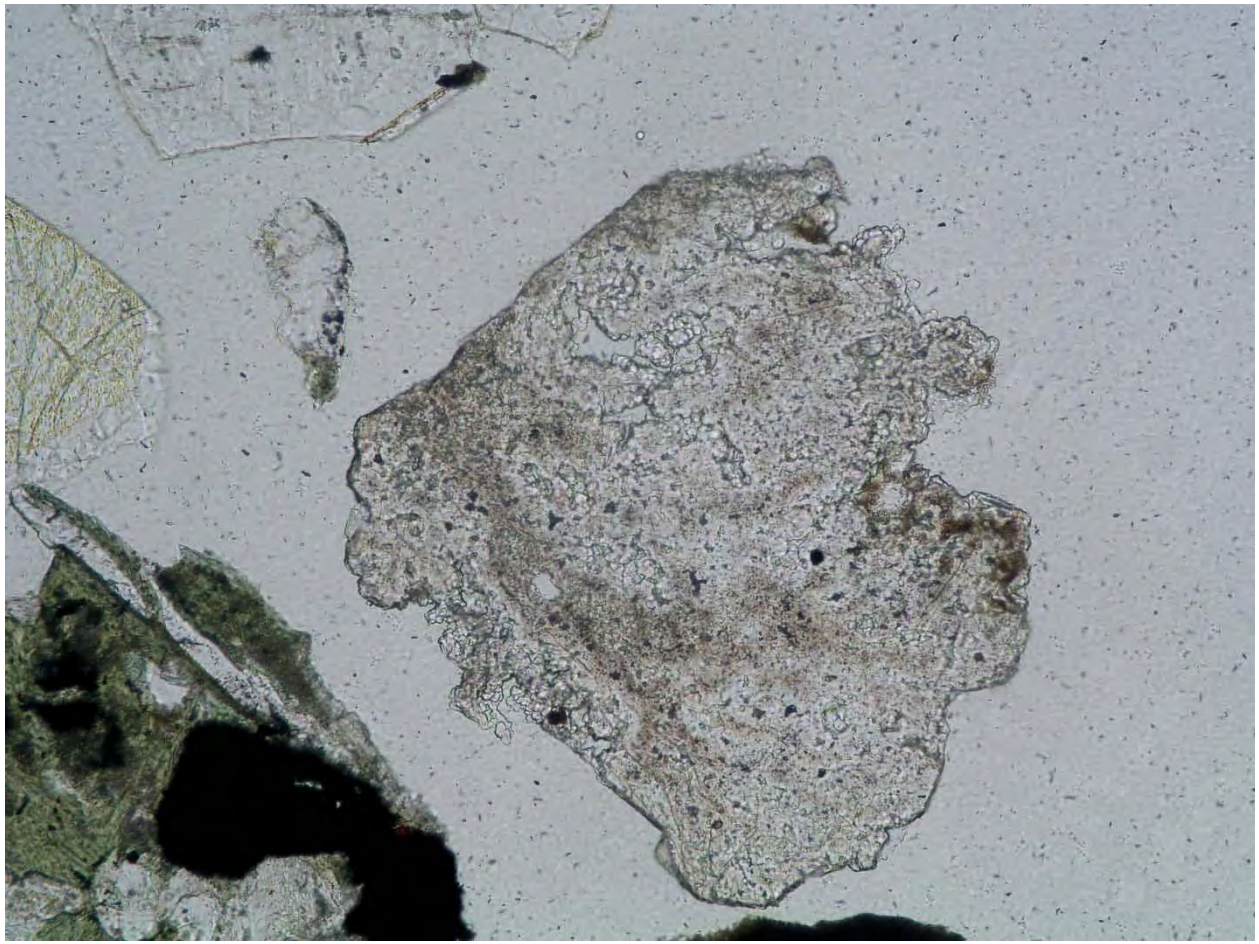

Fig. B.23. Amorphous silica scale from well 68-20RD (1707-1710 m depth) showing networks of spheres with silica infilling creating a dense texture. Mineral fragments are entrapped in the silica. Horizontal width is 0.86 mm.

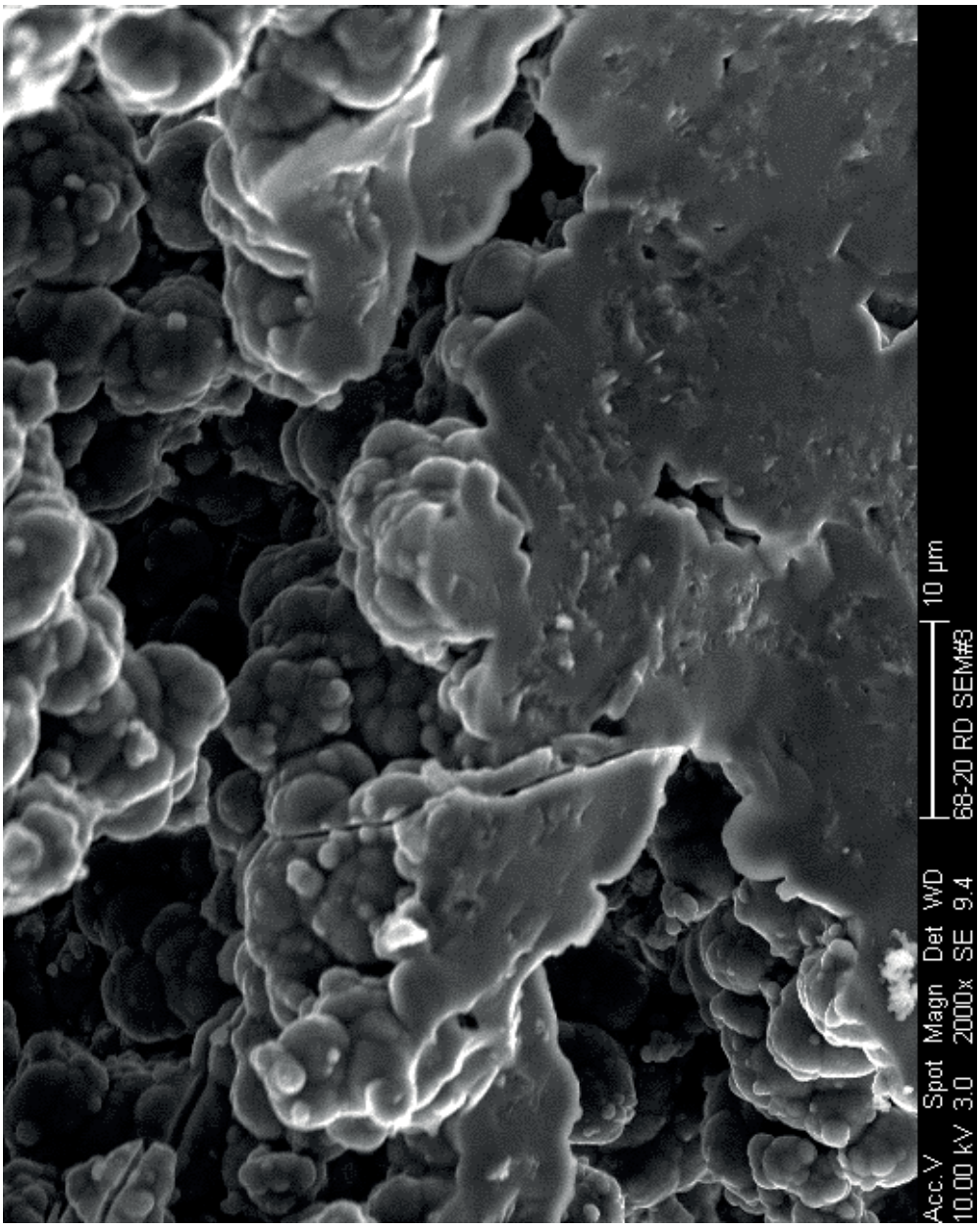

Fig. B.24. SEM image of amorphous silica scale from well 68-20RD (869-884 m depth).

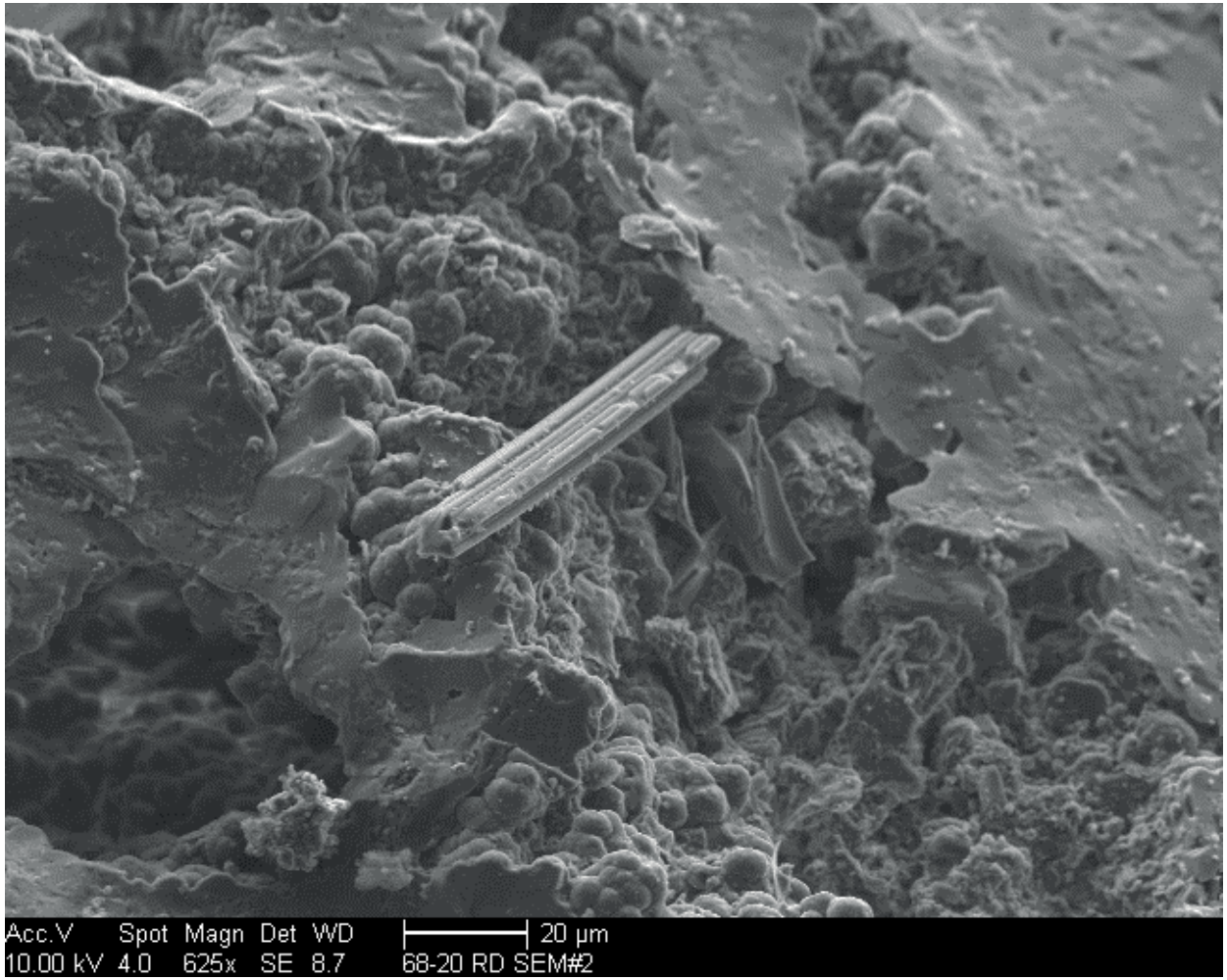

Fig. B.25. SEM image of amorphous silica scale from well 68-20RD (869-884 m depth) with a mineral fragment (center).

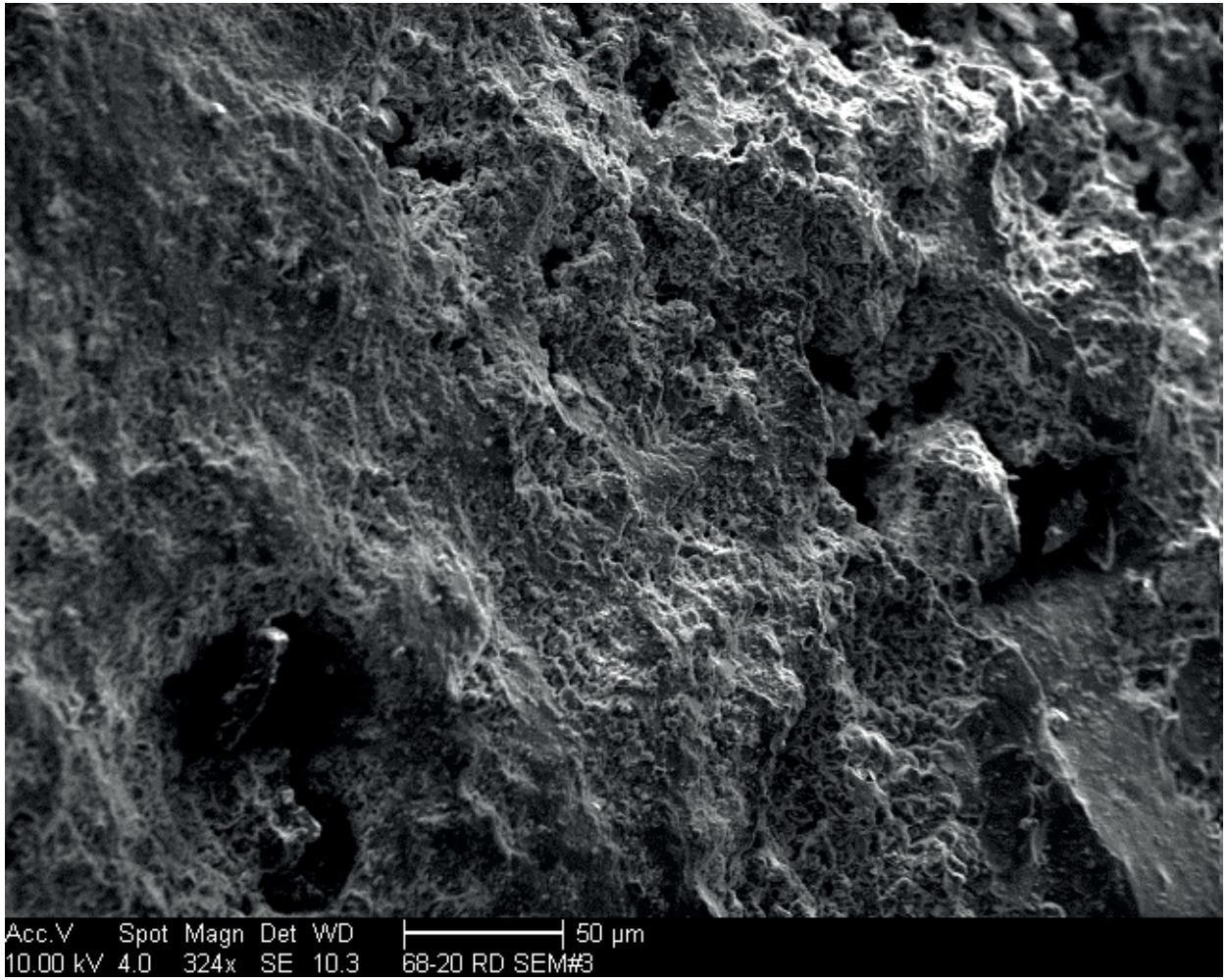

Fig. B.26. SEM image of amorphous silica scale from well 68-20RD (1710-1713 m depth).

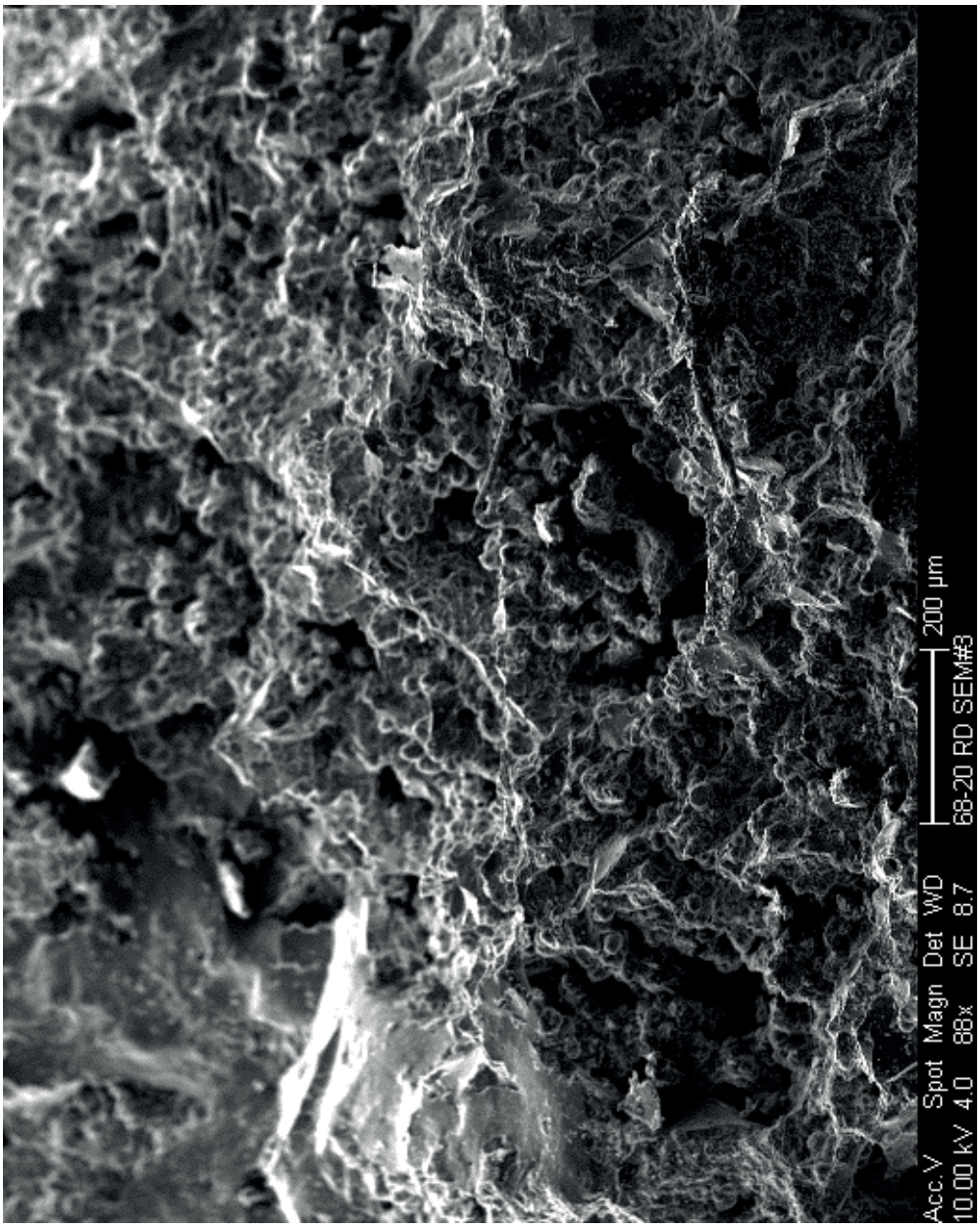

Fig. B.27. SEM image of amorphous silica scale from well 68-20RD (1710-1713 m depth).

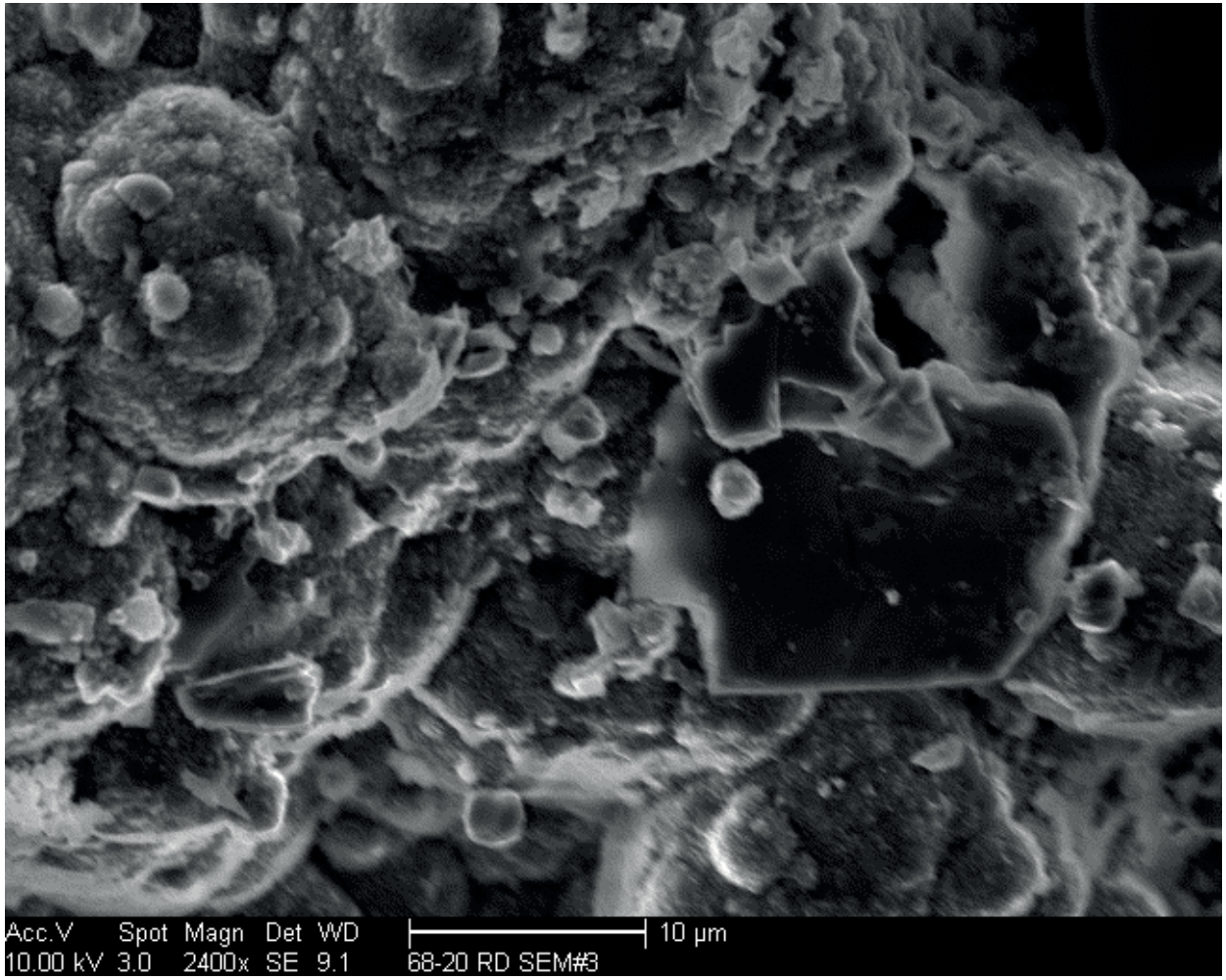

Fig. B.28. SEM image of amorphous silica scale from well 68-20RD (1710-1713 m depth).

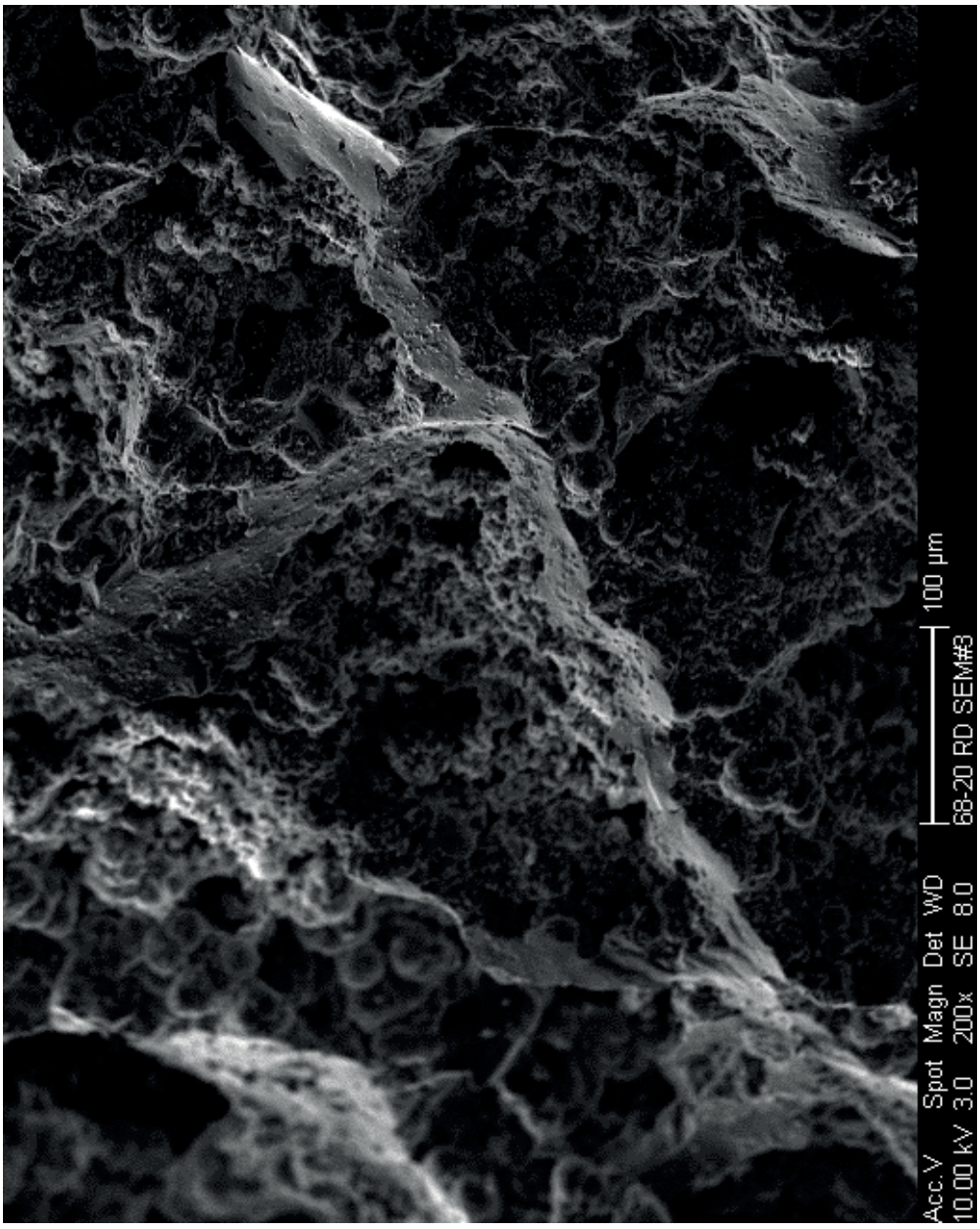

Fig. B.29. SEM image of amorphous silica scale from well 68-20RD (1710-1713 m depth).

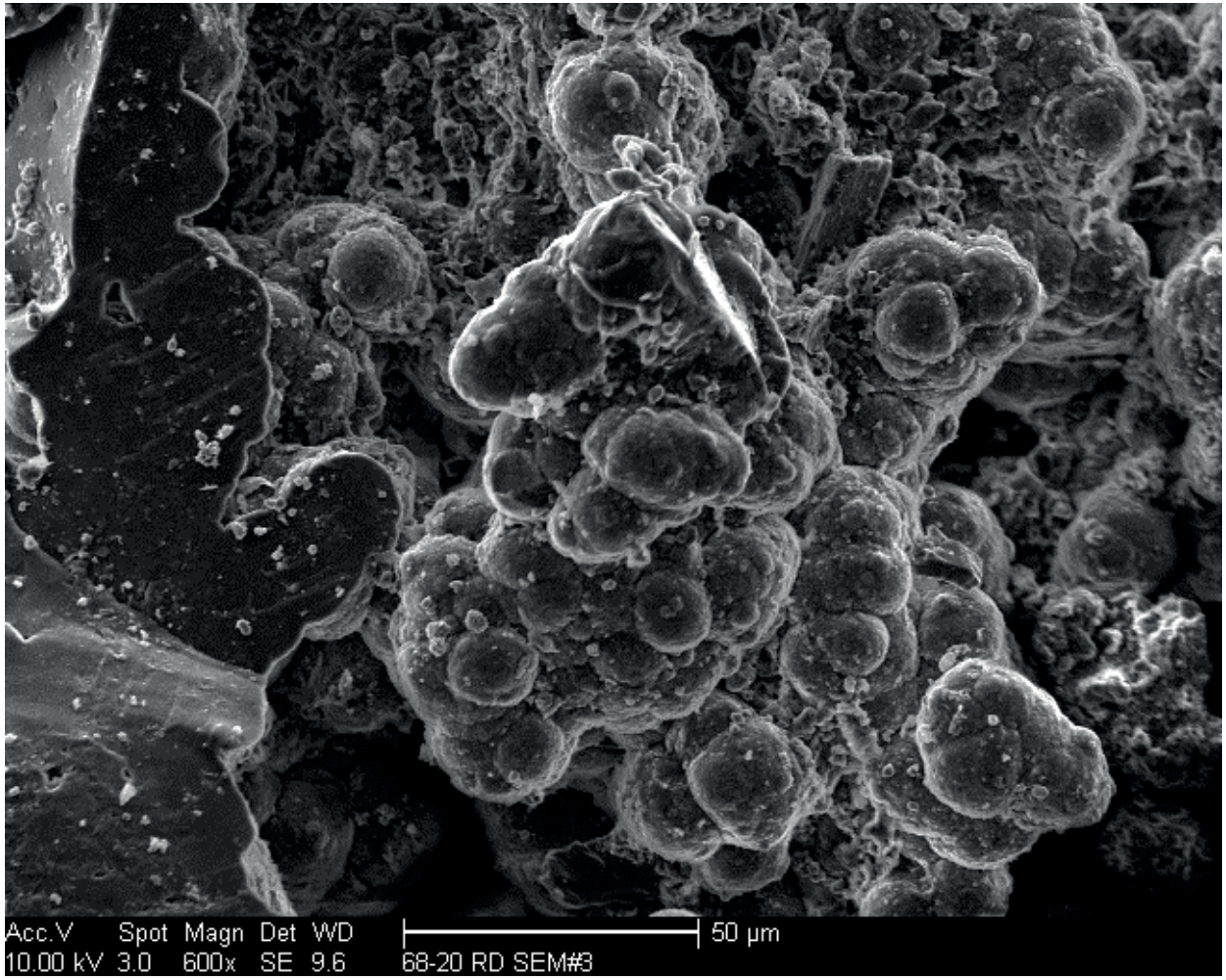

Fig. B.30. SEM image of amorphous silica scale from well 68-20RD (1710-1713 m depth).

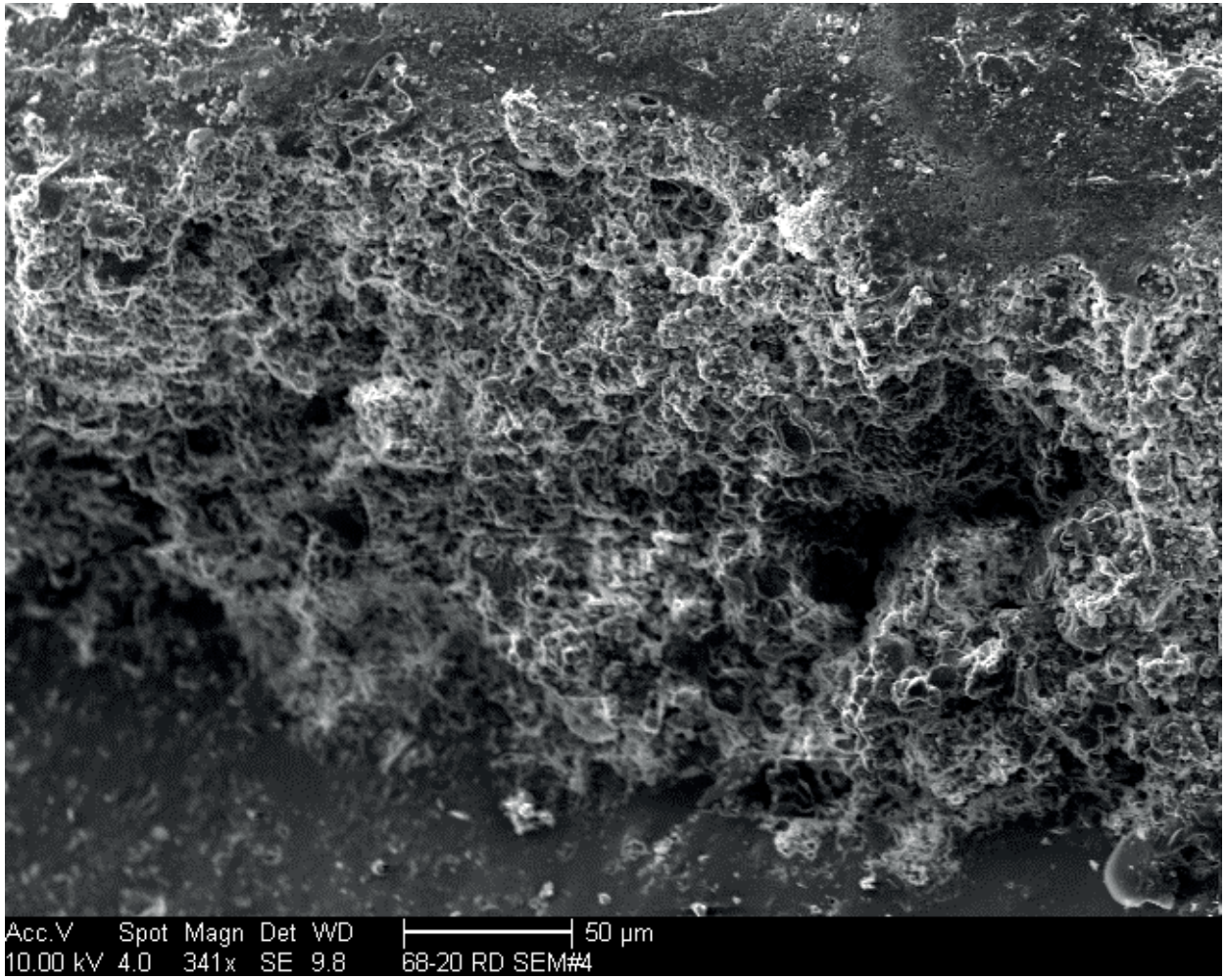

Fig. B.31. SEM image of amorphous silica scale from well 68-20RD (1710-1713 m depth).

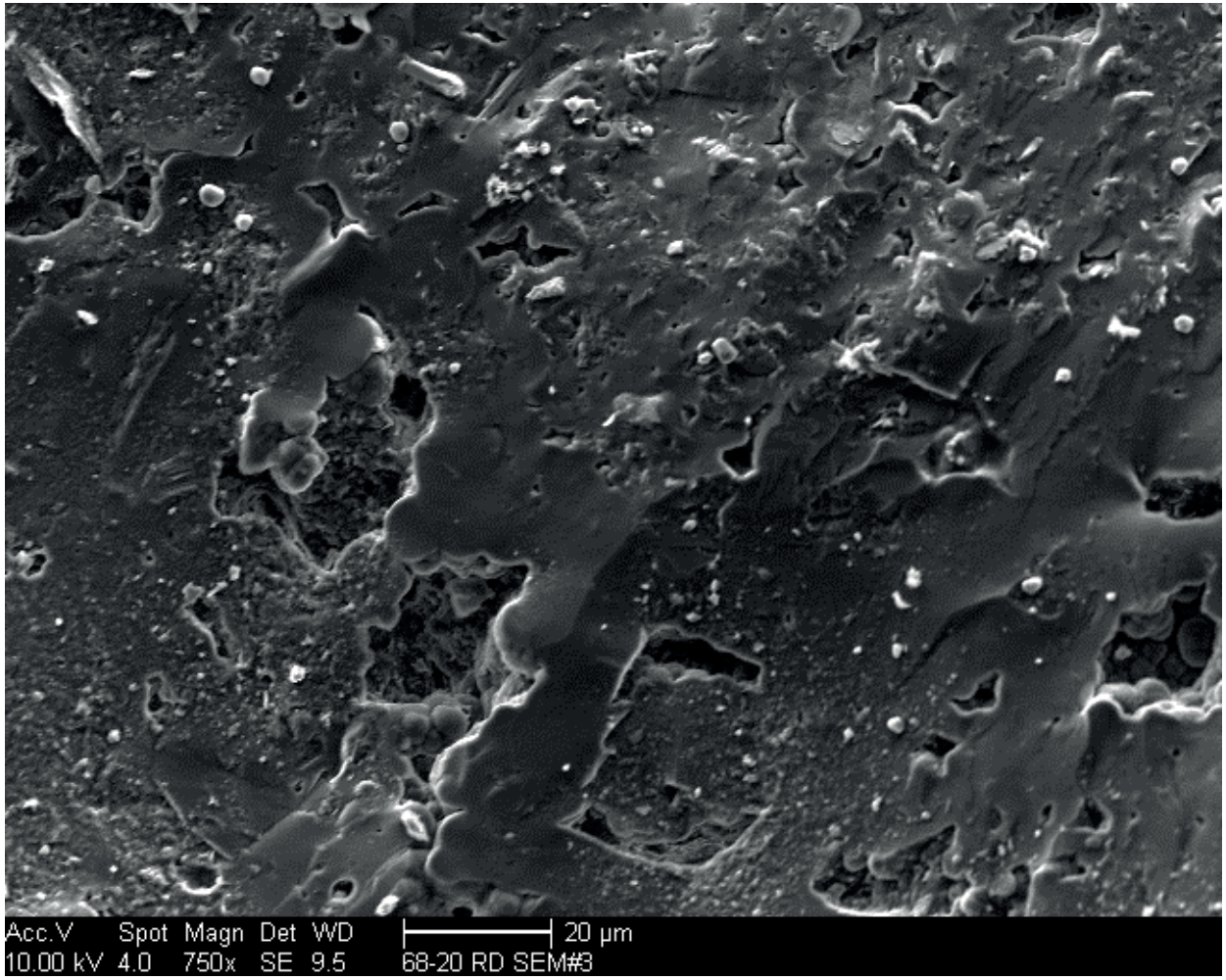

Fig. B.32. SEM image of amorphous silica scale from well 68-20RD (1710-1713 m depth).

Fig. B.33. SEM image of amorphous silica scale from well 68B-20RD (1030-1033 m depth).

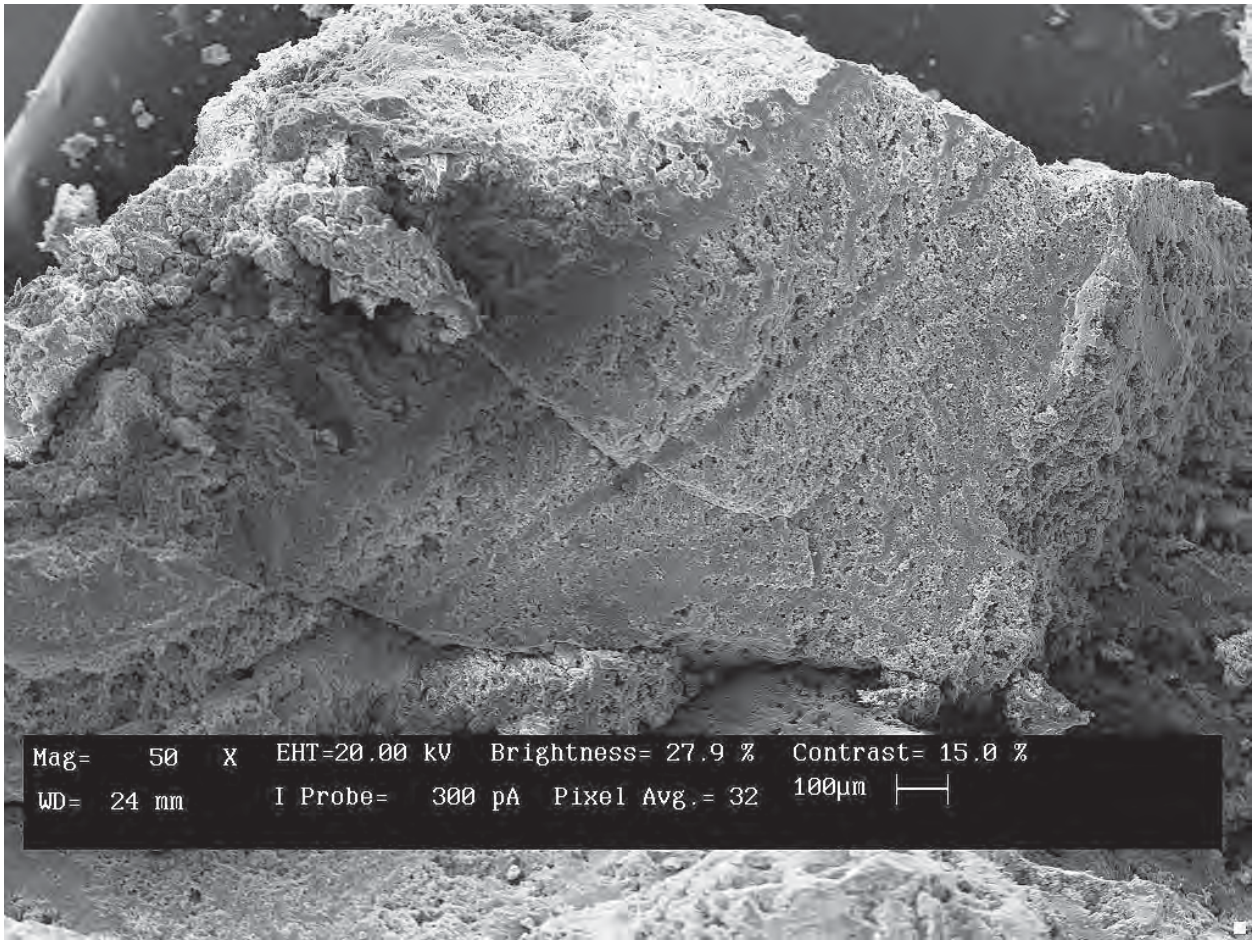

Fig. B.34. SEM image of amorphous silica scale from well 68B-20RD (1030-1033 m depth) showing some banding.

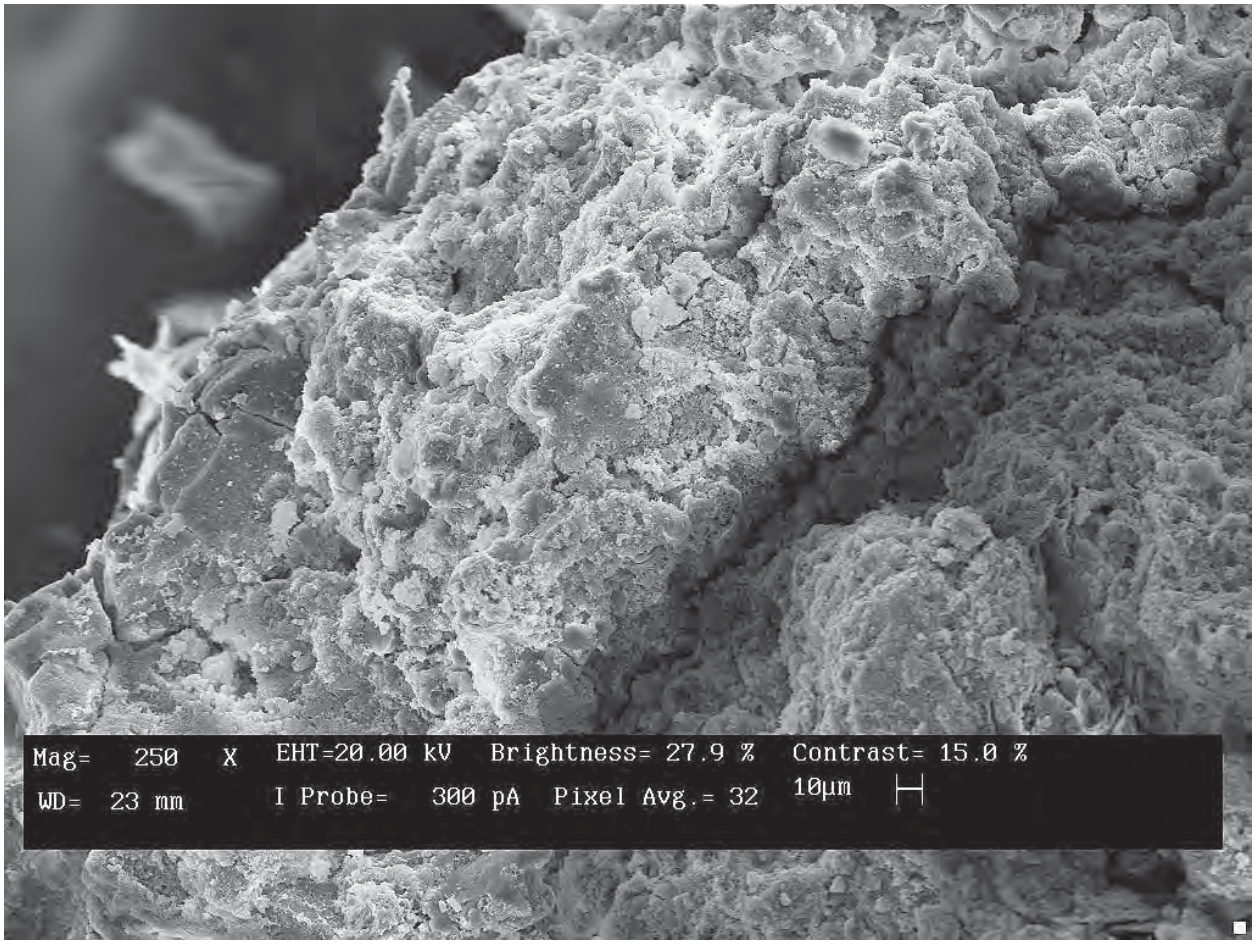

Fig. B.35. SEM image of scale from well 68B-20RD (1030-1033 m depth) showing a possible clay and/or anhydrite coating (EDX indicates Si>O>Ca>Al>S>Fe).

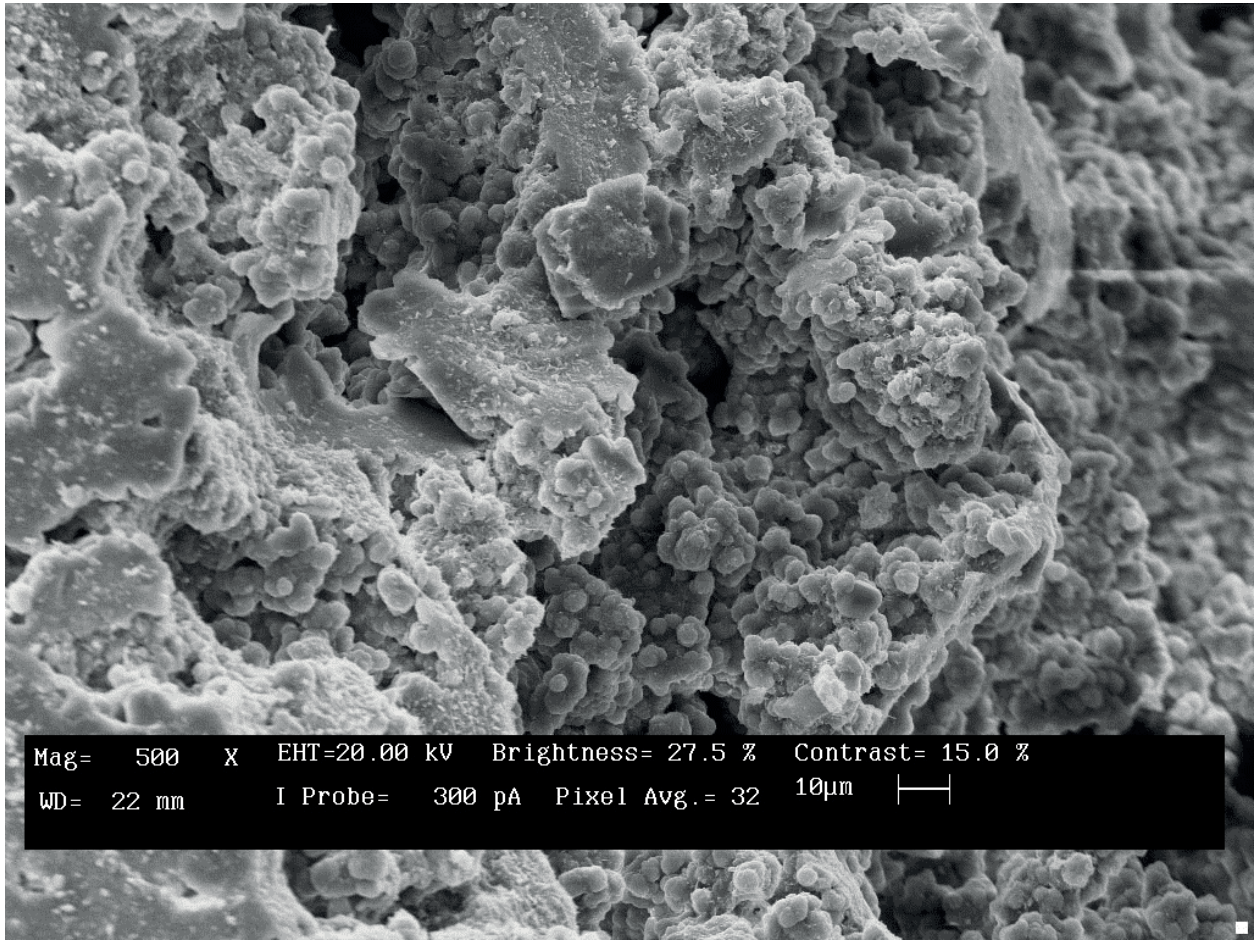

Fig. B.36. SEM image of amorphous silica scale from well 68B-20RD (1030-1033 m depth).

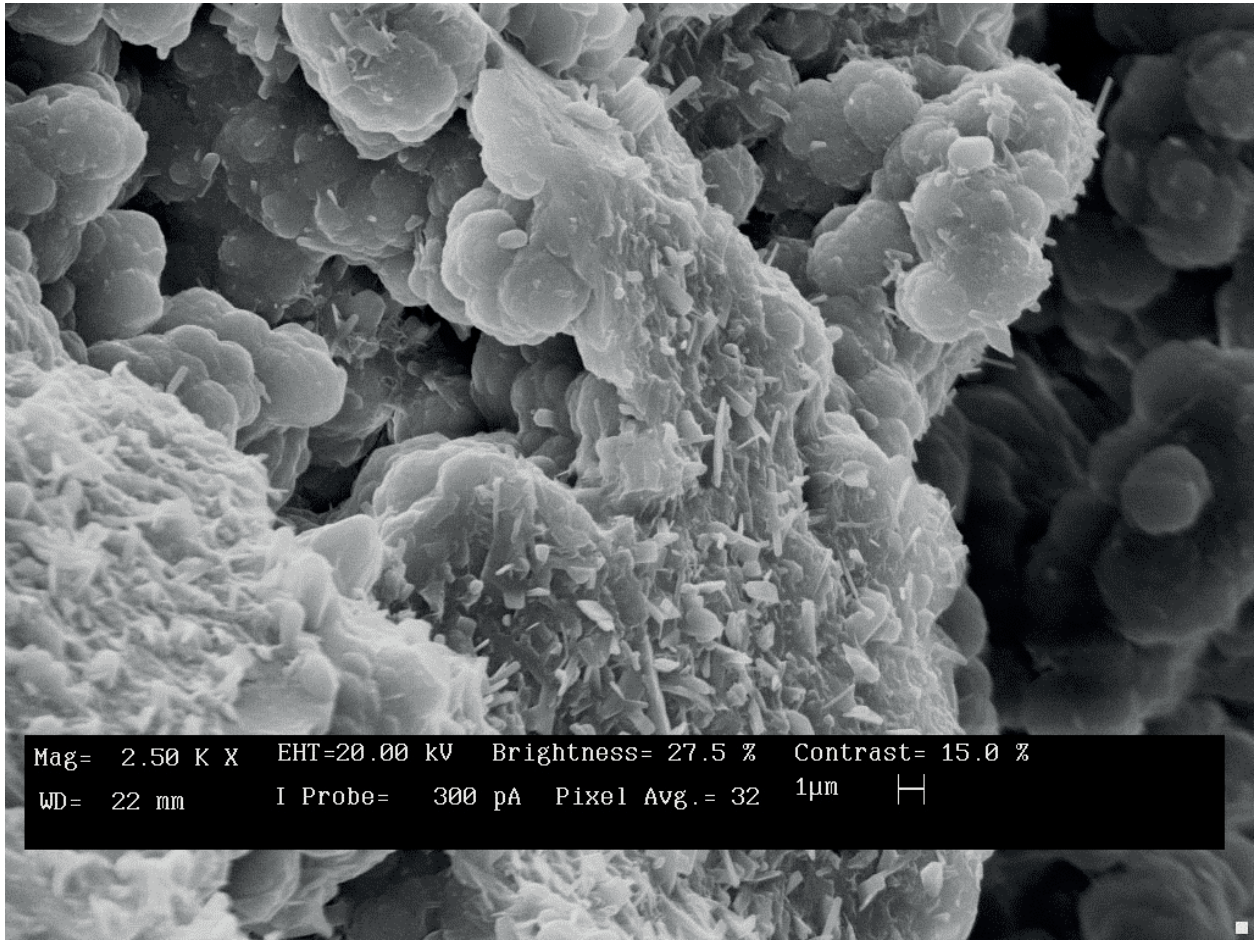

Fig. B.37. SEM image of amorphous silica scale from well 68B-20RD (1030-1033 m depth) coated with crystals. Could not get a very good EDX spectra for these small crystals.

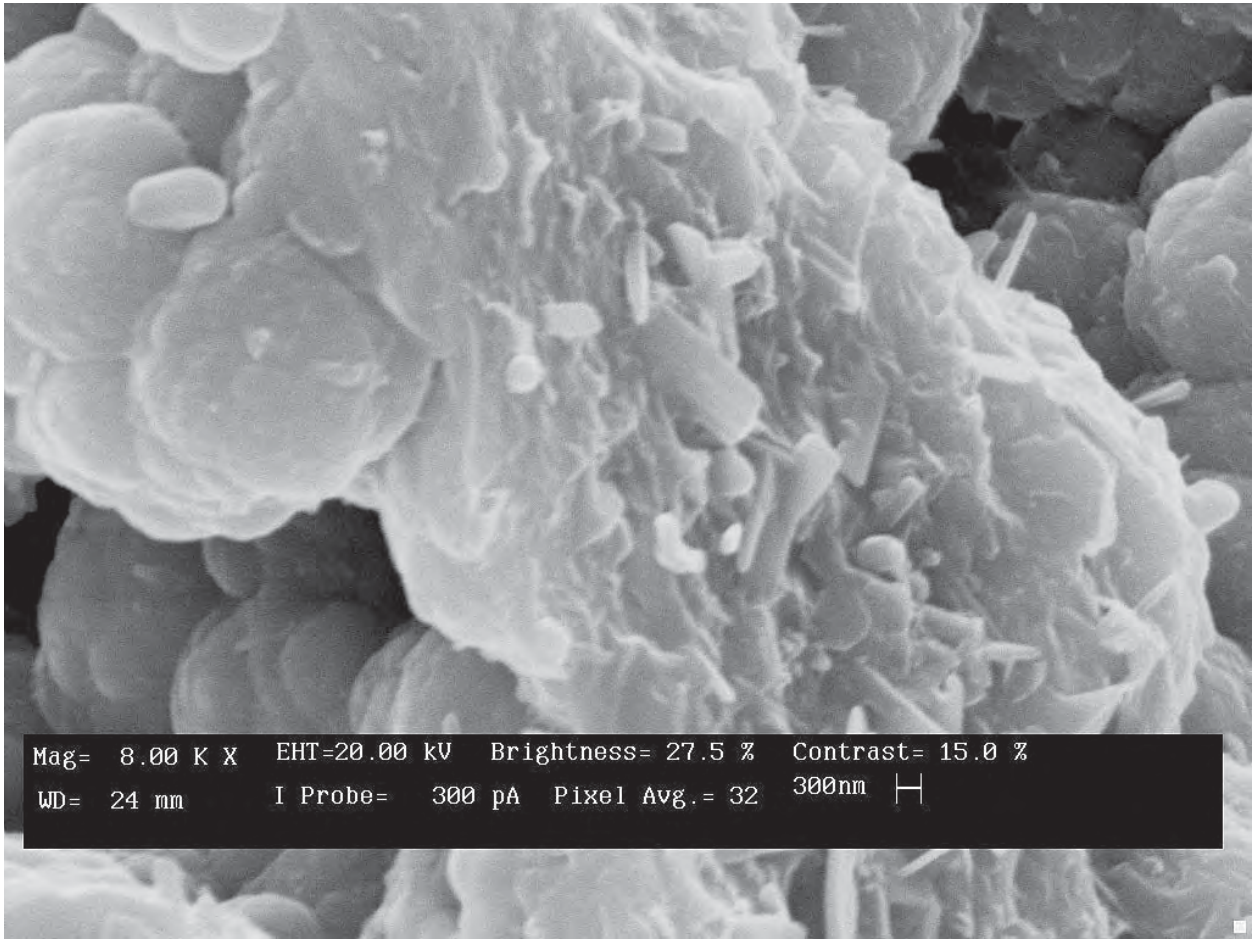

Fig. B.38. SEM image showing detail of the coating on amorphous silica scale from well 68B-20RD (1030-1033 m depth). Could not get a very good EDX spectra for these small crystals.

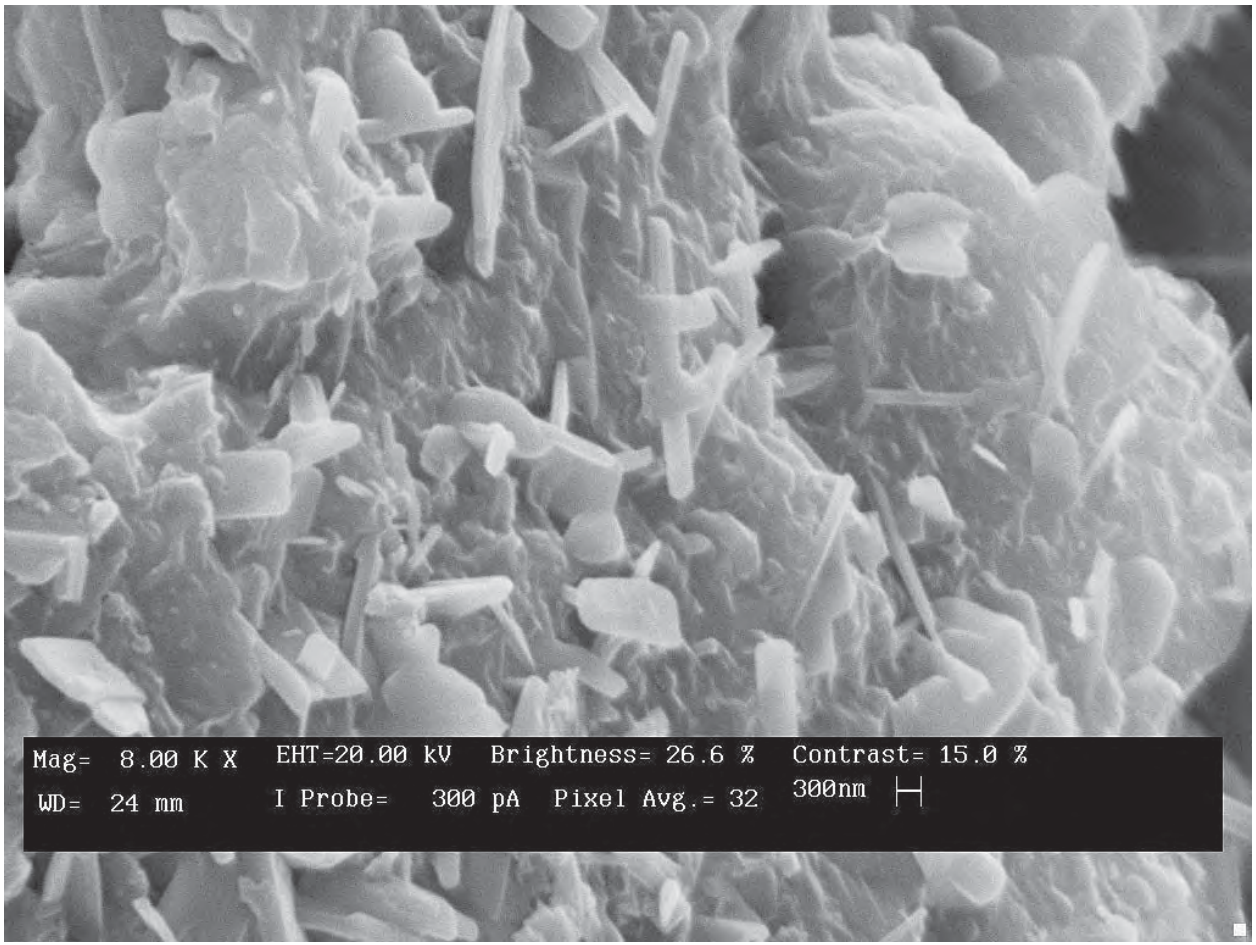

Fig. B.39. SEM image of small crystals on amorphous silica scale from well 68B-20RD (1030-1033 m depth). Could not get a good EDX spectra with such small crystals.

Fig. B.40. SEM image of amorphous silica scale from well 68B-20RD (1030-1033 m depth) with mineral coating of small crystals. EDX spectra shows Si>Ca>Na>O for the large crystal in the center.

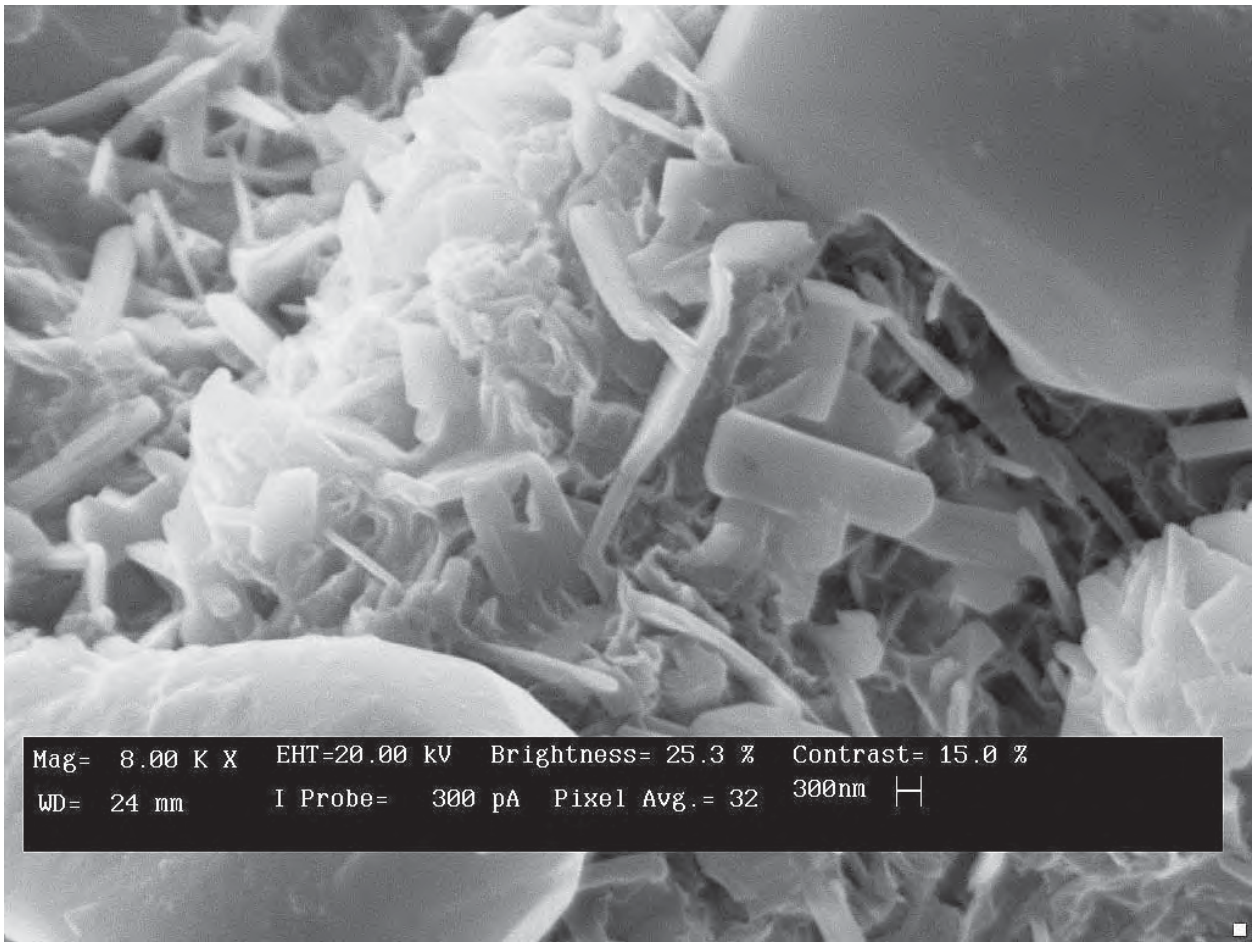

Fig. B.41. SEM image of small crystals coating amorphous silica scale from well 68B-20RD (1030-1033 m depth). EDX spectra shows Si>O>S>Al>Na>Ca for the small crystals (center).

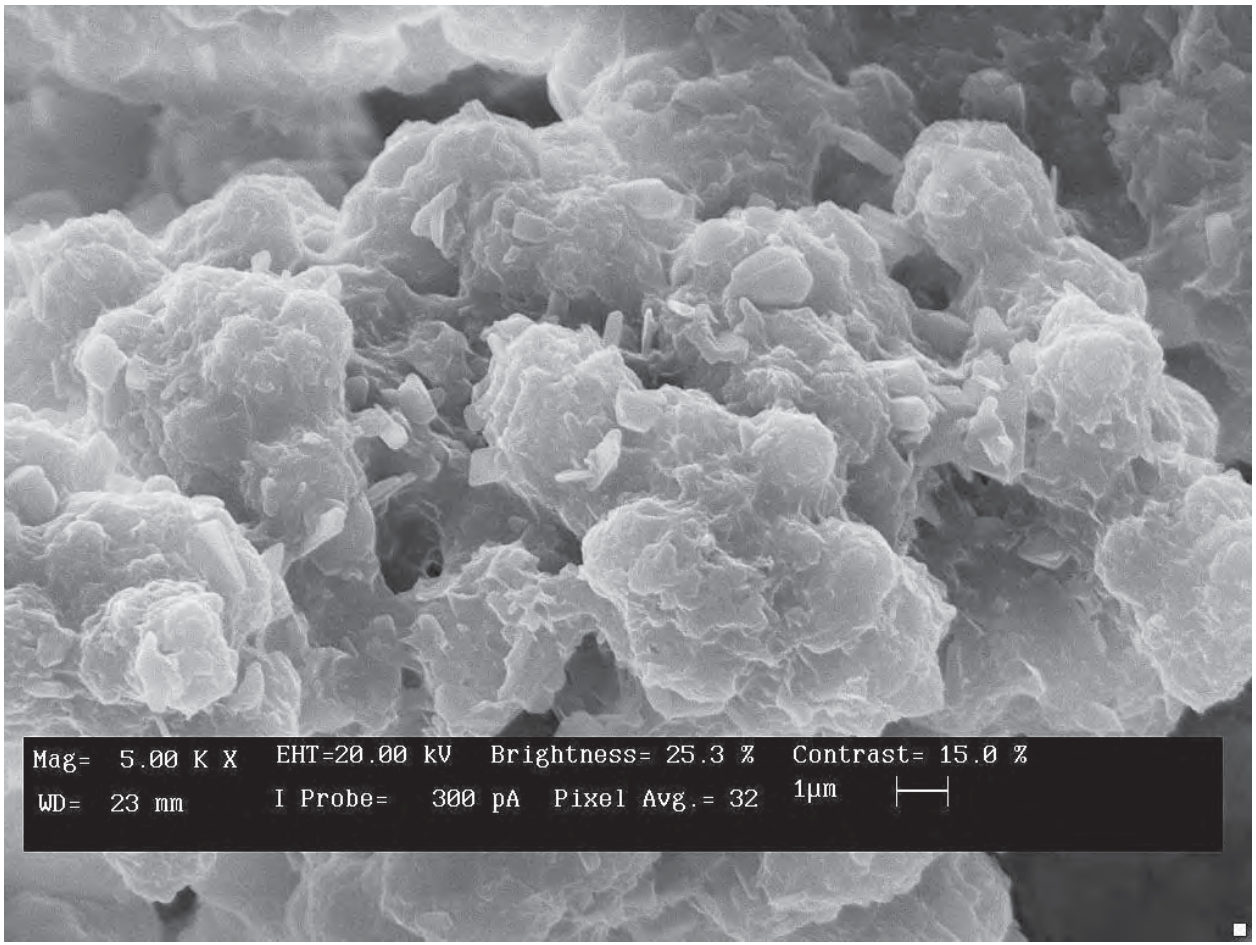

Fig. B.42. SEM image of amorphous silica scale from well 68B-20RD (1030-1033 m depth) showing an unusual texture that may be related to dissolution and more of the small crystals coating the silica. Could not get a good EDX spectra of these small crystals.

APPENDIX C

PHOTOMICROGRAPHS OF MINERAL SCALE FROM SALTON SEA WELL ELMORE IW-3 RD

This appendix consists of photomicrographs of mineral scale samples found in cuttings from Salton Sea well Elmore IW-3 RD. There are 9 images taken with a petrographic microscope and 12 images taken with a Leo 440 scanning electron microscope (SEM) with a tungsten filament electron source. An energy dispersive x-ray (EDX) was used for elemental analysis with the SEM.

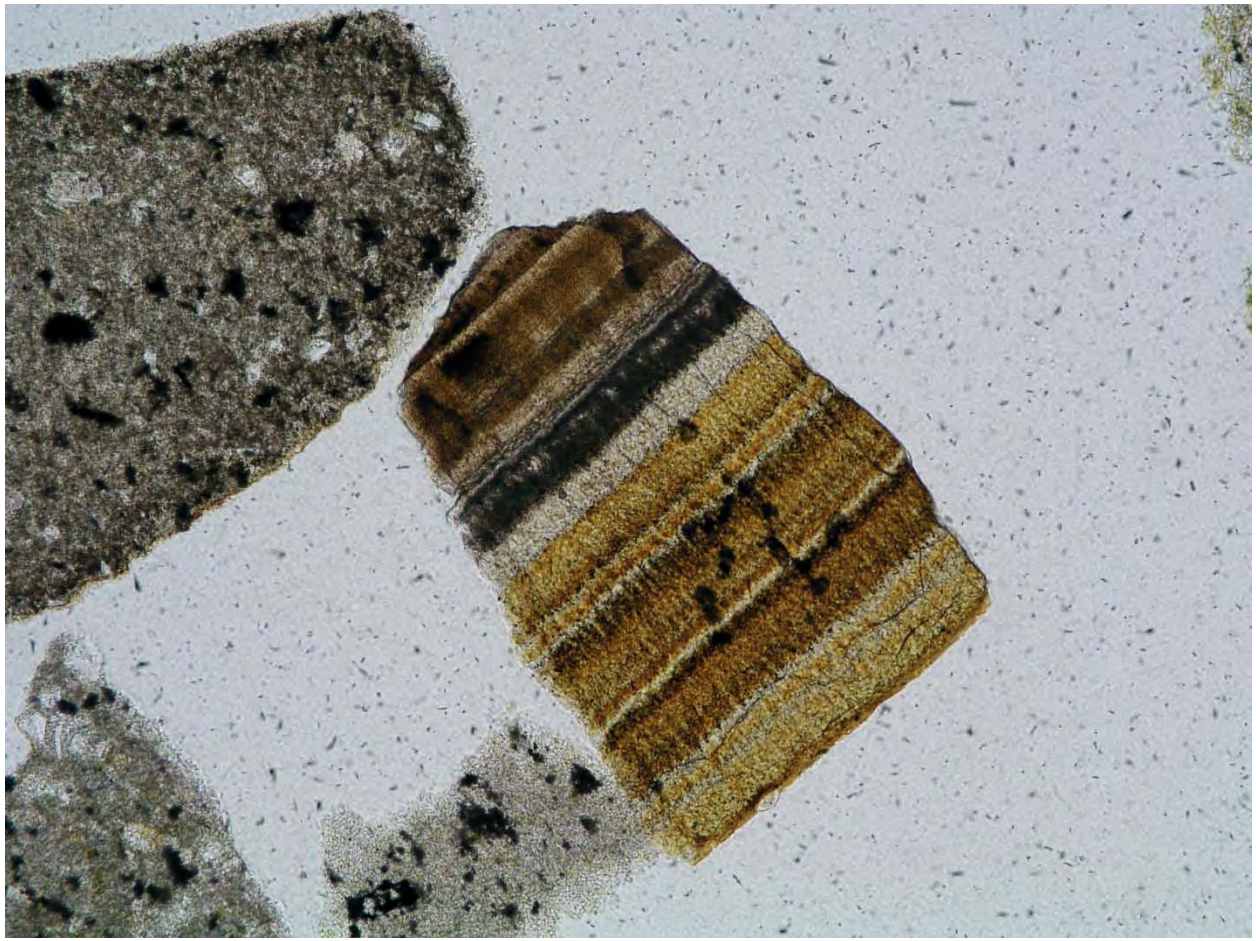

Fig. C.1. Banded mineral scale from Elmore IW-3 RD2 at 2365-2368 m depth (plain polarized light). Scale consists mainly of barite and fluorite. Horizontal width is 0.86 mm.

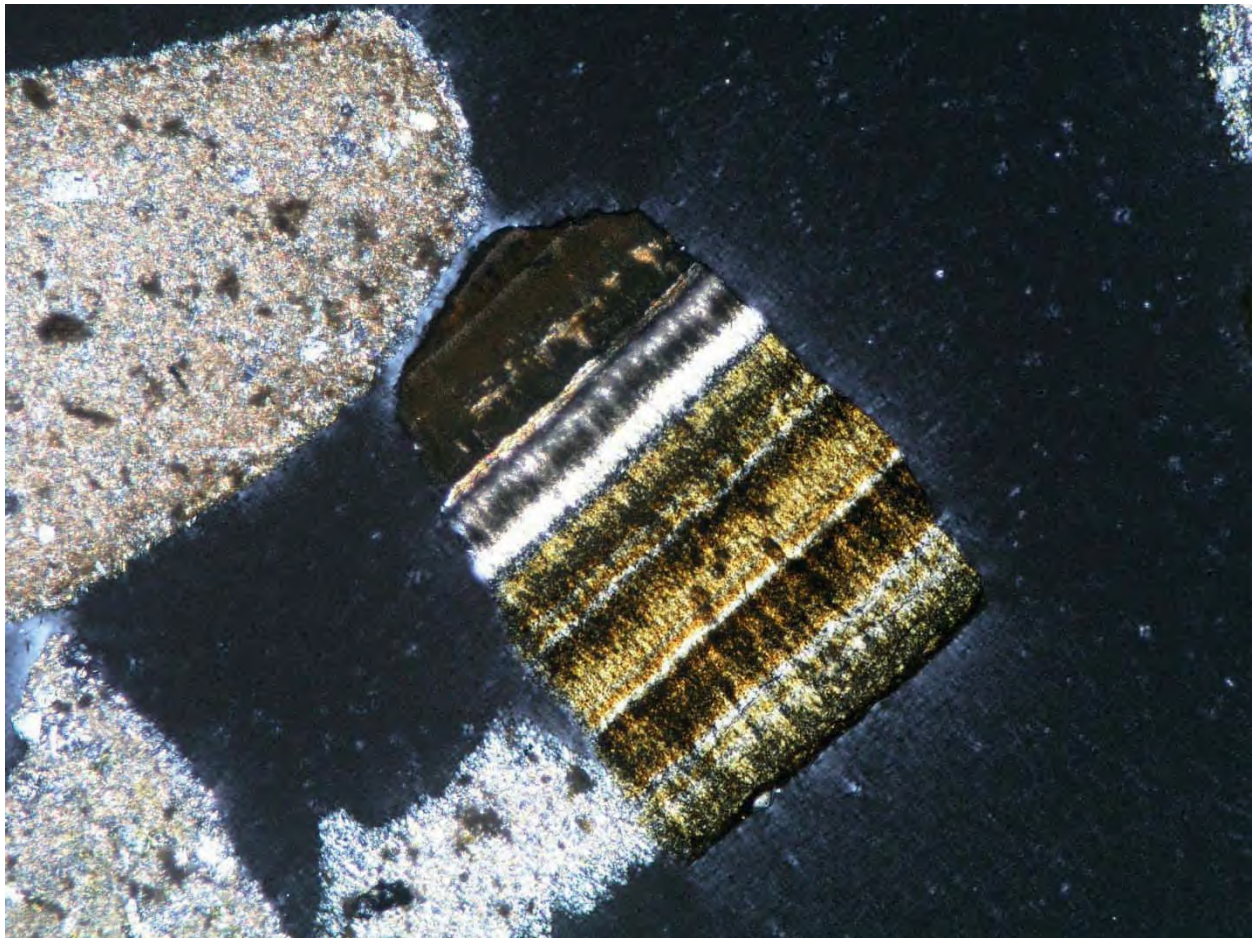

Fig. C.2. Banded mineral scale from Elmore IW-3 RD2 at 2365-2368 m depth (crossed nicols). Scale consists mainly of barite and fluorite. Horizontal width is 0.86 mm.

Fig. C.3. Banded mineral scale from Elmore IW-3 RD2 at 2365-2368 m depth (plane polarized light). Scale consists mainly of barite and fluorite. Horizontal width is 0.86 mm.

Fig. C.4. Banded mineral scale from Elmore IW-3 RD2 at 2365-2368 m depth (crossed nicols). Scale consists mainly of barite and fluorite. Horizontal width is 0.86 mm.

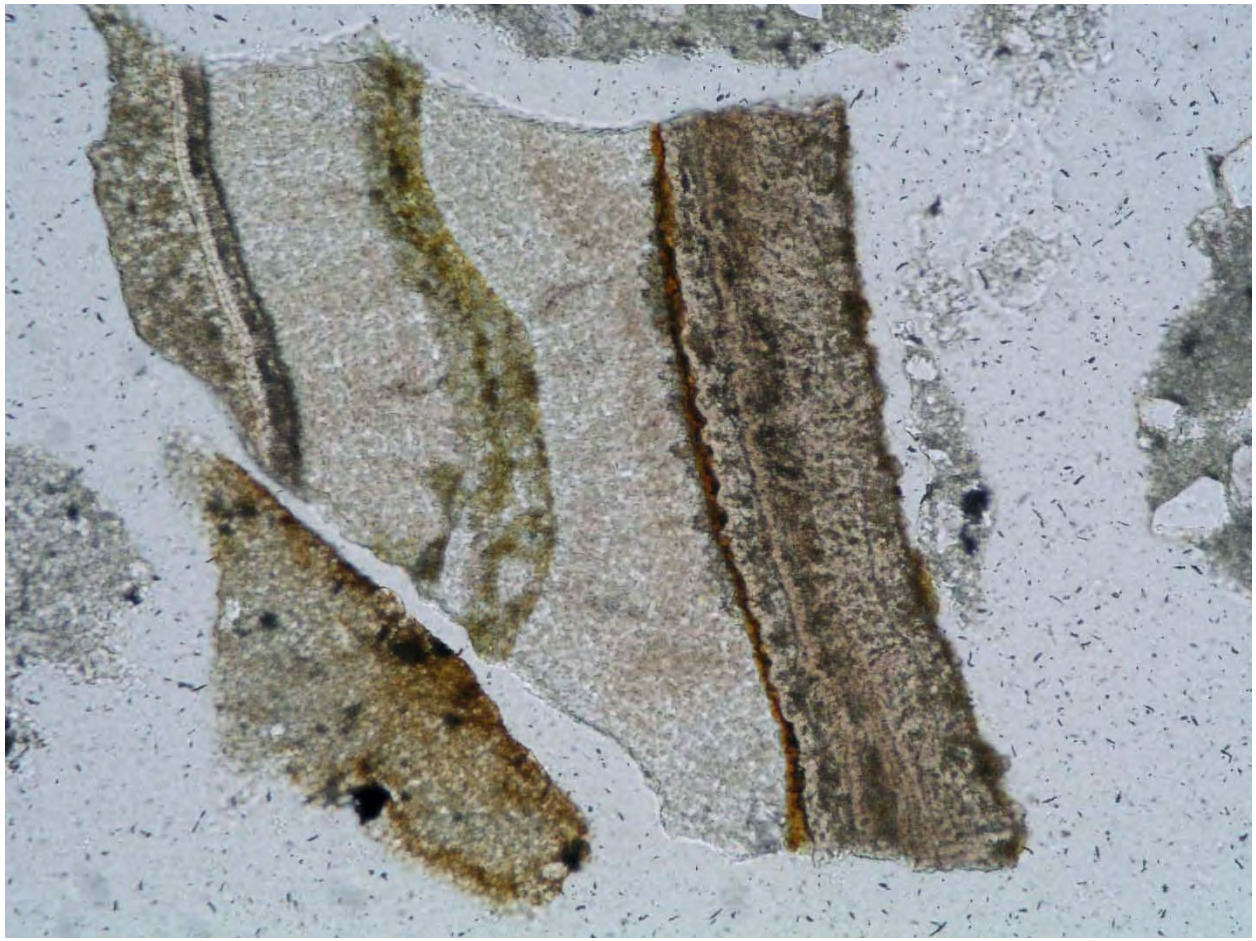

Fig. C.5. Banded mineral scale from Elmore IW-3 RD2 at 2368-2371 m depth (plane polarized light). Scale consists mainly of barite and fluorite. Horizontal width is 0.86 mm.

Fig. C.6. Banded mineral scale from Elmore IW-3 RD2 at 2368-2371 m depth (crossed nicols). Scale consists mainly of barite and fluorite. Horizontal width is 0.86 mm.

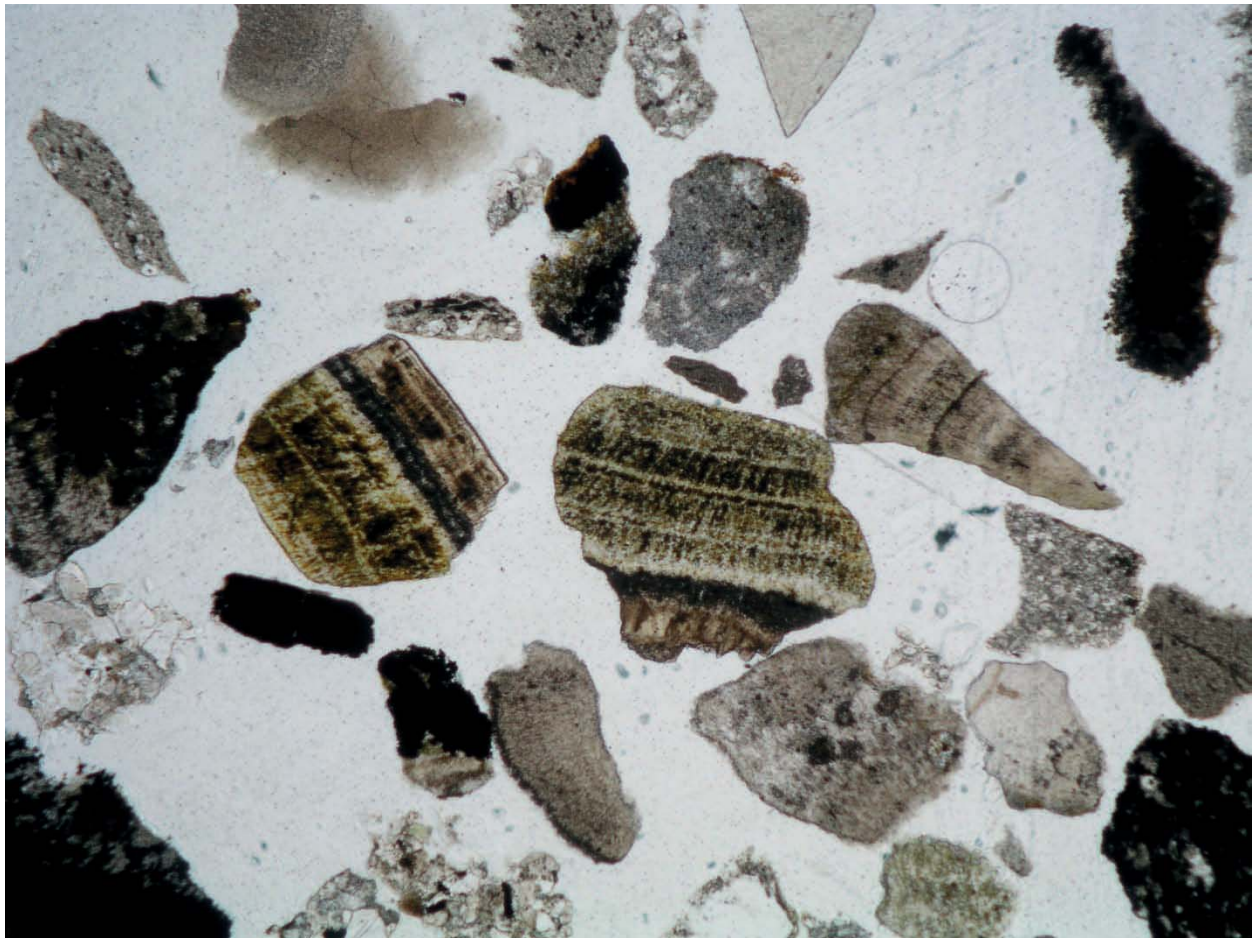

Fig. C.7. Banded mineral scale from Elmore IW-3 RD2 at 2365-2368 m depth (plane polarized light). Scale consists mainly of barite and fluorite. Horizontal width is 0.86 mm.

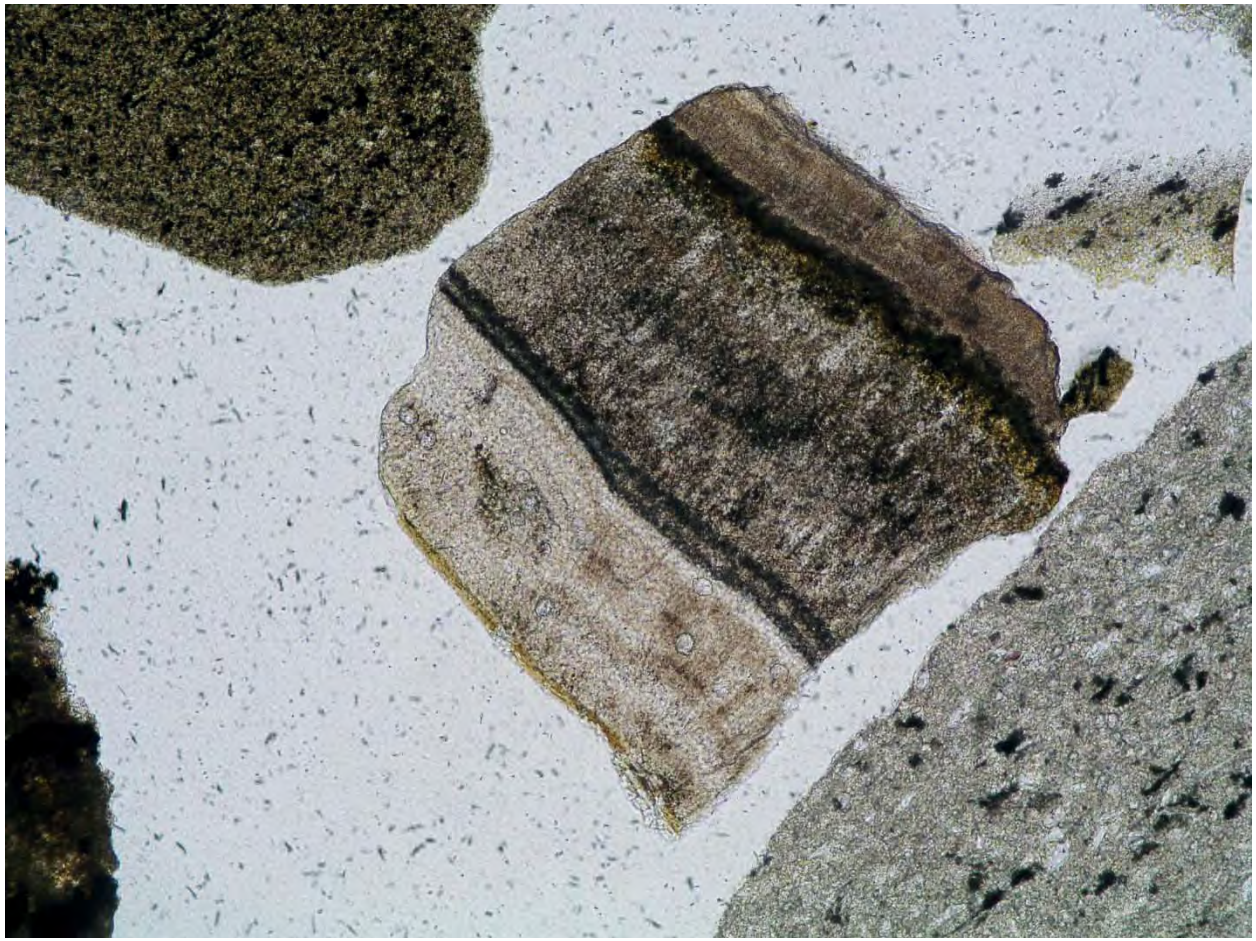

Fig. C.8. Banded mineral scale from Elmore IW-3 RD2 at 2365-2368 m depth (plane polarized light). Scale consists mainly of barite and fluorite. Horizontal width is 0.86 mm.

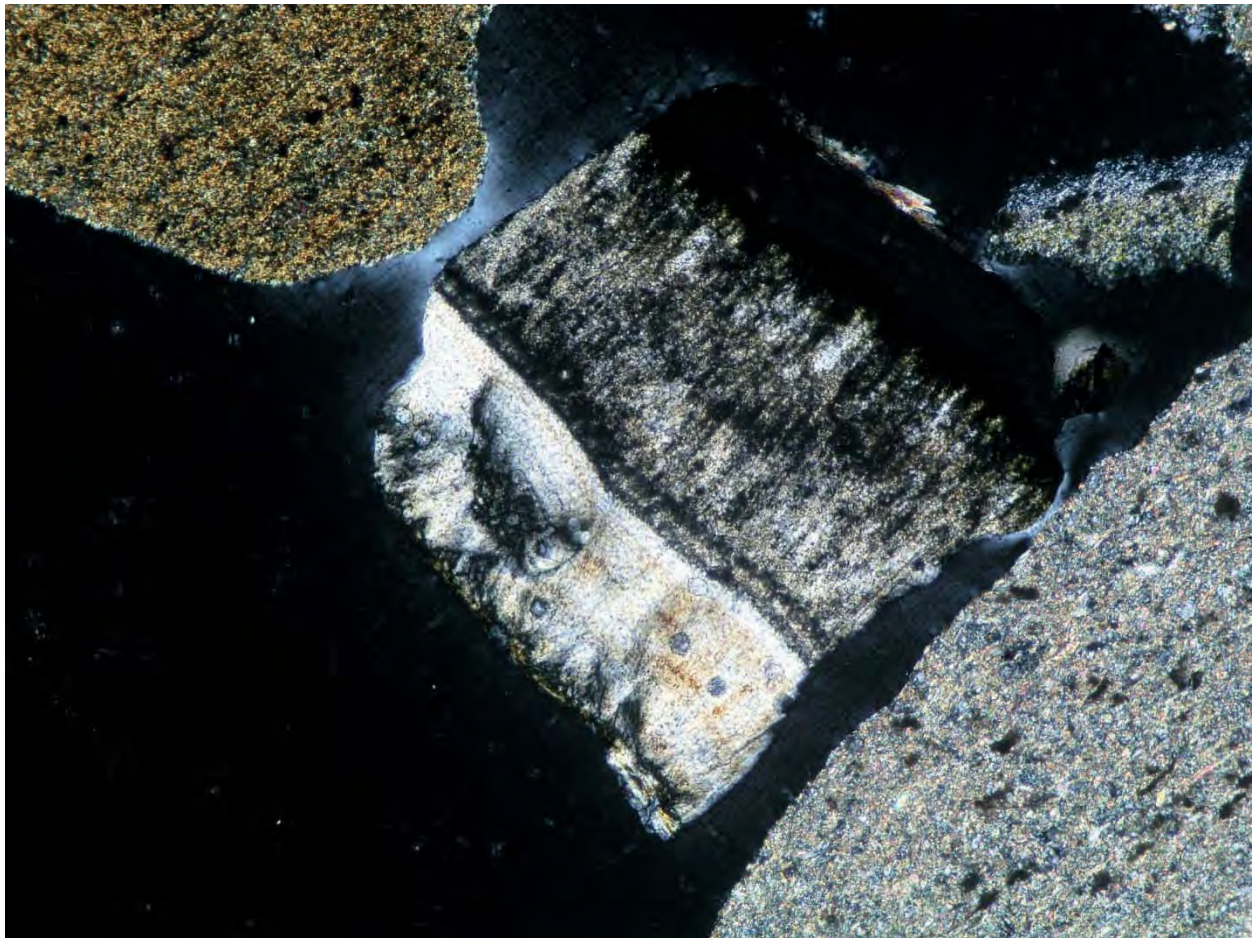

Fig. C.9. Banded mineral scale from Elmore IW-3 RD2 at 2365-2368 m depth (crossed nicols). Scale consists mainly of barite and fluorite. Horizontal width is 0.86 mm.

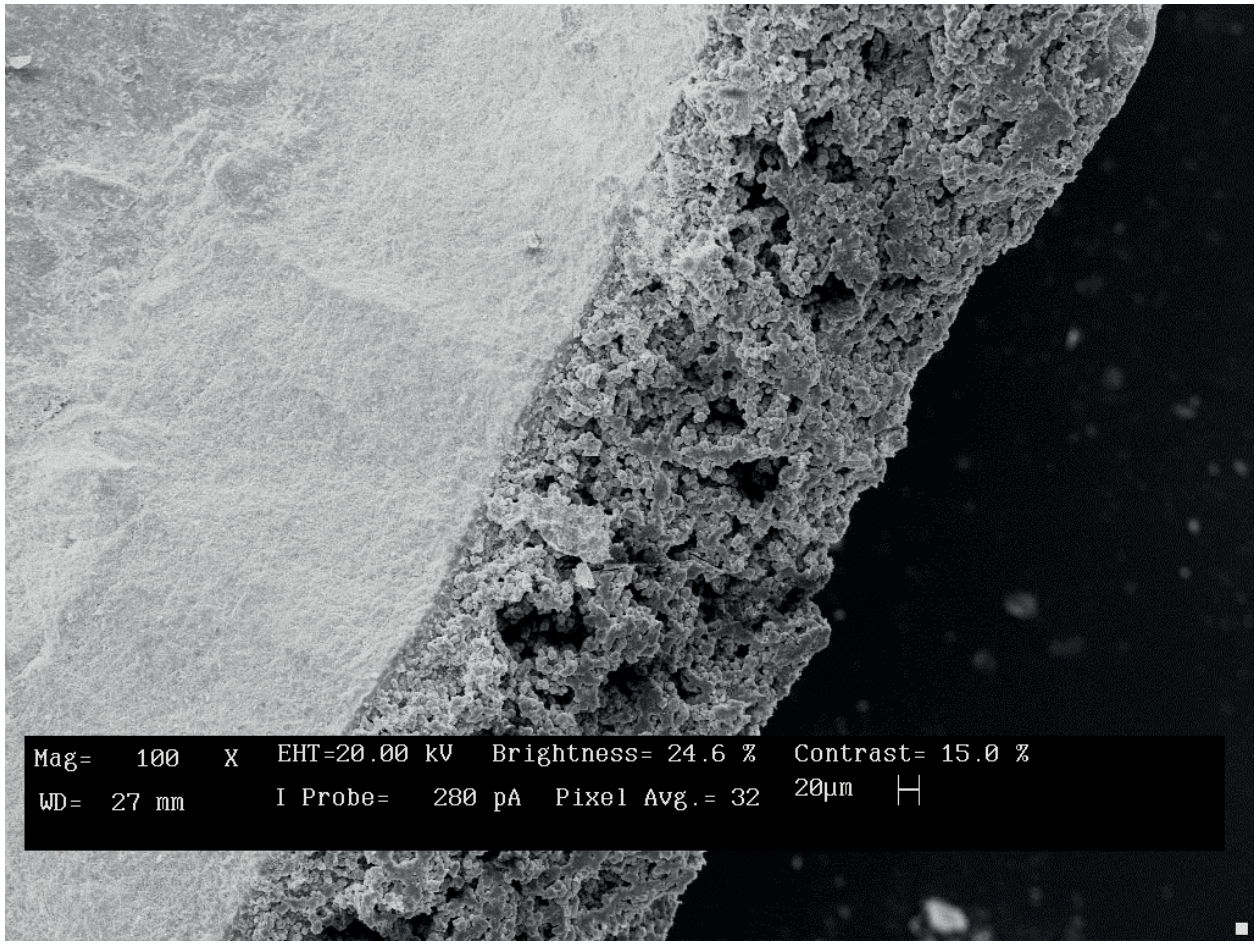

Fig. C.10. SEM image of banded mineral scale from Elmore IW-3 RD2 at 2365-2368 m depth. Band on left is barite, and band on right is Fe-bearing amorphous silica. EDX spectra also shows that the amorphous silica has trace silver.

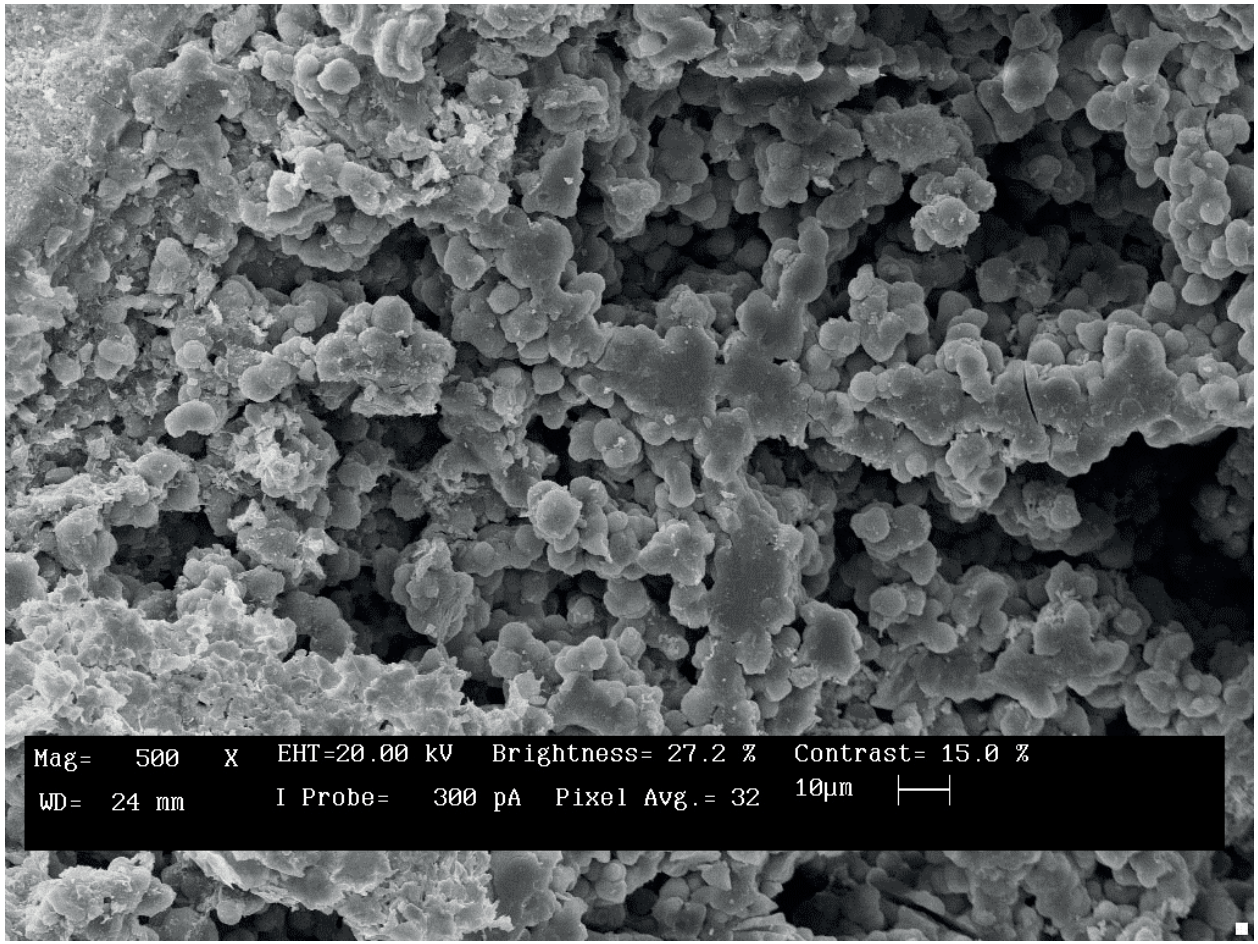

Fig. C.11. SEM image of Fe-bearing amorphous silica scale from Elmore IW-3 RD2 at 2365-2368 m depth.

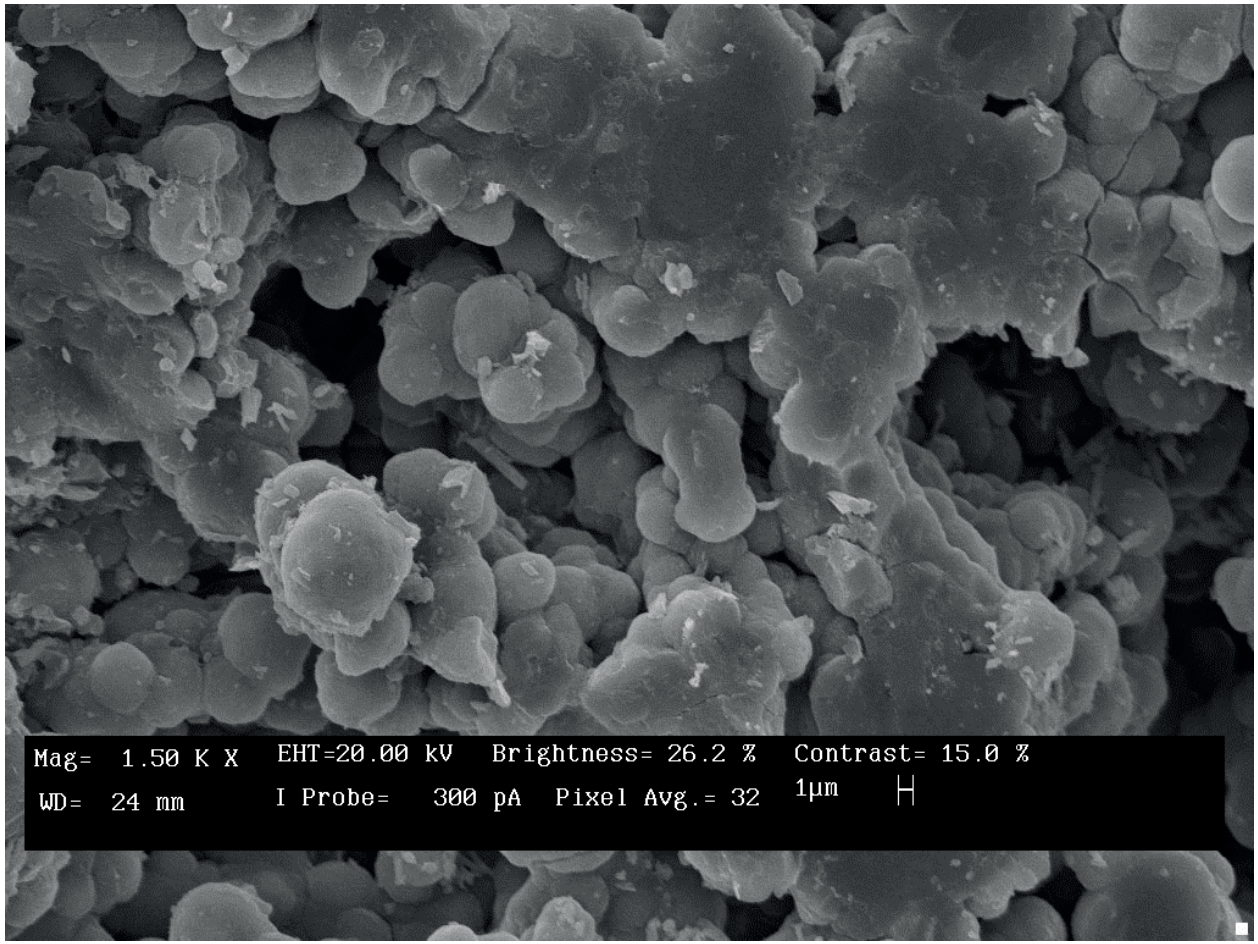

Fig. C.12. SEM image of Fe-bearing amorphous silica scale from Elmore IW-3 RD2 at 2365-2368 m depth.

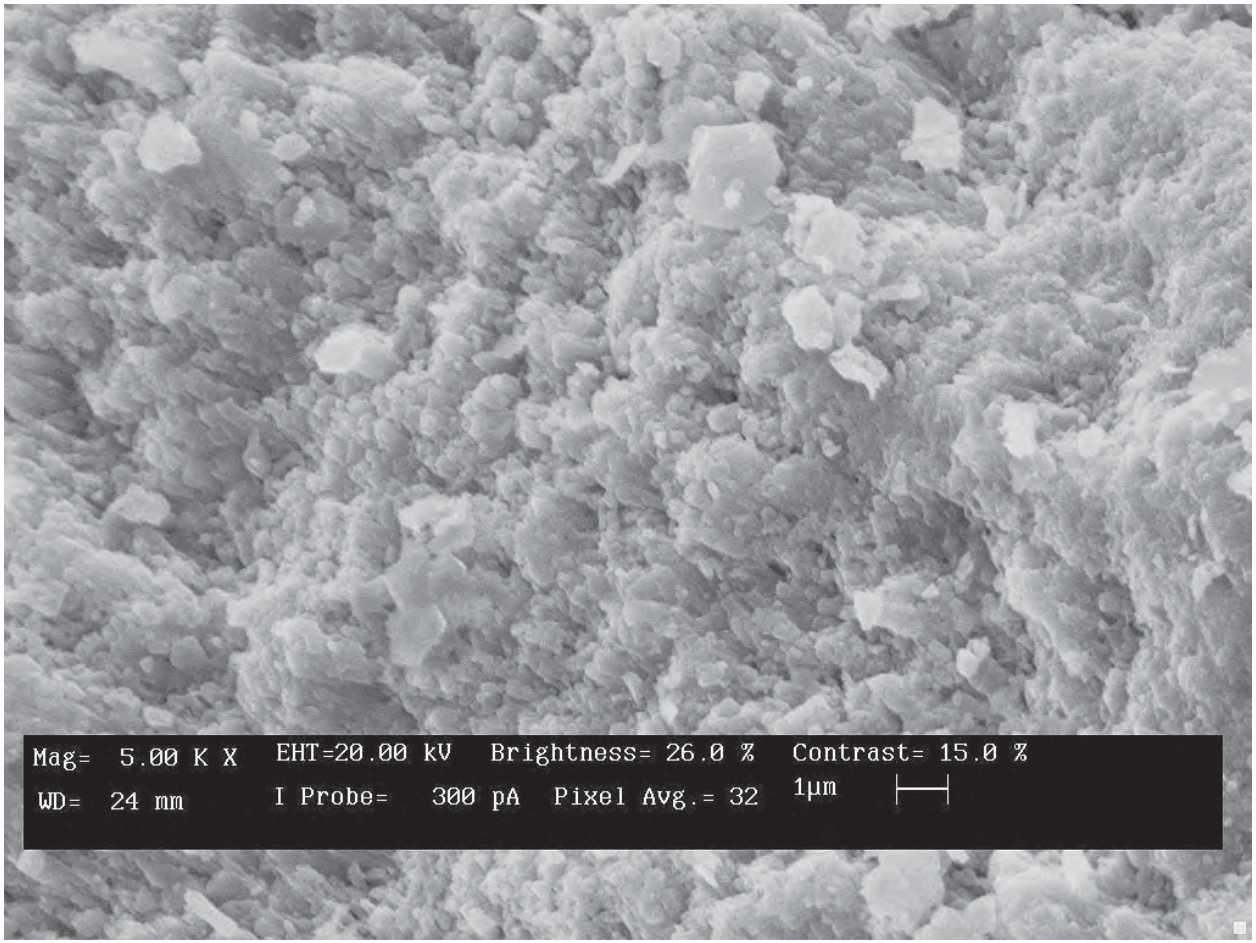

Fig. C.13. SEM image of Ti-bearing barite scale from Elmore IW-3 RD2 at 2365-2368 m depth.

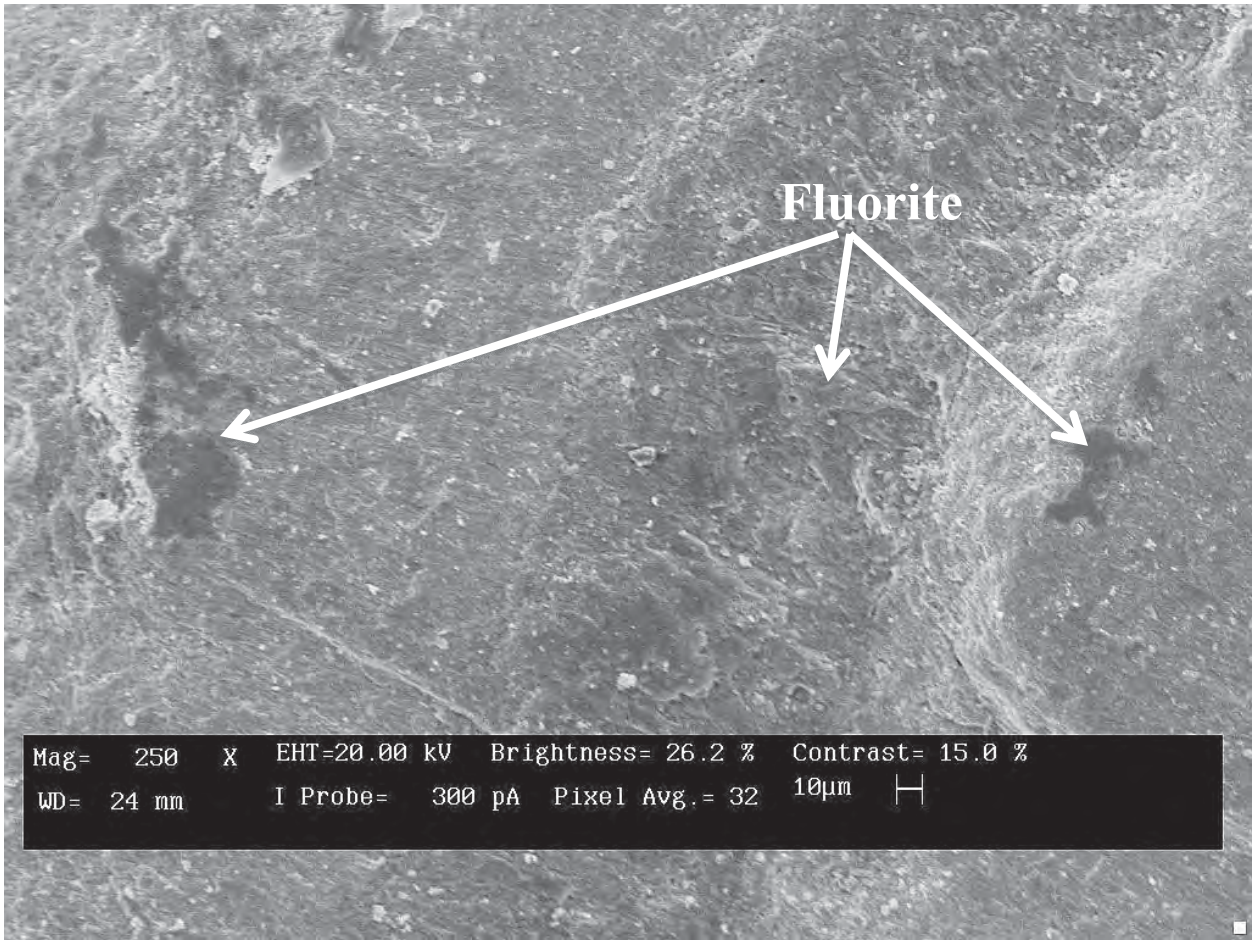

Fig. C.14. SEM image of barite and fluorite scale from Elmore IW-3 RD2 at 2365-2368 m depth. The darker mineral is fluorite within the lighter barite.

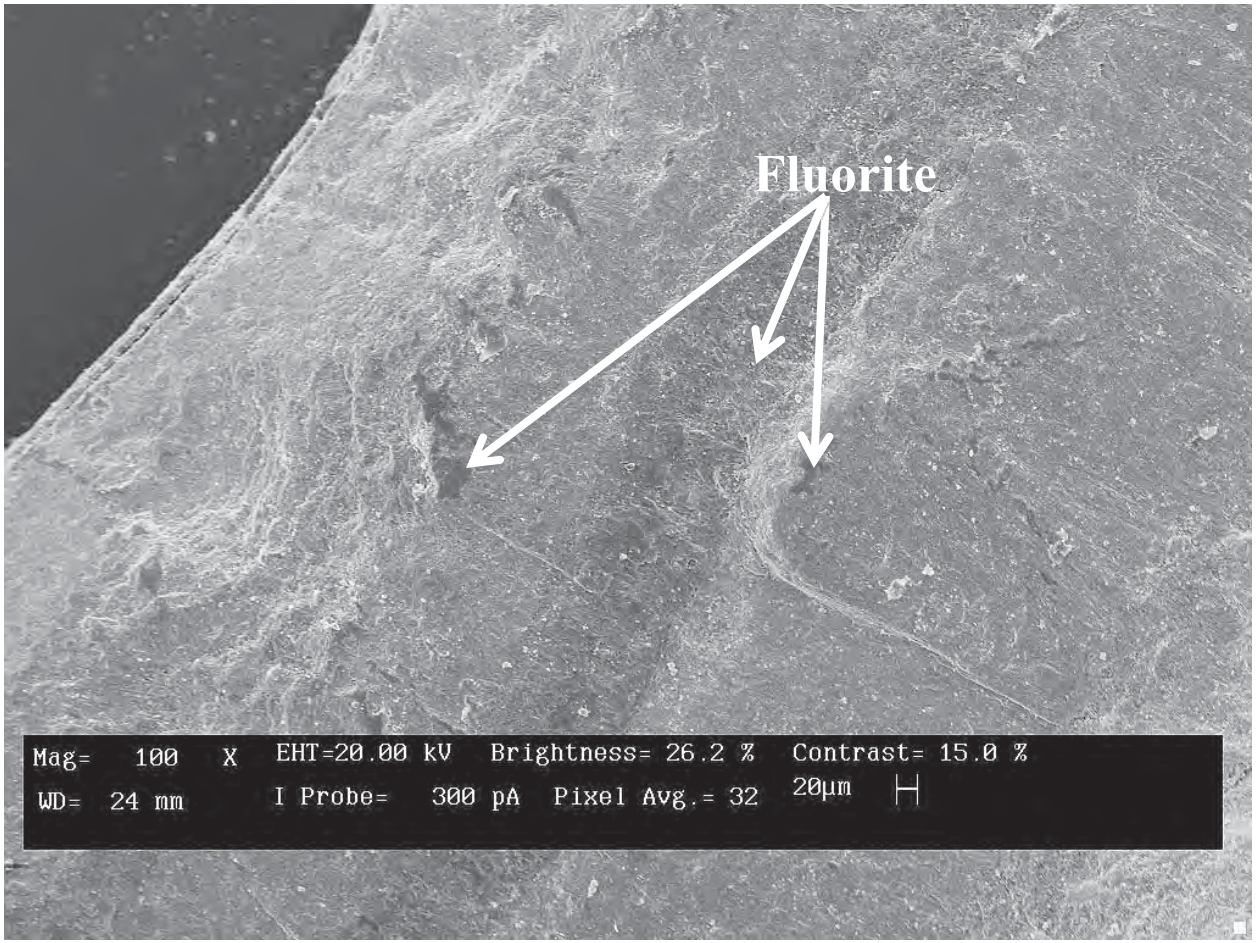

Fig. C.15. Zoomed out SEM image of barite and fluorite scale from Fig. C.14. The darker mineral is fluorite within the lighter barite.

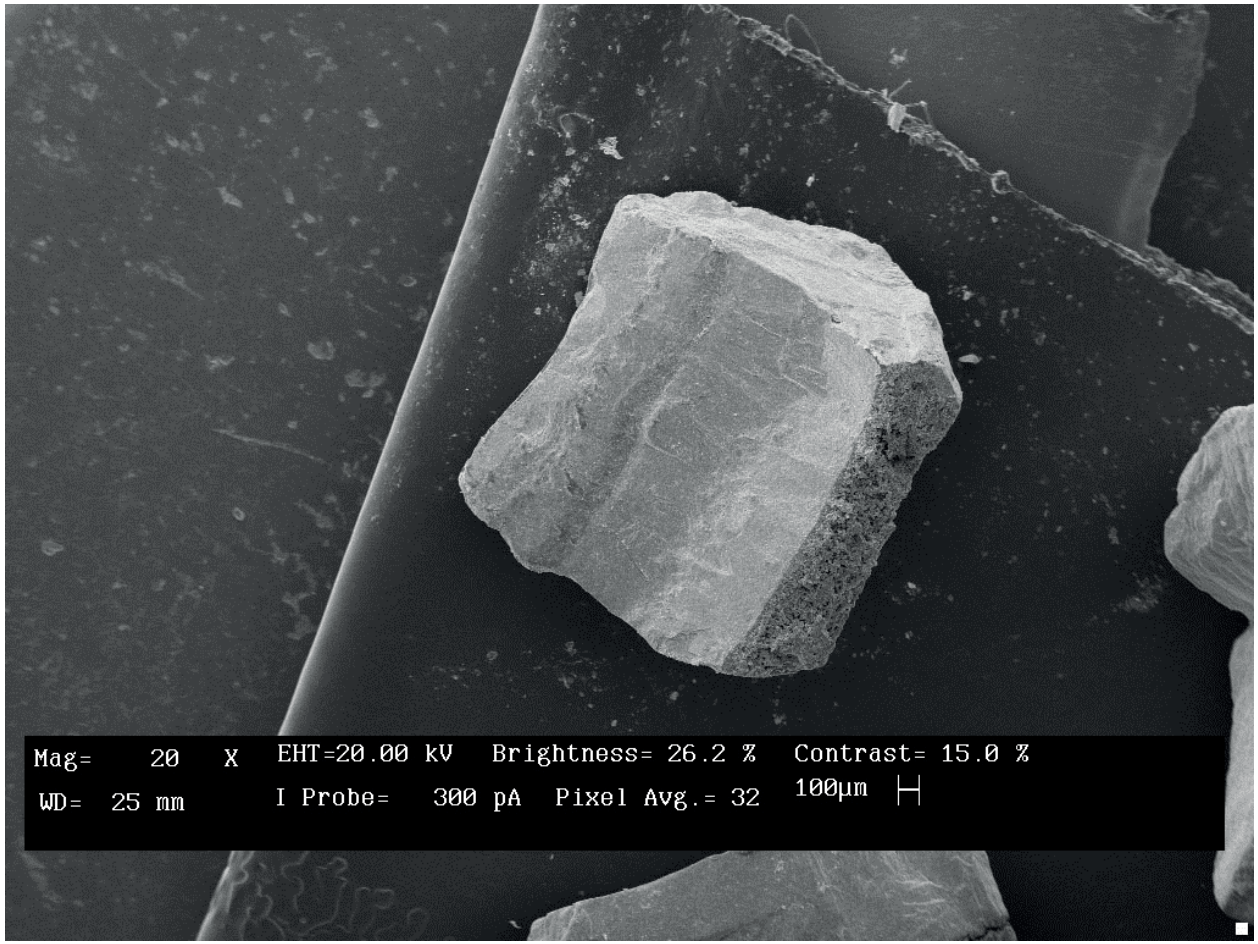

Fig. C.16. Zoomed out SEM image of barite, fluorite, and Fe-bearing amorphous silica scale from Figs. C.10 - C.15.

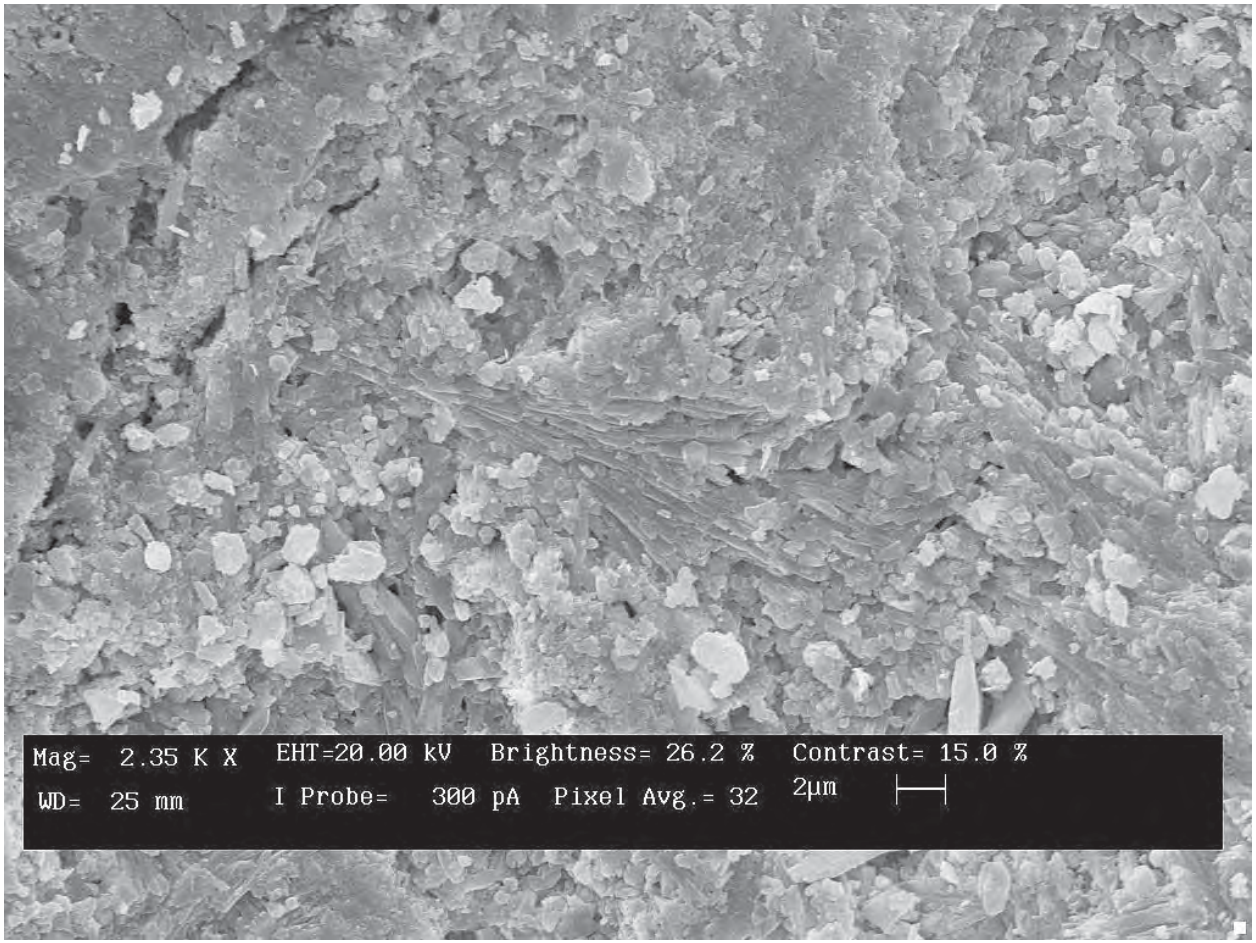

Fig. C.17. SEM image of Ti-bearing barite scale from Elmore IW-3 RD2 at 2365-2368 m depth.

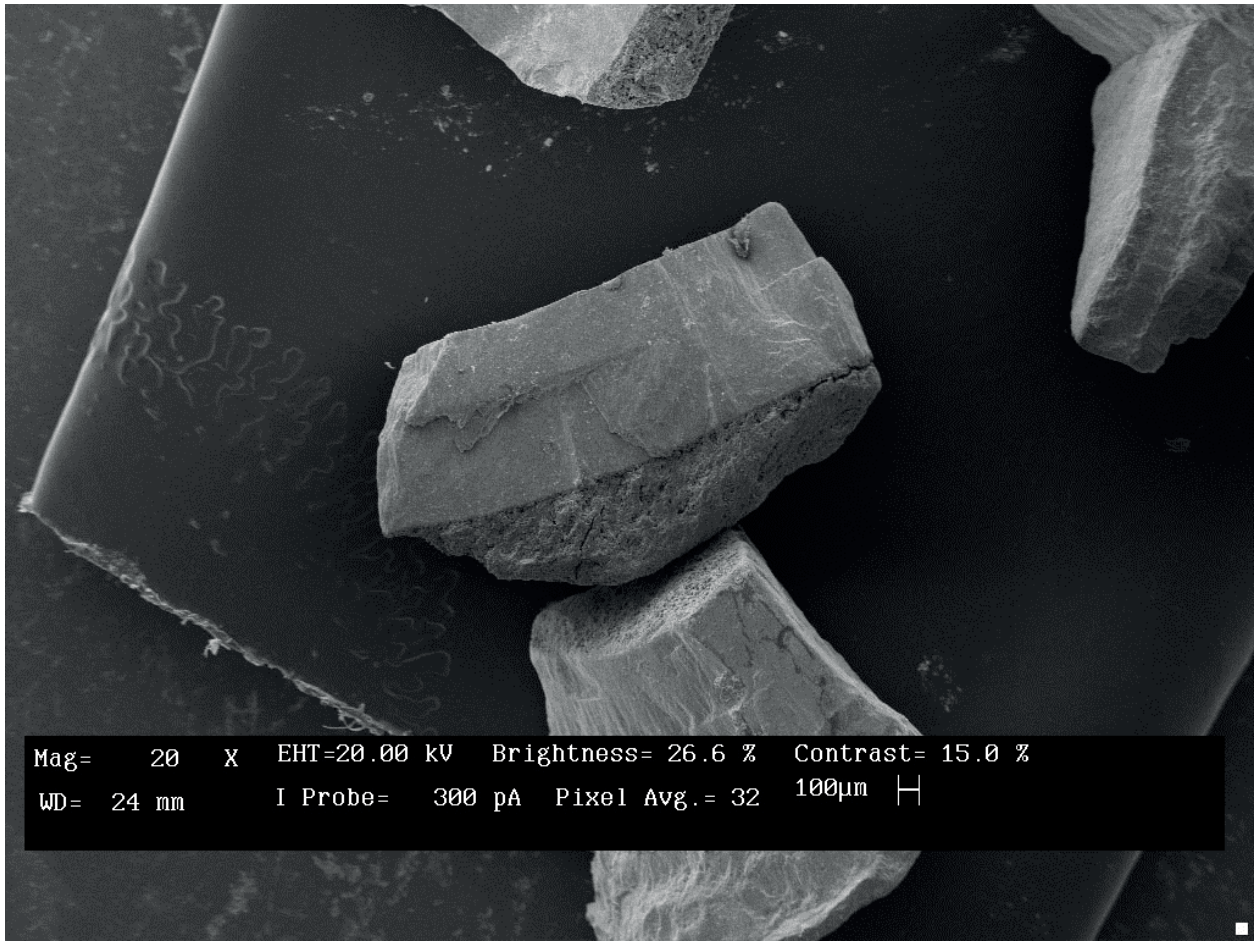

Fig. C.18. SEM image of pieces of scale from Elmore IW-3 RD2 at 2365-2368 m depth.

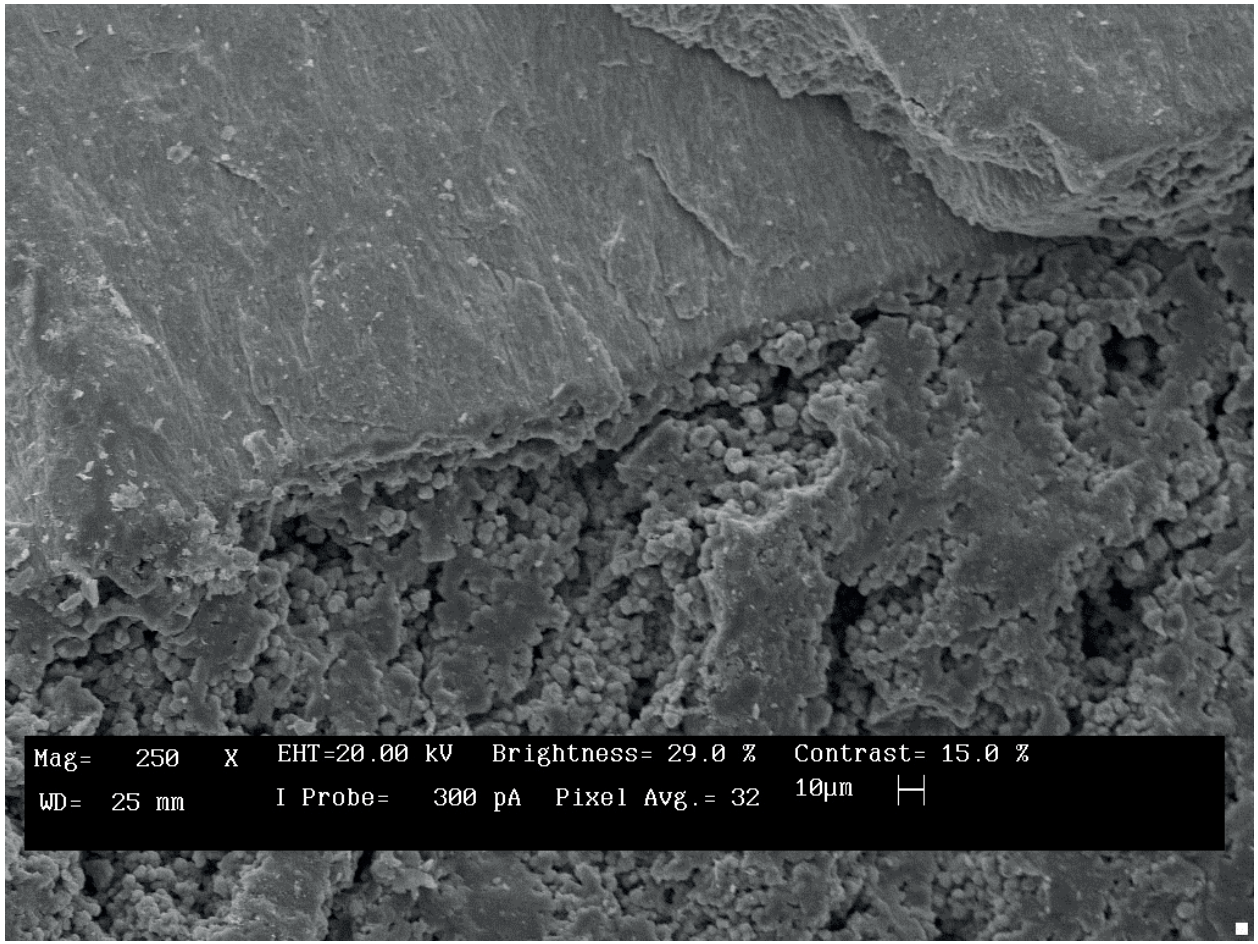

Fig. C.19. SEM image of Ti-bearing barite (top) and Fe-bearing amorphous silica (bottom) scale from Elmore IW-3 RD2 at 2365-2368 m depth.

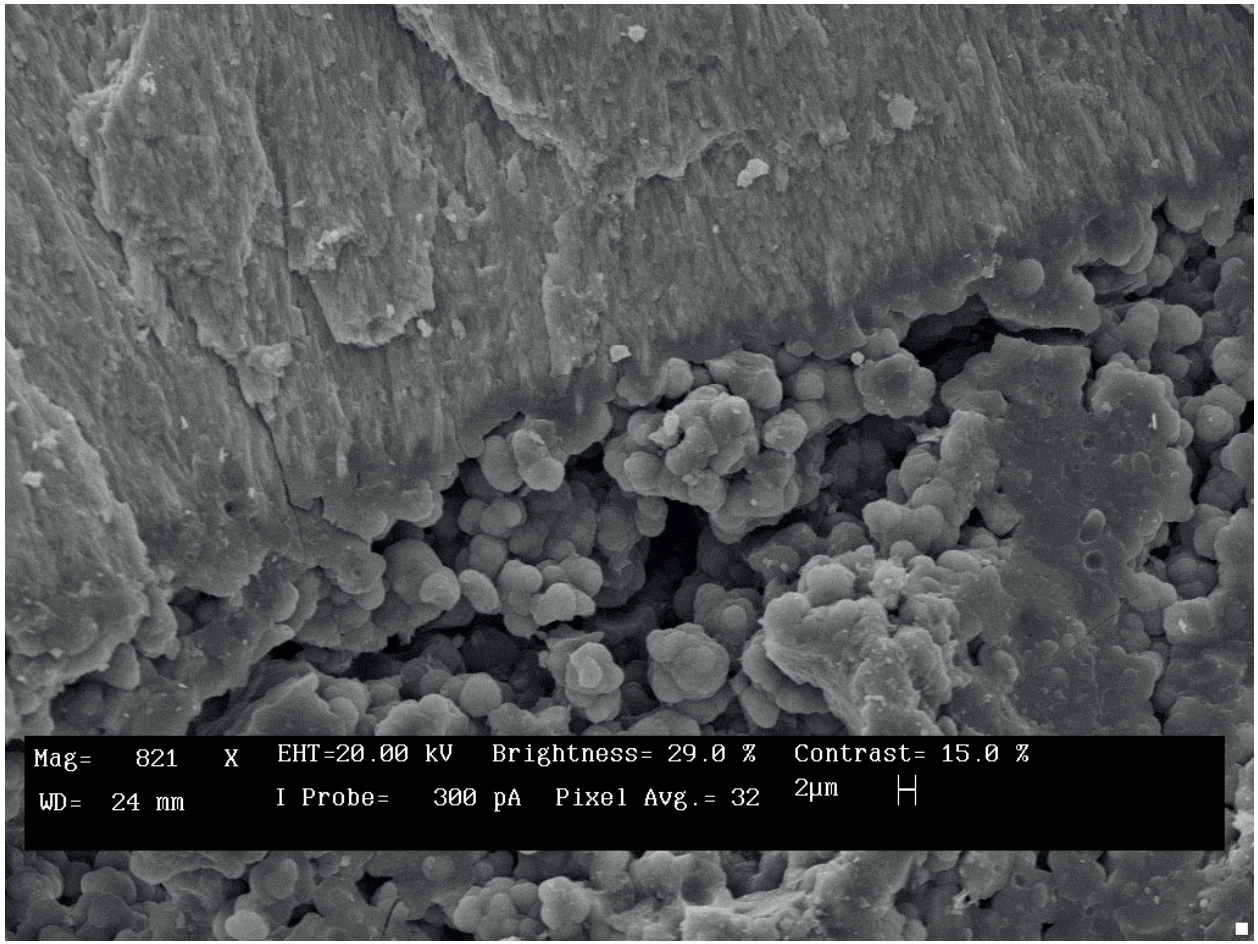

Fig. C.20. Zoomed in SEM image of Ti-bearing barite (top) and Fe-bearing amorphous silica (bottom) scale from Elmore IW-3 RD2 at 2365-2368 m depth.

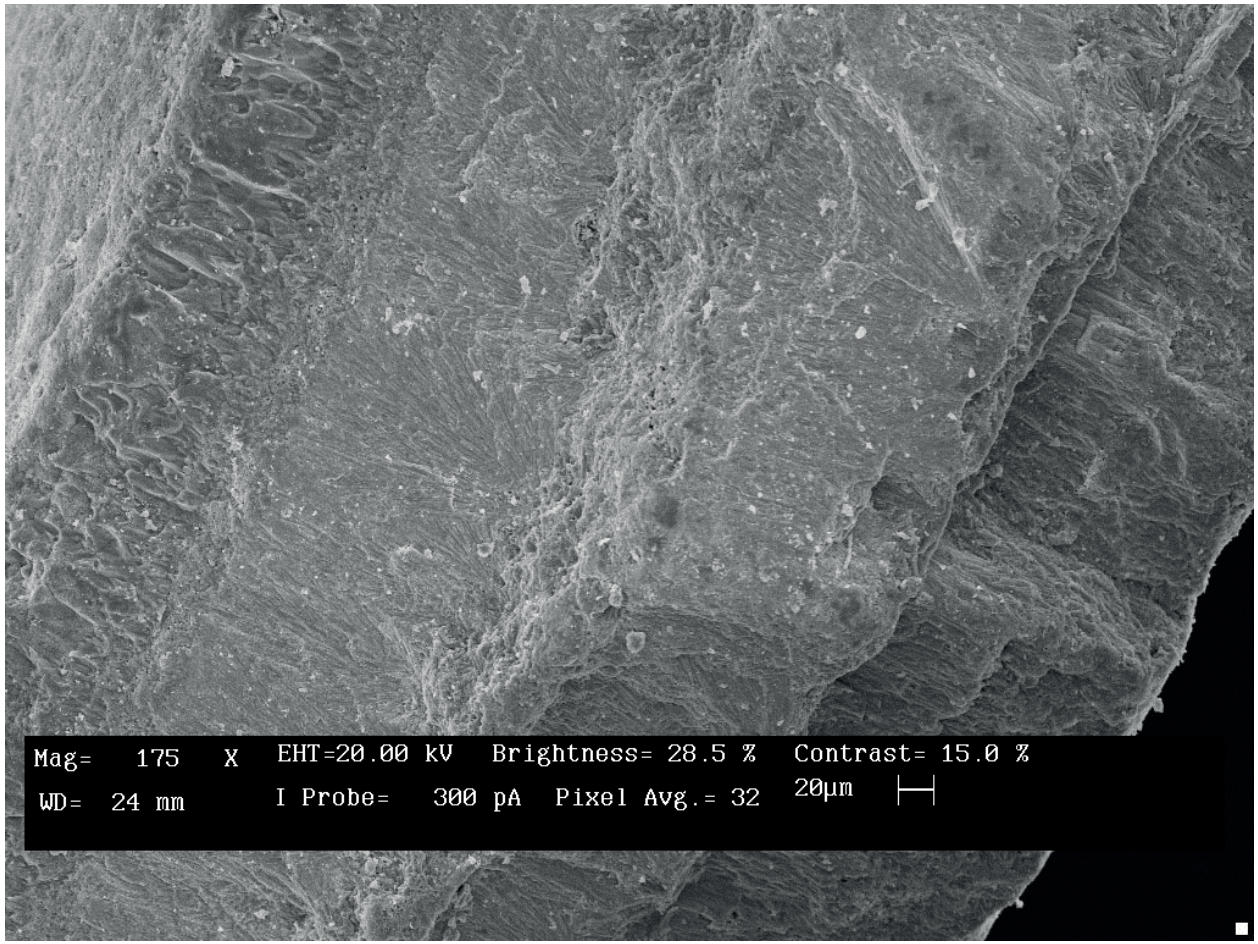

Fig. C.21. SEM image of two barite (middle) and two fluorite (far left and far right) scale from Elmore IW-3 RD2 at 2365-2368 m depth.

APPENDIX D

PHASE DIAGRAMS FOR THE H_2O-CO_2-NaCl SYSTEM

This appendix consists of phase diagrams for the H_2O-CO_2-NaCl system for T=400, 425, and 450^oC and P=100, 125, 150, and 200 Mpa calculated with the Mathematica based program of Gottschalk. The program calculates mineral stability and fugacities of water and CO_2 using the Gottschalk (1997) internally consistent database and the Duan et al. (1995) equation of state by minimization of Gibbs free energy. The fluid immiscibility fields are shown in dark (V+L) and light gray (V+L+Hl). L represents an H_2O-rich fluid, and V represents a CO_2-rich fluid. A solid halite phase is abbreviated as Hl. The antigorite + tremolite + calcite stability field (Atg+Tr+Cc) is orange, the tremolite + dolomite + calcite stability field (Tr+Dol+Cc) is blue, the talc + calcite + dolomite stability field (Tc+Cc+Dol) is red, and the quartz + dolomite stability field (Qz+Dol) is green.

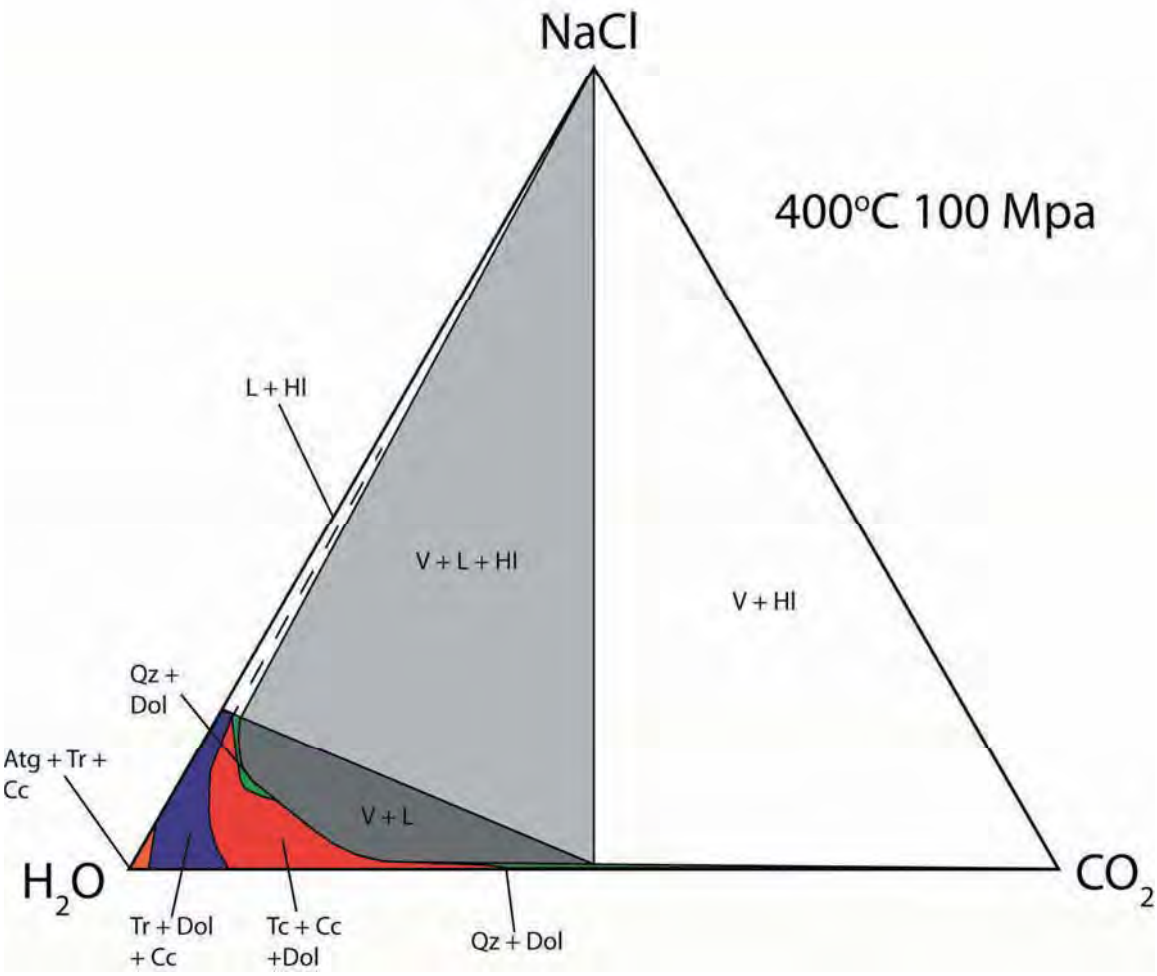
NaCl
400°C 100 Mpa
L + Hl
V + L + Hl
V + Hl
Qz +
Dol
Atg + Tr +
Cc
V + L
H2O
CO2
Tr + Dol
+ Cc
Tc + Cc
+Dol
Qz + Dol

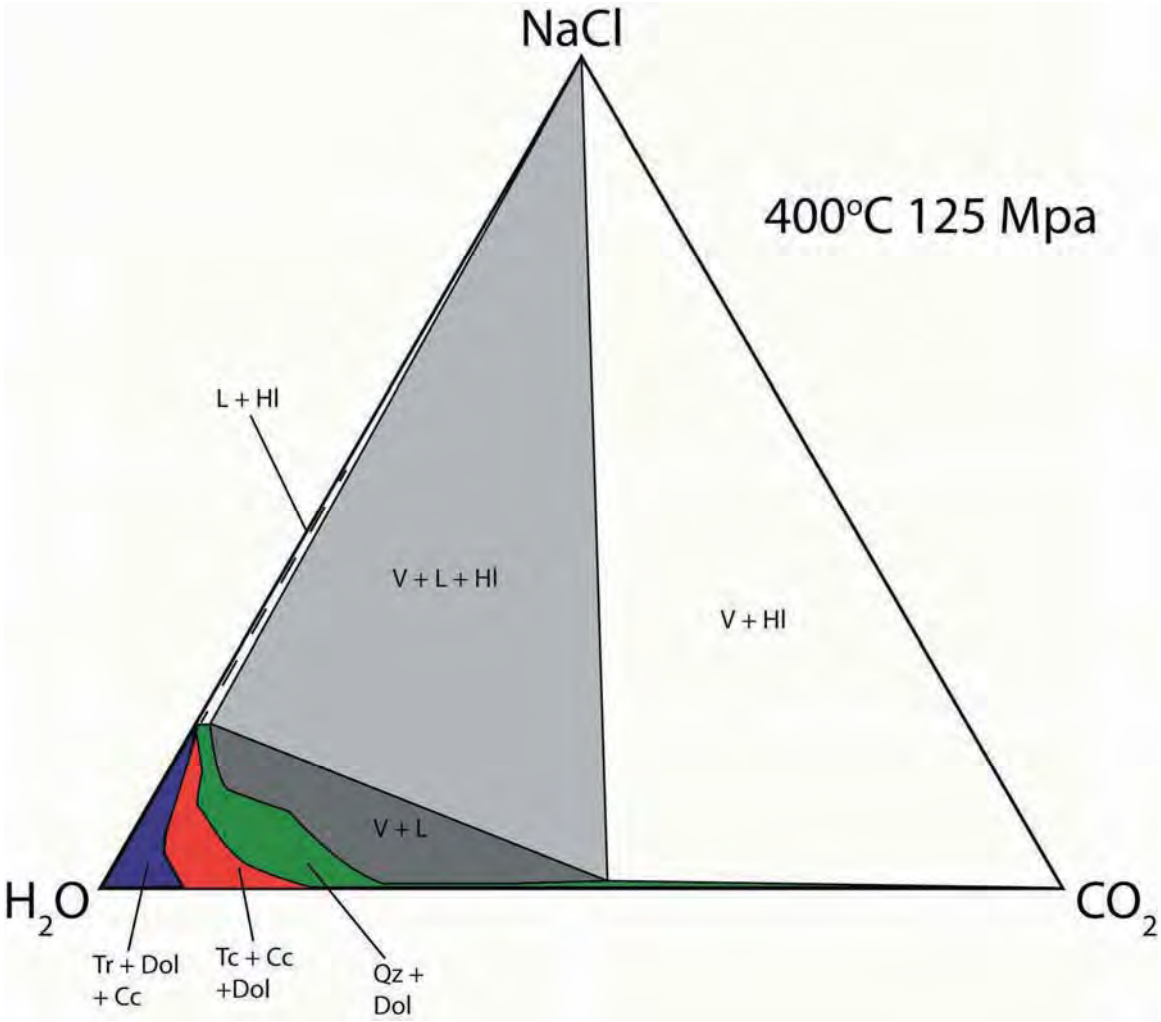
NaCl
400°C 125 Mpa
L + Hl
V + L + Hl
V + Hl
V + L
H2O
CO2
Tr + Dol
+ Cc
Tc + Cc
+Dol
Qz +
Dol

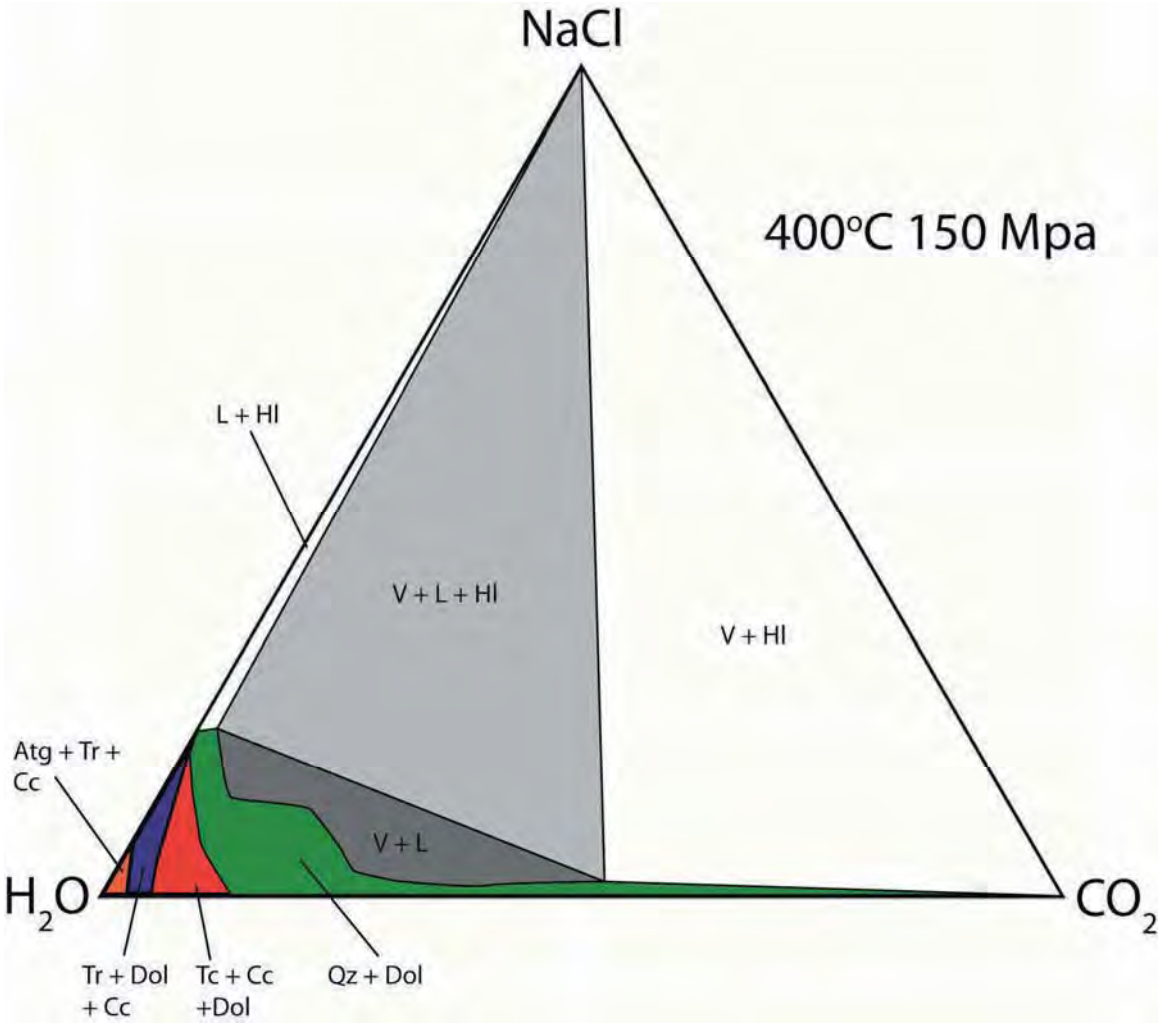
NaCl
400°C 150 Mpa
L + Hl
V + L + Hl
V + Hl
Atg + Tr +
Cc
V + L
H2O
CO2
Tr + Dol
+ Cc
Tc + Cc
+Dol
Qz + Dol

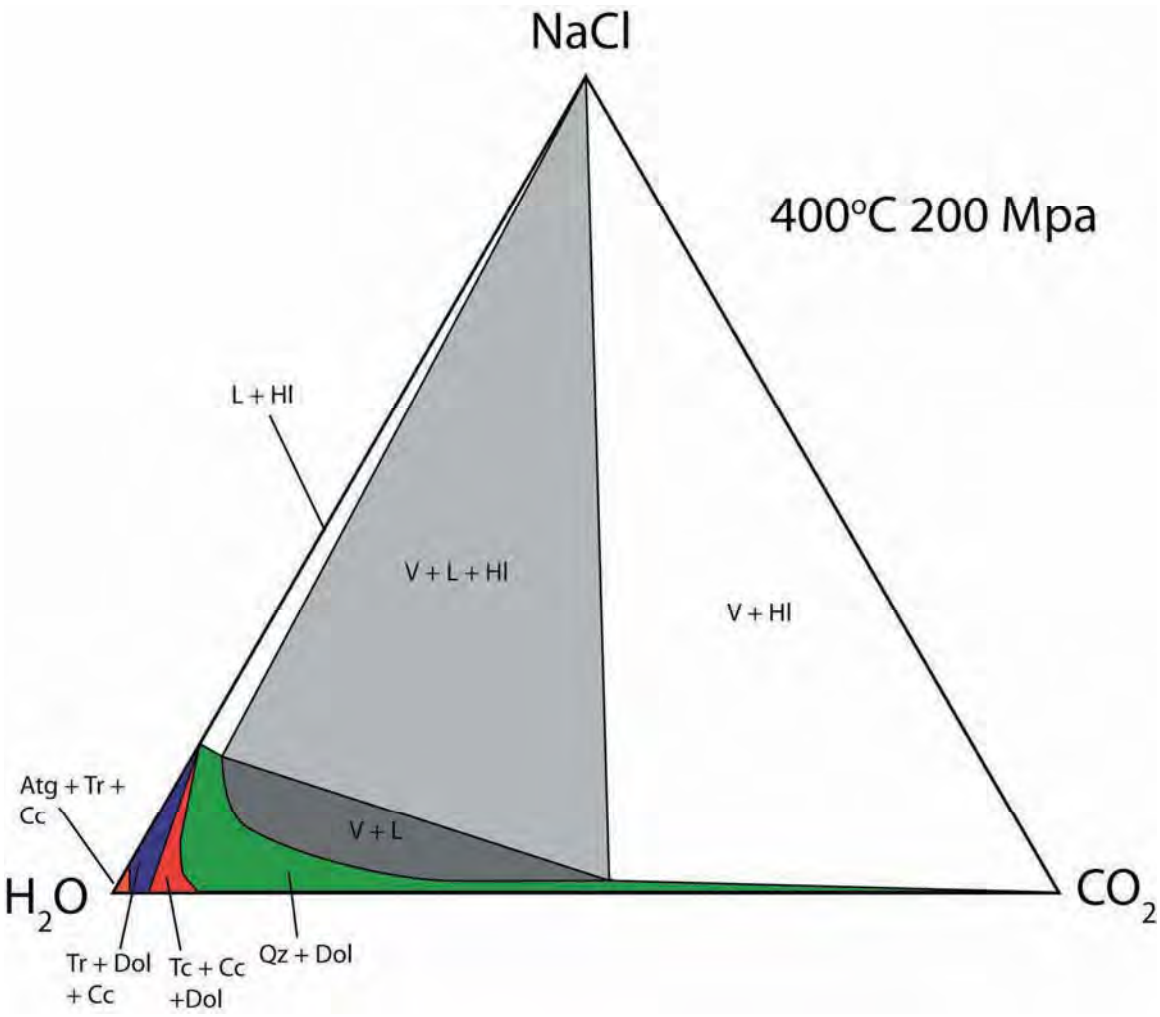
NaCl
400°C 200 Mpa
L + Hl
V + L + Hl
V + Hl
V + L
Atg + Tr +
Cc
H2O
CO2
Tr + Dol
+ Cc
Tc + Cc
+Dol
Qz + Dol

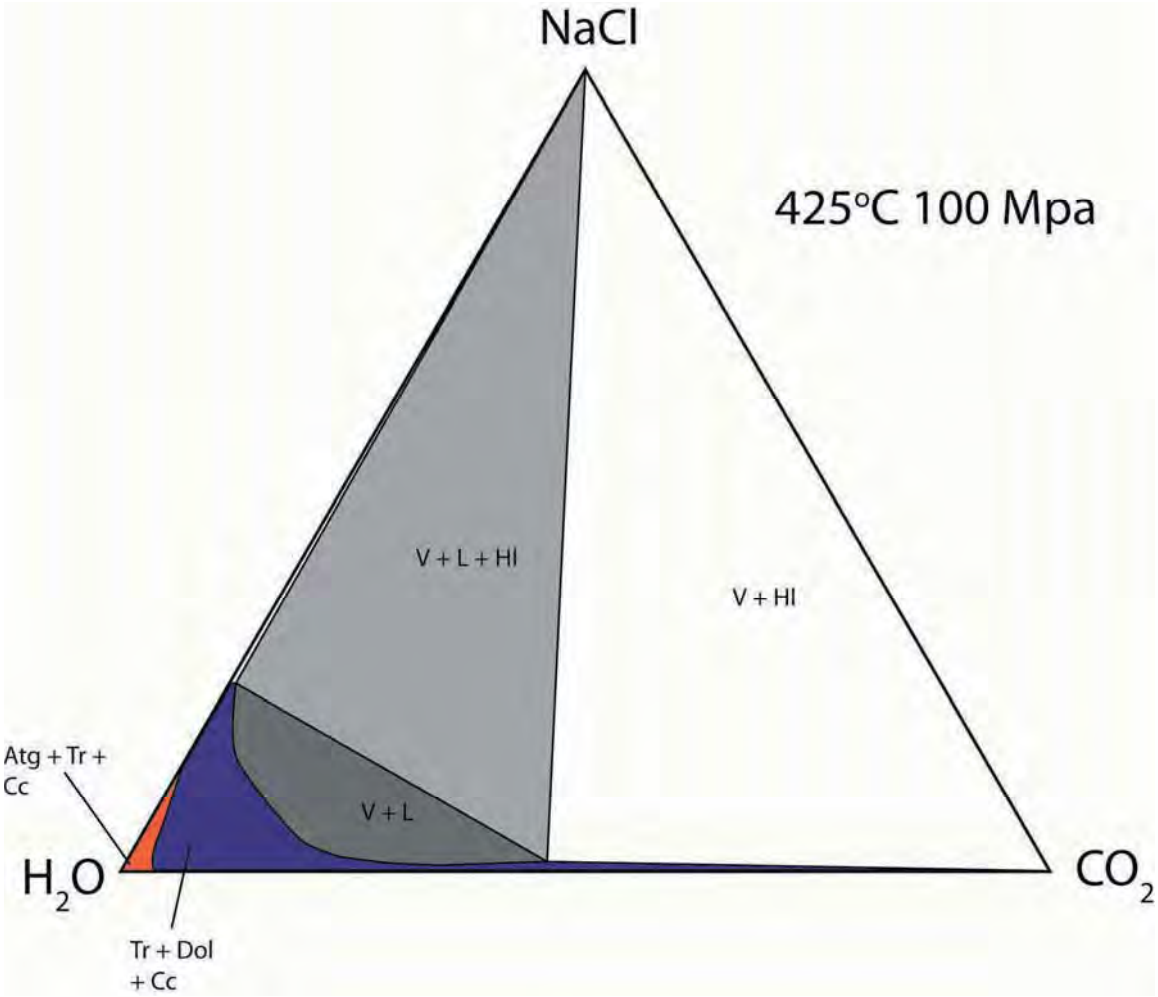
NaCl
425°C 100 Mpa
V + L + Hl
V + Hl
V + L
Atg + Tr +
Cc
H2O
CO2
Tr + Dol
+ Cc

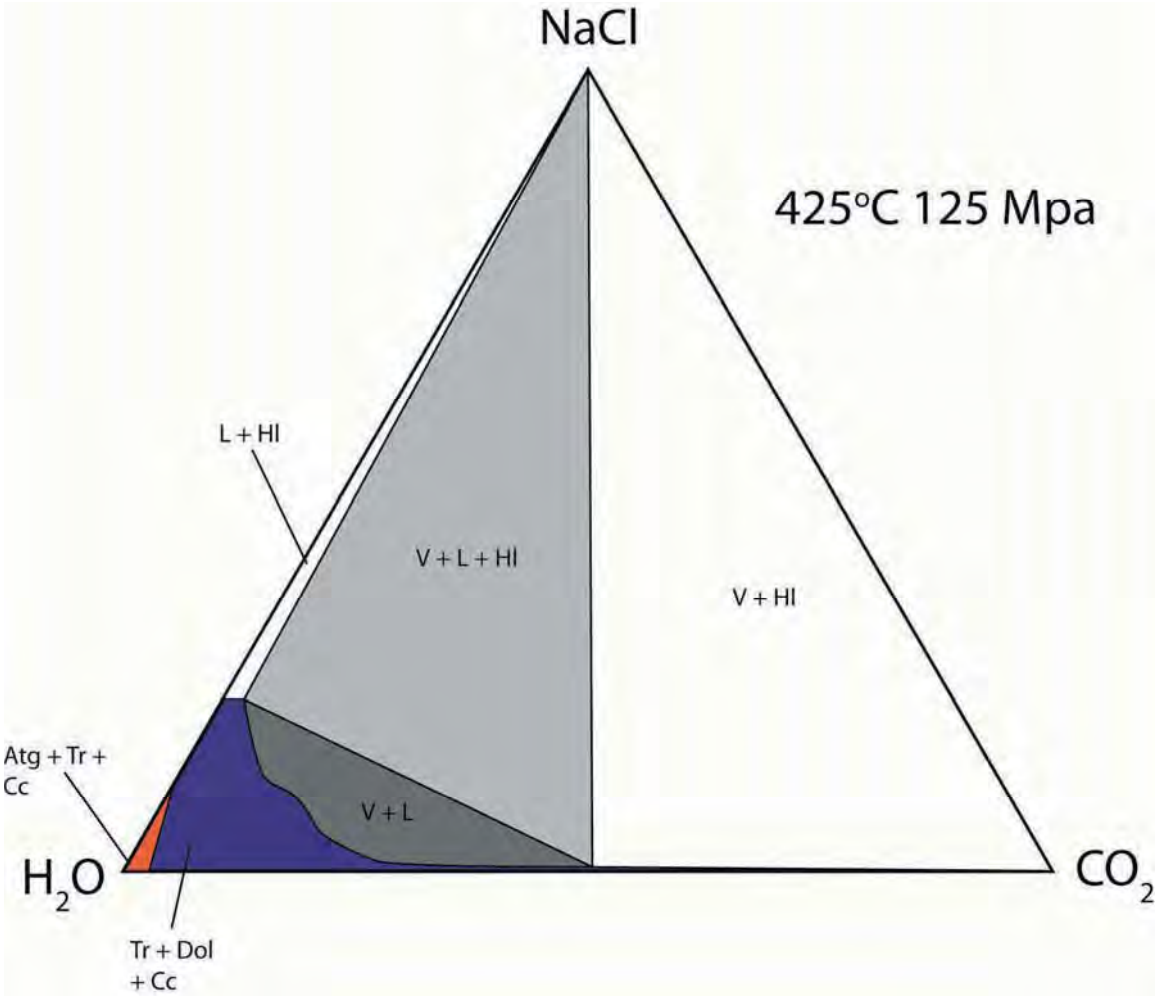
NaCl
425°C 125 Mpa
L + Hl
V + L + Hl
V + Hl
Atg + Tr +
Cc
V + L
H2O
CO2
Tr + Dol
+ Cc

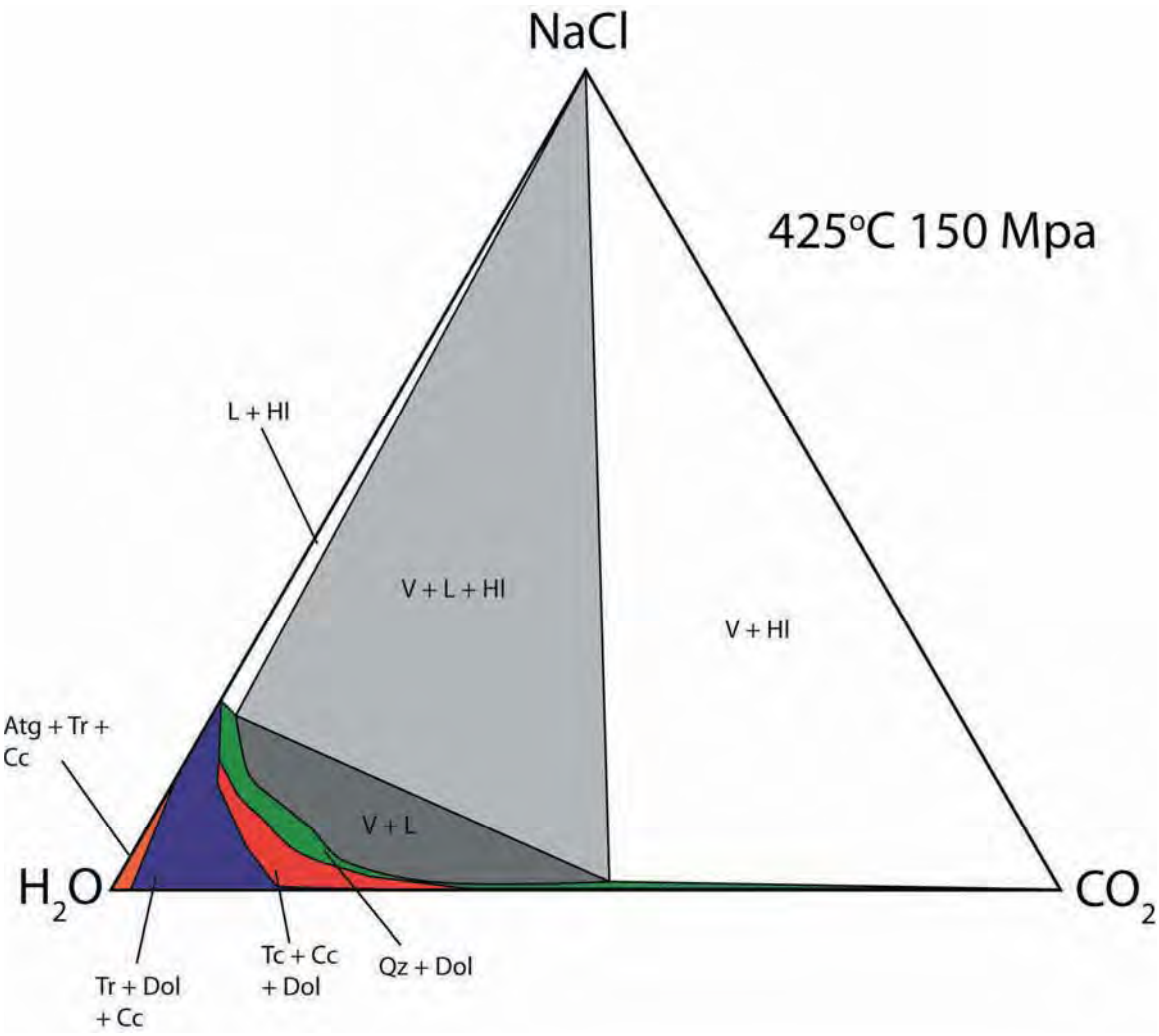
NaCl
425°C 150 Mpa
L + Hl
V + L + Hl
V + Hl
Atg + Tr +
Cc
V + L
H2O
CO2
Tr + Dol
+ Cc
Tc + Cc
+ Dol
Qz + Dol

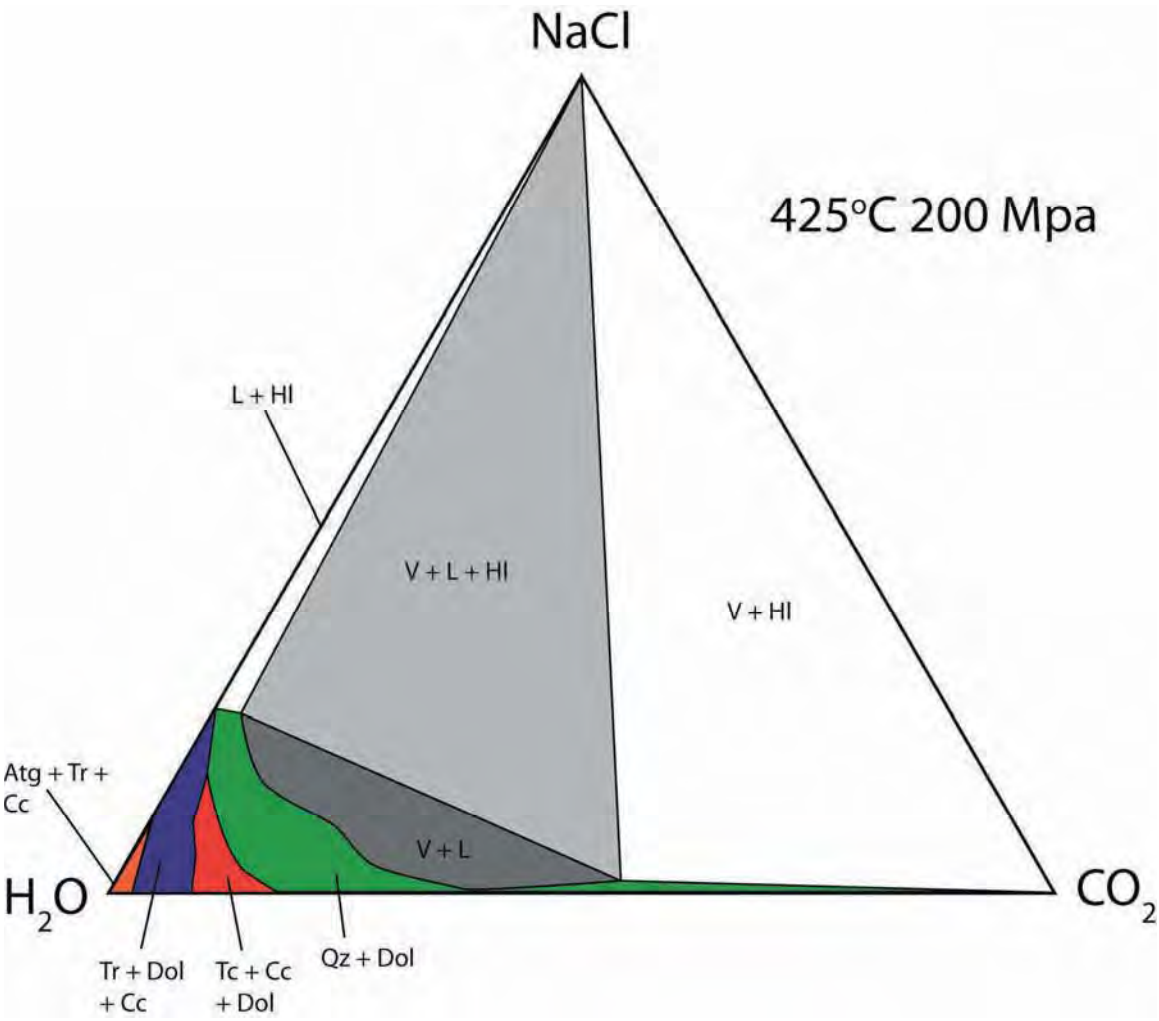
NaCl
425°C 200 Mpa
L + Hl
V + L + Hl
V + Hl
Atg + Tr + Cc
V + L
H2O
CO2
Tr + Dol + Cc
Tc + Cc + Dol
Qz + Dol

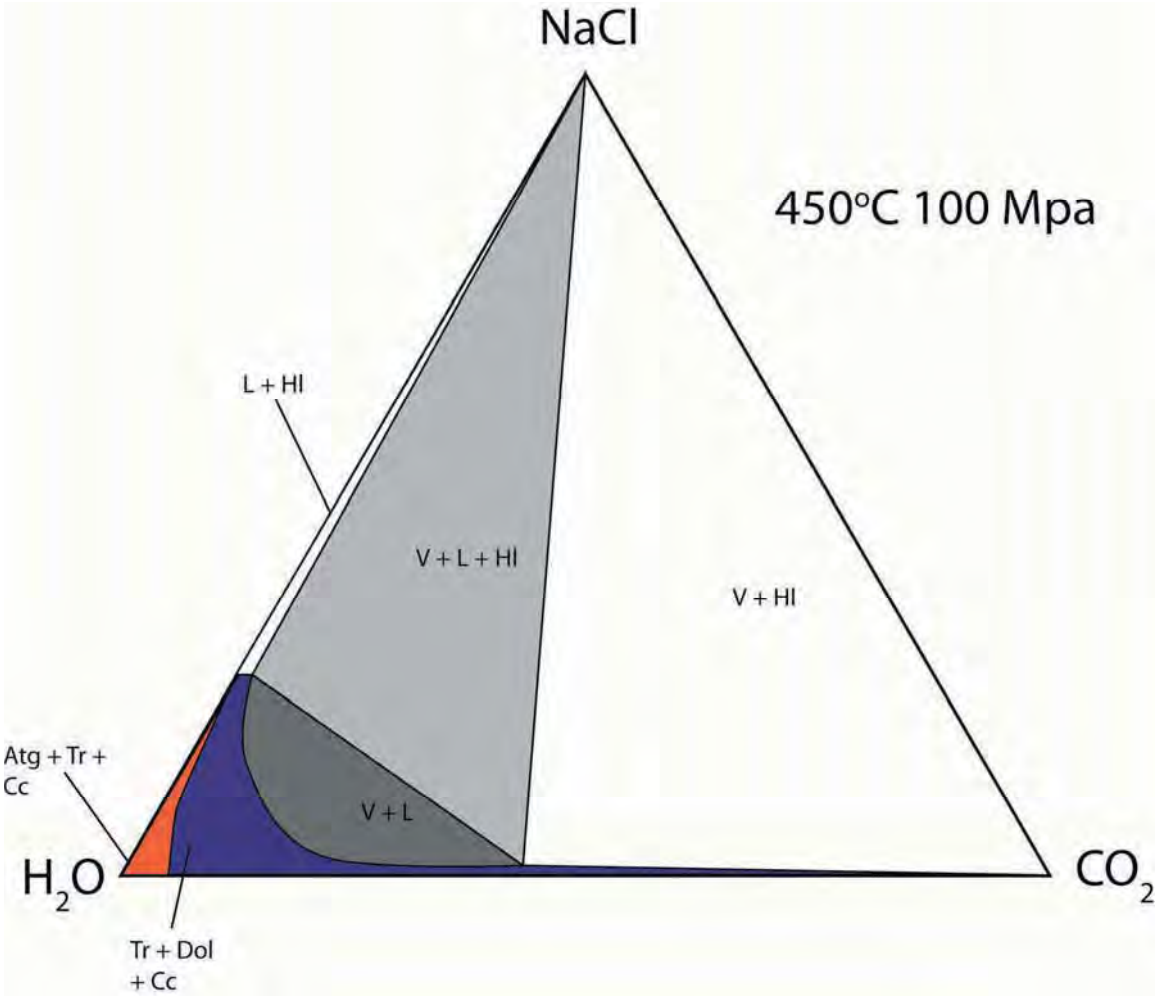
NaCl
450°C 100 Mpa
L + Hl
V + L + Hl
V + Hl
Atg + Tr +
Cc
V + L
H2O
CO2
Tr + Dol
+ Cc

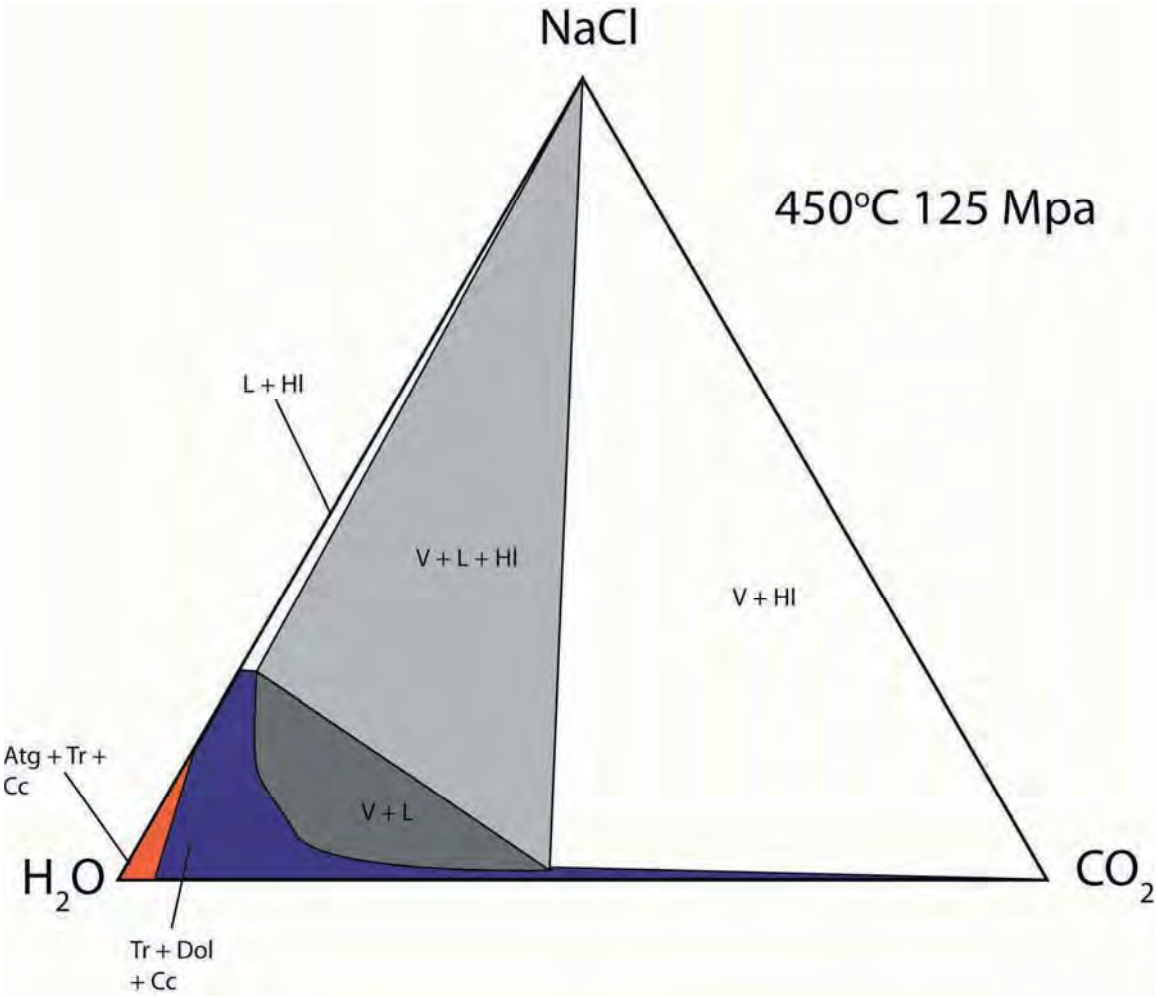
NaCl
450°C 125 Mpa
L + Hl
V + L + Hl
V + Hl
Atg + Tr +
Cc
V + L
H2O
CO2
Tr + Dol
+ Cc

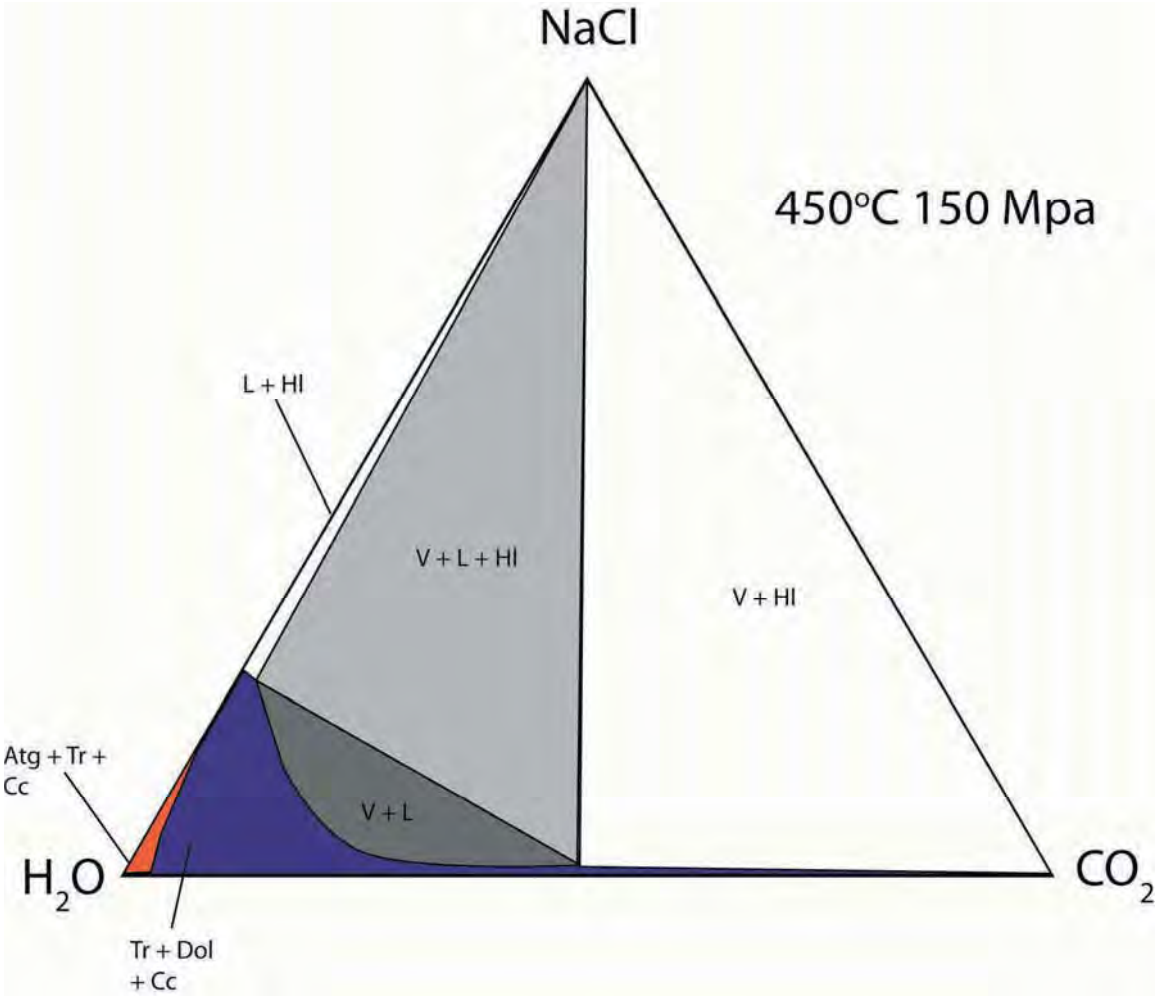
NaCl
450°C 150 Mpa
L + Hl
V + L + Hl
V + Hl
Atg + Tr +
Cc
V + L
H2O
CO2
Tr + Dol
+ Cc

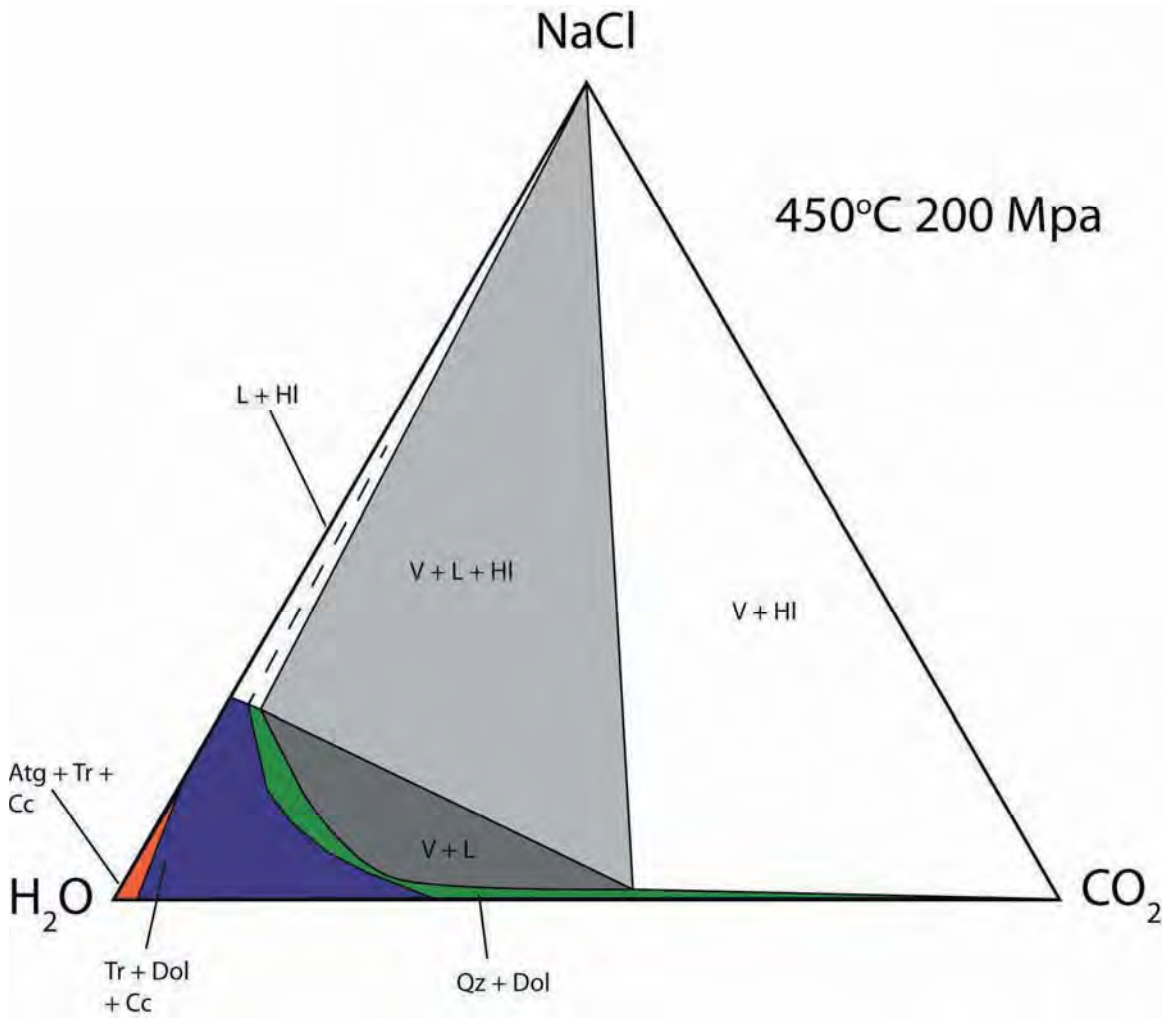
NaCl
450°C 200 Mpa
L + Hl
V + L + Hl
V + Hl
Atg + Tr +
Cc
V + L
H2O
CO2
Tr + Dol
+ Cc
Qz + Dol